Silicon Microdisk Resonators for Nonlinear Optics and Dynamics

Thesis by

Thomas Johnson

In Partial Fulfillment of the Requirements

for the Degree of

Doctor of Philosophy

California Institute of Technology

Pasadena, California

2009

(Defended March 17th, 2009)

Dedicated to Susan, Soren, my family, and my friends, with love

Acknowledgements

My thanks go out to my advisor, Oskar Painter. His continual striving to understand is a great example to us all. For the length of our association, I have been able to count on being pushed to dig into a problem, to probe, to understand. His broad and deep knowledge has been a priceless resource in my research and I am exceedingly grateful to have had the opportunity to work with him. He's been patient with my foibles and is always ready to try to motivate me and his other students, and I hope he's not been disappointed.

The colleagues I've been privileged with have taught me an incredible amount and have provided support and fellowship these last years. Whatever I have done, I doubt that it would have been possible without their steadying influences and generosity: Kartik Srinivasan, Matt Borselli, and Paul Barclay were my original cohort. Matt Borselli and I worked side-by-side for countless hours on the silicon project, and sat back-to-back as office-mates for years. His good humor, incredible process, optimism, and keen intellect are just some of his wonderful qualities. Kartik Srinivasan is the brightest, kindest, most dedicated colleague one could hope for. I deeply value his friendship and hold him in regard just short of embarrassing awe. Paul Barclay is fun, astute,

generous with his time and assistance, and will be well missed whenever he is not close by.

More recently, Raviv Perahia, Chris Michael, Matt Eichenfield, and Qiang Lin have enriched my work-life with their frequent presences. These gentlemen are wise, intelligent, and hard-working. Not a lot would get done without them, and I fully expect to hear amazing things come from them all.

My dear friends have supported me and celebrated with me all the while. I would list you and all you mean to me, but I don't think I could do you justice. The fondest of thanks and the promise that if I can help you as you've helped me, I will.

My parents are special folks. They put up with an incorrigible son, knowing, I suppose, that there might be something good going on in there. I must apologize for the "brain-drain", and thank you for making sure that what we needed, we had. I must apologize for all the library late-fees, and thank you for standing behind me when I needed a push forward. To my brother and my sisters: you are so very dear to me, and I wish you nothing but joy and fulfillment in all things. You've given me much, and I hope I've shared with you often enough that you know it.

Susan: thank you for lightening my burdens. Thank you for sheltering me, for cheering for me, for sharing my life. Our child is fortunate to have such a mother, and I have you and Soren as my promise for the future.

List of Publications

Pertinent publications

[1] M. Borselli, T. J. Johnson, and O. Painter, "Beyond the Rayleigh scattering limit in high-Q silicon microdisks: theory and experiment," Opt. Express **13**(5), 1515–1530 (2005).

[2] K. Srinivasan, M. Borselli, T. J. Johnson, P. E. Barclay, O. Painter, A. Stintz, and S. Krishna, "Optical loss and lasing characteristics of high-quality-factor AlGaAs microdisk resonators with embedded quantum dots," Appl. Phys. Lett. **86**, 151106 (2005).

[3] T. J. Johnson, M. Borselli, and O. Painter, "Self-induced optical modulation of the transmission through a high-Q silicon microdisk resonator," Opt. Express **14**(2), 817–831 (2006).

[4] M. Borselli, T. J. Johnson, and O. Painter, "Measuring the role of surface chemistry in silicon microphotonics," Appl. Phys. Lett. **88**, 131114 (2006).

[5] M. Borselli, T. J. Johnson, and O. Painter,"Accurate measurement of scattering and absorption loss in microphotonic devices," Opt. Lett., **32**(20), 2954-2956 (October 5, 2007).

[6] M. Borselli, T. J. Johnson, C. P. Michael, M. D. Henry, and O. Painter, "Surface encapsulation layers for low-loss silicon photonics," App. Phys. Lett., **91**(13) (Sept. 28, 2007).

[7] C. P. Michael, M. Borselli, T. J. Johnson, C. Chrystal, and O. Painter, "An optical fiber-taper probe for wafer-scale microphotonic device characterization," Opt. Express, **15**(8), 4745-4752 (February 8, 2007).

[8] Q. Lin, T. J. Johnson, R. Perahia, C. P. Michael, and O. J. Painter,"A proposal for highly tunable optical parametric oscillation in silicon micro-resonators", Opt. Express, **16**(14) 10596 (July 1, 2008).

[9] Q. Lin, T. J. Johnson, C. P. Michael, and O. Painter, "Adiabatic self-tuning in a silicon microdisk optical resonator", Opt. Express, **16**(19), 14801 (September 4, 2008).

Manuscript in preparation

[1] T. J. Johnson and O. Painter, "Measuring the role of surface chemistry in silicon photonics: chemical treatments and free carrier lifetime."

Abstract

Silicon is incredibly well-studied as an electronic material. Since the out-migration of William Noyce, Gordon Moore, and the rest of the original Fairchild Semiconductor class from Shockley Semiconductor, silicon has only grown in prominence. Untold billions have been expended on research, development, and manufacture, and now silicon is perhaps the most well-controlled commercial material on Earth. For all that, the use of silicon as a mechanical material, though envisioned in the late 1950s, largely became viable only after the advent of large-scale silicon processing for microelectronics. As an optical material, silicon also has a long pedigree, with most of the positive focus on its excellent optical transparency and the enormous potential for improvement residing in its lack of effective emission.

This thesis concerns an alternate route to the generation of light in silicon: the nonlinear route. Resonant elements play a critical role in making this viable. The ability to build up optical intensity in the confined volume of a microresonator reduces the input power required to achieve a given energy density. Silicon also has certain excellent nonlinear properties: a large Raman gain coefficient, for example, and an appreciable Kerr effect. Unfortunately, silicon also exhibits significant

two-photon absorption (TPA) in the convenient telecommunications wavelength bands. As such, the build-up of optical energy in silion may also be accompanied by a build-up of TPA-induced free-carrier populations. These populations may serve to limit the efficiency of nonlinear processes or to generate additional nonlinear behavior in their interactions with optical fields.

Thus two important stepping-stones on the way to the low-power, low-footprint use of silicon as an optical material are: the need to reduce optical losses in the optical elements, and to reduce or modify the populations of free carriers generated in the nonlinear optics regime. This thesis will present design considerations of, fabrication techniques developed for, and characterization techniques of high-Q silicon microresonators. In the course of this work, we have created silicon microdisk resonators with quality factors as high as 5×10^6, and high-Q silicon microdisks with free-carrier lifetimes in the deep subnanosecond regime (Q=5–6$\times 10^5$ and carrier lifetimes $\leq$ 240 ps). These results, with no indication that higher quality factors or shorter carrier lifetimes are not possible in similar structures, indicate that coherent, CW optical generation in passive silicon microresonators is approaching feasibility.

Contents

List of Figures

List of Tables

Glossary of Acronyms

MUX/DEMUX Multiplex/demultiplex

BOX Buried oxide layer for SOI wafers

FCA Free-carrier absorption

FCL Free-carrier lifetime

FEM Finite-element method

FWM Four-wave mixing

ICP/RIE Inductively coupled plasma / reactive ion etching

MUX Multiplexed

OSA Optical spectrum analyzer

Q Quality factor

PECVD Plasma-enhanced chemical vapor deposition

PL Photoluminescence

PLE Photoluminescence excitation

PVD Physical vapor deposition

SEM Scanning electron microscope

SOI Silicon-on-insulator

SPM Self phase modulation

TPA Two-photon absorption

WGM Whispering-gallery mode

XPM Cross-phase modulation

ZDWL Zero-dispersion wavelength

Chapter 1

Introduction

Silicon (Si) photonics has received renewed interest of late due to the rapidly approaching limits of "Moore's Law" scaling in Si microelectronics, and the potential to leverage the near half-century of processing development in the microelectronics industry [1, 2]. There has followed several recent advances in Si optoelectronics, chief among them the demonstrations of a Gbit/sec Si optical modulation [3], all-optical high-speed switching [4], and a nonlinear optical Si laser source based on the stimulated Raman effect [5–7]. Enabling these and other developments in integrated optical and electronic Si circuits is the availability of high-index-contrast silicon-on-insulator (SOI) wafers, which provide tight optical confinement of light which makes for high-density optoelectronic integration and nonlinear optics, and exceptional photonic and electronic isolation through the high-quality underlying thermal oxide. As Si microphotonic device functionality and integration advances, and light is more often routed into the Si, it will be important to develop low-loss Si microphotonic circuits in addition to the already low-loss glass-based planar lightwave circuits (PLCs) [8, 9]. One key element in

such circuits is the microresonator, where light can be distributed by wavelength or localized to enhance nonlinear interactions.

Because of the predicted saturation of "Moore's Law" scaling of transistor cost and density [10], silicon-based microphotonics is being explored for the routing and generation of high-bandwidth signals [3, 5–7, 11–16].

An additional development has been the incorporation of microelectronic devices (*pn*-junctions) with optical devices to enable certain nonlinear operations otherwise inhibited by free-carriers generated by the high optical intensities in the silicon waveguide [3,13]. Even that active technique may have limitations [17], inspiring added interest in passive measures of modifying free carrier lifetimes [18]. It must be noted, however, that demonstration of high-Q devices in lifetime-spoiled structures opens the door to further exploration of simple nonlinear silicon photonic devices.

This thesis discusses advances in the fabrication of silicon microdisk resonators and the reduction of free-carrier lifetime in high-Q resonators. We have created silicon microdisk resonators with $Q \sim 5 \times 10^6$ and small mode volumes ($V_{eff} \sim 10^1 - 10^2\,(\lambda/n)^3$). By using wet chemical processing techniques presented here, we have created fully passive microdisk resonators with quality factors $Q \sim 5$–$6{\times}10^5$ with free-carrier lifetimes $\tau_{fc} \sim 240$ ps. The trade-offs between Q and carrier lifetime are identified as critical, and the ramifications discussed in the context of nonlinear optics with low-power CW operation.

1.1 Thesis organization

Chapter 2 describes optical devices used in this work and presents the general theoretical framework used in the rest of this thesis. An approximate technique is described that allows for the deduction of certain general trends in microdisk properties and assists in the building-up of intuition regarding the optical properties of microdisk resonators. Some details regarding the characterization techniques used are presented, including the optical characterization of silicon microdisks via tapered optical fibers, and the use of optically injected free carriers for characterization of free carrier lifetime in silicon microdisks.

Chapter 3 describes the basic processing techniques used to create silicon microdisk and microring optical resonators. Basic processing flows for undercut silicon microdisk resonators, planar microring resonators, and "floating" microring resonators are described.

Chapter 4 presents experiments used to understand the origins of optical losses in high-Q silicon microdisk resonators, and fabrication techniques used to improve the quality factors of silicon optical microresonators. Different surface treatments are investigated with an eye to providing stable, low-loss device interfaces.

Chapter 5 reconsiders much of the work in Chapter 4 with emphasis on the effects of the surface treatments and passivations on the free-carrier lifetimes of charge carriers in silicon microphotonic resonators.

Chapter 6 describes some nonlinear phenomena in silicon. To begin,

the description of the basic theoretical framework is extended to include nonlinear polarization effects. Additionally, interactions between the optical modes and thermal and free-carrier populations are described theoretically.

An interesting phenomenon whereby the interactions between these effects creates a self-generated RF oscillation of the optical fields is experimentally demonstrated. A comparison between the theoretical description and experimental observations is presented and they are found to closely agree. Further theoretical consideration of a reduced model is presented and found to also produce fair agreement.

An experiment involving pulsed input to high-Q silicon microdisk resonators is described. This nonlinear dynamical measurement relies (as in the self-generated oscillations described previously) on interaction between the electromagnetic fields, two-photon absorption, and free-carrier populations. The same dynamical equations may be used to model both pheonomena. It is used as an additional probe of effective free-carrier lifetime in comparing hydrogen-terminated silicon microdisks with chemical-oxide-terminated silicon microdisks.

Effects due to the nonlinear susceptibility of silicon—particularly Raman emission and parametric oscillation— are discussed. A general parameterization of these effects is presented, exhibiting clearly that for silicon devices in the telecom wavelength range, the relevant figure of merit is the ratio of free-carrier lifetime to optical quality factor. Threshold relationships are shown and a relationship independent of

device geometry (material-parameter-dependence only) is shown, indicating that for OPO, the central telecom wavelengths have the most stringent requirements on Q and free-carrier lifetime, but the farther infrared region and the extreme blue telecom wavelengths are significantly more promising. We find that milliwatt threshold laser operation is possible in the E/O-band with currently achievable device properties.

Chapter 2

Silicon Microdisk Resonators

Light-matter interactions lie at the heart of a number of fields of both basic scientific and technological interest, including cavity quantum electrodynamics, optical sensing and detection of materials, and nonlinear and integrated optics. The potential for greatly enhanced interactions between light and matter is one of the primary driving forces behind the study of optical microcavities. Depending upon the nature of the interaction, this enhancement is typically a function of two key parameters that characterize the cavity: its quality factor Q and mode volume V_{eff}. Q is a measure of a photon's lifetime in the cavity, with $Q = \omega\tau_{ph}$, where ω is the frequency of light and τ_{ph} the photon lifetime. The effective mode volume V_{eff} may be related to the peak per photon electric field strength in the cavity, with:

$$V_{\text{eff}} = \frac{\int n^2(\mathbf{r}) |\mathbf{E}(\mathbf{r})|^2}{max[n^2(\mathbf{r}) |\mathbf{E}(\mathbf{r})|^2]}. \tag{2.1}$$

When the system has low losses, light circulating in a resonator may make many round-trips, interacting with the medium with each pass.

Thus a high-quality resonator may behave as though it was a much larger single-pass element. Similarly, by reducing the cavity volume, the optical intensities achieved for a given stored energy increase. Thus when the optical losses of the resonator under consideration are small (Q large), and the mode volume (V_{eff}) is small, tremendous circulating intensities of light ($I = P_i \frac{\lambda}{2\pi n_g} \left(\frac{Q}{V_{\text{eff}}}\right)$) can be achieved within the microresonator, even for modest input powers (P_i). These high circulating intensities can allow the system to display significant nonlinear effects.

The particular system considered in this work is one of great relevance to technology: semiconductor optical microresonators created in the dominant microelectronic material, silicon. In close analogy to microelectronics, microphotonic components and systems can derive many benefits from scaling down their characteristic dimensions. The increased density of devices could enable greater system functionality while decreasing cost. Decreasing the size of microphotonic devices can lead to increased efficiency, through varieties of cavity enhancement, and even make new device functions possible, through accessing highly nonlinear behavior.

In the silicon system, considered in this work, such nonlinear effects can include Raman scattering, Kerr nonlinearities, two-photon absorption (TPA), and the resulting generation of free carriers. These effects have been experimentally observed to give rise to a variety of interesting behaviors, both steady-state [19] and dynamical [20, 21] in nature.

A prototypical integrated semiconductor optical microresonator/waveguide

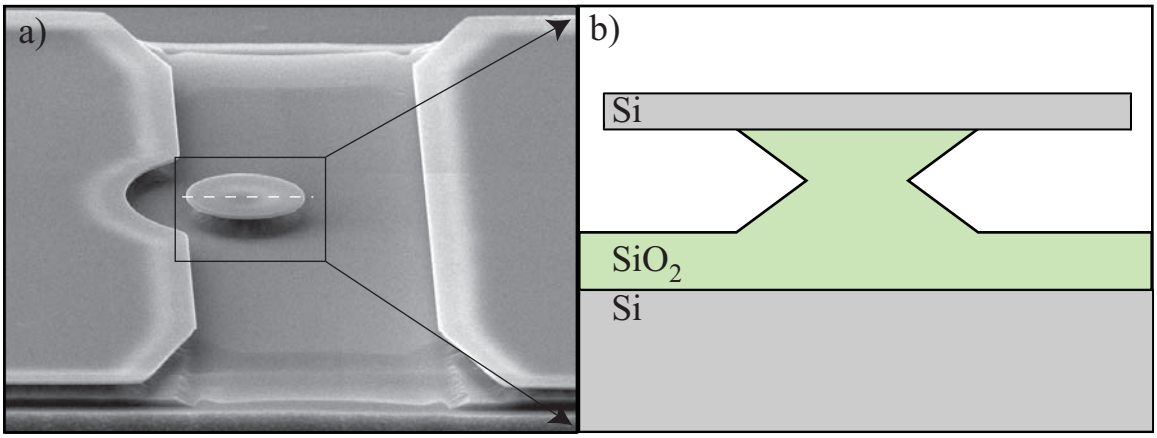

Figure 2.1: Typical disk (a) SEM micrograph. (b) Schematic.

system is pictured in schematic in Fig. 2.7. We see an example realized in the silicon system in Fig. 2. Panel (a) shows an scanning electron micrograph of a silicon microdisk resonator. Similarly, Fig. 6.1(b) shows an optical micrograph of a silicon microdisk resonator coupled evanescently to an optical fiber taper waveguide. This system allows us to launch light of a given frequency into a standard optical fiber and couple it into and out of a microdisk resonator. By monitoring the transmission of light vs. input frequency, the characteristics of the microdisk can be investigated [22, 23]. This method can be extended to other types of microphotonic resonators [24].

The resonators considered in this work are silicon microdisks and almost uniformly similar to the ones depicted in Fig. 2.1. Typically they are approximately one half-wavelength in optical thickness (0.1–0.35 μm), and vary in radius from $\sim 5\mu$m up to tens of microns. They rest upon silicon dioxide pedestals of much smaller diameter and 2–3 μm height.

2.1 Resonator modes

A useful and quite general expression of Maxwell's equations is

$$\begin{aligned} \nabla \cdot \mathbf{D}(\mathbf{r},\omega) &= \rho(\mathbf{r},t) & \nabla \cdot \mathbf{B}(\mathbf{r},t) &= 0 \\ \nabla \times \mathbf{E}(\mathbf{r},t) &= -\frac{\partial \mathbf{B}(\mathbf{r},t)}{\partial t} & \nabla \times \mathbf{H}(\mathbf{r},t) &= \mathbf{J}(\mathbf{r},t) + \frac{\partial \mathbf{D}(\mathbf{r},t)}{\partial t}. \end{aligned} \tag{2.2}$$

In most instances we will be considering situations without free charges or currents, where $\rho = 0$ and $\mathbf{J} = 0$. The constitutive relations between the macroscopic fields and their auxiliary fields are in terms of polarization and magnetization: $\mathbf{D} = \epsilon_0 \mathbf{E} + \mathbf{P}$ and $\mathbf{H} = \mathbf{B}/\mu_0 - \mathbf{M}$. If we carry Eqn. 2.2 into the frequency domain ($\mathbf{E}(\mathbf{r},t) = \mathbf{E}(\mathbf{r})e^{-iwt}$, etc.) with no free charges or currents we have

$$\begin{aligned} \nabla \cdot \tilde{\mathbf{D}}(\mathbf{r},\omega) &= 0 & \nabla \cdot \tilde{\mathbf{B}}(\mathbf{r},\omega) &= 0 \\ \nabla \times \tilde{\mathbf{E}}(\mathbf{r},\omega) &= i\omega \tilde{\mathbf{B}}(\mathbf{r},\omega) & \nabla \times \tilde{\mathbf{H}}(\mathbf{r},\omega) &= -i\omega \tilde{\mathbf{D}}(\mathbf{r},\omega). \end{aligned} \tag{2.3}$$

We have, then, from the curl equations and the constitutive relations and a partitioning of the polarization into linear and additional terms ($\tilde{\mathbf{P}}(\mathbf{r},\omega) = \tilde{\mathbf{P}}^L(\mathbf{r},\omega) + \tilde{\mathbf{P}}^{add}$), the following equation

$$\nabla^2 \tilde{\mathbf{E}}(\mathbf{r},\omega) + \left(\frac{\omega}{c}\right)^2 \epsilon(\mathbf{r},\omega)\tilde{\mathbf{E}}(\mathbf{r},\omega) = -\mu_0 \omega^2 \tilde{\mathbf{P}}^{add}(\mathbf{r},\omega). \tag{2.4}$$

Here we have assumed that any additional polarization is added in as

a perturbation, and that the LHS (left-hand side) of Eqn. 2.4 is valid in regions of constant dielectric (solutions in each must be matched through the appropriate boundary conditions).

We use the normal expansion of the total field in terms of the eigenmodes of the unperturbed system, under the assumption that the additional polarization (whether a linear perturbation or a nonlinear effect) presents a small perturbation, with $\tilde{\mathbf{E}}(\mathbf{r},\omega) = \sum_j \tilde{a}_j(\omega)\tilde{\mathbf{E}}_j(\mathbf{r},\omega_{0j})$. Substituting that ansatz into Eqn. 2.4 and integrating over the cavity, we have, upon use of mode orthogonality and transformation back into the time-domain, a set of coupled dynamical equations:

$$\frac{d^2 a_i}{dt^2} + \omega_{0i}^2 a_i = -\frac{\frac{d^2}{dt^2}\int d\mathbf{r}\tilde{\mathbf{E}}_i^*(\mathbf{r},\omega_{0i})\cdot\mathbf{P}^{add}(\mathbf{r},t)}{\epsilon_0\int d\mathbf{r}\epsilon_r(\mathbf{r},\omega_{0i})\left|\tilde{\mathbf{E}}_i(\mathbf{r},\omega_{0i})\right|^2}. \tag{2.5}$$

We consider fields at a frequency ω and restrict our attention to slowly varying mode-field amplitudes and polarizations. Making a substitution to that effect ($\tilde{a}_i(t) \rightarrow a_i(t)e^{-i\omega t}$ and $\mathbf{P}^{add}(\mathbf{r},t) \rightarrow \mathbf{P}^{add}(\mathbf{r},t)e^{-i\omega t}$) to first order we find

$$\frac{da_i}{dt} = i(\omega-\omega_i)a_i + \frac{i\omega}{2\epsilon_0}\frac{\int d\mathbf{r}\tilde{\mathbf{E}}_i^*(\mathbf{r},\omega_i)\cdot\mathbf{P}(\mathbf{r},t)}{\int d\mathbf{r}\epsilon_r(\mathbf{r},\omega_i)\left|\tilde{\mathbf{E}}_i(\mathbf{r},\omega_i)\right|^2}, \tag{2.6}$$

a set of coupled differential equations for the slowly varying mode-field amplitudes given a general input wave at frequency ω. (We take it as understood that the polarization denoted by $\mathbf{P}(\mathbf{r},t)$ incorporates any additional sources of polarization, $\mathbf{P}^{add} = \mathbf{P}^{NL} + \mathbf{P}^{other}$). The addition

of a phenomenological loss rate for the i-th mode, γ_i, which accounts for sources of loss like radiation, bulk material absorption, etc., takes the above into a more useful form:

$$\frac{da_i}{dt} = -\frac{\gamma_i}{2}a_i + i(\omega - \omega_i)a_i + \frac{i\omega}{2\epsilon_0}\frac{\int d\mathbf{r}\tilde{\mathbf{E}}_i^*(\mathbf{r},\omega_i)\cdot\mathbf{P}(\mathbf{r},t)}{\int d\mathbf{r}\epsilon_r(\mathbf{r},\omega_i)\left|\tilde{\mathbf{E}}_i(\mathbf{r},\omega_i)\right|^2}. \tag{2.7}$$

This coupled mode equation formalism can encompass both linear perturbations—like geometric roughness—and nonlinear phenomena, and so is useful in considering the formation of doublet modes by backscattering as well as nonlinear optical effects. The effects of nonlinear polarization will be considered in a later section.

2.1.1 Normal modes

If we reconsider Eqn. 2.4 with no nonlinear effects or sources of additional perturbation polarization, we have an equation for electromagnetic fields oscillating at some frequency ω corresponding to some dielectric function $\epsilon(\mathbf{r},\omega)$. If we consider such a rotationally symmetric, linear, dielectric configuration, it is natural to move to cylindrical coordinates, where we have

$$\left(\frac{\partial^2}{\partial\rho^2} + \frac{1}{\rho}\frac{\partial}{\partial\rho} + \frac{1}{\rho^2}\frac{\partial^2}{\partial\phi^2} + \frac{\partial^2}{\partial z^2} + \left(\frac{\omega}{c}\right)^2 n^2(\rho,z)\right)\mathbf{F}(\mathbf{r}) = 0, \tag{2.8}$$

where $\tilde{\mathbf{F}}(\mathbf{r},\omega) \in \left\{\tilde{\mathbf{E}}(\mathbf{r},\omega),\tilde{\mathbf{H}}(\mathbf{r},\omega)\right\}$. Inspection shows that the az-

imuthal angle, ϕ, separates, so that solutions to the above equation can be written as $\mathbf{F}(\rho, \phi, z) = \mathbf{f}_m(\rho, z)e^{\pm im\phi}$. Requiring the field to be single valued upon rotation by 2π limits the possible values of m to the integers, and the rotational symmetry ($\phi \to -\phi$ leaves the equations of motion unchanged) shows that the clockwise (CW) and counter-clockwise (CCW) going waves corresponding to ±m supported by the dielectric configuration are degenerate.

2.1.2 Doublet Modes

Quite generally we would then expect that spoiling the rotational symmetry of the dielectric structure described above would lift the degeneracy of the counterpropagating modes. We can apply Eqn. 2.1 to determine the effect of adding to our cylindrical dielectric configuration some roughness—expressed so that $\epsilon_r(\mathbf{r}, \omega) = \epsilon_{0r}(\mathbf{r}, \omega) + \delta\epsilon_r(\mathbf{r}, \omega)$, where ϵ_r is the new total relative dielectric function, ϵ_{0r} is the unperturbed relative dielectric function, and $\delta\epsilon_r$ is the perturbation to the relative dielectric function. Thus the polarization to employ in Eqn. 2.1 is given by $\mathbf{P}(\mathbf{r}, t) = \epsilon_0\delta\epsilon_r(\mathbf{r}, \omega)(a_m\tilde{\mathbf{E}}_m(\mathbf{r}, \omega_m) + a_{-m}\tilde{\mathbf{E}}_{-m}(\mathbf{r}, \omega_m))$. Assuming there is some m such that a resonance is found, and that other modes are well separated from it in energy, we find from Eqn. 2.1 a set of coupled equations:

$$\begin{aligned}\frac{da_m}{dt} &= -\frac{\gamma}{2}a_m + i(\omega-\omega_m)a_m + \frac{i}{2}\beta_{m,m}a_m + \frac{i}{2}\beta_{m,-m}a_{-m} \\ \frac{da_{-m}}{dt} &= -\frac{\gamma}{2}a_{-m} + i(\omega-\omega_m)a_{-m} + \frac{i}{2}\beta_{-m,m}a_m + \frac{i}{2}\beta_{-m,-m}a_{-m},\end{aligned} \tag{2.9}$$

where the coefficients $\beta_{m,m} = \beta_{-m,-m}$, which reflects the overall shift of the resonance due to the addition of the perturbation, and the coefficients $\beta_{m,-m}$ and $\beta_{-m,m}$ represent a coupling of the degenerate modes. Those coefficients are all given below:

$$\begin{aligned}\beta_{m,m} &= \frac{\omega}{\epsilon_0}\frac{\int d\mathbf{r}\,\delta\epsilon_r(\mathbf{r},\omega)\tilde{E}_m^2(\mathbf{r},\omega_m)}{\int d\mathbf{r}\,\epsilon_{0r}(\mathbf{r},\omega)\left|\tilde{\mathbf{E}}_m(\mathbf{r},\omega_m)\right|^2} \\ \beta_{m,-m} &= \frac{\omega}{\epsilon_0}\frac{\int d\mathbf{r}\,\delta\epsilon_r(\mathbf{r},\omega)\tilde{\mathbf{E}}_m^*(\mathbf{r},\omega_m)\cdot\tilde{\mathbf{E}}_{-m}(\mathbf{r},\omega_m)}{\int d\mathbf{r}\,\epsilon_{0r}(\mathbf{r},\omega)\left|\tilde{\mathbf{E}}_m(\mathbf{r},\omega_m)\right|^2} \\ \beta_{-m,m} &= \frac{\omega}{\epsilon_0}\frac{\int d\mathbf{r}\,\delta\epsilon_r(\mathbf{r},\omega)\tilde{\mathbf{E}}_{-m}^*(\mathbf{r},\omega_m)\cdot\tilde{\mathbf{E}}_m(\mathbf{r},\omega_m)}{\int d\mathbf{r}\,\epsilon_{0r}(\mathbf{r},\omega)\left|\tilde{\mathbf{E}}_{-m}(\mathbf{r},\omega_m)\right|^2} \\ \beta_{-m,-m} &= \frac{\omega}{\epsilon_0}\frac{\int d\mathbf{r}\,\delta\epsilon_r(\mathbf{r},\omega)\tilde{E}_{-m}^2(\mathbf{r},\omega_m)}{\int d\mathbf{r}\,\epsilon_{0r}(\mathbf{r},\omega)\left|\tilde{\mathbf{E}}_{-m}(\mathbf{r},\omega_m)\right|^2}.\end{aligned} \tag{2.10}$$

Inspecting the above equations we see that coupling between modes (through coefficients $\beta_{\pm m,\mp m}$) occurs when the perturbation has significant amplitude at the $\pm 2m$ Fourier coefficient.

We may re-write Eqn. 2.9 as superpositions of the original traveling waves which correspond to standing waves, in which we find that the steady-state response exhibits a characteristic doublet shape. We have, assuming that the perturbation we add is, on average, zero:

$$\begin{aligned}\frac{da_c}{dt} &= -\frac{\gamma}{2}a_c + i\left(\omega - \omega_0 + \frac{\beta}{2}\right)a_c \\ \frac{da_s}{dt} &= -\frac{\gamma}{2}a_s + i\left(\omega - \omega_0 - \frac{\beta}{2}\right)a_s,\end{aligned} \tag{2.11}$$

where we take the superpositions $a_c = (a_m + a_{-m})/\sqrt{2}$ and $a_s = (a_m - a_{-m})/\sqrt{2}$, let $\beta_{m,-m} = \beta_{-m,m} = \beta$, and generalize to any resonant frequency ω_0. Generally we allow the losses of the even and odd combinations of mode-field-amplitudes to take different values, and may easily include excitation in the system. Typically we select a normalization of the field such that the energy stored in the j-th mode of the cavity is given by $|\,a_j|^2$. When we are in the doublet basis, we find the energy stored in the cosine-(sine-)like modes to be given by $U_{c/s} = \left|\,a_{c/s}\right|^2$, respectively. The derivations above follow the formalism used by Lin et al. in Ref. [25]. Other workers use similar methods in Ref. [23, 26–28].

If we include a source term, we have our mode-field amplitude equations of motion as:

$$\begin{aligned}\frac{da_c}{dt} &= -\frac{\gamma_c}{2}a_c + i\left(\omega - \omega_0 + \frac{\beta}{2}\right)a_c + \kappa\, s \\ \frac{da_s}{dt} &= -\frac{\gamma_s}{2}a_s + i\left(\omega - \omega_0 - \frac{\beta}{2}\right)a_s + \kappa\, s,\end{aligned}$$

(2.12)

where κ is an input coupling coefficient (related to the input coupling coefficient for a standard traveling wave transmission resonator by a factor of $1/\sqrt{2}$), and $|s|^2$ is the input power. Here we assume that the coupling to each of the standing-wave modes is identical, though in general the coupling can be different. Experimentally we have noticed only small differences in coupling utilizing the input coupling methods we will discuss below. We find that very low power measurement of some transmission spectra of microdisk resonances (illustrated in Fig. 6.2(a)), display a "doublet" lineshape characteristic of this degeneracy lifting.

2.1.2.1 Mode coupling

If we relax the assumption that no other modes are present at a given frequency ω_0 aside from the counterpropagating degenerate modes, we find that modes with different m-numbers may still couple through roughness or departures from circularity, leading to mode coupling and repulsion between modes of different radial, vertical, or polarization characteristics. This effect would generally manifest as the spoiling of what we would expect to be a regular progression (roughly) of orders $(...m-1, m, m+1, ...)$ versus frequency $(...\omega_m - \Delta\omega_{FSR}, \omega_m, \omega_m + \Delta\omega_{FSR}, ...)$.

In addition to the coupling between resonator modes introduced by the imposition of imperfections on the dielectric structure, additional coupling may be induced between the resonator modes and radiation. As such, fabrication roughness represents a source of loss. In Ref. [23],

a volume-current method is used to estimate the impact of surface roughness. The index perturbation that the surface roughness represents can be viewed as polarizable elements with $\delta\epsilon(\mathbf{r})$ (as above) which are driven by the eigenmodes of the unperturbed system. The resulting polarization current is

$$\mathbf{J} = -i\omega\delta\epsilon\mathbf{E}. \tag{2.13}$$

The far-field vector potential sourced by $\mathbf{J}$ is given by [29]

$$\mathbf{A}_{rad}(\mathbf{r}) = \frac{\mu_o}{4\pi}\left(\frac{e^{-ik_1 r}}{r}\right)\int \mathbf{J}(\mathbf{r}')e^{-ik_1\hat{\mathbf{r}}\cdot\mathbf{r}'}d\mathbf{r}'. \tag{2.14}$$

Optical losses due to the perturbations can be calculated from the far-field electromagnetic solutions created by $\mathbf{J}$ [29]. In Ref. [22, 30] the roughness is simplified by an effective dimensional reduction, so that it is represented by a ring of dielectric perturbation with delta-function dependence in ρ and z directions. An additional assumption made in Ref. [22] is that the roughness is ergodic, and much smaller in extent than the wavelength, allowing a statistical evaluation of the integral for far-field vector potential in Eqn. 2.14 [30]. The statistical properties of the roughness can be captured by a correlation length, L_c and a roughness variance σ_R^2. Then some "typical" scatter has volume $V_s \equiv \sqrt{RL_c}h\sigma_r$.

One can then find a quality factor associated with the surface scattering:

$$Q_{ss} = \frac{\lambda_o^3}{\pi^{7/2} n_o \left(\delta n^2\right)^2 V_s^2 \sum_{\hat{\eta}} \bar{u}_s(\hat{\eta}) G(\hat{\eta})}, \tag{2.15}$$

where $\bar{u}_s(\hat{\eta})$ is the normalized, spatially averaged, $\hat{\eta}$-polarized electric field energy density at the disk edge given by [23]

$$\bar{u}_s(\hat{\eta}) = \frac{\epsilon_0 \left|\mathbf{E}^0(\hat{\eta})\right|^2_{s,avg}}{\frac{1}{2}\int \epsilon^0(\mathbf{r}) \left|\mathbf{E}^0\right|^2 d\mathbf{r}}. \tag{2.16}$$

It is found numerically that TE modes couple to far-field radiation modes roughly 50% more strongly than corresponding TM modes, mainly due to geometrical factors: the different field components couple energy to the far field with differing effectiveness, and the polarizations carry different proportions of their energy in different field components, as will be noted below.

2.1.3 Evaluation of the eigenmodes

The general Maxwell equations in the geometry of the cylindrical disk or ring are not amenable to direct solution. For the most part, we therefore utilize the finite element method (FEM) to calculate the electromagnetic modes of a given dielectric structure. A commercial software package, COMSOL Multiphysics, is used with some modifications to the RF electromagnetic modules to incorporate an $e^{\pm im\phi}$ field dependence, allowing the calculation of the full electromagnetic field with high fidelity and resolution. A complete description of procedures which may be used to solve the electromagnetic problem for the axisymmetric

microdisk-type resonators with COMSOL Multiphysics software may be found in [31].

Beyond the use of direct numerical calculation of full electromagnetic eigenmodes, various workers have developed approximations to the properties of such structures, examination of which may help one develop intuition.

2.1.3.1 Approximate and analytical methods

In Ref. [22], the authors employ a self-consistent effective index approximation and find that for thin structures, the transverse fields are fairly well approximated thereby, though not the longitudinal field components. Heebner et al. make a similar treatment with somewhat more accurate assumptions, keeping complex Hankel functions outside of the curved structures in lieu of approximating the outside behavior with simple exponential decay [32]. It is found in both those references that the results of the methods employed can be utilized in more accurate numerical calculations as initial guesses of mode frequencies and free spectral wavelengths for targeted solvers. In Ref. [33, 34], the method of conformal transformation is used to map the problem of two-dimensional curved waveguiding structures onto rectilinear coordinates.

The method of conformal transformation provides a very useful picture for understanding the form of the whispering gallery modes. By applying a logarithmic transform given by $W = R2ln(z/R_2)$, the cylin-

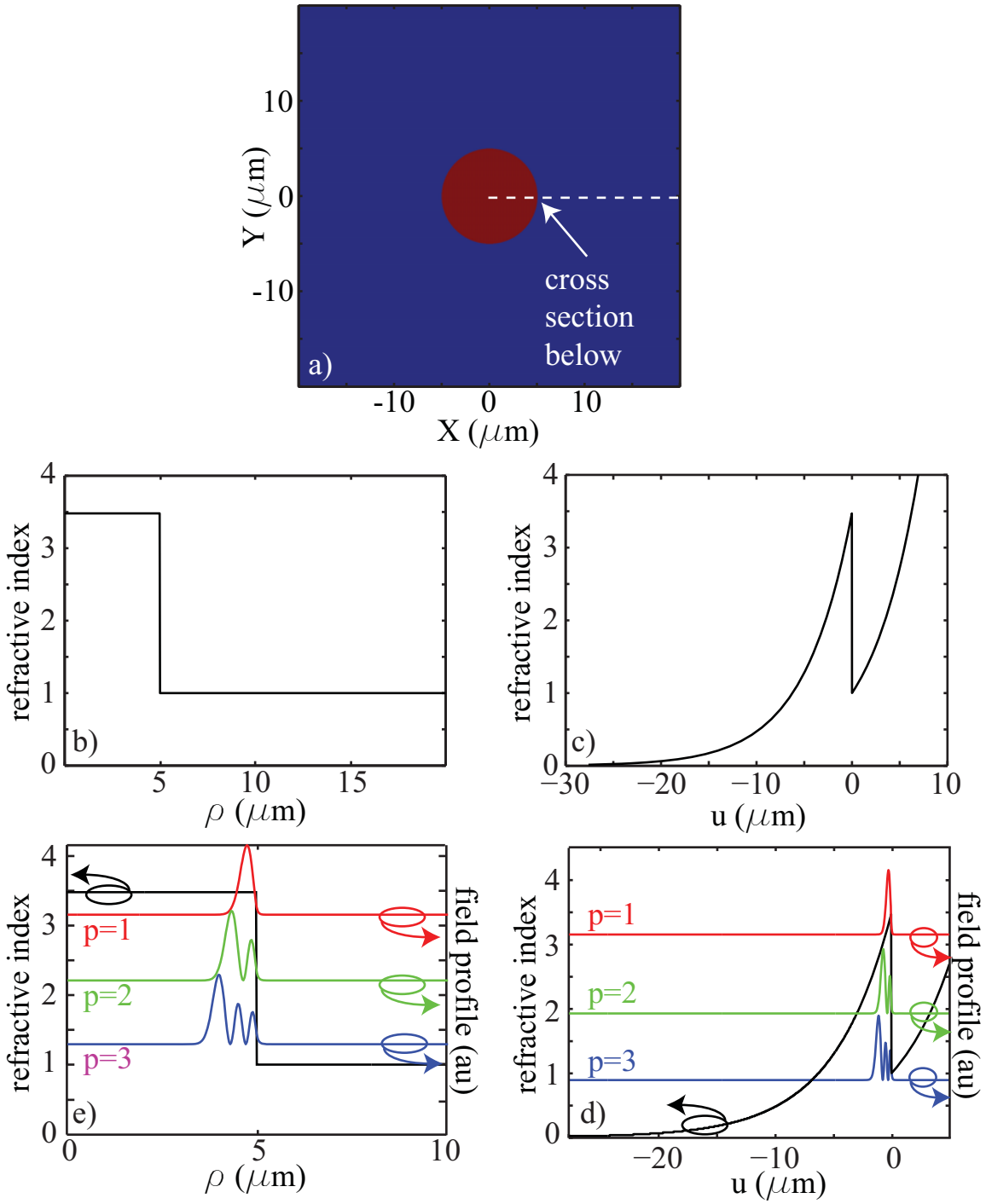

Figure 2.2: Conformal transform and microdisk modes. (a) Top view of microdisk with refractive index by color. (b) Crosssection of refractive index. (c) Crosssection of transformed refractive index. (d) Transformed refractive index with scalar-approximation modes superimposed. (e) Crosssection of refractive index with inverse mapped approximate modes

drical shape in Fig. 2.2(a) is mapped to a a rectangular geometry. In Fig. 2.2(b)–(c) we see a cross section of the index profile of a silicon rod and the effect of the mapping. Examination of this figure can lend a great deal of intuition.

Thus the impact of the "centrifugal" force is made plain: the central region of the disk is effectively held at a lower refractive index than the outer portion of the disk. Moreover, the refractive index is effectively increasing exponentially outside of the silicon region. Such an increased index region separated from the local peak index region near the disk edge represents a location of effectively lower "potential" for photons than the local minimum associated with the annulus near the disk periphery; the WGM modes are not fully bound, but are actually quasi-normal modes which may transport energy to infinity [35].

Figure 2.2(d) shows some approximate solutions to the scalar wave equation in the transformed index configuration. Note the concentration of the field near the disk periphery, and that the successive radial-order modes are progressively moved in from the disk edge, having lower effective radius as the mode order increases. When the transformation is undone, as in the (e) panel, we see a sharp decay outside the silicon region, indicating a tightly bound set of modes.

Application of WKB theory to the case of a local minimum in potential separated by a barrier shows that the decay rate depends critically upon the depth and width of the barrier, with approximate dependence $\sim exp(-W\sqrt{D})$ (where W is an effective width of the barrier

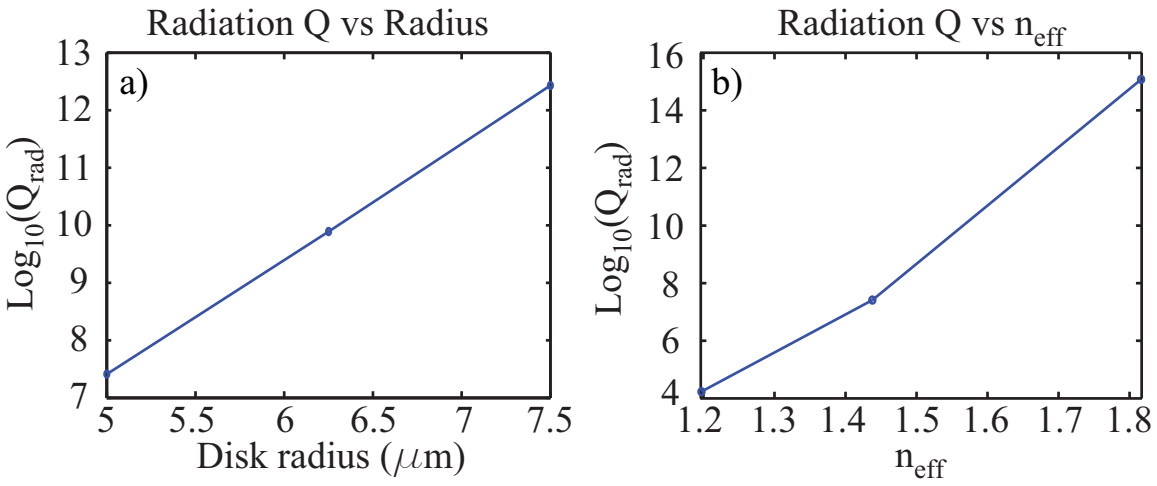

Figure 2.3: Numerical check of approximate conclusions. (a) Dependence of Q on microdisk radius at 1.5 μm, h = 220 nm, TM-like mode. (b) Dependence of Q on effective index at 1.5 μm, disk radius 5 μm. Thickness ranging from 200—250 nm

region, and D an effective height of the barrier) [36]. If we apply the conformal transform to a medium which approximates the vertical dependence of a microdisk via an effective index method, and then make an analogy to the decay dependence from WKB, we find that for tightly bound modes, $Q \sim exp(R\, n_{\text{eff}}/\lambda)$. Thus we expect that other things being equal, the quality factor associated with radiation losses should increase exponentially with radius. Similarly, for a given radius, other things being equal, resonant modes with higher effective index have higher quality factor, with the increase being roughly exponential in effective index. Also evident, for a given effective index and radius, Q should decrease with increasing wavelength.

Additionally, we may see by inspection that in the transformed coordinates, the effective width of the well presented by the microdisk refractive index increases roughly linearly with the microdisk index.

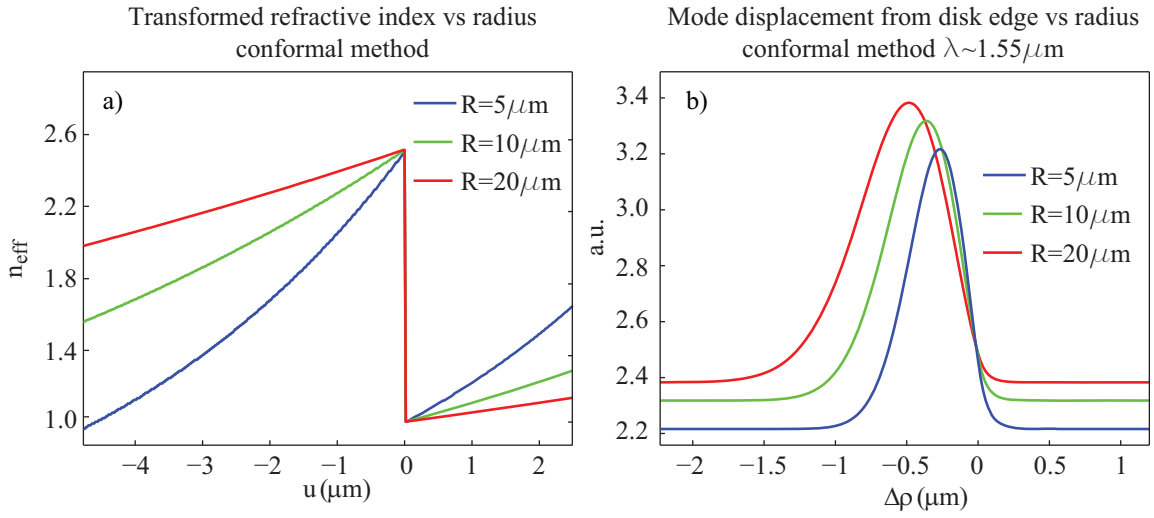

Figure 2.4: Intuitive picture of effect of microdisk radius increase. (a) The result of the conformal transformation of refractive index profile of microdisks of 5, 10, and 20μm. Note the widening of the effective potential well. (b) Approximate modes (scalar solution) given refractive index profiles from (a). Note the increasingly buried modes with increased microdisk radius.

Thus it is expected that the separation between microdisk edge and mode localization increases with increasing microdisk radius. This is reflected by the shallowness of the increase in index profile up to disk edge as disk radius increases, as depicted in Fig. 2.4(a). Resulting optical modes should spread to a wider extent and see more of the increased effective refractive index of the disk interior, as depicted in Fig. 2.4(b).

In a later section, the numerical calculation of eigenmodes is further described. However, taking the use of the COMSOL simulations as a given, we can check the validity of the approximate results above. In Fig. 2.3(a)—(b), we find that our intuitions developed above were indeed correct: the radiation decay rate (Q) decreases (increases) exponentially with microdisk radius, and approximately exponentially with

effective index. The conformal transform thus moves the resonator problem into an index configuration with relatively simple interpretation, and from which some conclusions are easily drawn.

Still more information can be gleaned from consideration of the system without recourse to numerical integration of Maxwell's equations. In 2.1.1 we already considered the impact of one symmetry of a silicon microdisk resonator: its rotational invariance and the consequent angular behavior of the solutions to the equations of motion. Additionally, the ideal microdisk resonator has a mirror-plane located at its equator. As a result, the solutions to Maxwell's equations partition into two sets: solutions such that the electric field normal to the mirror plane have even parity and those that have odd parity. Because of the additional confinement imposed by the boundary of the microdisk, the modes are not fully transverse. However, the even(odd) parity modes can be identified as TM(TE)-like, and will be so identified throughout.

In reality, however, the microdisk geometry will deviate from the perfect mirror symmetry most importantly in two ways. The first difference from ideality is that the sidewalls defining the disk are likely to be sloped. Secondly, the microdisks fabricated here typically rest upon a silicon dioxide post. This latter difference is unlikely to play a major role for the low-radial-order modes, though, as the post diameter is much, much less than the disk diameter in most every case of interest. Because the mirror symmetry will not be perfect, the strict division into modes classified by parity is lost, though it will still be

a useful concept, as it is approximately valid. Additionally, with the imposition of a sloped outer boundary, in transformed coordinates, it is immediately obvious that the index profile is such that the "tunnel" barrier to infinity is slightly reduced, and so we may expect a small decrease in cavity Q. Numerically it is found to be so in Ref. [37].

2.1.3.2 Numerical solutions

As discussed above, we use the commercially available COMSOL Multiphysics software to numerically solve Maxwell's equations with FEM. Fig. 2.5 depicts some details of the simulations. In Fig. 2.5(a) we see the configuration we use for simulation. The silicon core is labeled, and surrounded by an air medium. The simulation domain is terminated by unphysical layers which effect an open boundary [38]. This allows for radiation losses to be calculated, reflected in the imaginary component of the eigenfrequencies found.

Fig. 2.5(b)—(c) show a representative meshing of the structure, illustrating that high index regions are more densely meshed than low index regions. Moreover, regions where high concentrations of field are expected have a yet denser mesh, reflecting the need for many degrees of freedom to represent the field accurately there.

The solutions to Maxwell's equations calculated by FEM for a typical silicon microdisk resonator of thickness 220 nm and radius 5 μm at wavelength $\lambda \sim 1.5\mu$m are plotted in Fig. 2.6. The expected TE-like and TM-like modes are found. We find that the TE-like mode has the

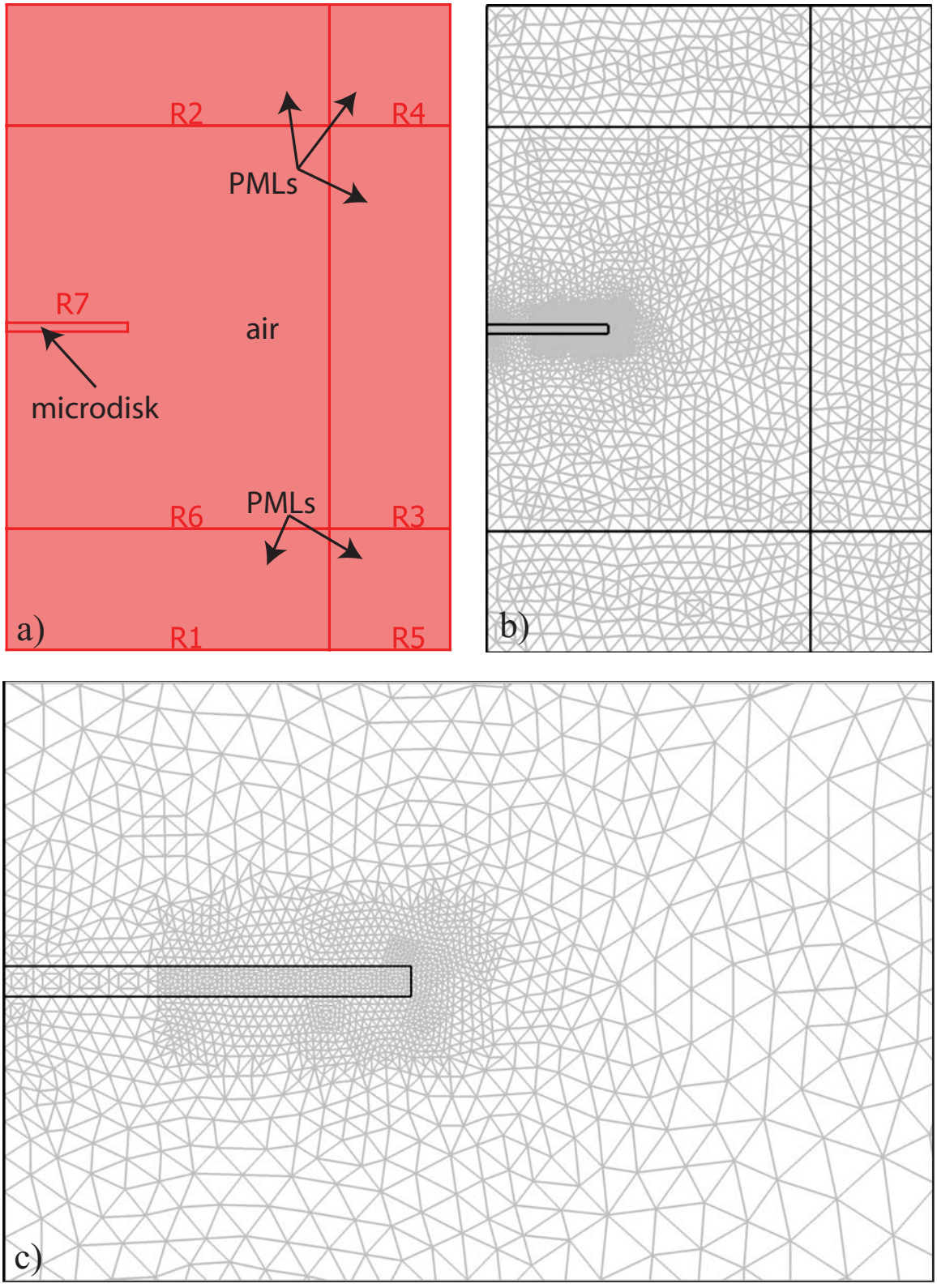

Figure 2.5: FEM simulation setup. (a) Simulation domains. (b) View of meshing. (c) Detail of mesh

majority (92%) of its energy in the radial field component ($\sim 8\%$ in the longitudinal component), and the energy is very tightly confined in the microdisk (98% overlap). The azimuthal order of the field is $m = 52$, meaning the mode has an effective index of ~ 2.7, using the following estimate,

$$n_{eff} \sim \frac{m\lambda}{2\pi\rho_{eff}}, \tag{2.17}$$

where ρ_{eff} is the mode-averaged energy density defined below:

$$\rho_{eff} = \frac{\int d\mathbf{r}\rho\, n^2(\mathbf{r})\, |\mathbf{E}(\mathbf{r})|^2}{\int d\mathbf{r}\, n^2(\mathbf{r})\, |\mathbf{E}(\mathbf{r})|^2}. \tag{2.18}$$

For the TE-like mode pictured in Fig. 2.6, $\rho_{eff} \sim \rho_{peak} \sim 4.6\mu$m, where ρ_{peak} is the radial location of the greatest energy density. This mode is determined to have a radiation Q $\sim 10^{15}$.

The TM-like mode also pictured has a most of its energy concentrated in the transverse z-component and longitudinal ϕ-component (36% and 61%, respectively). The TM mode is less well bound by the microdisk, with 79% of its energy overlapping with the microdisk. Its azimuthal order is $m = 31$, corresponding through a similar estimate to an effective index of ~ 1.64. This significantly lower effective index is, as expected, accompanied by reduction in radiation Q, to $\sim 10^8$. Also of note is the difference in mode-averaged radius: the TM mode $\rho_{eff} = 4.5\mu$m.

An additional parameter computed via FEM is the effective mode

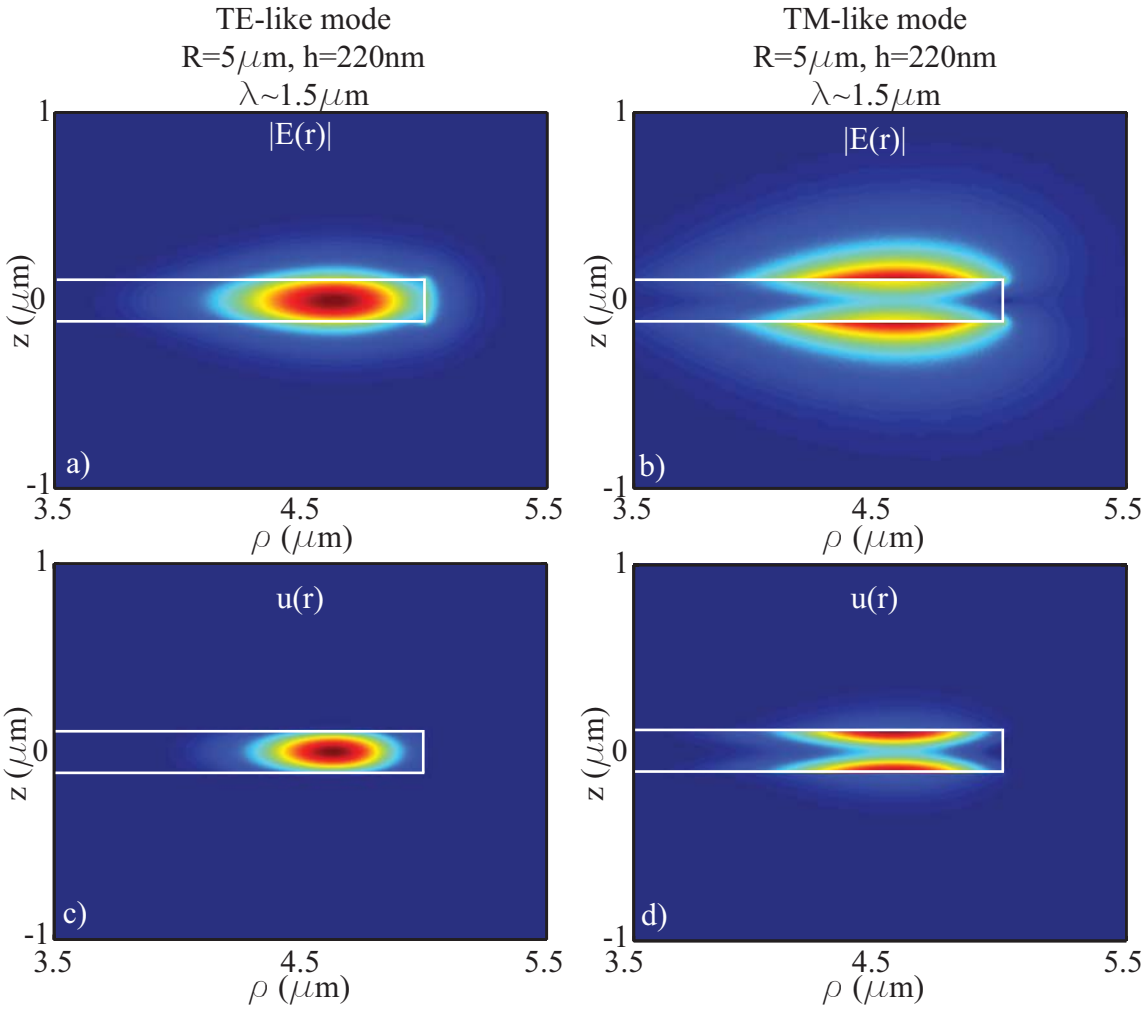

Figure 2.6: Mode profiles from FEM. (a) Norm of E-field, TE-like mode. (b) Norm of E-field, TM-like mode. (c) Electric energy density, TE-like mode. (d) Electric energy density, TM-like mode

volume. The effective mode volume is not a simply defined quantity, as the "correct" expression to use depends upon the application of interest. For instance, a variety of nonlinear mode volumes can be defined, corresponding to different orders of intensity (or energy density) involved in a given process [19, 39]. A simple definition corresponds to the physical volume taken up by the mode: $V = 2\pi\rho_{eff}A$, where A is determined by the products of the mode widths in different Cartesian directions, determined by ($A = \sqrt{\overline{(\rho - \rho_{eff})^2(z - z_{eff})^2}}$, where the averages are taken with respect to energy density), or by energy density half-widths. Yet another common definition of mode volume is intimately tied to the magnitude of the cavity electric field per photon, and is given by [40]:

$$V_{eff} = \frac{\int d\mathbf{r}\, n^2(\mathbf{r}) \left|\mathbf{E}(\mathbf{r})\right|^2}{max\left\{n^2(\mathbf{r}) \left|\mathbf{E}(\mathbf{r})\right|^2\right\}}. \tag{2.19}$$

We will typically use this definition unless otherwise indicated. The TE and TM modes depicted in Fig. 2.6 have similar mode volumes. The TE mode has $V_{eff} = 2.42\mu\text{m}^3$, while the TM mode has $V_{eff} = 3.35\mu\text{m}^3$.

2.2 Characterization methods

2.2.1 Fiber taper coupling

To characterize the microdisk resonators an evanescent fiber taper coupling technique is employed [22, 41]. In this process, an optical fiber

is adiabatically drawn to a 1—2 μm diameter using a hydrogen torch so that its evanescent field is made accessible to the environment. Using DC motor stages with 50 nm encoded resolution, the fiber taper can be accurately positioned within the microdisk near-field so as to couple power into the microdisks. Measurements of the taper transmission as a function of the taper-microdisk gap and input power are performed using swept wavelength tunable laser sources (λ = 1410–1625 nm, linewidth $<$ 5 MHz). A set of paddle wheels is used to adjust the polarization state of the fiber taper mode in the microdisk coupling region, providing selective coupling to the TE-like (TM-like) whispering gallery modes (WGMs) with dominant electric field parallel (normal) to the plane of the microdisk. In many experiments, a variable optical attenuator (HP Agilent 8156a) is used to adjust the power delivered to the coupling region of the fiber taper, and a second attenuator is used to maintain a constant power delivered to the detector or receiver. Refs. [22, 24, 41–45] employ just such a technique to couple to different configurations of hiqh-Q resonators.

The next section will briefly elaborate on the important theoretical aspects of the fiber taper coupling technique. After that, the fabrication of fiber tapers is described. Finally, we see the utility of the fiber taper coupling technique in testing semiconductor microdisk resonators.

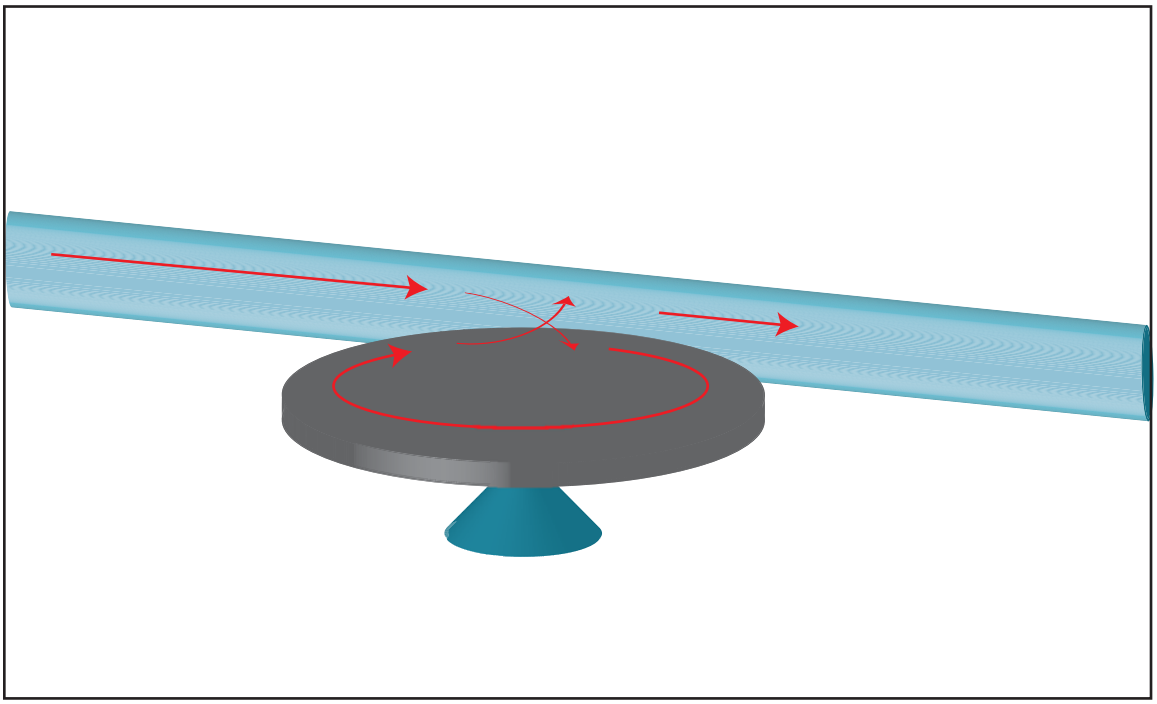

Figure 2.7: An illustration depicting fiber coupling scheme

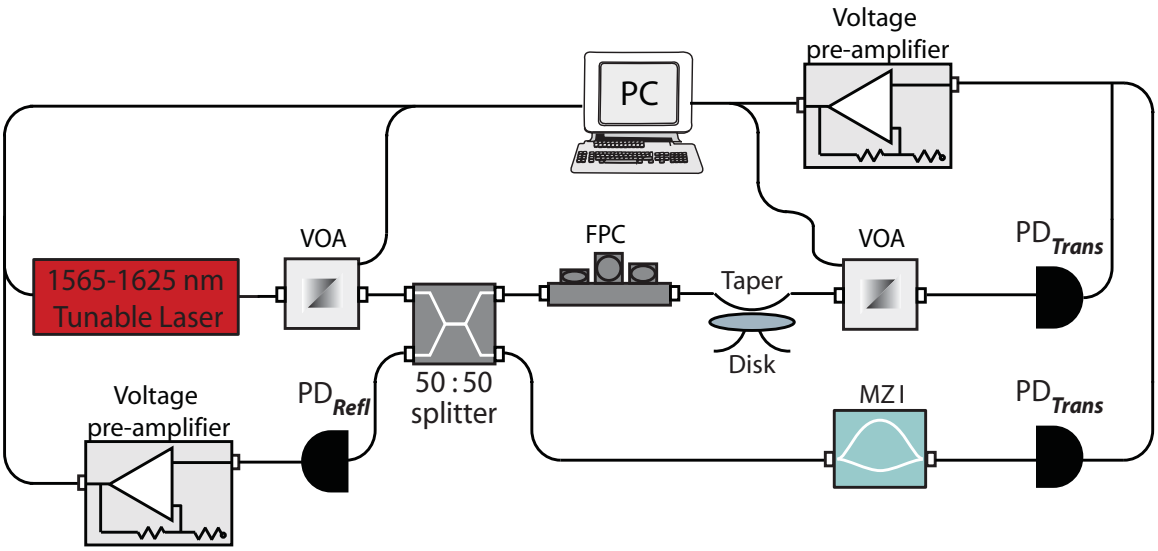

Figure 2.8: A typical experimental setup utilizing the fiber taper coupling technique with various fiber optical components. The configuration depicted would be suitable for simultaneous transmission and reflection measurements.

2.2.1.1 Theoretical overview

A theoretical approach similar to that presented above for use in mode coupling and the evaluation of the impact of perturbations can be employed to calculate the coupling between fiber taper waveguides used for resonator loading. All that is required is to consider a different basis for expansion of the electromagnetic field (including fiber and disk modes) and a partitioning of the global dielectric function into microdisk, taper, and background. We may consider a single mode of a microdisk resonator and a single mode of a tapered optical fiber. The tapered optical fiber is assumed to be uniform in the direction of propagation in the coupling region and its propagation axis parallel to the microdisk equatorial plane.

Taking those assumptions into account by writing the total dielectric function as $\epsilon(\mathbf{r}) = \epsilon_0 + \sum_k \delta\epsilon_k(\mathbf{r})$ (where ϵ_0 is a background dielectric constant and $\delta\epsilon_k(\mathbf{r})$ account for the disk and fiber dielectrics) and the total field as $\mathbf{E}(\mathbf{r}, t) = e^{-i\omega t} \sum_j a_j(t)\mathbf{E}_j(\mathbf{r})$ (where the sum is over dielectric strutures—disk and fiber), we may then find an expression related to the coupling between the electromagnetic modes (i and j) of the dielectric bodies (also i and j):

$$\beta_{ji} = \frac{\omega}{2} \frac{\int d\mathbf{r}\, (\epsilon_0 + \sum_{k \neq \mathrm{j}} \delta\epsilon_k(\mathbf{r}))\mathbf{E}_i(\mathbf{r}) \cdot \mathbf{E}_j^*(\mathbf{r})}{\int d\mathbf{r}\, \epsilon_j(\mathbf{r}) \left|\mathbf{E}_j(\mathbf{r})\right|^2}, \tag{2.20}$$

where $\epsilon_j = \epsilon_0 + \delta\epsilon_j(\mathbf{r})$ is the total dielectric function for the j-th body. If we then restrict our attention to a situation where just one mode

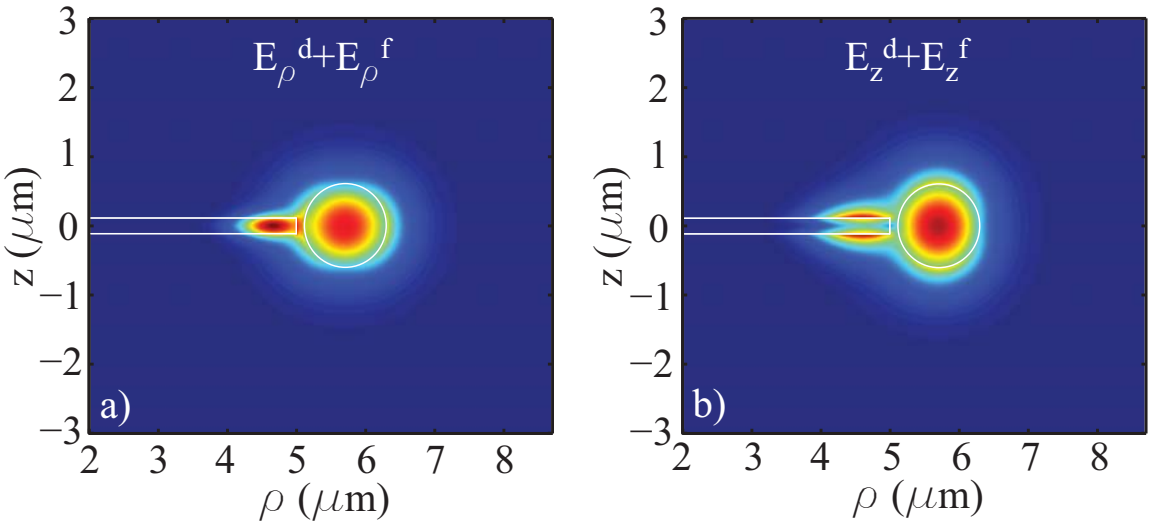

Figure 2.9: Illustration of disk fiber overlap. (a) TE-like disk mode dominant component overlap with fiber. (b) TM-like disk mode dominant component overlap with fiber.

(indexed with d) of a microdisk is considered and just one mode of a fiber is considered (indexed with f) we have an expression relating to the coupling between disk and fiber:

$$\beta_{df} = \frac{\omega}{2} \frac{\int d\mathbf{r}\, \epsilon_f(\mathbf{r}) \mathbf{E}_f(\mathbf{r}) \cdot \mathbf{E}_d^*(\mathbf{r})}{\int d\mathbf{r}\, \epsilon_d(\mathbf{r}) \left|\mathbf{E}_d(\mathbf{r})\right|^2}. \tag{2.21}$$

Examination of this expression for the coupling coefficient immediately reveals that there are two important aspects: overlap of the electromagnetic modes of the structures and the relative (spatial) phase of the modes. For effective coupling, high electromagnetic overlap is desired, and the phase velocities of the fields in the coupling regions should be close. With regards to electromagnetic ovelap, an appreciable portion of the electromagenetic energy carried by the fiber should penetrate the disk region (and vice versa). In Fig. 2.9(a)–(b) we see the mode of a 1.2 μm diameter fiber (at 1.5 μm wavelength) added to

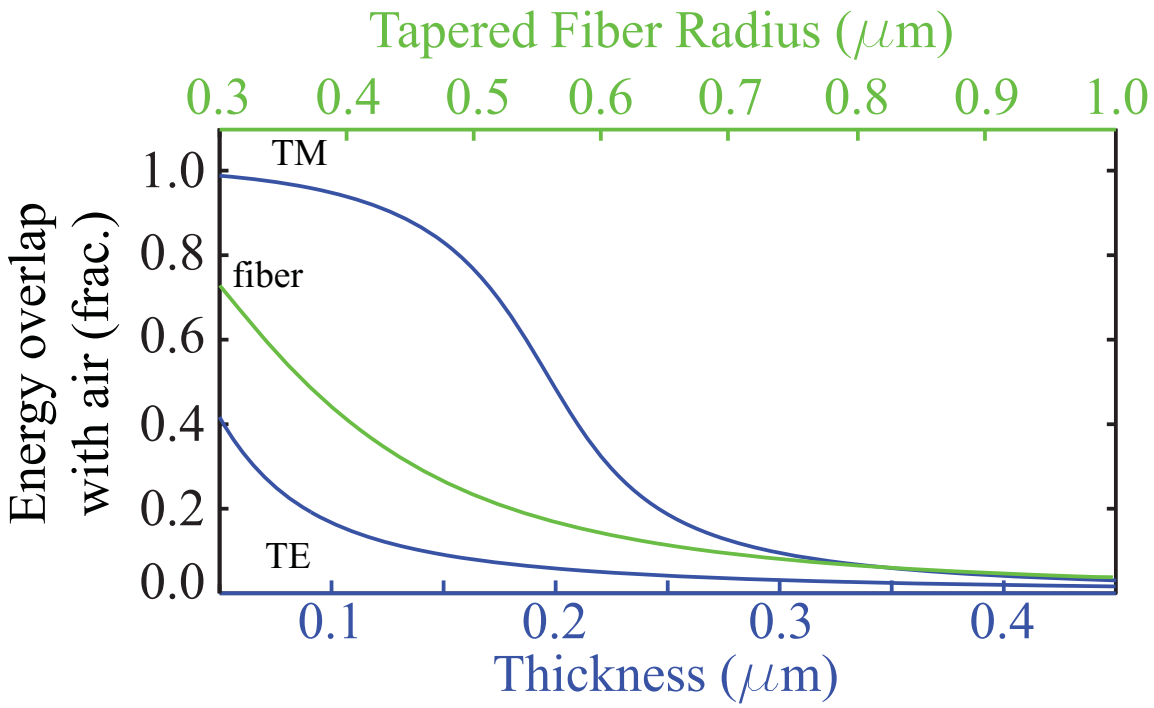

Figure 2.10: Illustration of effect of evanescence: guided-wave structures with fields exponentially decaying in the surrounding medium (in most cases, air, though any lower-index material shows the same behavior)

the mode of a 0.22 μm thickness microdisk with radius 5 μm also at 1.5 μm wavelength. We see the TE-like mode and TM-like mode interact well with the appropriately polarized fiber taper mode. More generally, in Fig. 2.10 we see that, as expected, thinner microdisks should have more mode energy penetrating the air region, and that TE-like modes are more concentrated in the disk region. For the disk thicknesses we are typically concerned with, TE-like modes carry 1–20% of their energy in the air, while TM-like modes carry 20–40%. Similarly, the portion of energy in the fiber mode carried in air decreases with increasing fiber radius. In the region of fibers we typically use, the energy overlap with air is $\sim$20–30%.

In the coupling region, the fiber carries a travelling wave with field dependence like $\mathbf{E}(\mathbf{r})e^{i\beta_f z}$, where the fiber axis is the z direction, $\mathbf{E}(\mathbf{r})$ is z-independent, and β_f is the phase velocity. The microdisk mode has an $e^{im\phi}$ dependence about the disk axis, which, projected onto the fiber coordinates, behaves like a z-dependent phase velocity of the approximate form $e^{im\,tan^{-1}(z/(R+\delta))}$, where R is the disk radius and δ is the minimum taper-disk gap. For fiber regions near the minimum gap point, $z \sim 0$ and $tan^{-1}(z/(R+\delta)) \sim z/(R+\delta)$, which corresponds to an effective phase velocity in the fiber region of approximately m/R (for $\delta << R$). Thus for good phase matching, it is desired that $m/R \sim \beta_f$. A rough guide to the behavior of the fundamental disk modes is the effective index of a slab with the same thickness. In Fig. 2.11 we depict the effective indices of TE-(TM-)like modes vs. varying slab thicknesses, as well as the effective index for fiber modes vs. fiber radius. We see that TE-like modes have much higher effective index than the fiber for any thickness-radius combination we are likely to try, while TM-like modes have a much more similar effective index (for relatively thin disks $\sim$0.2 μm).

On balance, we expect that TM-modes are much more likely to be easily fiber coupled, an expectation that is borne out experimentally. Higher-order radial modes, however, take up some of the difference in effective index, meaning that TE-like modes can still be quite effectively coupled, more so for the second, third, and fourth radial order modes.

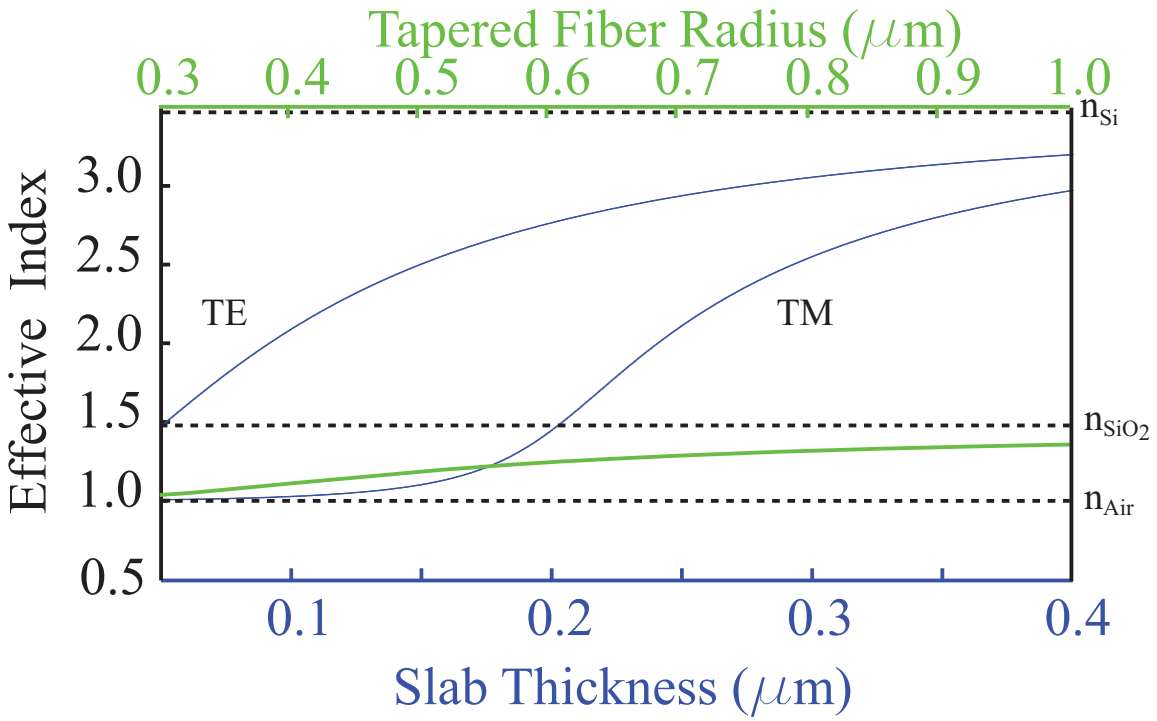

Figure 2.11: Illustration of differences in effective index between TE- and TM-like modes of a slab, and the fundamental mode of a narrow-diameter optical fiber taper

2.2.1.2 Taper fabrication

Optical fiber tapers are formed from a $\sim$ 2 m length of standard single mode fiber with a $\sim$ 2 cm section of acrylate jacketing mechanically removed. The freshly bared region of cladding is then thoroughly cleaned with lint-free wipes and isopropanol. The fiber ends are affixed in Thorlabs HFF003 fiber clamps mounted on oppositely directed Suruga-Seiki K162-50 optically encoded DC stepper stages. During mounting, care is taken to ensure that no twist or shear strain is introduced to the fiber, else the taper transmission upon completion of the tapering operation may be suboptimal. The taper may then be tensioned before the taper pulling operation by advancing the DC stepper a set distance. A Na-

tional Torches Type 3H hydrogen-burning torch (flowing ~ 40 sccm of H2), having been previously lit well away from the fiber to avoid any sparking or sooting of the fiber, mounted on a third optically encoded stepper motor, is then brought nearby the fiber taper to melt a section of the bared glass, and the stepper motors set into motion to draw the fiber ends away from each other at ~ 1 cm/min.

During the taper pull, 1550 nm light from an ANDO AQ4320 tunable laser coupled into the fiber with a spring-loaded manual fiber coupler is monitored with a New Focus nanosecond detector (coupled again with a manual fiber coupler) and National Instruments A-to-D converter with computer control. During the course of the fiber pull, certain regions of the fiber may develop cross-sectional changes sufficiently rapid to couple light from the forward-going fundamental mode launched into backward going modes, unguided cladding modes, and higher-order core-guided modes. The excited modes then interfere at the detector leading to time-varying detected transmission. By monitoring the interference it is possible to approximately identify the point at which multiple modes are no longer guided in the narrow section of the fiber, allowing us to approach single-mode operation of the fiber taper.

When the single-mode condition is achieved, the fiber taper is still too large to use as an effective probe: as seen above, effective coupling requires both approximate phase-matching and efficient mode-overlap. Therefore, the pull is allowed to continue until the desired radius is approximately achieved. The hydrogen torch is then moved away and

the fiber-pull motors stopped. The resulting fiber, fabricated with a constant-size "hot-zone", or melting region, is expected to have an approximately exponential profile along the fiber axis [46, 47].

The fiber is then mounted onto a ruled fiber mount in a "U-bend" configuration allowing for straight fiber testing or fiber "dimple" formation.

In fiber dimple formation, a second SMF28 fiber is stripped and cleaned and brought into contact with the center of the tapered region, significantly deforming the fiber taper. A hydrogen-burning torch is brought nearby the tapered fiber in contact with the second fiber end– now acting as a mold. The flame heats the fiber taper above glass-transition and holds the taper at a temperature just visibly glowing in a darkened laboratory. The torch is then removed, along with the mold-fiber, leaving a "dimple" in the fiber: a region with significantly reduced radius of curvature, whose local variation in position (perpendicular to fiber axis-deflections of micron-scale) increases the utility of the fiber probe technique to encompass planar and closely arrayed devices.

For greatest flexibility, the dimpled fiber taper is placed on a ruled mount with tensioning screw, allowing one to vary the "stiffness" of the probe with a tradeoff in the depth of the fiber dimple [48].

2.2.1.3 Testing

Once prepared for test, the dimpled fiber-taper (plus tensioning mount) is mounted on a motorized Suruga-Seiki KS201-20MS optically encoded

DC stage with 50 nm resolution and computer control of z-axis motion (normal to optical table). A sample with the device under test (DUT) on it is placed on a second stage with identical motors and control of x- and y-axis control. Thus we are able to position the DUT relative to the fiber with 50 nm resolution in all Cartesian directions. The stage with the DUT is outfitted with a rotation stage and goniometer to allow for angular adjustments to be made, and a thermoelectric cooler to allow sample heating and cooling over a range of temperatures (within roughly 0–100°C). All components are placed in an acrylic test enclosure that is continuously purged with clean, dry N2 plumbed into the enclosure though elements made to diffuse the flow and avoid undue atmospheric disturbance of taper or DUT. Figs. 2.7 and 2.8 depict aspects of the integrated test setup (detail of spatial arrangement for coupling and subsidiary equipment, respectively).

In Fig. 2.12 we see example transmission spectra of a microdisk's resonance in the 1496–1564 nm range. The fiber in this case had a dimple and was supported by narrow silicon cantilevers to stabilize coupling with the fiber laterally displaced from the disk. Examination of the field profiles of TE- and TM-like modes shows that side-coupling is naturally somewhat more difficult for TM- than TE-like modes, an effect illustrated by the fact that both types of modes are able to significantly couple, despite the natural advantages of TM-like modes in fiber coupling. When approached from above, the situation is reversed, to some extent: TM-modes couple at much greater disk-fiber gap, a

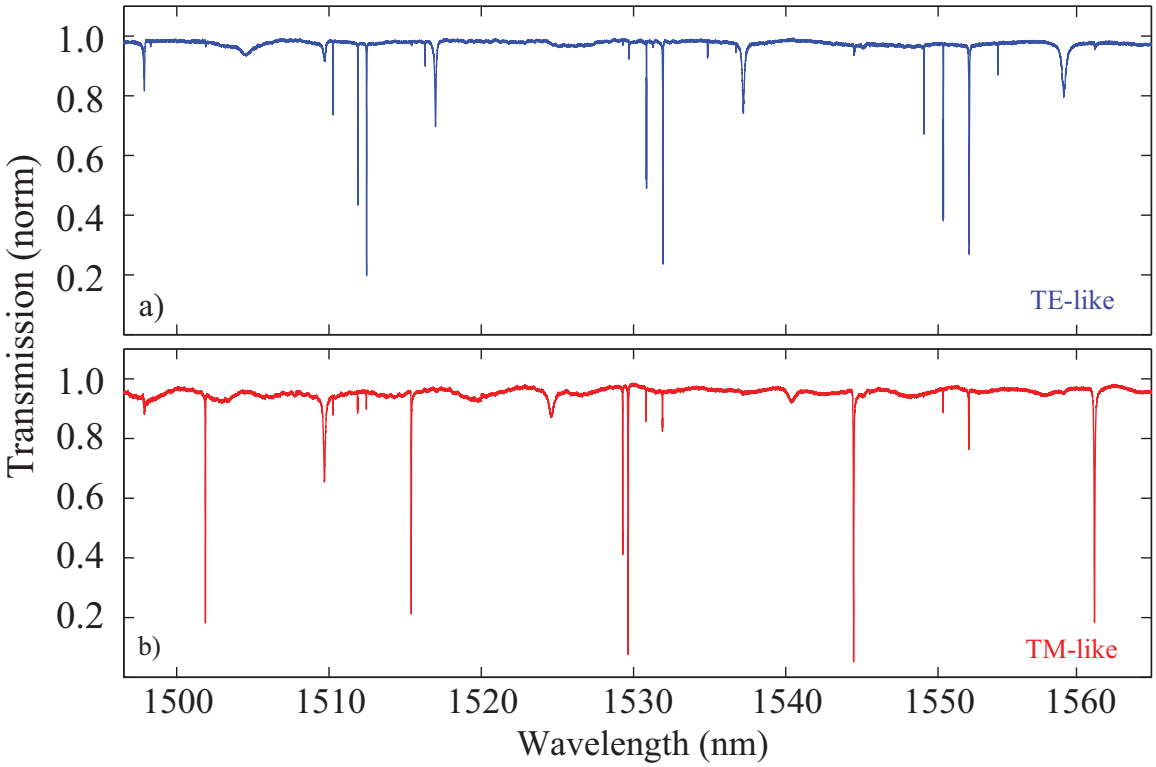

Figure 2.12: Transmission versus wavelength for an optical fiber taper coupled to a silicon microdisk resonator. (a) TE-like modes of a microdisk with thickness approximately 220 nm, diameter approximately 13μm for wavelengths in the 1495–1564 nm band. (b) TM-like modes of the same microdisk. The taper in this case was supported by protruding cantilevers to promote coupling stability. We see a nonflat loss background. Note also the relatively better coupling of the TM-like modes based on multiple radial orders having deep coupling.

fact sometimes used in mode-family identification.

2.2.2 Measurement of free-carrier lifetime

The method used to measure free-carrier lifetimes in silicon microphotonic resonators is described.

We characterize the resonator transmission with a tapered-optical fiber probe. With relative motion in three axes controlled to 50 nm steps, the fiber probe is placed in the near field of the microdisk, allow-

ing transfer of light between the elements. A tunable diode laser (New Focus 6238 Velocity, wavelength range 1496–1564 nm and linewidth $<$ 300 kHz) and combination of photodetector (New Focus 1623 Nanosecond detector) and high-speed oscilloscope/photo-receivers (HP 83480A 50 GHz DCA with HP 83485 optical/electrical plugin) allows collection of transmission spectra and time-domain behavior of the microdisks, respectively. Free carriers are optically created within the microdisk via a fiber-coupled mode-locked Ti:sapphire laser (SpectraPhysics Tsunami 3960-X1S) producing $\sim$150 fs pulses at $\sim$80 MHz of 810 nm light, which is directed through neutral density filter wheels for adjustable intensity control and onto the microdisk with a tapered lensed fiber (OZ optics TSMJ-X-1550-9/125-0.25-7-14-2) mounted on motorized stages.

Photo-generated free carriers modify the microdisk refractive index, decreasing the real part and increasing the imaginary part, both in proportion to the density of charge carriers per unit volume. The time-dependent population thus changes the resonance wavelengths and linewidths. By monitoring the transmission of a stationary CW probe beam coupled into and out of the disk via the optical fiber taper, we may monitor the dynamics of the free-carrier population.

Details of the experiment are discussed below, and the configuration of equipment is depicted in Fig. 2.13.

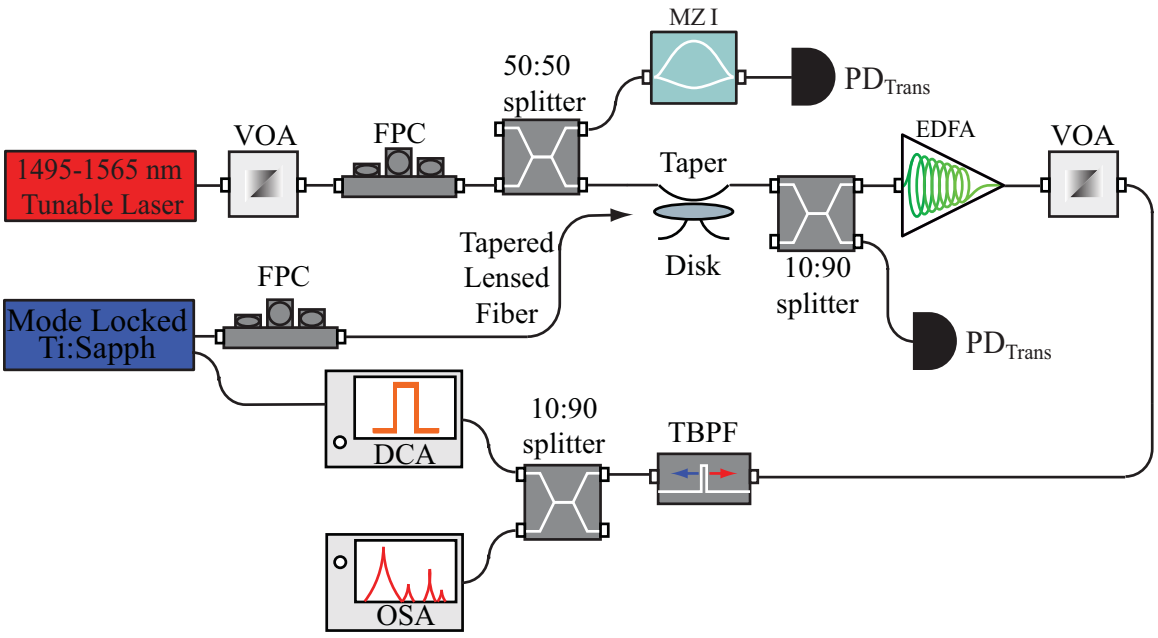

Figure 2.13: Schematic of experimental setup used to experimentally determine free-carrier lifetime in silicon microdisk resonators. Typical setup includes a fiber-based Mach-Zehnder interferometer used to accurately measure wavelength differences, variable optical attenuators for intensity control, and a variety of measurement tools: in this case, an optical spectrum analyzer (OSA) and a digital communications analyzer (DCA) are used for wavelength monitoring and high-speed time-domain acquistion (respectively)

2.2.3 Carrier dynamics

A brief consideration of the dynamics of charge carriers in silicon is in order here. Considering recombination, imposition of external fields, generation and diffusion, we have the following equations of motion for excess electron and hole populations (disregarding Auger and other multi-particle processes in the explicit description):

$$\frac{\partial N(\mathbf{r},t)}{\partial t} = -\gamma_N(\mathbf{r})N(\mathbf{r},t) \tag{2.22a}$$
$$+\nabla\cdot(D_N(\mathbf{r})\nabla N(\mathbf{r},t)+\mu_N N(\mathbf{r},t)\mathbf{E}(\mathbf{r},t))+G_N(\mathbf{r},t)$$
$$\frac{\partial P(\mathbf{r},t)}{\partial t} = -\gamma_P(\mathbf{r})P(\mathbf{r},t) \tag{2.22b}$$
$$+\nabla\cdot(D_P(\mathbf{r})\nabla P(\mathbf{r},t)-\mu_P P(\mathbf{r},t)\mathbf{E}(\mathbf{r},t))+G_P(\mathbf{r},t)$$

where N and P are the excess free electron and hole densities, γ_N and γ_P are location dependent free-carrier decay coefficients for electrons and holes, D_N and D_P are the diffusion coefficients for electrons and holes, μ_N and μ_P are the electron and hole mobilities, G_N and G_P are local generation rates for electrons and hole densities, and $\mathbf{E}$ is the DC electric field present, whether due to an external applied field or due to a relatively stable distribution of trapped charge.

Most generally the decay rates γ_i depend on position, through, e.g., proximity to surfaces, contaminants, or defects where recombination can be facilitated, as well as the local density of free carriers–due to multiparticle effects like Auger recombination or Shockley-Read-Hall processes [**?**, 49, 50].

In most cases, we will be interested in casting the response of optical components in terms of cavity mode-field amplitudes (or waveguide mode-field amplitudes), as a function of time (distance) treating the device as a lumped element. Further, the work here primarily concerns electrically passive devices, and we will ignore the impact of stable

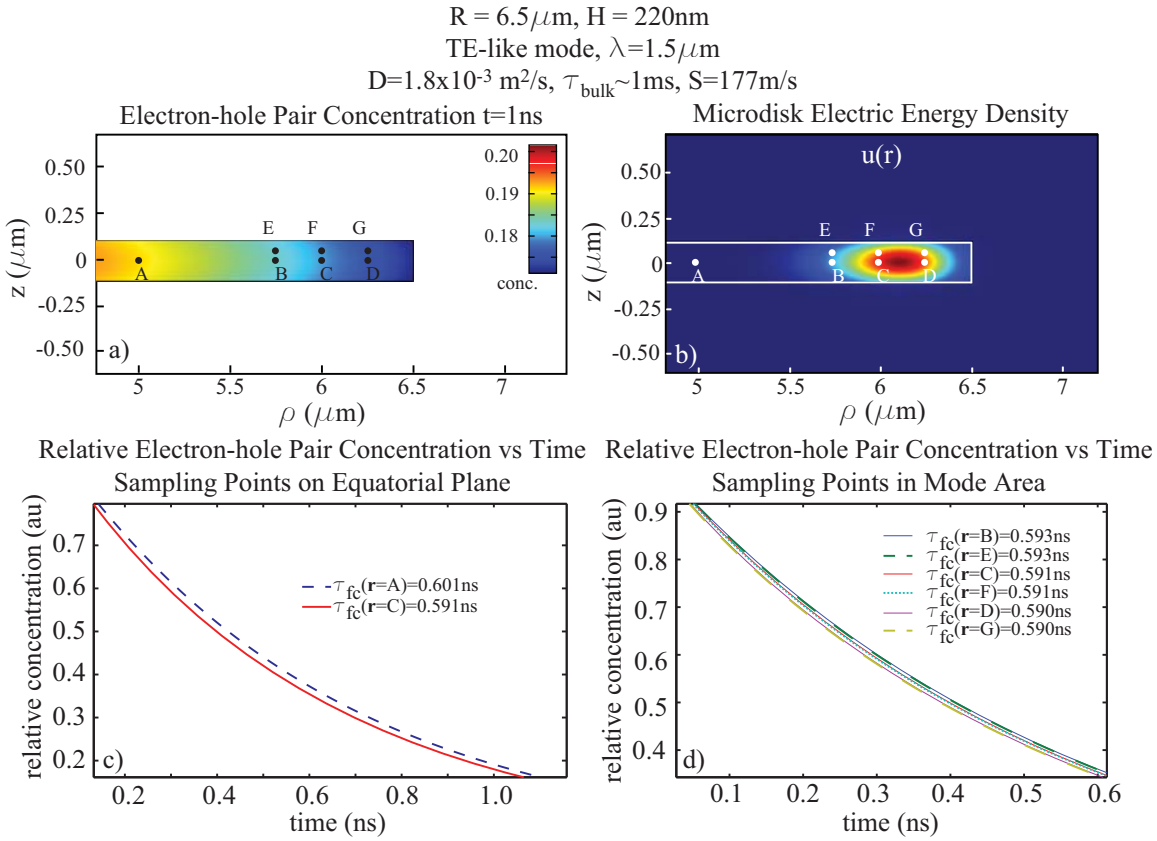

Figure 2.14: Illustration of need for mode-averaging procedure. (a) Spatially varying carrier distribution. At a given time, different locations have different carrier densities. (b) Energy density for TE-like mode. Also has spatial variations. (c) Local densities versus time for points on disk equator inside and out of mode area. (d) Local density versus time for points within mode area

trapped charges—which assumptions amount to positing a zero electric field **E**.

If the surface states mediating electron-hole recombination have a long lifetime or are small in number relative to the population of charge carriers, the surface (or defect) recombination route would become saturated. As a consequence, trapped charges would generate static fields tending to alter the bands as a function of position, thus modifying the dynamical behavior of free carriers. Similarly, depending on the termi-

nation of the silicon surfaces, the reconstruction of dangling bonds may lead to a charged surface, similarly bending bands [51].

If the assumptions in the previous paragraphs hold, however, we may perform a mode averaging of the relevant equations of motion, and cast the effects of diffusion into the averaged equations of motion as part of an effective lifetime incorporating carrier recombination and diffusion, whatever the exact dynamics. We then have:

$$\frac{d\bar{N}(t)}{dt} = \frac{\bar{N}(t)}{\tau_{fc}} + \bar{G_N}(t), \tag{2.23a}$$

$$\frac{d\bar{P}(t)}{dt} = \frac{\bar{P}(t)}{\tau_{fc}} + \bar{G}_p(t). \tag{2.23b}$$

Where the averaging of the spatial dimensions of the electron population density is taken, per usual, with respect to the electromagnetic energy density of the optical mode in question, as:

$$\bar{N(t)} = \frac{\int d\mathbf{r}\, n(\mathbf{r})^2 \mathbf{E}^2(\mathbf{r}) N(\mathbf{r})}{\int d\mathbf{r}\, n(\mathbf{r})^2 \mathbf{E}^2(\mathbf{r})}, \tag{2.24}$$

and that of the hole density as:

$$\bar{P(t)} = \frac{\int d\mathbf{r}\, n(\mathbf{r})^2 \mathbf{E}^2(\mathbf{r}) P(\mathbf{r})}{\int d\mathbf{r} n(\mathbf{r})^2\, \mathbf{E}^2(\mathbf{r})}. \tag{2.25}$$

The incorporation of a surface recombination into the consideration of the dynamics is usually done by specifying an outgoing surface current density at the boundaries of the conductive media. In many models, the recombination rate at the surface is treated as due to some

areal density of recombination centers with energy in the bulk bandgap, and the total recombination rate depends upon the position of the recombination center within the bandgap (relative to the Fermi level), equilibrium carrier concentrations, and recombination center density.

Electron and hole recombination through defect states has long been treated with a formalism, due to W. Shockley, W. T. Read [50], and R. N. Hall [52]. Because surface recombination proceeds via a similar process (surface states take the place of recombination centers), the same formalism may be used to describe both [49, 51].

Derived under the assumption of charge carriers thermalizing immediately [53, 54], the net recombination rate may be given as [50, 52]

$$R = \frac{\sigma_p \sigma_n \, v_{th} \left(pn - n_i^2 \right) N_t}{\sigma_n \left(n + n_i e^{\left(\frac{E_t - E_i}{k_b T} \right)} \right) + \sigma_p \left(p + n_i e^{\left(-\frac{E_t - E_i}{k_b T} \right)} \right)}, \tag{2.26}$$

where σ_k are capture crosssections of the recombination center of the k-th type of charge carrier, v_{th} is a carrier thermal velocity, p and n are the electon and hole volume concentrations at the surface, n_i is the intrinsic carrier volume density, N_t is the surface density of recombination centers, E_t the energy level of the recombination centers, E_i the Fermi level, and $k_b T$ the thermal energy associated with the system temperature, T. This expression further assumes that the recombination centers lie at one energy and have no internal degrees of freedom, and that the bands are unchanged by the presence of the recombination centers.

In either the high or low injection limit, the expression for the surface recombination velocity simplifies to expressions independent of the details in the above equation. In the high injection limit, we may approximately model the surface recombination velocity as $S = \sigma\, v_{th} N_t$, where S is the surface recombination velocity, $\sigma\, v_{th}$ is an ambipolar capture rate, and N_t is a recombination center surface density [55]. In this case, the details of surface recombination are ignored and the surface characterized by that single surface recombination velocity, which practice we will adopt. While not strictly correct, it is a frequently adopted convention. In that limit, we would use as boundary conditions at the interfaces:

$$D_N \frac{\partial N}{\partial \hat{n}}|_{\mathbf{r}\in\partial V} = S_N \left(N(\mathbf{r} \in \partial V) - N_o\right) \tag{2.27a}$$

$$D_P \frac{\partial P}{\partial \hat{n}}|_{\mathbf{r}\in\partial V} = S_P \left(P(\mathbf{r} \in \partial V) - P_o\right), \tag{2.27b}$$

where, because we will assume the high injection limit, D_N and D_P are replaced by the ambipolar diffusion coefficient, S_N and S_P are replaced with the appropriate unilateral surface recombination velocity, ∂V is the bounding surface of the volume, and a single population is considered for electron-hole pairs.

We assess the ability of the simplified model to capture the relevant dynamics by comparing the mode-averaged population decay to an exponential decay. The time-varying distribution of electron-hole pair density is calculated in a disk geometry via the finite-element method

(FEM), using a commercially available software package, COMSOL Multiphysics.

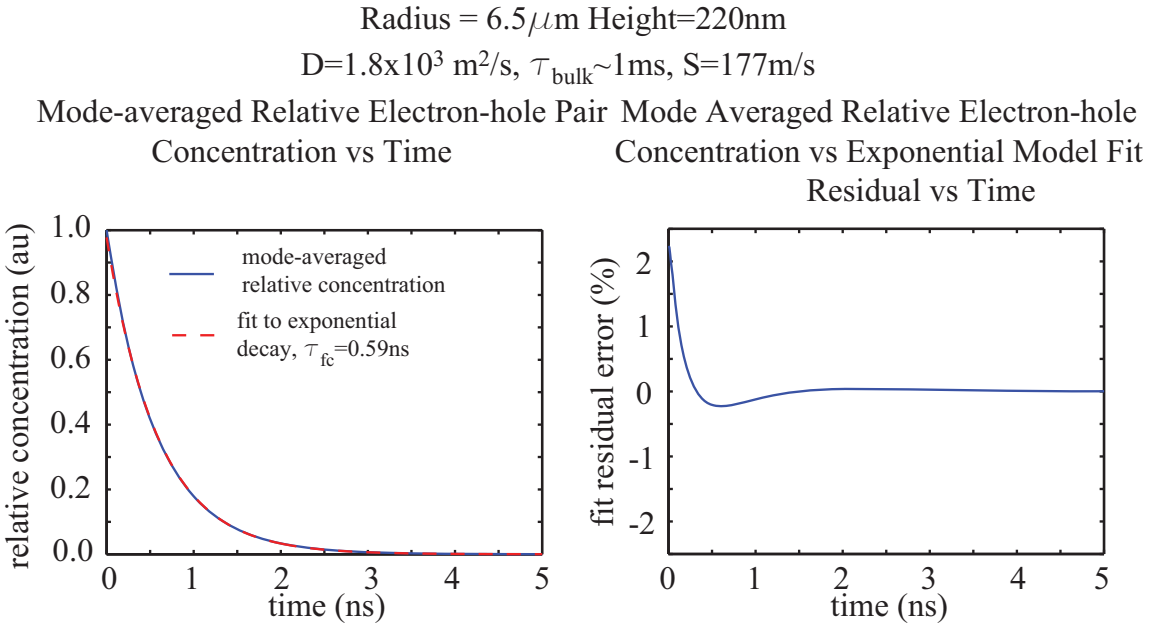

Figure 2.15: Comparison of mode-averaged free-carrier lifetime and exponential model. (a) Comparison between mode-averaged carrier density versus time. Also shown is an exponential fit to that behavior. (b) Residual to the exponential fit from (a)

The calculation of the carrier populations is set up as follows: an initially uniform distribution of carriers is specified and then evolved in accordance with the governing diffusion equation, to determine the population over time at each location within the microdisk. Fig. 2.15(a)—(b) show that a mode-averaged carrier population follows an exponential decay reasonably well when diffusion, surface recombination (implemented as a simple surface recombination boundary condition), and bulk decay are present. Therefore we have adequate justification for employing a mode-averaged equation of motion for the free carrier dynamics using our simple surface recombination boundary condition, and

will do so going forward. However, as is obvious from Fig. 2.15, for many optical modes in disk-like structures, the mode-averaging has only a small effect, as the surface recombination and diffusion so dominate other effects that the free carrier population behaves essentially the same (small time constant differences) at individual points as in the mode-averaged case. More complicated geometries may exhibit different behavior. As we will be employing optical injection techniques, each electron will be accompanied by a hole: we will be using a single population for electron-hole pairs, ambipolar carrier diffusion, and a pair lifetime. We have, then, for the electron-hole populations, the following equation of motion:

$$\frac{d\overline{N}(t)}{dt} = \frac{\overline{N}(t)}{\tau_{fc}} + \overline{G}(t), \tag{2.28}$$

τ_{fc} is the free carrier lifetime, and $\bar{G}(t)$ the mode-averaged photo-carrier generation rate depending on the generation process responsible for carrier population build-up. Leaving aside electronic injection, free carriers could be generated through TPA or absorption of photons with energy above the silicon band gap. In this section, we will specialize to a direct generation process via absorption of above-gap photons. Thus the generation rate will be taken as:

$$G(t) = \eta \frac{P(t)}{\hbar\omega_p V}. \tag{2.29}$$

Where η includes the overlap of the incident pump beam with the

microdisk and the effective absorption of the beam in the microdisk, ω_p is the pump frequency, and V is the disk volume. This approximation requires an effectively uniform pump field in the microdisk to be strictly valid, but unless the intensity varies significantly over the mode dimensions, it should be adequate.

As noted above, the pump light in the free carrier measurements is at 810 nm, or 1.5 eV, well above the 1.1 eV bandgap of silicon. Thus, as reflected in the above equation, each absorbed photon will create an electron-hole pair. The near-IR laser used is also a mode-locked laser, producing pulses at a repetition rate of 80 MHz and width of 150 fs. Because the duration of these pulses is much, much shorter than the other dynamical effects present, we may take the pulses to be effectively instantaneous, allowing us to represent the time dependence of the pump laser as a train of delta-functions. The mode-locked laser pulses carry an energy such that approximate peak power is proportional to the CW power through the pulse bandwidth and repetition rate. Under that approximation, we solve the mode-averaged free-carrier EOM as:

$$N(t) = \frac{\Delta N_0 e^{\frac{-t}{\tau_{fc}}}}{1 - e^{\frac{-1}{\tau_{fc}\nu}}} \left[\frac{e^{\frac{\lfloor \nu t \rfloor + 1}{\tau_{fc}\nu}} - 1}{e^{\frac{1}{\tau_{fc}\nu}} - 1} \right], \tag{2.30}$$

where τ_{fc} is the effective free-carrier lifetime, ν is the repetition rate, $\lfloor f \rfloor$ indicates the floor function of f, and ΔN_0 is the added density of electron-hole pairs generated by single pulse. As noted above, the free-carrier populations generated by the mode-locked laser pulses change

the refractive index in the regions they build up, adding both real and imaginary contributions. The change in refractive index influences the behavior of the resonant modes, and we may incorporate it into their EOMs. We can utilize the framework developed above to that end, with the polarization response of the free-carrier population as the source of added polarizable material.

The evolution of the resonator modes will depend upon the free-carrier populations, and so can be used to probe the system for that effect. It has been found that free-carrier effects can be well described by a Drude model [56] and we shall incorporate them in a way similar to that described above for dielectric perturbations. In the Drude model, charge carriers are assumed to be free particles (not interacting with each other) which may transfer momentum to imperfections in the lattice, vibrations, or impurities [57]. A simple implementation of the dielectric constant associated with this Drude model takes the dielectric (both real and imaginary parts) as proportional to the charge carrier density, so again applying Eqn. 2.7, taking

$$\Delta\epsilon(\mathbf{r},t) = \epsilon_0 \sum_{k=e,h} \overleftrightarrow{\chi}_k 2n_{si} \left(\Delta\, n_k(\mathbf{r},t) + ic\alpha_k(\mathbf{t},t)/(2\omega)\right), \quad (2.31)$$

where $\Delta\, n_k$ and α_k reflect the free-carrier dispersion and absorption in

$\Delta\epsilon$, due to the k-th type of charge carrier, respectively. These populations are time- and space-dependent and the effective dielectric constant due to their presence is time- and space-dependent through that fact. However, we do not expect significant azimuthally dependent spatial structure to the free-carrier distributions due to the impacts of relatively uniform generation and rapid density diffusion. Then coupling between modes of different azimuthal order m will not be an important effect and we consider the modes a_i in Eqn. 2.7 to be uncoupled by the free-carrier populations, and move to the mode-averaged excess-carrier distributions. The dispersion and absorption due to the free-carrier populations in the Drude model may be written at optical frequencies as [56, 58]

$$\Delta\, n_k(t) = -\frac{q^2}{2\epsilon_0 n_{si}\omega^2}\left(\frac{\overline{N}_k(t)}{m_k^*}\right), \tag{2.32}$$

$$\alpha_k(t) = \frac{q^3}{2\epsilon_0 c n_{si}\omega^2}\left(\frac{\overline{N}_k(t)}{\mu_k m_k^{*2}}\right), \tag{2.33}$$

where q is the magnitude of electric charge, ϵ_0 the free space permittivity, μ_k the mobility of the k-th charge carrier type, and m_k^* its effective mass. In Ref. [56, 59] the authors show that free-carrier dispersion and absorption coefficients can be modeled near 1.55μm more accurately than the above, as

$$\Delta\, n_k(t) = -\left(8.8 \times 10^{-4}\overline{N}_e(t) + 8.5\overline{N}_h^{0.8}(t)\right) \times 10^{-18}, \tag{2.34}$$

$$\alpha_k(t) = \left(8.5\overline{N}_e(t) + 6.0\overline{N}_h(t)\right) \times 10^{-18}, \tag{2.35}$$

where the populations are in cm^{-3} and the absorption is the linear absorption rate in cm^{-1}. Typically these values are then scaled for use at other wavelengths as suggested by Eqns. 2.32—2.33 by taking $\alpha(\Delta\, n)' = \alpha(\Delta\, n) \times (\omega_r/\omega)^2$, where ω is the frequency of light and ω_r a reference frequency (corresponding to 1550 nm light). Our polarization due to free carriers is then

$$\mathrm{P(r,t)} = \Delta\epsilon(\mathbf{r}, t; \overline{N}(\mathbf{r}, t)) \left(\textstyle\sum_j a_j(t)\mathbf{E}_j(\mathbf{r})\right). \tag{2.36}$$

We can then write the EOM relevant to the free-carrier lifetime measurement (assuming for simplicity of presentation that the modes under consideration are "singlet" modes) as:

$$\begin{aligned} \frac{da(t)}{dt} &= \left(-\gamma_0/2 + i\left(\omega - \omega_0\right)\right) a(t) + i(\zeta + i\xi)\overline{N}(t)a(t) + \kappa\, S \\ \frac{d\overline{N}(t)}{dt} &= \frac{\overline{N}(t)}{\tau_{fc}} + G(t). \end{aligned} \tag{2.37}$$

Where, of course, $a(t)$ is the complex mode-field amplitude, γ_0 the total optical decay rate in the absence of additional charge carriers, $\omega - \omega_0$ is the detuning of probe and bare cavity frequency, κ the external coupling of the probe between optical fiber probe and microdisk, S the square-root of the power carried by the probe fiber, and ζ and ξ stand in for the dispersion and absorption calculated from Eqn. 2.34—2.35. As above, $a(t)$ is normalized so that its squared-amplitude is equal to the cavity energy, U_{cav}. The impact of excess free carrier density is seen to be included in the second term on the right-hand side (RHS) of the first equation.

We may then infer the free-carrier lifetime of a microdisk, τ_{fc}, by simultaneously fitting several time-domain transmission measurements to solutions of the above equations of motion, computed numerically. If we consider a set of reasonable cavity parameters and excitations, we find that the characteristic free-carrier lifetime exerts a clear impact on the cavity dynamics as monitored by the transmission past the resonator. Fig .2.16 shows a few such combinations, demonstrating the potential utility of this method for discriminating between different lifetimes.

By incorporating the solution of the dynamical equations into a optimization routine in MATLAB, several transmission traces corresponding to different laser-cavity detunings can be simultaneously fit (least-squares-wise). Generally we incorporate the analytical solution for the free-carrier evolution as given in Eq. 2.30, and then numerically

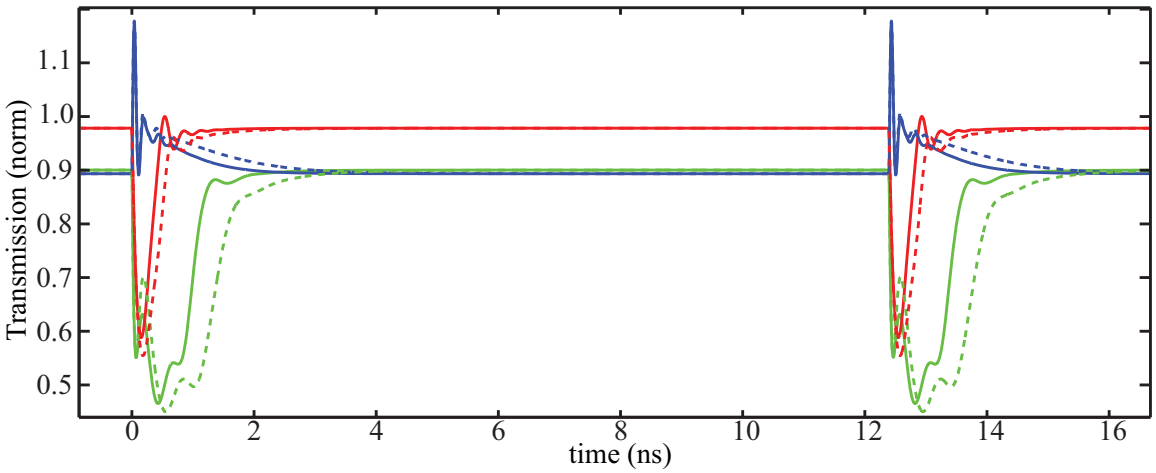

Figure 2.16: Examples of solved equations of motion for free-carrier lifetime measurement. The color of the lines indicates detuning (red = -3×$\Delta\lambda$, green = -1.5×$\Delta\lambda$, blue = 1.5×$\Delta\lambda$), the linetype indicates free-carrier lifetime (solid = 0.5 ns, dashed = 0.75 ns), and the assumed average pump pulse power is 2 mW

integrate the mode-field amplitude equations of motion.

This technique is used in a later chapter to examine the impact on free-carrier lifetime due to surface treatments used in silicon photonics.

Chapter 3

Processing of Silicon Microdisk and Microring Resonators

In this section we consider the basic processing used to create silicon microdisk and microring resonators, from pattern definition and transfer to postprocessing treatments.

3.1 Microdisks

The silicon microdisks studied in this thesis are fabricated from a variety of silicon-on-insulator (SOI) wafers with device layer thicknesses ranging from 219–344 nm with doping ranging from p-doped to resistivity 1–3 Ω·cm to p-doped to resistivity 10–14 Ω·cm on buried SiO_2 layers ranging from 2–3 μm in thickness (Fig. 4.1(c)).

In initial devices, processing of the microdisks began with the deposition of a 20 nm SiO_2 protective cap layer using plasma-enhanced chemical-vapor-deposition (PECVD). In later experiments it was found that the inclusion of the PECVD-cap layer was suboptimal, and processing proceeded without it. Most likely, the chemical configuration

of the silicon top-surface was less than ideal, resulting in added losses. Also possible is deposition-induced lattice damage to underlying silicon [60].

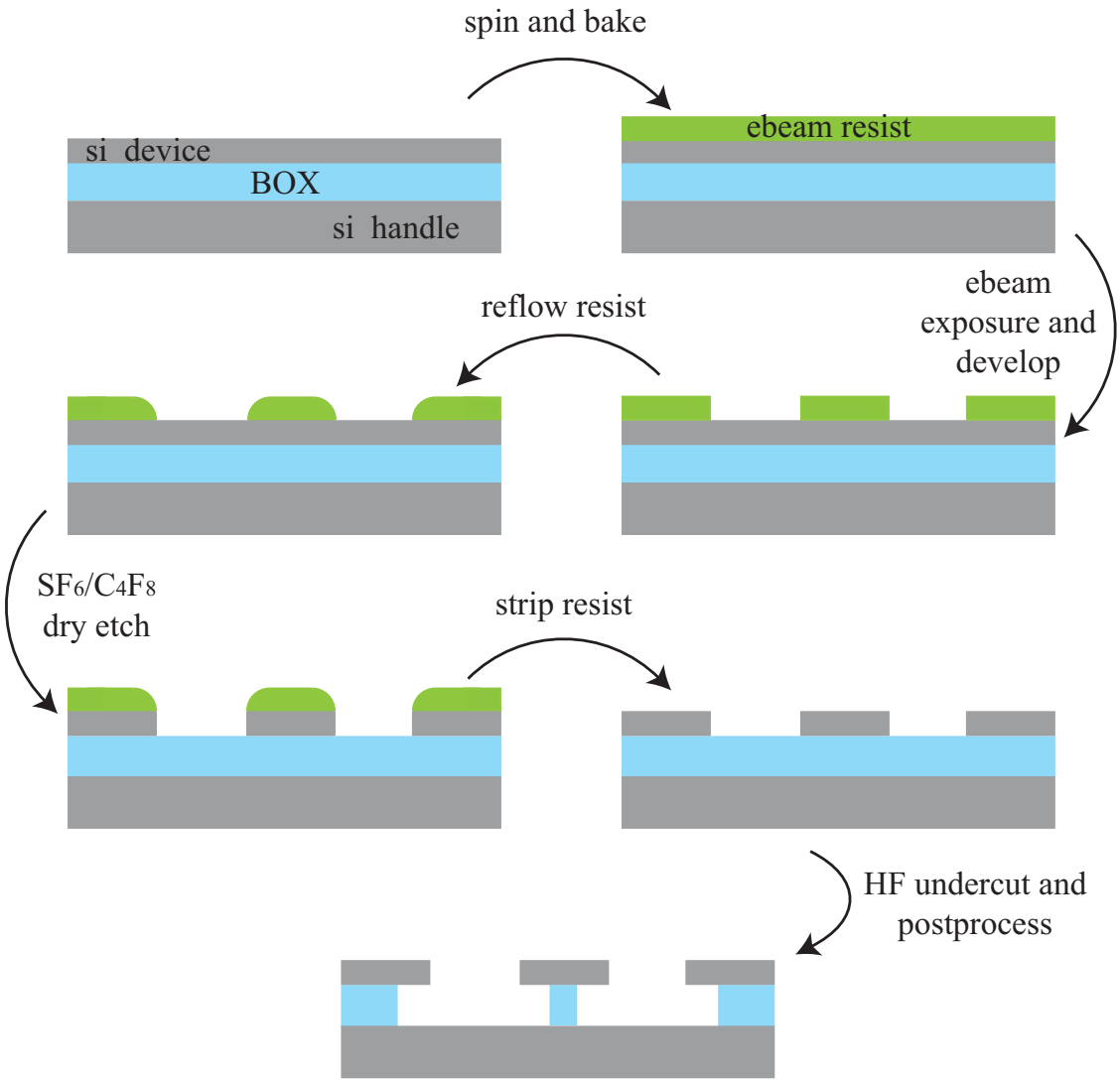

Figure 3.1: Basic process flow of silicon microdisk fabrication

Fig. 3.1 depicts the general processing steps followed in the fabrication of a high-Q silicon microdisk resonator. The steps are discussed below.

An electron-beam resist, Zeon ZEP520A, is spin-coated onto the

wafer at 4000–6000 rpm for 60–120 sec, and oven-baked at 180°C for 20 min, resulting in a ∼400 nm thick film. Disks of radii ranging from 5–30 μm are defined in the electron-beam resist. The patterns exposed by electron beam scanning are developed with Zeon ZEDN50A and rinsed in Zeon ZMD-D (100% methylisobutylketone (MIBK)). The wafer is then subjected to a post-lithography bake. By suitable choice of temperature and duration, this bake can significantly reduce imperfections in the electron-beam resist pattern by reflow. Temperatures too low do not result in resist reflow, while temperatures too high can cause significant loss of resist to sublimation. A temperature high enough to allow the resist to reflow must be reached and maintained for the imperfections in the resist pattern to be reduced. The appropriate duration and temperature for the resist prepared as described above was empirically determined to be 5 minutes at 160°C.

Figs. 3.2–3.4 show the effect of the reflow bake step on ebeam resist. During the exposure step, the electron beam deflection is stationary between pattern repetitions while the sample stage translates from one pattern to the subsequent pattern location. When the patterns are developed, the resulting "dwell"-line can be observed. As is clear from Fig. 3.2(a), the result is a high-aspect-ratio structure which is ideal for demonstrating the impact of a post-development bake. The second panel shows the same feature after a bake as described above. The high-aspect-ratio gap is seen to have partially closed, indicating the edges have advanced. Further, we can see that sharp features are softened.

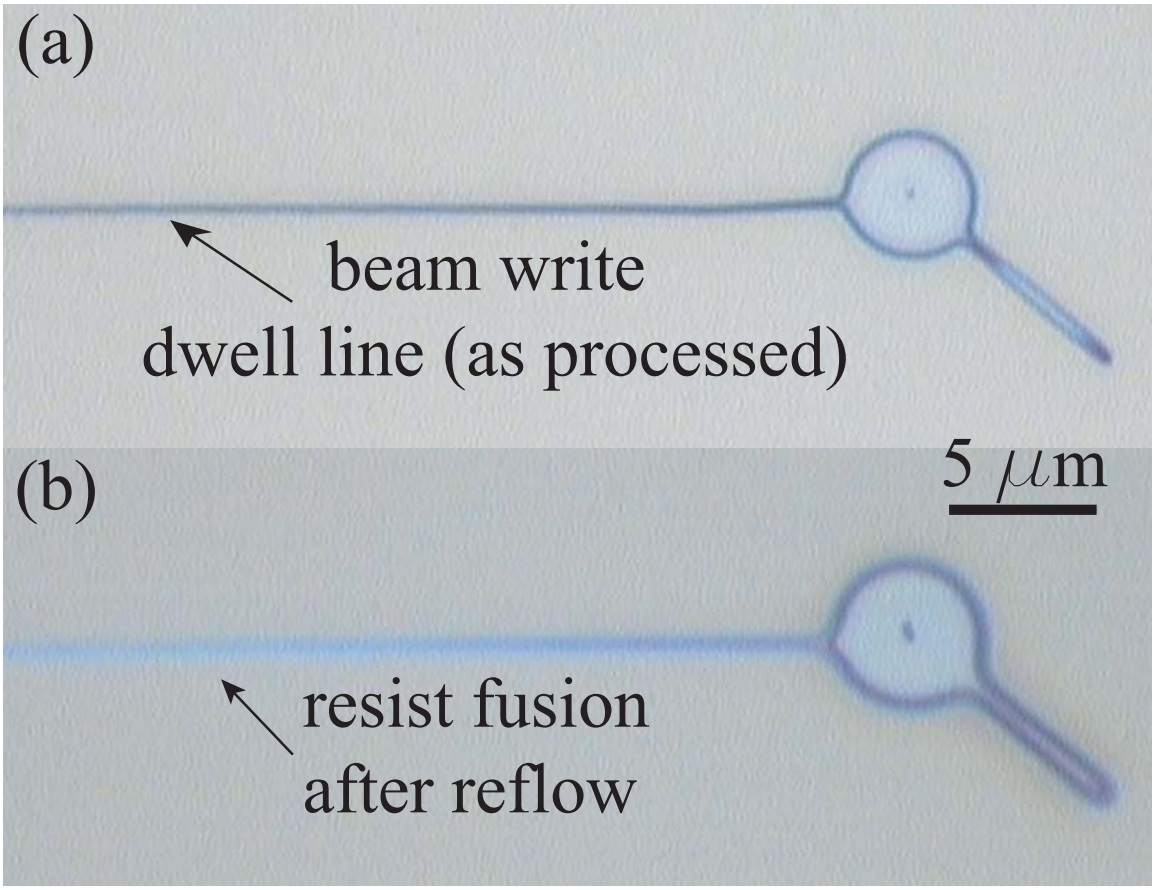

Figure 3.2: The effect of reflow on ebeam resist. (a) As-defined ebeam resist pattern, upon developing. (b) After reflow, sharp angles are rounded and the resist exhibits signs of thinning near the edges. Cracks are partially "healed".

These observations indicate we may achieve a nearly surface-tension-limited mask.

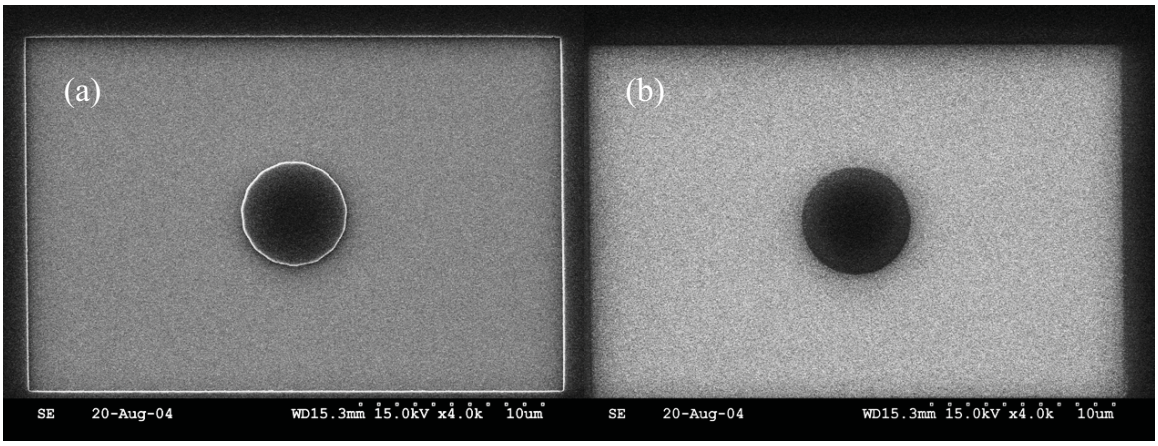

Figure 3.3: Further effects of reflow on ebeam resist. (a) As-defined ebeam resist pattern after developing. (b) After reflow, sharp angles are rounded and the resist exhibits signs of thinning near the edges. Where the sharp angles from (a) were highly effective at generating secondary electrons the detector can detect and thus appeared white, in (b) the profile has rounded-over and smoothed, and the edges are much more difficult to image

We may see a more stark demonstration of the impact or resist post-processing. Using a electron beam lithography similar to that described above, a noncircular (fifteen-sided regular polygon) shape is created. With the same process described above, we reflow the resulting ebeam resist patterns. In Fig. 3.3(a) we see the as-patterned ebeam resist. Note the sharp corners present in the polygon and the bounding box. After reflow, depicted in Fig. 3.3(b), the pattern is significantly smoothed. After the reflow process, the roughness in the patterns is greatly reduced, and the sidewall angle is reduced from 90° to approximately 45° (see Fig. 3.4). The resulting angled mask is prone to erosion during the etch process, and so the inductively coupled plasma, reactive-ion etch is optimized for a smooth device sidewall.

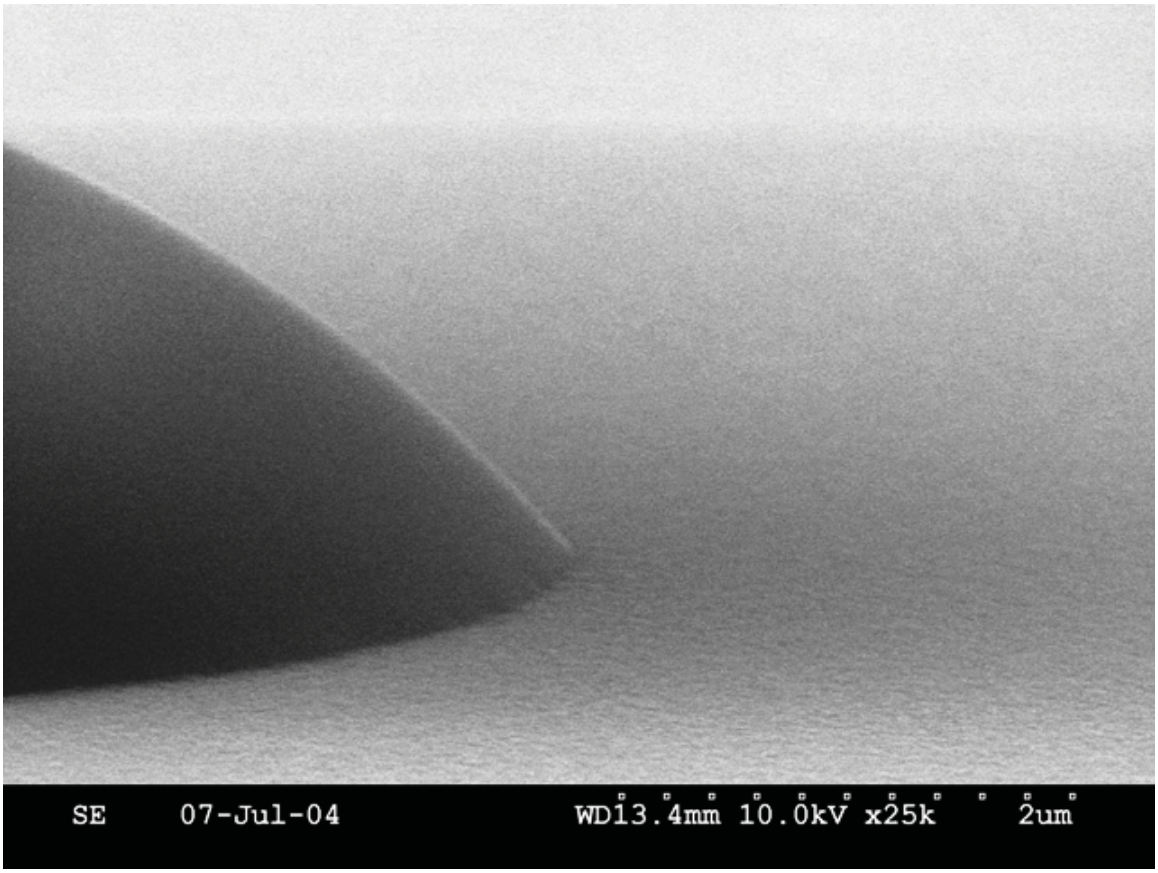

Figure 3.4: Impact on mask angle due to reflow. As-processed resist has vertical or nearly vertical sidewalls which take on significantly angled profile after reflow.

The patterns are then transferred into the Si device layer using a low DC-bias, inductively coupled plasma, reactive-ion etch with SF_6/C_4F_8 chemistry [41, 61]. A scanning electron micrograph of such an etched structure defined by a reflowed mask is shown in Fig. 3.5.

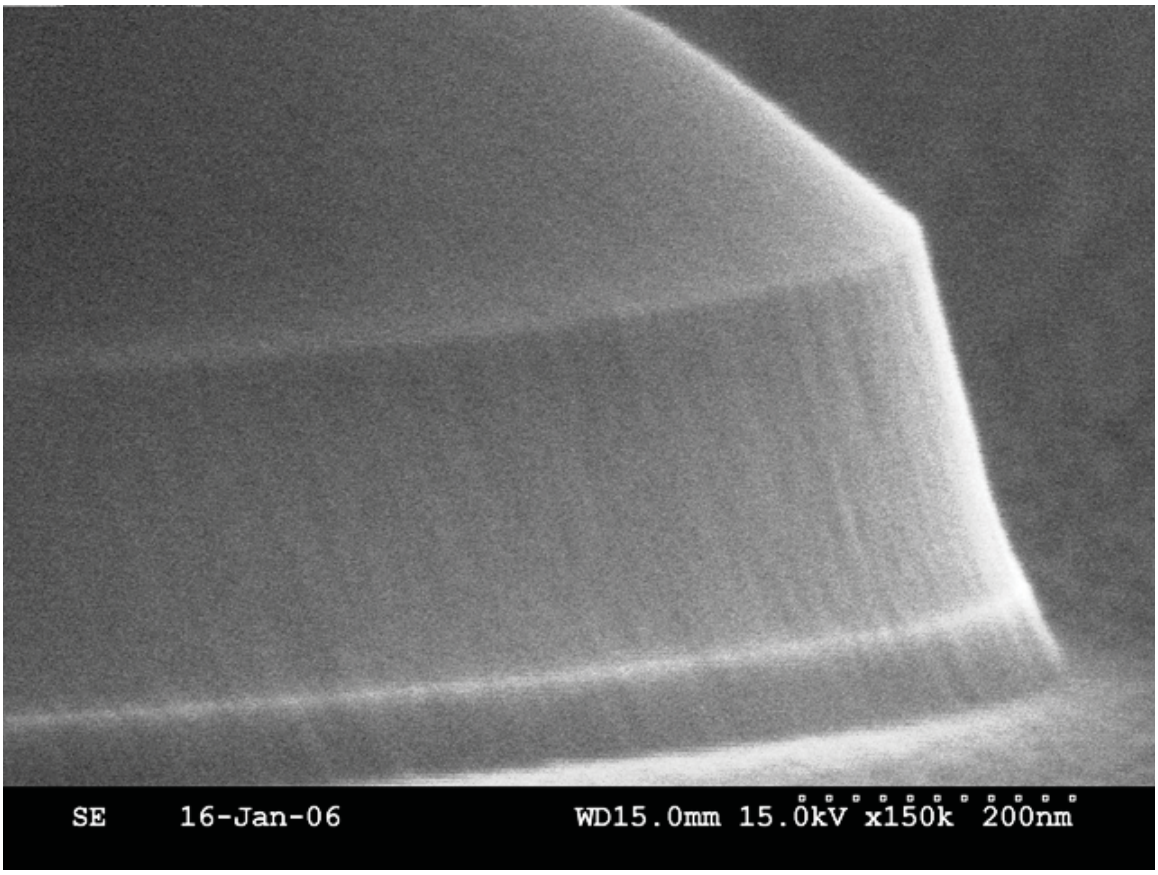

Figure 3.5: Result of carefully optimized dry etch after mask patterning and reflow. Note the angled sidewall and the absence of signs of polymerization of etch reactants and products. Slight deviations from perfection can be seen.

Devices to be tested with a straight fiber taper, our initial probe, require an additional step that is omitted from the process flow depicted above: a mesa-etch to make the silicon handle surface remote from the device under test and allow fiber taper access. In this isolation step, an etch-mask surrounding the disks is photolithographically defined and

the wafer surrounding the disks etched down several microns, leaving the devices isolated on a mesa. Following a Piranha etch to remove organic materials, typical device fabrication resumes.

A dilute hydrofluoric acid solution is used to remove the protective SiO_2 layer and partially undercut the disk (see Fig. 3.6).

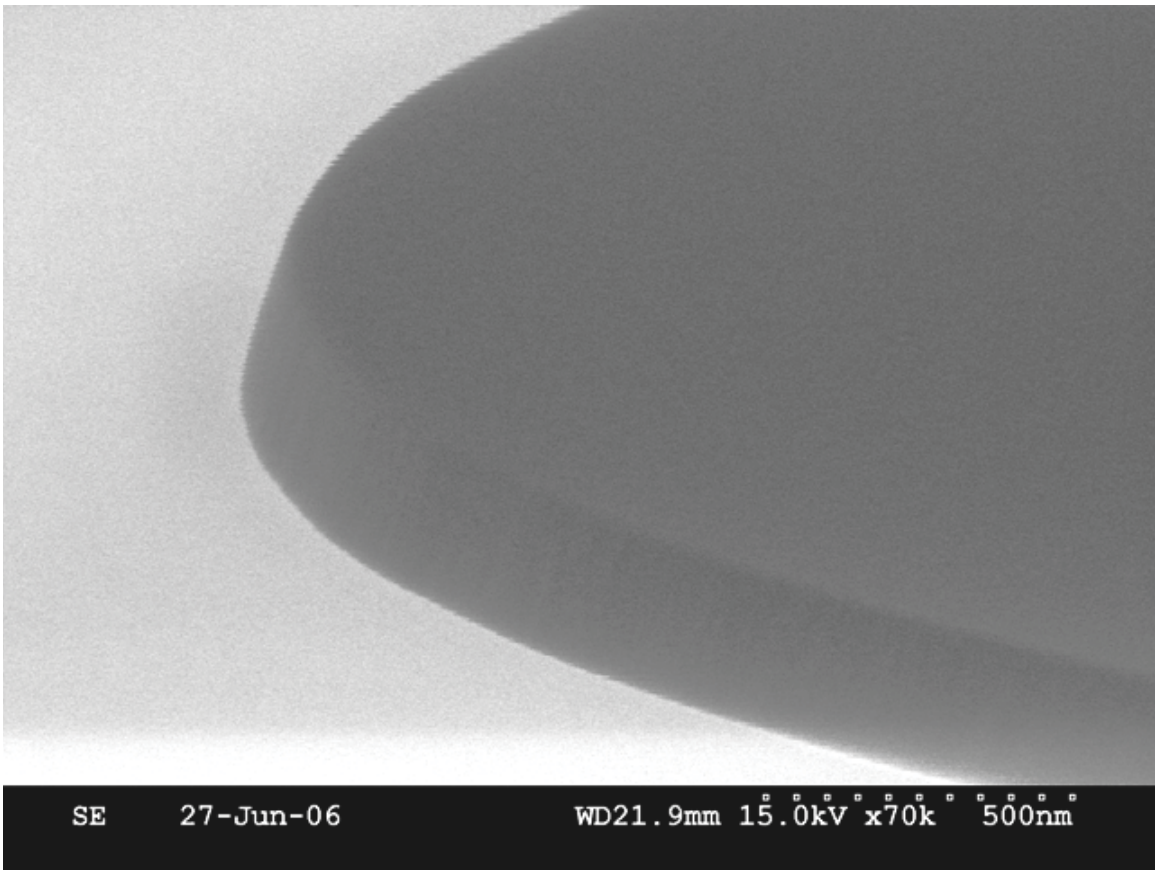

Figure 3.6: An example microdisk. After pattern definition, reflow, and etch, mask is removed by solvent soak and Piranha. A dilute HF etch then partially removes the SiO_2 underneath the disk, leaving it suspended.

During the manufacture of SOI wafers, an interface between bonded device and handle workpieces is created in the buried oxide (BOX). This interface between oxide layers is high quality but displays an etch rate high, relative to bulk silica [2]. This relative etch rate makes the

undercut pedestal take on an angular hour-glass shape (see Fig. 4.1(c)). The wafer is then rinsed in deionized water and dried with clean, dry N_2. Upon completion of the processing, the wafer is immediately removed to an N_2-purged enclosure for characterization. In later device fabrication, postprocessing steps may be included to manipulate the surfaces or passivate them to optical loss or modify the free-carrier lifetimes.

3.2 Planar and floating rings

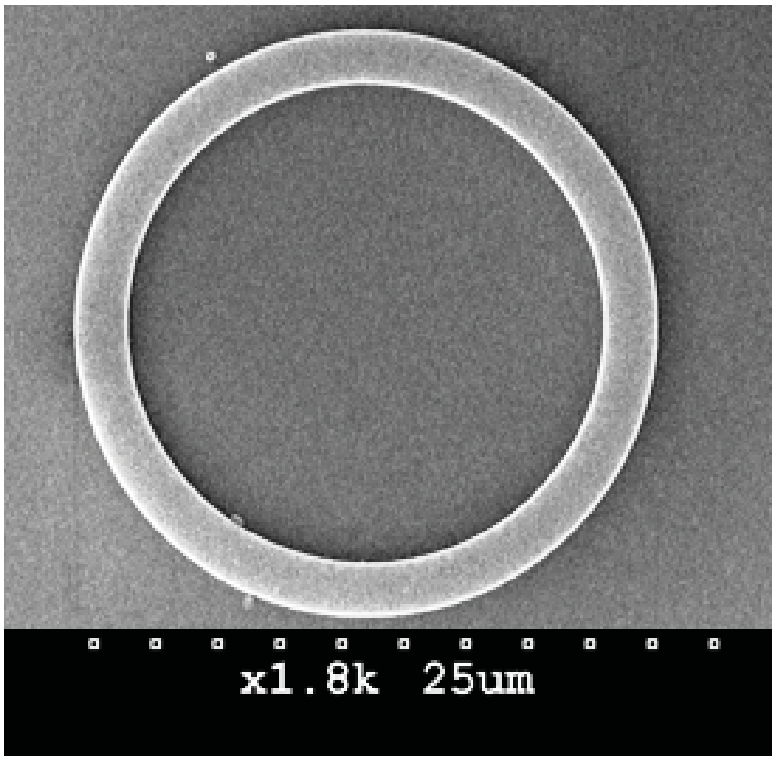

Figure 3.7: Scanning electron micrograph of a planar ring resonator. 20 μm diameter ring with 2 μm width, 220 nm thickness. Transmission test data is shown in Fig. 6.25. The process flow to define such a structure is given in Fig. 3.9.

One aspect of the deployment of silicon microresonators for nonlinear applications that has been ignored in this work thus far is phase

matching. The exceedingly simple geometry of the silicon microdisk resonator has some drawbacks with respect to changing the higher-order dispersive properties: the dependence of the higher-order dispersion on disk radius is very weak, leaving only the thickness to adjust the dispersion properties. By incorporating additional variations in the geometric specification of the resonant device, more flexibility is afforded: partially etched ring structure may, if properly designed, maintain the high quality factors desired while achieving the desired dispersive properties.

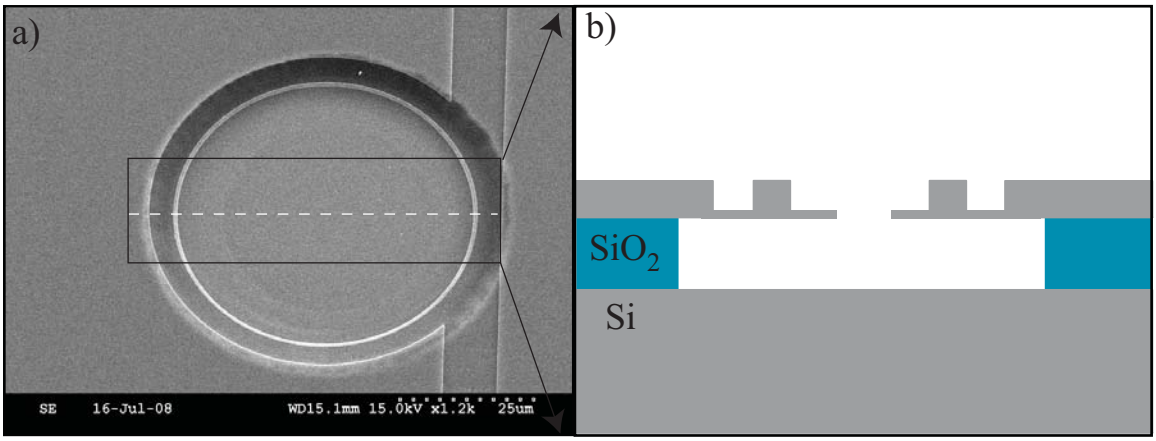

Figure 3.8: Two views of a "floating-ring" geometry. (a) Scanning electron micrograph of a floating ring. The suspending membrane is barely discernible inside and concentric to the ring. The undercut extent is visible outside and concentric with the ring. (b) Schematic depiction of crosssection

By exposing all sides of the ring device to the environment, we may apply the treatments described above, thus modifying the free carrier lifetime of the structure. Simple additional processing steps can be performed leading to a "floating-ring" structure: a partially etched circular ridge supported on a thin diaphragm of silicon, with full access to all sides for chemical passivation or modification. Fig. 3.8(a) is a

schematic view of such a device, and (b) is a micrograph of an example of a fabricated device. Pertinent fabrication information is presented below, and aspects of the design and test are discussed in a later section.

The process flow described above for microdisk resonators can be easily adapted and extended to include these geometries. A simpler process flow than even the microdisk processing is available for planar microrings and is presented in Fig. 3.9. The process flow is largely identical to that of simple microdisk resonators. We find that the only real difference is that microring resonators are not subject to an undercut step. We can see an example of the result of a device fabricated according to that process flow in Fig. 3.7.

The partially etched microring resonator process flow is much the same as that for microdisk resonators, with a few key differences. A partial-thickness etch is used to define the microrings, and after the electron beam resist is cleared away, a second mask deposition and definition may be used to open access for an undercut step. Fig. 3.11 depicts, in schematic fashion, the process flow.

As noted above, the process flow for the floating ring is shown in Fig. 3.11. An example of a structure fabricated according to it is depicted in Fig. 3.8(a), and schematically in (b).

Fig. 3.10(a)–(c) also depicts a floating ring resonator as tested. Panels (a)–(b) show scanning electron micrographs of a fabricated sample. The undercut extent and hole edge are visible in (a). Panel (b) shows a detail of the partially etched ring. The third panel is an optical

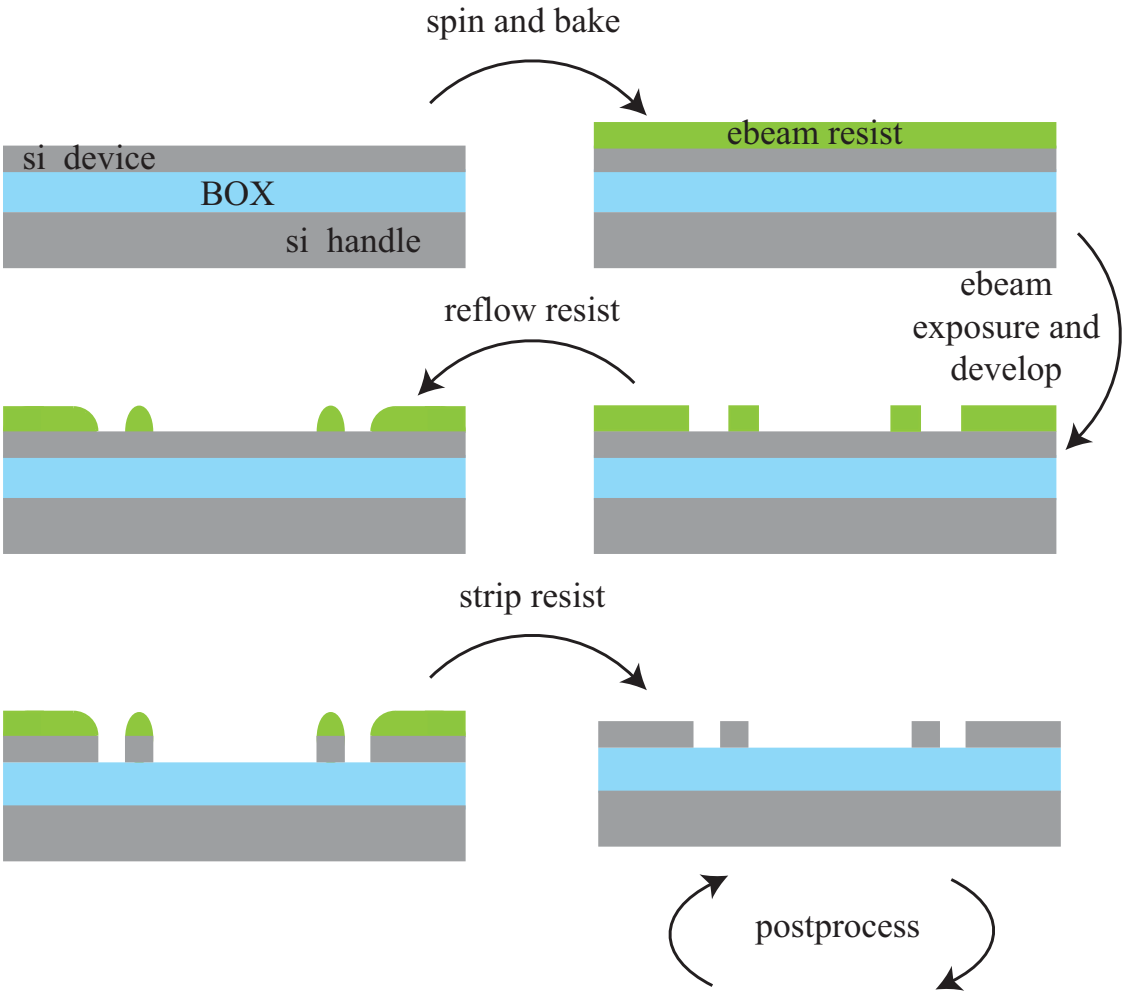

Figure 3.9: The process flow for simple ring resonators.

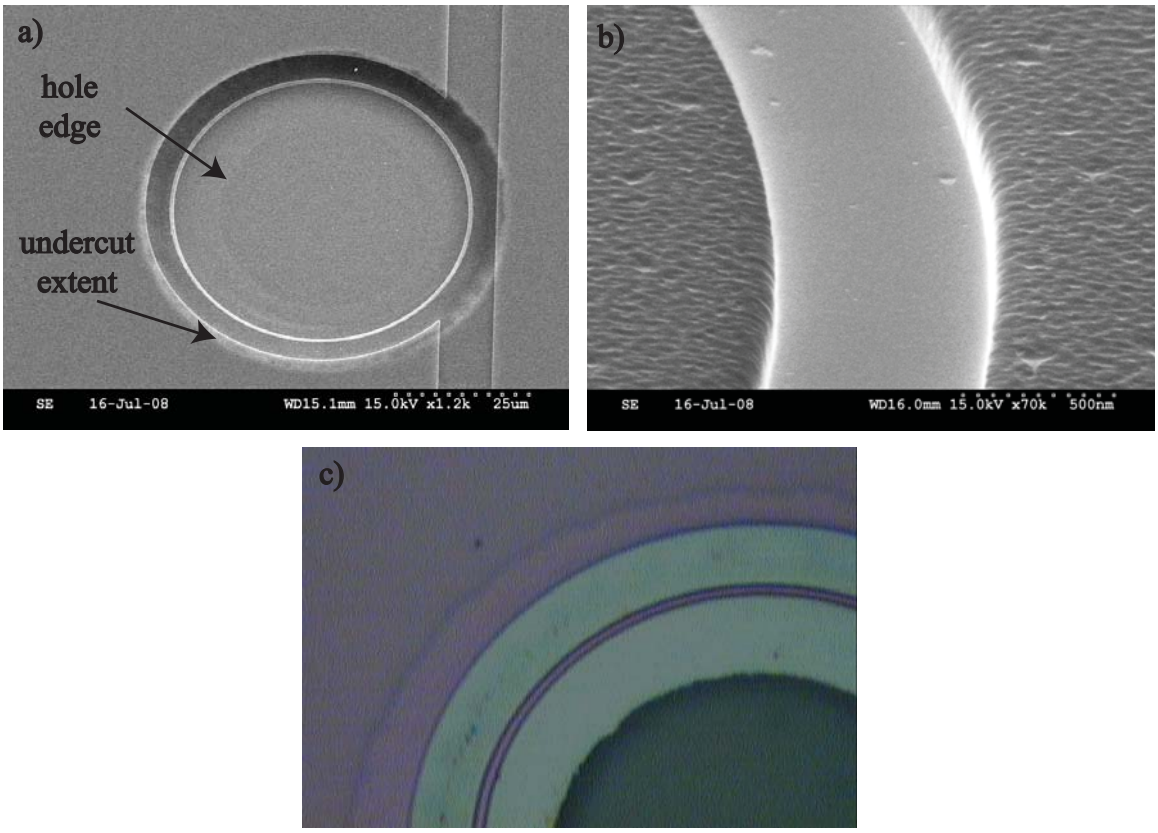

Figure 3.10: Details of as-fabricated "floating ring". (a) A top-down scanning electron micrograph. The thin Si membrane supporting the ring is thin enough to be effectively transparent to the accelerated electrons. (b) A close-up scanning electron micrograph of the partial ring. The sidewall and membrane roughness visible shows there is much room for improvement, despite the relatively high Q of the structures demonstrated. (c) An optical micrograph of same

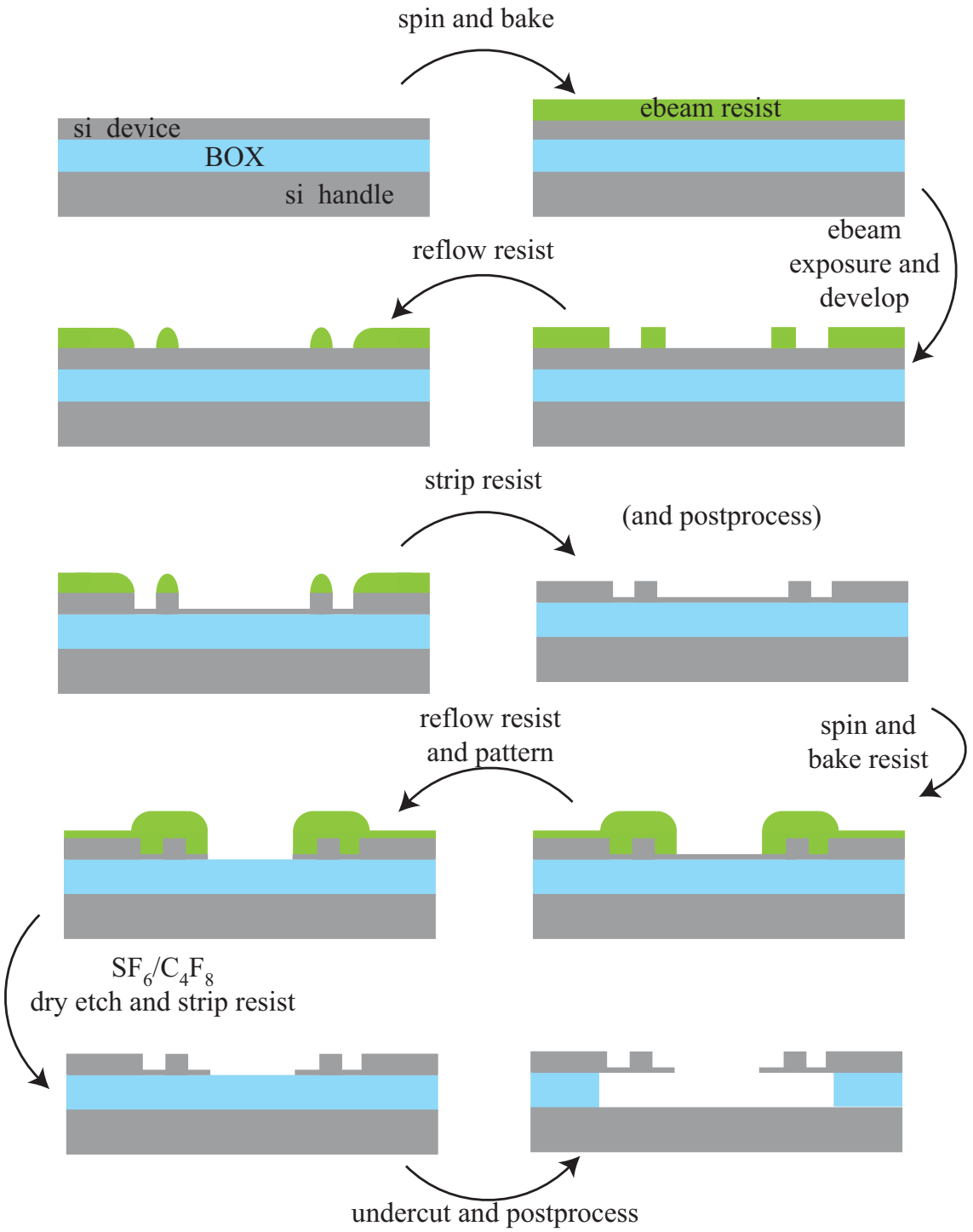

Figure 3.11: The process flow for partial ring resonators. The latter steps may be optional depending upon the desired structure

micrograph in which the hole edge and undercut is more clearly visible.

Chapter 4

Loss Reduction in Silicon Microdisk and Microring Resonators

The resonators fabricated according to the processing described in Chapter 3 are interesting devices. However, for use as nonlinear devices, it is important to achieve the highest quality factors practicable. This section discusses measures taken to characterize and improve the loss properties of silicon microdisk and microring resonators. Moreover, it will be shown later that the free carrier lifetimes of nonlinear silicon devices for use in the telecommunication wavelength regime present a significant obstacle, and enter direct competition with the optical quality factor in terms of figure of merit. This section will discuss methods for characterizing the losses in silicon microdisk resonators and some methods for improving them.

Linear resonances may be usefully characterized by their frequency and loss rate, which together are related to the optical quality factor, $Q = \omega/\gamma$ (for a low-loss resonance), where ω is the resonant frequency

and γ the energy loss rate. Real resonators, of course, are not perfectly closed to their environment: energy can be fed in and extracted in some way. So the total quality factor must take into account the "loading" processes as additional loss channels, and we partition the total loss γ into intrinsic and extrinsic components (subscripted i and e, respectively), which are additive (if the loss channels are independent). Thus the inverse of the quality factors add, and so $1/Q_t = 1/Q_i + 1/Q_e$, where Q_t is the total quality factor including all loss channels.

Typically we are able to modify the extrinsic coupling which loads these resonators: the optical fiber test technique affords flexibility, which is to say that Q_e is largely within our control. We can measure Q_t through transmission experiments, allowing us to infer the intrinsic quality factor. Understanding the losses which comprise the intrinsic resonance behavior is the next task. The intrinsic optical loss in these structures can be quantified by four different components of a modal quality factor,

$$1/Q_i = 1/Q_r + 1/Q_b + 1/Q_{ss} + 1/Q_{sa}, \tag{4.1}$$

where Q_r, Q_b, Q_{ss}, Q_{sa} are related to optical loss due to radiation, bulk absorption, surface scattering, and surface absorption, respectively. In subsequent sections we will discuss these factors.

In order to study the optical loss mechanisms within Si microdisk resonators, a series of disks with radii $R = 5, 10, 15, 20, 30$ μm was created. Due to the excellent optical confinement of the silicon whispering-

gallery-mode (WGM) resonator, radiation losses become increasingly negligible as the disk radius is increased, as in Section 2.1.3.1. Moreover, as described in Section 2.1.3.1, increase of the microdisk radius results in WGMs being pulled away from the microdisk edge. Thus, varying the disk radius provides a means to discriminate between sidewall surface effects, quantified by Q_{ss} and Q_{sa}, and bulk effects, Q_b.

4.1 Radiation losses

It is possible to keep radiation losses low by design. As we saw above, the radiation Q is exponentially increasing with radius and with effective index. So if the radiation Q approaches a limit on the total Q, a small increase in either disk thickness or radius can dramatically decrease the radiation losses experienced by a given mode.

For the most part, then, we will discount radiation loss as a factor for the device thicknesses and radii considered in this work; by design they are not typically radiation limited.

4.2 Bulk absorptions

We may incorporate (small) bulk absorptions perturbatively as small imaginary components of additional dielectric. Ignoring any mode-coupling that might result from the smll additional imaginary dielectric means that Eqn. 2.7 results in the following

$$\frac{\Delta\omega}{\omega} = -\left\langle \frac{\Delta\, n}{n} \right\rangle. \tag{4.2}$$

Where the angled brackets indicate mode-averaging. Then if all absorption is due to that addition of imaginary-index material, and it is spatially uniform, that simplifies to

$$Q_b = \frac{\omega}{\Gamma\, \Delta\, n}, \tag{4.3}$$

and the overlap between mode and the index perturbation is Γ and the index change (also the disk) is $\Delta\, n$.

In the section regarding surface scattering we find, using resistivity measurements from the manufacturer of the boron-doped SOI material (1–3 Ω·cm) and silicon absorption studies [59], that residual free carriers in our material should limit $Q_b \lesssim (3.7\text{–}8.8\times 10^6)$. Later work uses SOI material with higher resistivity (10–14 Ω·cm, p-type, $Q_b \lesssim (3\text{–}4\times 10^7)$).

4.3 Surface scattering

Inspired by the ultra-smooth glass microspheres [62–65] and microtoroids [66] formed under surface tension, in this work an electron-beam resist reflow technique is used to significantly reduce surface imperfections in the edge of the microdisk resonator.

A typical taper transmission spectrum of an $R = 30$ μm microdisk is shown in Fig. 4.2. The observed double resonance dip (doublet) is a result of Rayleigh scattering from disk surface roughness, illustrated

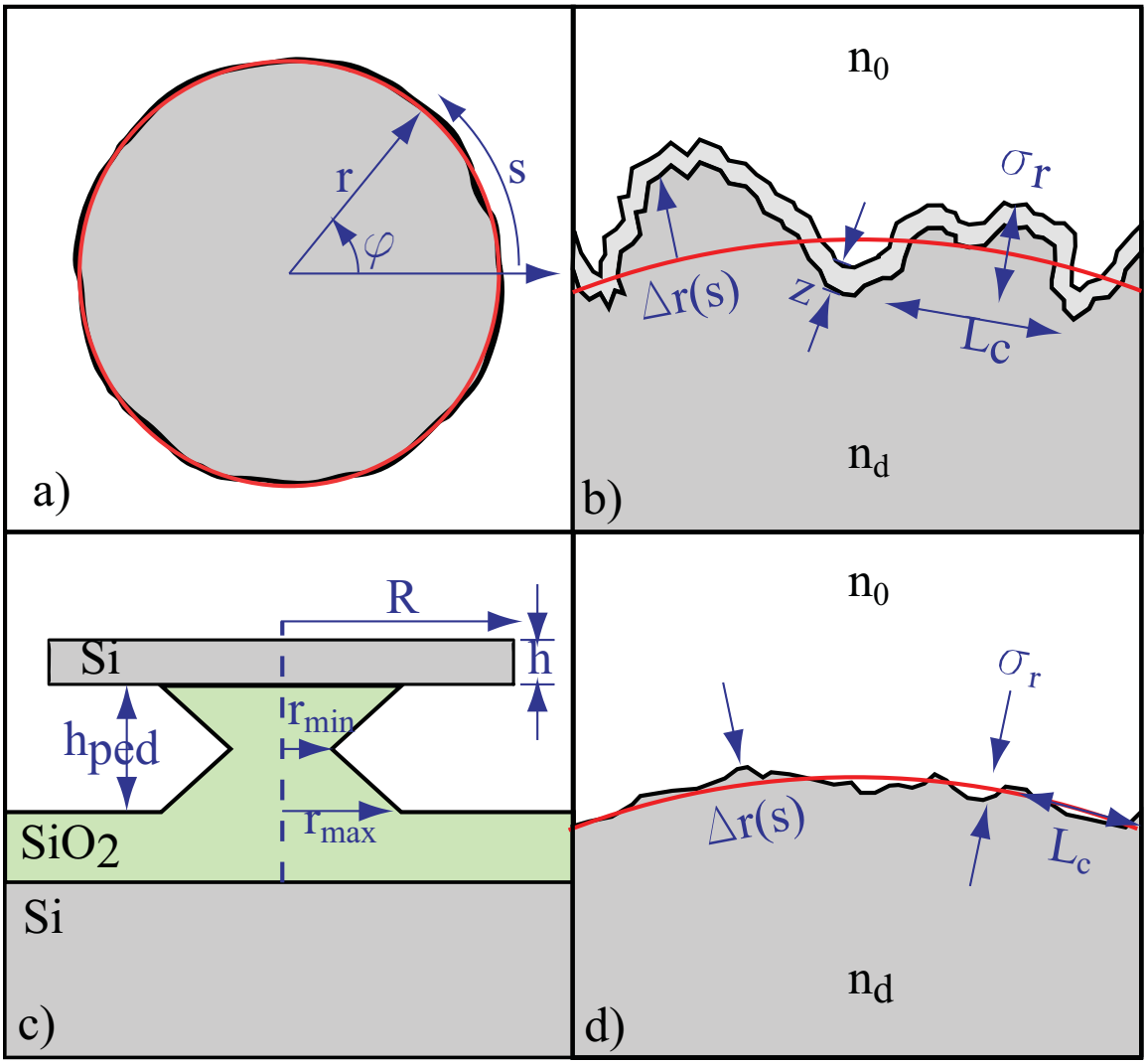

Figure 4.1: Schematic representation of a fabricated silicon microdisk. (a) Top view showing ideal disk (red) against disk with roughness. (b) Top view close-up illustrating the surface roughness, $\Delta r(s)$, and surface reconstruction, ζ. Also shown are statistical roughness parameters, σ_r and L_c, of a typical scatterer. (c) Side view of a fabricated SOI microdisk highlighting idealized SiO_2 pedestal. (d) Schematic top view of improvements due to resist reflow: amplitude of roughness is decreased.

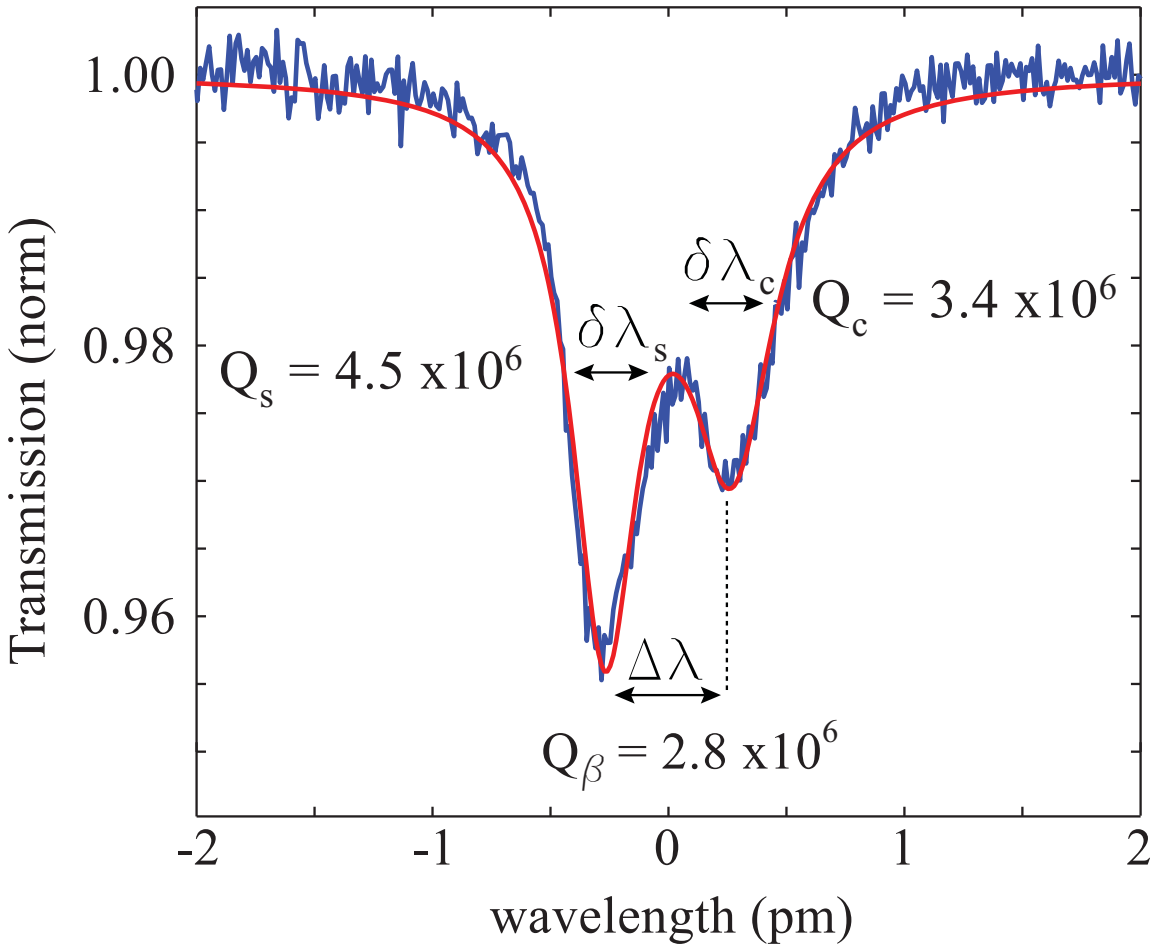

Figure 4.2: Taper transmission versus wavelength showing a high-Q doublet mode for the $R = 30$ μm disk. $Q_c \equiv \lambda_0/\delta\lambda_c$ and $Q_s \equiv \lambda_0/\delta\lambda_s$ are the unloaded quality factors for the long and short wavelength modes, respectively, where $\delta\lambda_c$ and $\delta\lambda_s$ are resonance linewidths. Also shown is the doublet splitting, $\Delta\lambda$, and normalized splitting quality factor, $Q_\beta \equiv \lambda_0/\Delta\lambda$.

in Fig. 4.1(b) as $\Delta r(s)$. The surface imperfections created during fabrication lift the degeneracy of clockwise-(cw) and counter-clockwise-(ccw) propagating WGMs in the microdisk, creating instead standing wave modes [26–28, 30, 67]. As described in Ref. [22], the highest Q WGMs in these microdisks are found to be of TM-like polarization and of radial mode number $n = 1$, where the field interaction with the disk-edge surface is minimized [22]. For the wavelengths studied here, the corresponding azimuthal number is $M \sim 60$ for the $R = 5$ μm disks, and scales approximately linearly with radius for larger microdisks. All of the WGMs studied in this work were confirmed TM-like polarization and of radial number $n \sim 1$ through studies of their polarization and position-dependent coupling to the fiber taper [22].

A statistical model for the doublet splitting was constructed using an effective index model and time-dependent perturbation theory described in Chapter 2 and Refs. [22, 23]. The resulting model [26, 68] is used to fit the data in Fig. 4.2 with linewidth parameters, $\delta\lambda_c$ and $\delta\lambda_s$, and doublet splitting, $\Delta\lambda$. A normalized measure of the mode splitting is defined to be the free-space wavelength, λ_0, divided by the total resonance splitting ($\Delta\lambda$), given here by Q_β. In the case where $Q_\beta \gg Q_i$, we would find no doublet splitting and pure cw and ccw traveling WGMs; $Q_\beta \ll Q_i$ would correspond to large doublet splitting and well-separated standing wave WGMs. In the latter case, Q_β is the appropriate measure of the coupling strength needed to achieve critical coupling, and the useful bandwidth there, as depicted in the inset of

Fig. 4.3).

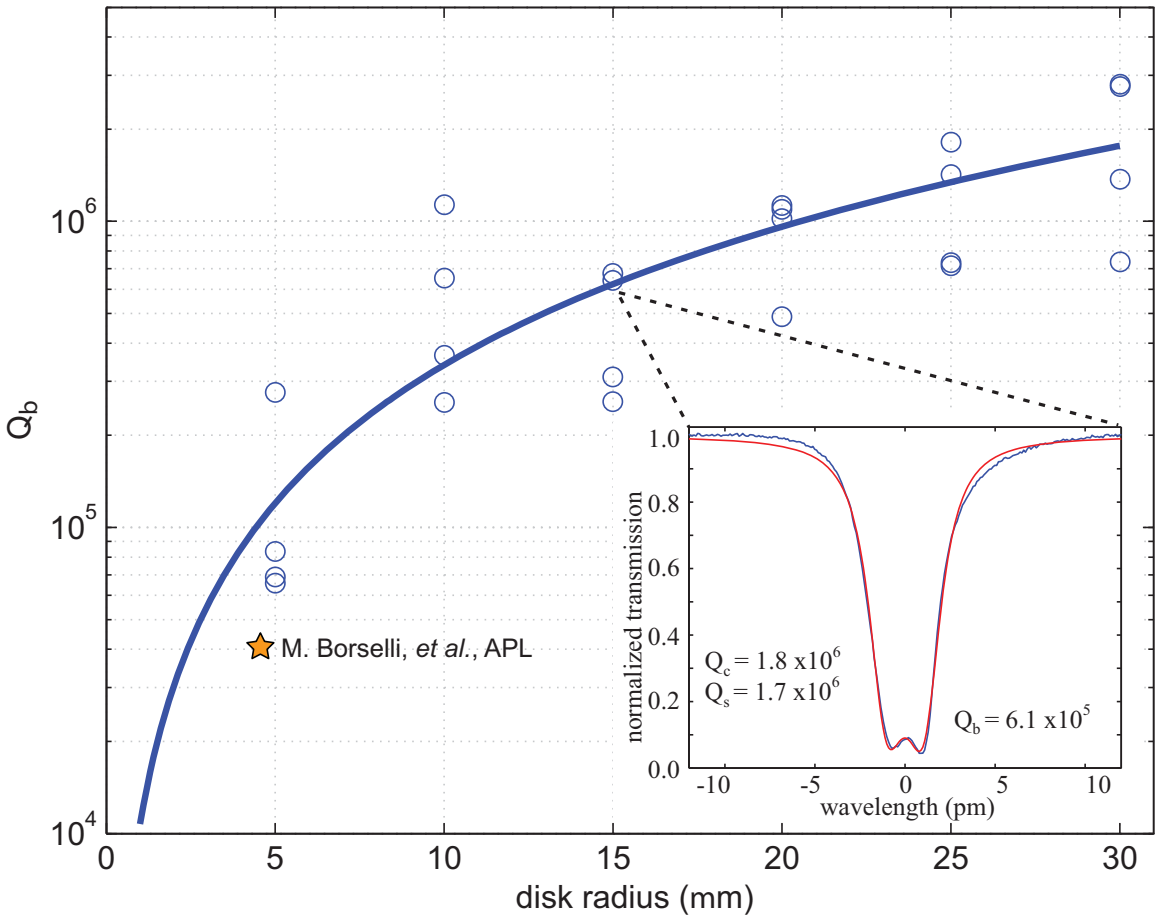

Figure 4.3: Normalized doublet splitting (Q_β) versus disk radius. (inset) Taper transmission data and fit of deeply coupled doublet demonstrating 14 dB coupling depth

Figure 4.3 plots Q_β for each of the measured microdisk radii, where for each microdisk we plot the results for the four highest Q_i doublet modes in the 1410–1500 nm wavelength range. From Ref. [22,23] we get the following equation for the normalized doublet-splitting parameter:

$$Q_\beta \equiv \frac{\lambda_0}{\Delta\lambda} = \frac{1}{\sqrt{2}\pi^{3/4}\xi}\left(\frac{V_d}{V_s}\right), \tag{4.4}$$

where V_d is simply the physical volume of the microdisk and a relative dielectric contrast is defined as ξ, and given by

$$\xi = \frac{\bar{n}^2\left(n_d^2 - n_0^2\right)}{n_d^2\left(\bar{n}^2 - n_0^2\right)}. \tag{4.5}$$

n_d, n_0, and $\bar{n}$ are the indices of refraction for the disk, cladding, and 2-D effective slab, respectively [69, 70]. A critical parameter in this formalism is the effective volume of a typical scatterer, defined as $V_s \equiv \sqrt{RL_c}h\sigma_r$, where L_c is the correlation length of the roughness, h is the disk height, and σ_r is the standard deviation of the roughness amplitude (illustrated in Fig. 4.1(b)). For the the doublet splitting versus disk radius in Fig. 4.3 (solid blue curve with $Q_\beta \sim R^{3/2}$ dependence shown in Eqn. 4.4, a best-fit value of $\sqrt{L_c}\sigma_r = 2.7\ \mathrm{nm}^{3/2}$ is found. Because the same Rayleigh scattering mechanism responsible for lifting the azimuthal degeneracy couples the unperturbed microdisk modes to radiation modes, this scattering volume is important in quantifying the surface scattering losses [29, 68].

From an analysis similar to that used for the mode coupling, the surface scattering quality factor, Q_{ss}, is approximated as:

$$Q_{ss} = \frac{3\lambda_0^3}{8\pi^{7/2}n_0\delta n^2\xi}\left(\frac{V_d}{V_s^2}\right), \tag{4.6}$$

where $\delta n^2 \equiv n_d^2 - n_0^2$ [22, 23]. Fig. 4.4 plots the measured linewidths ($\delta\lambda_{c,s}$) of each of the microdisk modes represented in Fig. 4.3 as a dimensionless quality factor, $Q_i \equiv \lambda_0/\delta\lambda_{c,s}$ (shown as black circles, one for each mode of a doublet pair). From Eqn. 4.6, we expect a linear dependence versus disk radius of the surface scattering quality

factor, Q_{ss}. The dash-dotted blue curve shown in Fig. 4.4 represents the resulting surface-scattering component of the total loss as predicted by the fit to $\sqrt{L_c}\sigma_r$ from the observed doublet splitting (thus we find the mode-coupling-induced doublet splitting provides a measure of surface roughness-induced scattering losses). In comparison to recently reported results not incorporating the e-beam resist reflow technique [22] (shown as an * in Fig. 4.3), the doublet splitting has been reduced by nearly a factor of 2.5. This results in an increase in the predicted Q_{ss} by more than a factor of 6. Given that the measured quality factor of the current microdisk resonators has only doubled, this suggests these resonators are limited by loss mechanisms not significant in previous work [22], and the remaining mechanism is surface absorption.

4.4 Surface absorption

Subtracting the fit to Q_{ss} from the data, a strong linear dependence with radius still remains. Since the optical losses decrease as the modes are pulled in toward the center of the microdisk, we assume that neither the pedestal nor the top and bottom surfaces are significant sources of optical loss, because the exposure to top and bottom surfaces, as well as to the effects of the silica pedestal, should *increase* with increasing microdisk radius. A disk edge surface absorption component of optical loss should have a linear dependence with microdisk radius, similar to that of surface scattering [22, 23]. Ref. [23] finds that the approximate dependence of the surface absorption quality factor, Q_{sa}, is:

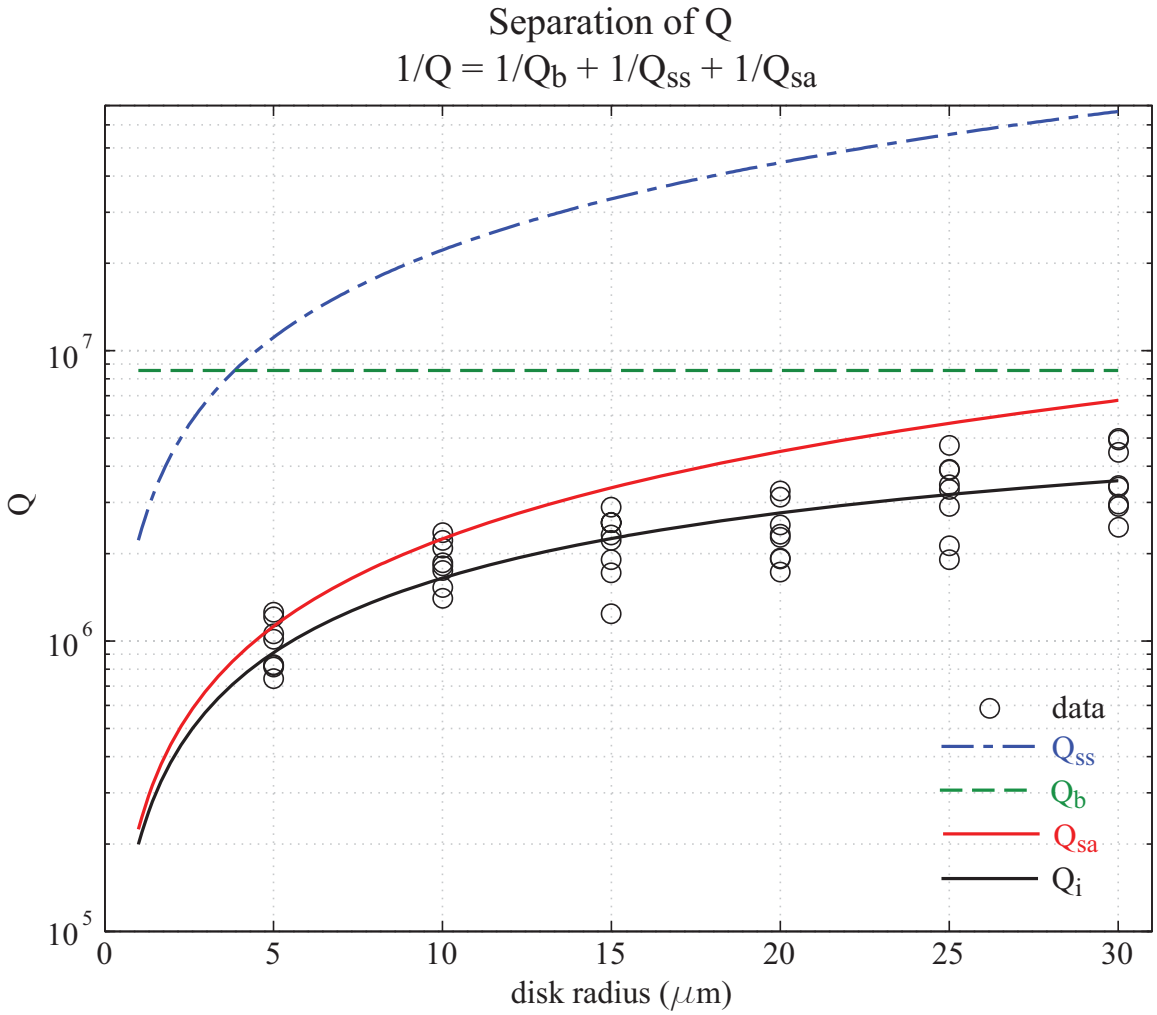

Figure 4.4: Measured intrinsic quality factor, Q_i, versus disk radius and resulting breakdown of optical losses due to: surface scattering (Q_{ss}), bulk doping and impurities (Q_b), and surface absorption (Q_{sa})

$$Q_{sa} = \frac{\pi c \left(\bar{n}^2 - n_0^2\right) R}{\lambda_0 \bar{n}^2 \gamma_{sa} \zeta}. \tag{4.7}$$

Since great care is taken to preserve the quality of the top and bottom surfaces of the silicon microdisk, a plausible assumption is that the dominant lattice damage occurs at the disk sidewalls during the etch. While efforts are taken to minimize etch damage, it remains clear that reactive ion etching locally damages the lattice during the material ablation allowing for the incorporation of various lattice impurities and defects [61]. The local surface absorption rate coefficient, $\gamma_{sa}(\mathbf{r})$, is used to calculate a spatially averaged loss coefficient according to:

$$\bar{\gamma}_{sa} = \frac{\int \gamma_{sa}(\mathbf{r}) n^2(\mathbf{r}) \left|E(\mathbf{r})\right|^2 d\mathbf{r}}{\int n^2(\mathbf{r}) \left|E(\mathbf{r})\right|^2 d\mathbf{r}}, \tag{4.8}$$

where the appropriate weighting function is proportional to the electric field energy density of the optical mode [19]. An approximate model for $\gamma_{sa}(\mathbf{r})$ would be to assume that there exists a layer of damaged, impure, and reconstructed material of depth ζ, with some approximately constant loss rate, γ_{sa}, and zero elsewhere. Thus, the electric field in the numerator of Eqn. 4.8 is approximately constant over a cylindrical shell with volume $\delta V_{sa} = 2\pi R \zeta h$. Using Eqn. 2.16 and further assuming that the surface-damaged layer has approximately the same index of refraction as the undisturbed material [61], we find

$$\bar{\gamma}_{sa} = \gamma_{sa} n_{\mathrm{Si}}^2 \frac{\int_{\delta V_{sa}} \left|E(\mathbf{r})\right|^2 d\mathbf{r}}{\int n^2(\mathbf{r}) \left|E(\mathbf{r})\right|^2 d\mathbf{r}} = \frac{1}{2} \gamma_{sa} n_{\mathrm{Si}}^2 \bar{u}_s \delta V_{sa}. \tag{4.9}$$

Defining $Q_{sa} = \omega/\bar{\gamma}_{sa}$, we then have a surface-absorption quality factor for the device, where γ_{sa} is the bulk absorption rate of a material consisting entirely of that at the microdisk surface. Schematically illustrated in Fig. 4.1(b), we propose that the dominant form of surface absorption occurs at the edge of the microdisk along the etched sidewalls, where reactive ion etch damage of the Si lattice can result in damage or impurity over many monolayers spanning a thickness ζ [61]. Fitting the remaining unaccounted for optical loss (i.e., subtracting out the predicted surface scattering component) versus microdisk radius with a linear (Q_{sa}, solid red curve) and constant (Q_b, dashed green curve) component, we arrive at Fig. 4.4, our partitioning of optical losses into different components.

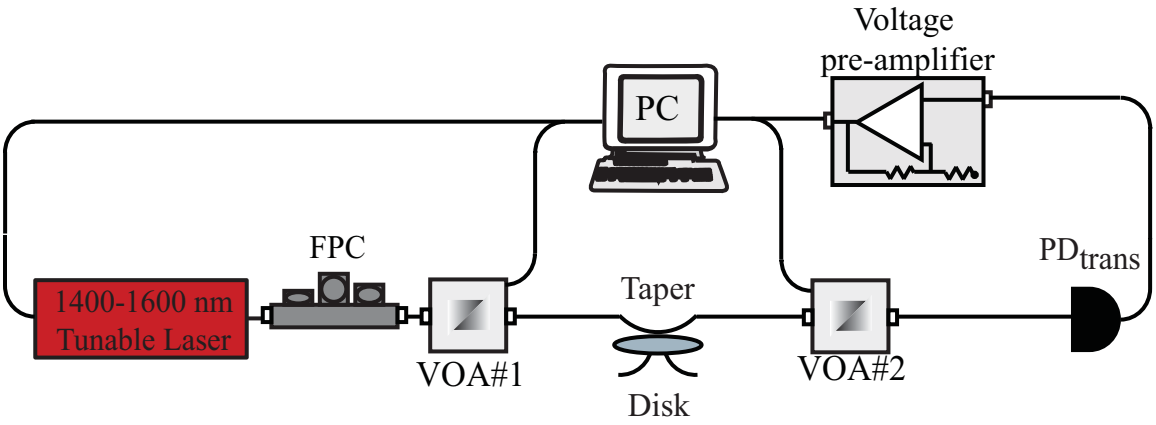

Figure 4.5: (a) Schematic representation of testing apparatus. The variable optical attenuators allow for control of the power delivered to the resonator.

In support of conclusions regarding surface absorption above, a series of power-dependent experiments was performed using an experimental configuration depicted schematically in Fig. 4.5. To control the amount of power reaching the microdiska, a computer-controlled

variable optical attenuator is interposed between disk and laser source. A second variable attenuator maintains constant uncoupled power impinging upon the photodetector.

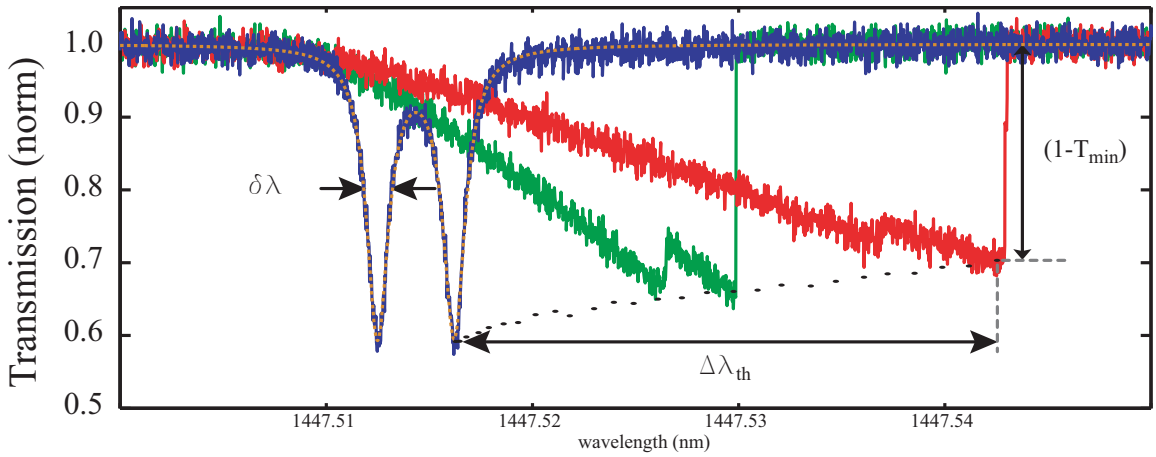

Figure 4.6: Examples of power-dependent transmission versus wavelength data generated by the experimental configuration in Fig. 4.5. The wavelength shift data ($\Delta\lambda_{th}$) and the transmission contrast data ($1 - T_{min}$) are used to infer the relative contributions of linear and nonliear absorptions. The dashed orange line is a fit to the doublet transmission at very low input power (blue curve), while the green and red traces show transmission versus wavelength at slightly higher powers. The black dots indicate the transmission minimum (of the redder of the doublet dips) for many input powers.

The orange dashed curve in Fig. 4.6 is the result of a doublet model fitted to very low input power transmission (blue curve). It is used to calculate the resonator's total linear loss ($Q_t \equiv \omega_0/\gamma_t \approx \lambda_0/\delta\lambda = 1.5\times10^6$), doublet splitting, and strength of fiber waveguide to resonator coupling in the "cold-resonator" case.

The amount of absorbed power (P_{abs}) in a microphotonic resonator can be related to the total rate of power loss (P_{loss}) via the relationship $P_{\text{abs}} = (\gamma_a/\gamma_t)P_{\text{loss}}$, where γ_a is the rate of optical absorption. For a lossless coupler in steady state, the total power loss will be equal

to the power dropped into the cavity given by $P_d = (1 - T_{\min})P_i$, where $T_{\min}$ is the normalized transmission minimum and P_i is the power carried by the input waveguide entering coupling region. P_{abs} can in principle be related to the power-dependent resonant wavelength shift ($\Delta\lambda_{th}$) through a thermal model incorporating absorption, temperature decay, and the thermo-optic effect as described in, for example, Refs. [19, 23, 71]. Up to a single proportionality constant (C), then, γ_a may be inferred from the directly measurable relationship, $\Delta\lambda_{th} = C(\gamma_a/\gamma_t)P_i$. Practically, however, absolute measurements of P_i are challenging because of the uncertainties in bus waveguide losses. The additional uncertainties in a thermal model (thermal resistances, other channels of temperature relaxation, thermo-optic coefficients, geometry, etc.) and input power make accurate determination of C difficult. It is possible, though, by controlling the fraction of optical absorption loss through nonlinear absorption, to make the proportionality constant C an indirectly measurable quantity, thus eliminating the uncertainties in the thermal model and input power.

The total optical loss coefficient may be written as a combination of a cold-cavity loss rate and nonlinear absorption by $\gamma_t = \gamma_c + \gamma_{nla}$. In the same fashion, the absorption coefficient can be separated into linear absorption and nonlinear absorption as $\gamma_a = \gamma_{la} + \gamma_{nla}$. Using a doublet transmission model, along with the low power measurements of resonator parameters (intrinsic, extrinsic, and mode-coupling parameters), the power-dependent change in resonant transmission depth

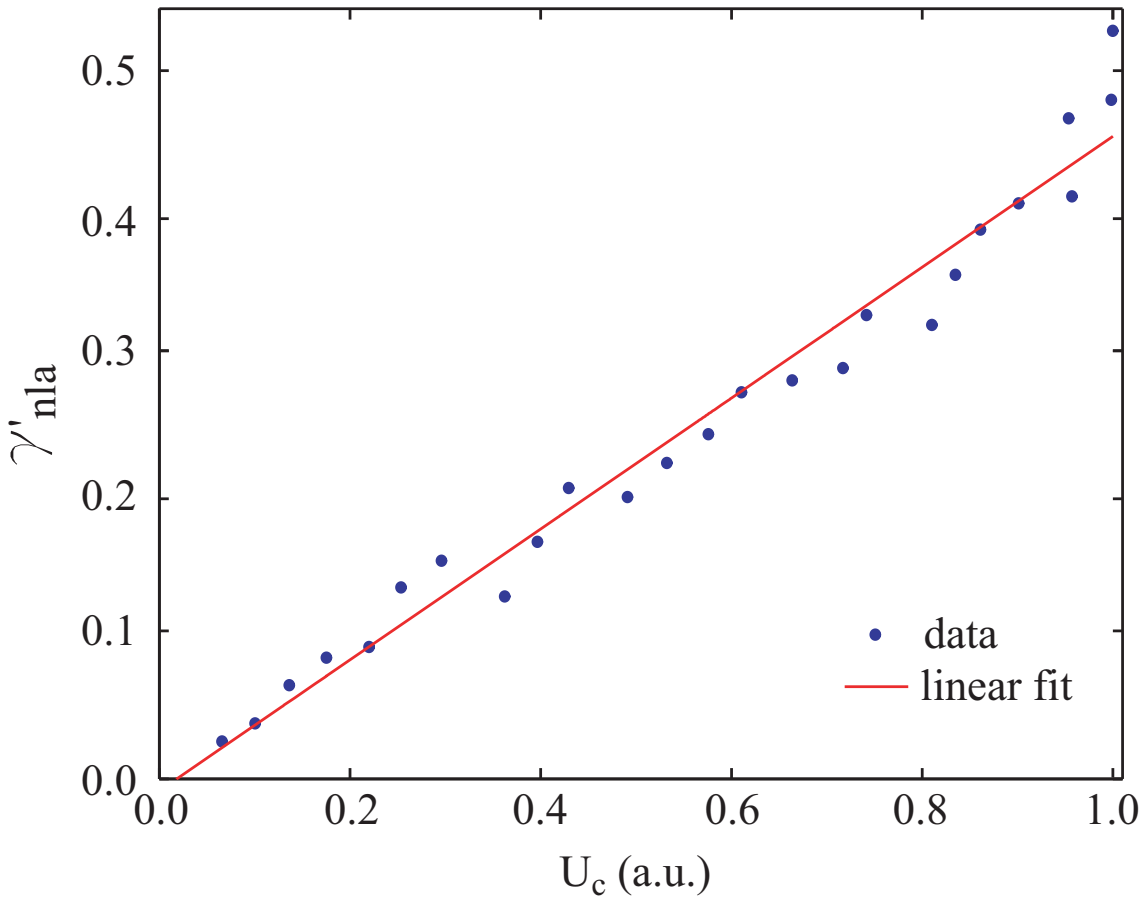

Figure 4.7: Plot of normalized nonlinear absorption versus relative electric-field cavity energy along with a linear fit

($T_{\min}$) can then be used to find the nonlinear absorption. Fig. 4.7 shows the normalized nonlinear absorption ($\gamma'_{nla} \equiv \gamma_{nla}/\gamma_c$) as a function of relative cavity energy ($U_c/max(U_c)$). The linear dependence of γ'_{nla} versus U_c shows that two-photon absorption is dominant for the input powers considered in that figure, avoiding the complication of blue-shifting free-carrier dispersion [14, 19] (just because the TPA is dominant over FCA does not mean FCD is absent). In this case the absorbed power is linearly proportional to the thermal resonance shift ($\Delta\lambda_{th}$), and so the linear absorption can be calculated unambiguously from

$$\Delta\lambda_{th} = C\left[\frac{\gamma'_{la} + \gamma'_{nla}(P_d)}{1 + \gamma'_{nla}(P_d)}\right] P_d, \tag{4.10}$$

where the losses are normalized by γ_c and C is a constant determined by fit.

Fig. 4.8(a) depicts resonance shifts from Fig. 4.6 versus P_d along with a fit to Eqn. 4.10 and a linear fit to the very low power data as a visual aid. The global slope, $\Delta\lambda_{th}/P_d$, versus P_d for the same dataset is shown in the inset to the figure. While this method does require knowledge of absolute powers, the maximum input powers for these experiments were $\sim 100\ \mu$W, which corresponds to absolute cavity energies of ~ 30 fJ. This analysis finds that $\gamma'_{la} = 0.57 \pm 0.03$, indicating that linear absorption accounts for more than half the optical loss at this wavelength in these devices. This separation of linear absorption from total loss is depicted in Fig. 4.8(b) at the grey arrow along with

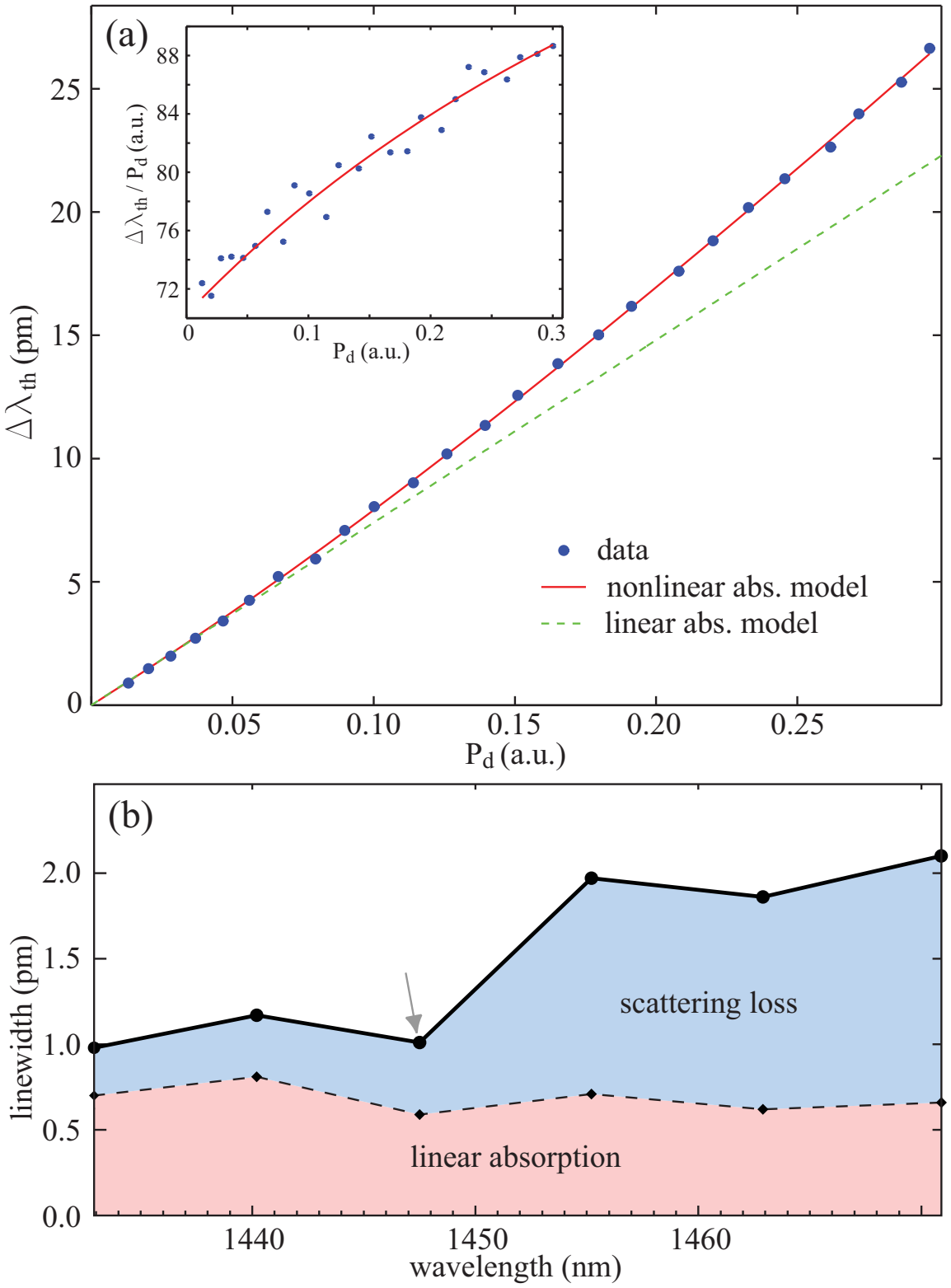

Figure 4.8: (a) Thermal wavelength shift ($\Delta\lambda_{th}$) versus relative dropped power (P_d) along with fits to linear (green dashed line) and nonlinear (red solid line) absorption models. (inset) $\Delta\lambda_{th}/P_d$ versus P_d for the same dataset. (b) Wavelength-dependent intrinsic linewidth for a family of high-Q WGMs, along with the measured partitioning of scattering loss and linear absorption. Note that the fit shown in (a) generated the data point at 1447.5 nm in (b).

similar measurements on the neighboring WGMs of the same radial order and polarization.

4.5 Surface chemistry

Utilizing a high quality factor ($Q \sim 1.5 \times 10^6$) optical microresonator to provide sensitivity to fractional surface optical loss at the $\alpha'_s \sim 10^{-7}$ level, we find that optical loss within Si microphotonic components can be dramatically altered by Si surface preparation. Chemical oxide surfaces may be prepared with $\alpha'_s \sim 1{\times}10^{-5}$. Hydrogen-terminated Si surfaces may have $\alpha'_s \leq 1{\times}10^{-6}$. These results indicate that the optical properties of Si surfaces can be significantly and reversibly altered by standard microelectronics treatments, and that stable, high optical quality surface passivation layers are critical to future Si micro- and nano-photonic systems.

Historically, studies of Si surface and interface states have primarily focused on their electronic properties [72–74]. Three exceptions are deep-level optical spectroscopy [75], cavity-ringdown spectroscopy [76], and photothermal deflection spectroscopy (PDS) [77,78], which are sensitive to fractional optical absorption down to $\alpha l \sim 10^{-8}$. None of those techniques, however, is at all well suited for studying as-processed planar or quasi-planar microphotonic elements. In this work we utilize a specially designed microdisk optical resonator to study the optical properties of surfaces typical in silicon-on-insulator (SOI) microphotonic element in a noninvasive, rapid, and sensitive manner. The high

quality factor (Q) Si microdisk resonators used in this work provide surface-specific optical sensitivity due to the strong overlap of the top and bottom surfaces of the active Si layer with the electric field energy density of appropriately polarized bound optical modes of the microdisk.

A normalized measure of surface sensitivity for a guided-wave mode in a waveguide or resonator can be defined as $\Gamma'_s \equiv \Gamma_s/t_s$, where Γ_s is the fractional electric field energy overlap with a surface perturbation of physical depth t_s. If optical loss is dominated by interactions with the surface, then the modal loss coefficient per unit length (α_m) measured from experiment can be related to a fractional loss per pass through the surface given by $\alpha'_s = \alpha_m/\Gamma'_s = 2\pi n_g/(\lambda_0 Q\Gamma')$, for a resonator with quality factor Q and modal group index of refraction n_g). For a truly two-dimensional surface in which the perturbation depth is infinitesimal, α'_s is the relevant quantity characterizing the surface and is equivalent to the proportion of power lost for a normally incident plane wave propagating across the surface [79]. From FEM simulations, it is determined that the transverse magnetic (TM) polarization whispering-gallery-modes (WGMs) of the microdisk are $\sim 90\times$ more sensitive to the top and bottom $\langle 100\rangle$ Si surfaces than the etched sidewall at the microdisk edge; specifically, $\Gamma'_{top} = \Gamma'_{bot} = 3.5 \times 10^{-3}$ nm^{-1} and $\Gamma'_{side} = 8.1 \times 10^{-5}$ nm^{-1}. This implies that $\sim 0.2\%$ of the optical mode energy exists in a single monolayer at the top (bottom) Si surface, while little of the TM mode energy is subject to imperfections

at the microdisk perimeter. For the measured devices described below ($Q \sim 1.5 \times 10^6$), a surface absorption of one-tenth of the full linewidth was measurable, corresponding to a sensitivity limit of $\alpha_s' \sim 10^{-7}$.

The silicon microdisks in this section were fabricated from an SOI wafer from SOITEC, consisting of a 217-nm-thick silicon device layer (p-type, 14-22 Ω·cm resistivity, $\langle 100 \rangle$ orientation) with a 2 μm SiO_2 buried oxide (BOX) layer. Microdisks of 5 μm radius were fabricated [23], finishing with a 10 minute acetone soak and Piranha etch to remove organic materials. A 1 hour dilute hydrofluoric acid (HF) solution comprised of five parts 18.3 MΩ deionized (DI) water to one part concentrated aqueous HF (49%) was used to remove a protective SiN_x cap and partially undercut the disk. The wafer was then rinsed in deionized water, dried with nitrogen (N_2), and immediately transferred into an N_2-purged testing enclosure. The DI rinse-steps are kept relatively brief, though for time scales into the minutes, the growth of native oxide on silicon is slow (10 minutes rinse leads to less than 1.5$\mathring{A}$ film growth) [80].

The microdisk resonators were characterized using a swept-wavelength external-cavity laser (New Focus Velocity, λ =1420–1498 nm, linewidth $<$ 300 kHz) connected to a fiber taper waveguide probe. A fiber-based Mach-Zehnder interferometer was used to calibrate the high-resolution, piezo-controlled wavelength scans to $\pm$0.01 pm linewidth accuracy. The micron-scale fiber taper probe was used to evanescently excite the WGMs of the microdisk with controllable loading. Fig. 4.9(a)

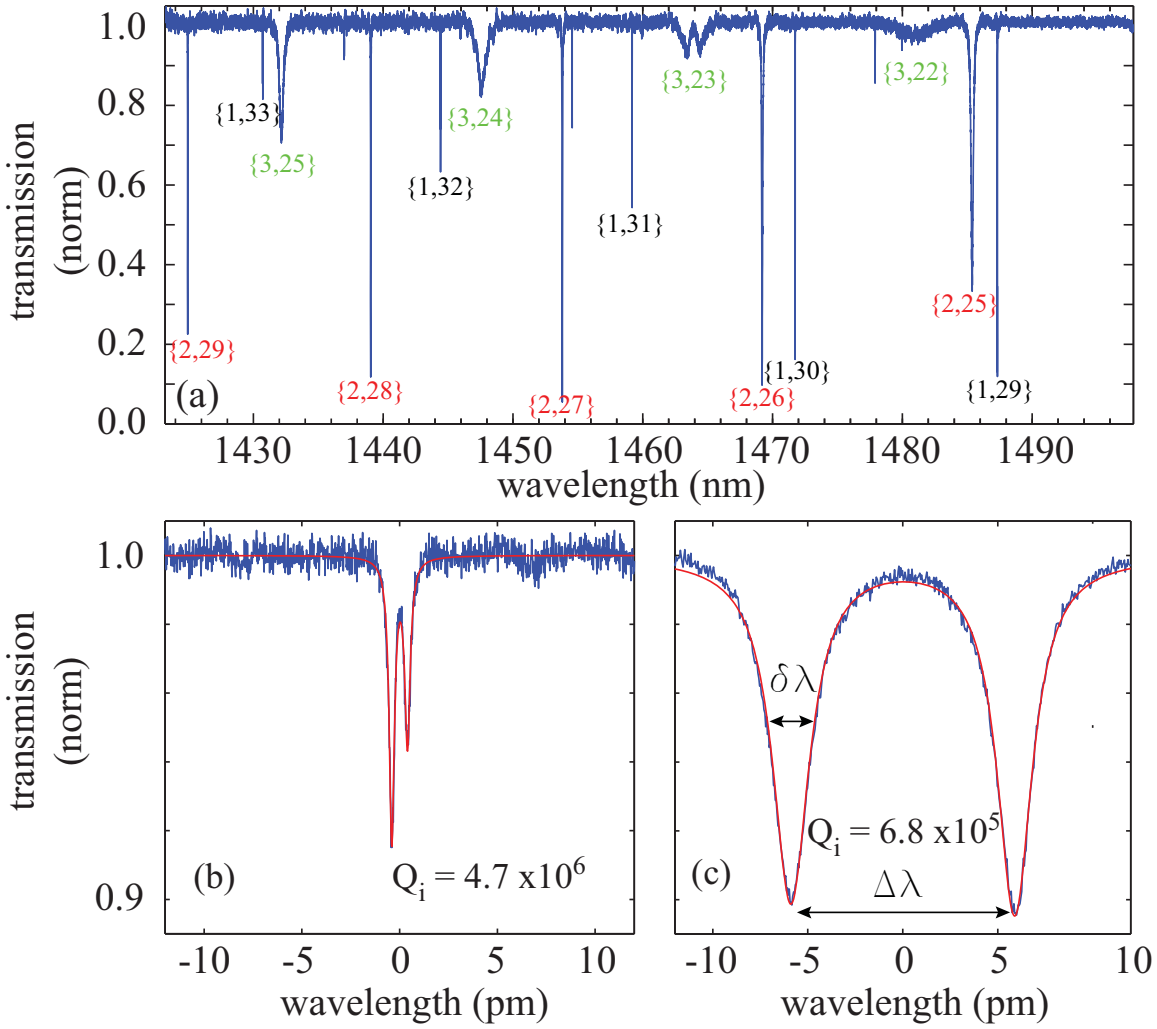

Figure 4.9: Normalized spectral transmission response of Si microdisk resonators. (a) Broad scan across $\lambda = 1400$ nm band for a 5 μm radius microdisk with the fiber taper placed 0.6 ± 0.1 μm away from the disk edge and optimized for TM coupling. The spectrum was normalized to the response of the fiber taper moved 3 μm laterally away from the disk edge. (b) High-resolution scan of a 40 μm radius microdisk, showing the reduced loss of a bulk TE WGM. (c) High-resolution scan of the $TM_{1,31}$ mode at $\lambda = 1459$ nm in (a). $\Delta\lambda$ and $\delta\lambda$ indicate the CW/CCW mode splitting and individual mode linewidth, respectively.

shows the normalized spectral transmission response of a 5 μm radius microdisk resonator, illustrating clear families of modes having similar linewidth, $\delta\lambda$, and free-spectral range (FSR). Comparison to FEM simulations of the Si microdisk allows each mode in Fig. 4.9(a) to be identified as $TM_{p,m}$, where p and m label the radial and azimuthal number, respectively.

Exploiting the great surface sensitivity of $TM_{1,m}$ modes, the optical properties of those modes can be used to determine the quality of the optical surfaces. Fig. 4.9(c) shows a high resolution scan across the $TM_{1,31}$ mode of a microdisk. The observed doublet resonance, a result of surface roughness coupling of the normally degenerate clockwise (CW) and counter-clockwise (CCW) propagating WGMs [23, 30, 68], is fit to a doublet model. The resulting parameters are: $\Delta\lambda = 11.9$ pm and $\delta\lambda = 2.2$ pm, corresponding to an intrinsic modal quality factor of $Q_i \equiv \lambda_0/\delta\lambda = 6.8\times10^5$ for this $TM_{1,31}$ mode. This should be contrasted with the transmission spectrum shown in Fig. 4.9(b) for a more confined, and less-surface-sensitive, TE WGM of a much larger 40 μm radius microdisk ($\Gamma'_{top} = \Gamma'_{bot} = 1.2 \times 10^{-3}$ nm^{-1} and $\Gamma'_{side} = 2.3 \times 10^{-5}$ nm^{-1}). From the fit parameters ($\Delta\lambda = 0.8$ pm, $\delta\lambda = 0.3$ pm), the Q of the buried TE mode is $Q_i = 4.7\times10^6$, corresponding to a loss per unit length of $\alpha_i = 0.13$ dB/cm. This is nearly an order of magnitude smaller optical loss than that of the as-processed $TM_{1,m}$ modes. This great difference provides an upper bound on the bulk Si optical loss of the SOI material and aptly illustrates the relative sensitivity of TE and

TM modes.

The tremendously disparate responses of the surface-sensitive TM and bulk-like TE modes indicate that the as-processed Si surfaces are far from ideal. Etch-induced surface damage on the microdisk sidewall accounts for only a small portion of this difference between TM- and TE-like mode losses, due to the enhanced sensitivity of the $TM_{1,m}$ to the top and bottom Si surfaces. Damage to the top and bottom Si surfaces my have a variety of possible sources, including chemical mechanical polishing (CMP) during wafer preparation, native oxide formation during storage, deposition of PECVD layers, or adventitious organic matter [81].

To remove damaged material from the Si microdisks and prepare them with a high-quality surface, a series of chemical oxidation treatments was performed on the devices. Repeated chemical oxidation in Piranha etch (H_2SO_4/H_2O_2) and oxide removal by dilute HF was employed to controllably prepare the Si surfaces, as in Refs. [74, 82, 83].

The as-processed devices were subjected to three cycles of the Piranha/HF process (recipe shown in Table 4.1). From the blue-shift in the WGM resonances we estimate 1.9 ± 0.1 nm of Si was removed from the surface of the microdisk. Fit to the $TM_{1,31}$ transmission spectrum, shown in Fig. 4.5(b), indicates that a significant improvement to the optical quality of the surfaces took place, yielding a $\Delta\lambda = 7.2$ pm and $\delta\lambda = 1.1$ pm.

To separate the effects of the Piranha oxidation and the HF etch,

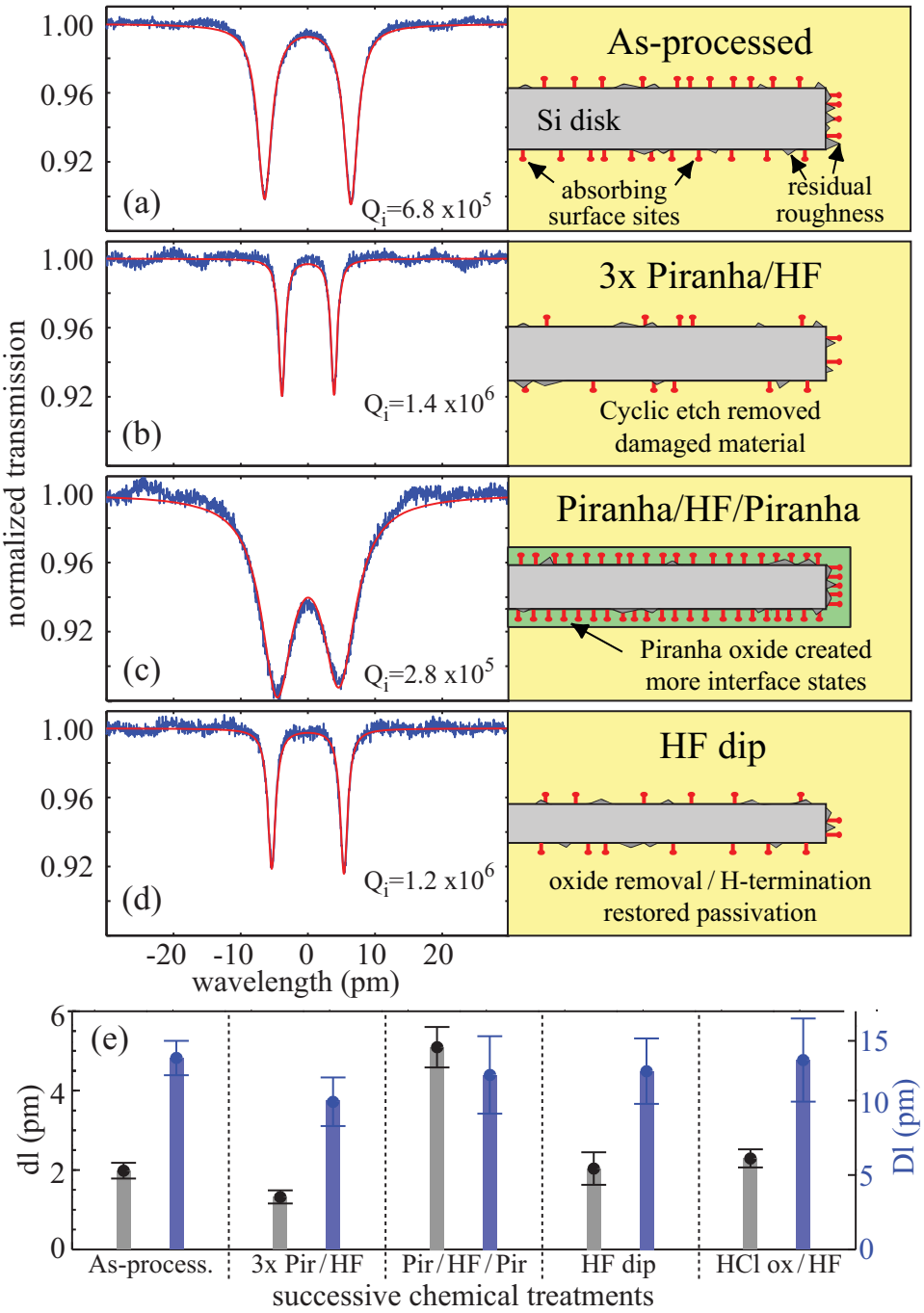

Figure 4.10: (a–d) Wavelength scan of the $TM_{1,31}$ doublet mode after each chemical treatment and accompanying schematic of chemical treatment. (a) As-processed, (b) triple Piranha/HF cycle (Table 4.1), (c) single Piranha/HF/Piranha step allowing measurement of Piranha oxide, and (d) HF dip to remove chemical oxide from previous treatment and restore passivation. (e) Average intrinsic linewidth, $\delta\lambda$, and average doublet splitting, $\Delta\lambda$, for all $TM_{1,m}$ modes within the 1420–1470 nm spectrum after each chemical treatment step.

a Piranha/HF/Piranha treatment was performed. The first cycle of Piranha/HF was used to prepare the disk surface with hydrogen passivation before re-oxidizing the Si surface with Piranha. Fig. 4.5(c) shows the fit to the now barely resolvable $TM_{1,31}$ doublet yielding $\Delta\lambda = 8.6$ pm and $\delta\lambda = 5.6$ pm. The increase in linewidth and lack of significant effect on doublet splitting indicates a significant creation of absorbing surface states without an increase in surface scattering. Removal of the chemical oxide (via the HF dip recipe in Table 4.1) and re-test shows that an oxide film equivalent to 2.8 ± 0.1 nm of SiO_2 had been grown in the Piranha solution (based on simulated wavelength shifts). The transmission spectrum of the $TM_{1,31}$ mode was fit and shown in Fig. 4.5(d). The best fit parameters were found to be $\Delta\lambda = 9.7$ pm and $\delta\lambda = 1.2$ pm, demonstrating that the preparation of the Si surfaces by Piranha chemical oxidation is reversible.

Many common wet-chemical silicon wafer cleaning processes involve several steps: removal of native oxides, followed by removal of carbon contaminants, followed by removal or surface contamination by metal-ions [84]. The removal of certain metal-ion contaminants is sometimes based on a solution of HCl with H_2O and H_2O_2 [85, 86]. We applied this treatment instead of the H_2SO_4 base treatment to a 5μm silicon microdisk sample after Piranha/HF preparation (recipe 8:1:2 H_20:HCl:H_2O_2, heated to 60° C). The average behavior of all $TM_{1,m}$ in the 1420–1470 nm range is graphically depicted in Fig. 4.5(e). We see that HCl oxidation was slightly less effective at passivating the sil-

icon surface than the Piranha oxidation; however, it is expected that the optimum solution for chemical oxidation will depend upon the Si crystal orientation and previous chemical treatments [87, 88].

Though observations that repeated chemical oxidation and removal of silicon can provide a smoothing action on etched sidewalls have been reported [83], the significant shifts in optical loss with chemical treatment described above appear linked to surface-state absorption as opposed to surface scattering. To date, highly confined Si waveguide measurements have been sensitive to changes in loss at only the 1 dB/cm level. These highly confined microdisks, by contrast, are sensitive to changes of loss more than an order of magnitude smaller (< 0.03 dB/cm), where surface chemistry is more likely to play a role. As mentioned above, the TM-polarized WGMs are selectively sensitive to the top and bottom Si surfaces, which are extremely smooth in comparison to etched surfaces. The negligible change in average mode-splitting, $\Delta\lambda$, with chemical treatment (Fig. 4.5(e)) is further indication that there is negligible change in surface roughness. Power-dependent measurements show that $\sim 50\%$ of residual optical loss, after Piranha/HF treatment and hydrogen surface passivation, is still due to surface-state absorption (bulk absorption is negligible at this level), as described below and in Ref. [89].

Comparison of cavity Q before and after Piranha oxide removal allows the estimate of the fractional per pass loss by surface absorption. $\alpha_{s,ox}^{'} \sim 1\times10^{-5}$ is estimated for the Piranha oxide. This large frac-

tional absorption in the $\lambda = 1400$ nm wavelength band ($\hbar\omega \sim 0.85$ eV) is attributed to single-photon absorption by mid-gap interface states. Such electronic interface states at the Si/(Piranha)SiO_x interface have been observed in Ref. [90–92], with three sets of state-density maxima in the bandgap of silicon occurring at 0.3, 0.5, and 0.7 eV (relative to the valence-band maximum), with a Fermi energy of $\sim$ 0.4 eV. The observed surface absorption is most likely dominated by the transition from the filled 0.3 eV surface-state band to the conduction band at 1.1 eV. In comparison, the modal absorption loss of the hydrogen-passivated Si surface was measured [89] to be as small as $\alpha_m^H \sim 0.08$ cm^{-1},with a corresponding fractional surface absorption loss per pass of $\alpha_{s,H}^{'} \sim 1{\times}10^{-6}$ for the top (bottom) Si active layer surface, a difference of an order of magnitude.

The measurements described above were performed over the course of weeks in an environment purged by clean, dry, N_2. Even in such an environment, however, changes in the hydrogen passivated surfaces were observed over times as short as a few days. Left in an unprotected air environment, degradation of the optical surface quality was evident in just hours. These relatively rapid changes show that development of stable surface passivation techniques optimized for optical quality is an important step in the future development of Si photonics. This data suggests that surface chemistry as much as surface roughness may ultimately limit the performance of Si microphotonic devices. Further development of Si passivation techniques may be able to reduce optical

Table 4.1: Summary of Piranha oxidation surface treatment

Step	Composition[1]	Temp.	Time
Piranha	3:1 H_2SO_4/H_2O_2	100°C	10 min
3× Rinse	DI H_2O	23°C	30 sec
HF dip	10:1 H_2O/HF	23°C	1 min
2× Rinse	DI H_2O	23°C	15 sec

losses by as much as an order of magnitude (towards the bulk *c*-Si limit) while improving the stability and manufacturability of future Si photonic components.

With the evidence above that surface chemistry is a strongly influential factor in optical absorption in silicon microphotonics, the natural next step is investigation into surface treatments that may leave the silicon interfaces in a condition persistent over time while avoiding incurring excessive optical losses. The silicon photovoltaics community has long sought to reduce the presence of recombination centers at silicon termination, in order to increase operating efficiencies [60, 93, 94], and so provides guidance. Two of these commonly employed techniques were applied to microdisk resonators similar to those above and the results are discussed below.

Schmidt et al. report in Ref. [60] that SiN_x passivation layers deposited via PECVD, with or without an underlying thin thermal oxide layer, achieved effective free-carrier lifetimes of $\sim 1\,\mathrm{ms}$, comparable to the best passivation schemes to date. The SiN_x layers best capable of passivating the surface were found to be nearly stoichiometric Si_3N_4, and were deposited in a direct (as opposed to remote-plasma) parallel-

plate reactor system. Furthermore, they found that the first 50 min of a 400°C anneal in forming gas (5% H_2, 95% N_2) improved the effective lifetime, while further annealling eventually reduced the effectiveness of the passivation. Ambient hydrogen was found to have negligible effect, and the increase of lifetime was then attributed to a large reservoir of hydrogen in the silicon nitride (∼15–20 at.%) releasing during the deposition and anneal. An initial thermal oxide was found to provide a higher-quality Si interface further improved by the thermal diffusion of the released hydrogen to the interface, additionally passivating interface states.

McCann et al. found that a 25-nm-thick thermal oxide grown at 900°C followed by a 30 min FGA at 400°C was sufficient to obtain equally high effective lifetimes [94]. Additionally, they found that the effective lifetimes could be reduced by a 1-hr high-temperature 900–1000°C N_2 anneal and subsequently repaired by FGA. They attributed this effect to reversibly adding or removing hydrogen from the Si/SiO_2 interface, though careful thermal management is critical in the preparation of high-quality silicon interfaces: precipitous temperature changes may induce additional surface- and bulk-states [95].

Following recipes similar to the two above, silicon microdisks were prepared with PECVD SiN_x and dry thermal oxide (TOX) encapsulation layers (see Fig. 4.11). The samples for these trials were fabricated from silicon-on-insulator (217 nm Si device layer, p-type 14–20 Ω·cm,$\langle 100 \rangle$ orientation, 2 μm buried SiO_2 layer) material, similar to

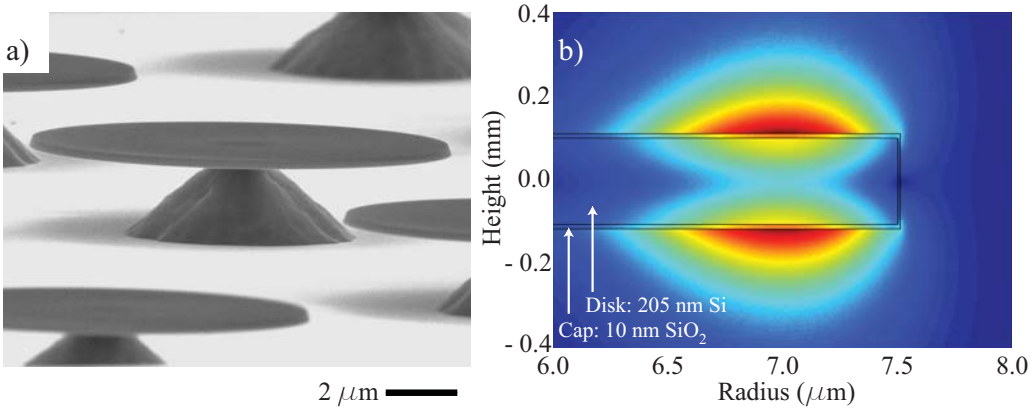

Figure 4.11: (a) Silicon microdisk cavity with a radius of 5 μm. (b) Finite element simulation of normalized electric-field energy density for the TM cavity mode in Fig. 4.13. Note the concentration of energy density near the TOX layers.

that above. Microdisk resonators with radii of 5, 7.5, and 10 μm were patterned with electron-beam lithography and a resist reflow process using ZEP520A resist and were defined with a SF_6-C_4F_8 inductively coupled plasma reactive-ion etch, all consistent with the processing described above.

To prevent contamination during oxidation and anneal steps, all were performed in a custom-built HF-cleaned quartz-tube oxidation furnace. Electronic grade II O_2, N_2, and forming gases were flowed into the 2-inch diameter furnace using electro-polished stainless steel tubing. Each gas flow rate was independently controlled with a (MKS 1479A Mass-Flo) mass flow controller; typical flow rates inside the approximately 1-m-long quartz furnace were 0.3 standard liters per minute. The unheated portion of the furnace tube was used as a staging area where the samples

were allowed to slowly warmup and cooldown before transfer into or out of the heated portion of the chamber, thus avoiding the problems associated with too-rapid temperature change (defect states caused or preserved by overly rapid cooling) [95].

The loss of each surface treatment is assessed by tracking the linewidth of a single surface-sensitive [96] TM mode throughout a given processing sequence, with the characterization being accomplished with the conventional fiber-taper technique.

The first encapsulation trial was performed on a sample with an initial 50 nm SiN_x cap deposited on the surface prior to lithography and etching. After removing the ZEP resist with an hour-long Piranha etch, Fig. 4.12(a) shows a bar graph summary of the best linewidths at selected intermediate points during the fabrication. The best linewidth after the initial Piranha clean (over many devices on the sample) was $\delta\lambda = 4.5\,\mathrm{pm}$. After an hour-long HF undercut which also removed the SiN_x cap, the linewidths reduced to 0.8 pm, while further Piranha/HF treatments [96] had no discernible effect on the linewidths.

After testing and an additional 3× Piranha/HF treatment was done on the sample (ensuring a clean and well-passivated silicon surface), a nearly stoichiometric 30-nm-thick SiN_x encapsulation was then deposited on the sample. The PECVD conditions were adapted from Ref. [60]: a gas chemistry of 450 sccm of 5% SiH_4/N_2 and 50 sccm of NH_3 was applied to the chamber held at 200 mTorr and 400°C. The gas was cracked with 60 W from a 13.56 MHz radio-frequency source;

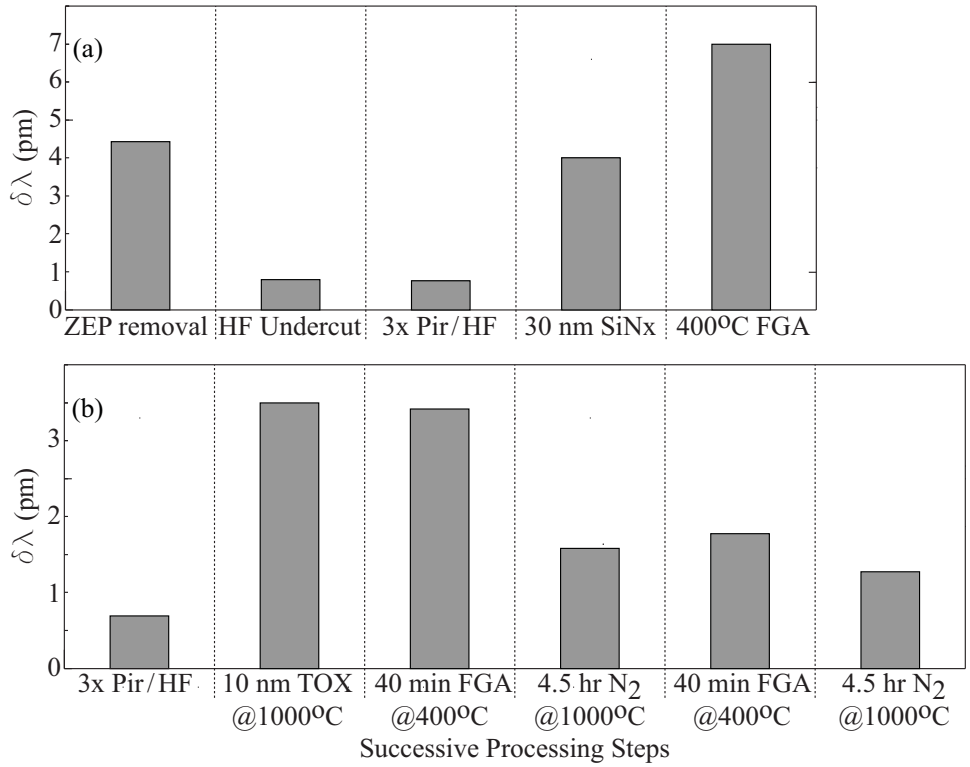

Figure 4.12: Summary of best linewidths after selected processing steps for 5–10 μm radii disks fabricated with (a) a stoichiometric SiN_x encapsulation layer and (b) a thermal oxide encapsulation layer along with various annealing trials

no low-frequency source was used in an attempt to avoid deposition damage from ions oscillating below the ~ 4 MHz plasma frequency [97]. Unlike in the photoconductance decay measurements of free-carrier lifetimes on silicon solar cells [60], the losses of the cavities increased, with linewidths going to 4 pm, a difference of 3.2 pm, corresponding to a roughly fourfold-increase in optical loss rate.

After optical test of the microdisks with PECVD-deposited silicon nitride cap, a 40 min forming gas anneal (FGA) at 400°C was performed. Optical tests revealed that the FGA had further increased losses in the devices: the best linewidth was found to be 7 pm, as in Fig. 4.12(a). Assuming a SiN_x index of refraction of 1.9, FEM simulation of the composite resonator shows that 11% of the optical energy of TM modes resided inside the SiN_x (energy overlap factor $\Gamma_{SiN_x} = 0.11$). Thus, if the sources of loss were evenly distributed throughout the SiN_x, the material quality factor of the as-deposited material would be $Q_{SiN_x,mat} = \Gamma_{SiN_x}\lambda o/(\delta\lambda_{after} - \delta\lambda_{before}) \approx 5.0{\times}10^4$, corresponding to an attenuation coefficient of $\alpha_{SiN_x,mat} = \beta_g/Q_{SiN_x,mat} \approx 7.1$ dB/cm where β_g is the group propagation constant of the cavity mode. It is known that PECVD deposited materials have relatively high absorption coefficients (1–10 dB/cm) in the telecommunications wavelength bands due to Si-H, O-H, N-H bond overtones. As the FGA anneal would not be expected to harm the Si surfaces, a very likely interpretation of the results in Fig. 4.12(a) is that any benefits of a hydrogenated silicon surface were overwhelmed by the increased hydrogen content in the bulk

SiN_x layer. Pure PECVD Si-rich nitride disks have been independently fabricated and tested achieving quality factors $\sim 2\times10^5$. Thus it is also likely that the PECVD process damaged the high-index silicon surface during the deposition, producing additional loss.

A second sample, fabricated just as the sample used to characterize the effectiveness of SiN_x as passivation, was made and optically tested. The best measured linewidth of 0.7 pm, was very similar to the previous sample and is shown in Fig. 4.12(b). Then a 10 nm TOX layer was grown on the Si surface at 1000°C (0.3 slm of O_2 for 3.1 min). After the O_2 flow was halted, the sample was allowed to cool slowly under an N_2 ambient for $\sim$ 5 min before retesting. The best linewidth after thermal oxidation was 3.5 pm, a result similar to the silicon nitride cap. A 40 min FGA, as above, had virtually no impact on the sample with a thermal oxide cap. A 4.5-hr high-temperature anneal, consisting of holding the sample under 0.3 slm flow of N_2 in the furnace at 1000°C for 3 hr, then allowing the temperature to ramp slowly down to 400°C over the course of 1.5 hr was then performed. Upon optical test, this treatment was found to significantly improve the optical losses, with linewidth reducing from 3.5 pm to 1.6 pm.

Assuming that the high-temperature anneal successfully healed the Si interface and bulk TOX, a 40 min FGA was conducted on the sample. The FGA was found to slightly reduce the quality factor of the best resonance, where the linewidth was measured to be 1.8 pm. A second 4.5-hr high-temperature anneal resulted in a $\delta\lambda = 1.2$ pm on the best

resonance, likely due to the thermal freeing of excess hydrogen. This also illustrates that some annealling treatments are reversable under subsequent high-temperature processing, an important consideration in the thermal budget for processing.

A third similar sample was created but lacking an initial silicon nitride cap prior to lithography and dry-etching. After HF undercutting and 3× Piranha/HF treatments, the best linewidths were measured to be 1.0 and 0.6 pm, respectively [Fig. 4.13]. The marginal improvement in this case was attributed to a simplified single-material dry-etch (previously the nitride cap was etched with a slightly different chemistry to the silicon device layer) and a less-damaged top Si surface. A 10 nm TOX cap (growth just as above) with 5 min cool-down showed a best linewidth of 2.0 pm, much better than the second sample's 3.5 pm linewidth after oxidation, indicating that the top surface was damaged by the initial silicon nitride cap deposition.

Finally, the 4.5-hour high-temperature anneal described above was repeated, resulting in resonance linewidths identical to those prior to oxidation. Fig. 4.13(b) shows a high-resolution transmission spectrum of the 1444.2 nm resonance on a 7.5 μm radius disk after the final high-temperature anneal, along with a fit of the transmission to a doublet model. Similarly processed samples with fully oxidized and annealed silicon device layers were found to have $Q > 3 \times 10^6$. As these silica disks were most likely surface-scattering limited due to their design, quality factors this high indicate that the encapsulating oxide is of

extreme quality after high-temperature anneals. Also indicating the suitability of TOX layers for surface encapsulation, TOX encapsulated nonundercut microrings were observed [48] to have quality factors up to 4.8×10^6 for TE modes.

Recently, Soltani et al. also demonstrated [98] TE modes with $Q = 3 \times 10^6$ in nonundercut microdisks using a TOX hard mask. Since this TOX layer was not removed, it protects the top Si surface during processing and may passivate loss sources.

Microdisks with 5 μm radii and a 3 nm TOX cap support TE resonances with Q up to 3.3×10^6 after nine months stored in a clean-room environment ($\sim 22^\circ$C, 44% relative humidity), indicating also that the TOX passivation is very stable over time.

The results shown in Fig. 4.13 represent the successful encapsulation of the once-delicate Si-surfaces, as 10 nm of thermal oxide will completely prevent native or chemical oxide growth during subsequent fabrication steps and in relatively benign environments.

4.6 Loss-reduction conclusions

Using a combination of resist reflow to form a surface-tension-limited smooth etch mask and a low DC bias dry etch to reduce roughness and damage in the etched Si sidewalls, we have fabricated high-index contrast Si microdisk microresonators with strong optical confinement and losses as low as 0.1 dB/cm ($Q > 5 \times 10^6$). Passive fiber optic measurements of the scaling of optical loss with microdisk radius, along

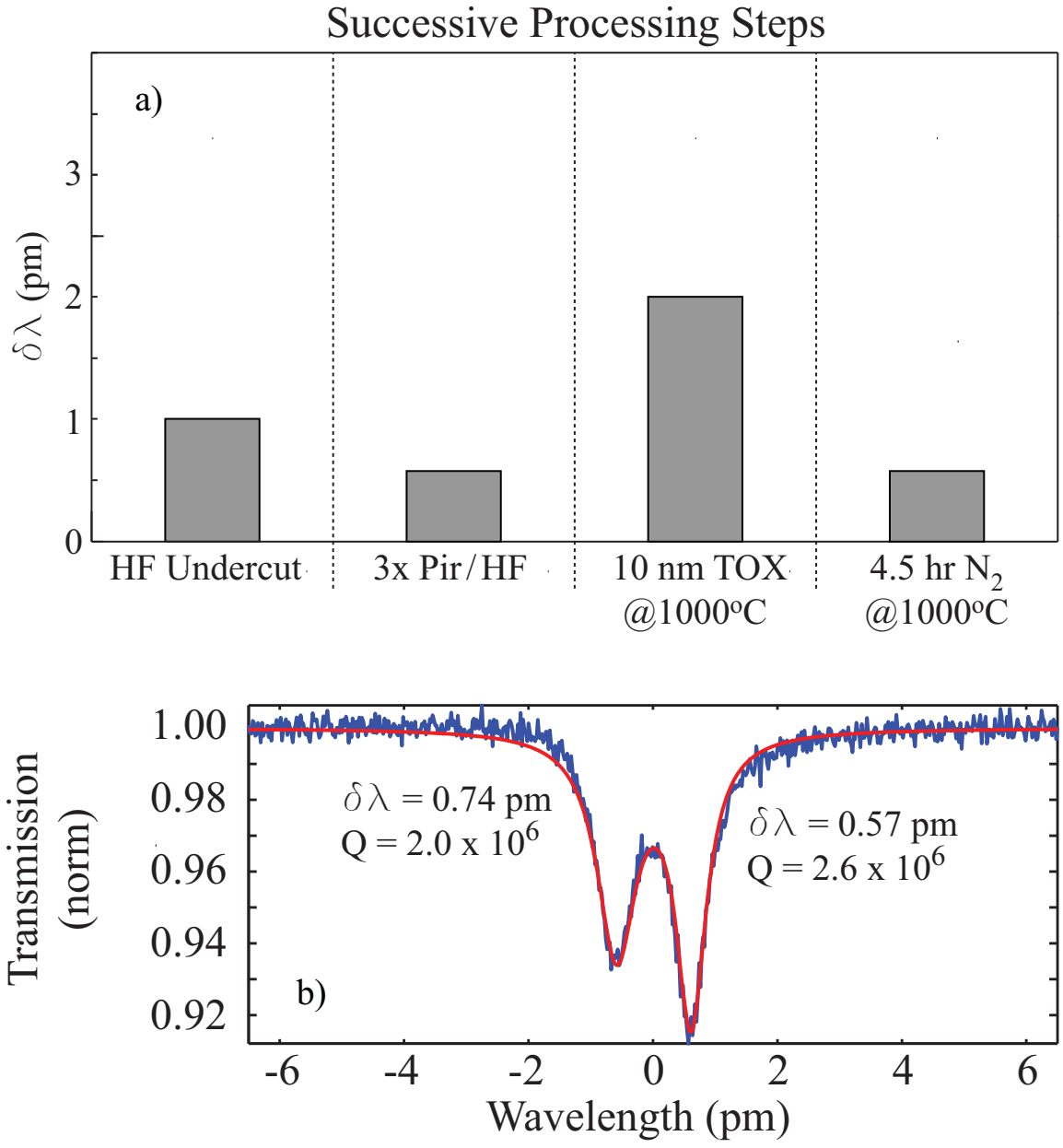

Figure 4.13: (a) Summary of best linewidths after selected processing steps for 5–10 μm radii disks fabricated without an initial protective cap. This sample also had a thermal oxide encapsulation layer but no FGA. (b) High-resolution transmission spectrum of 1444.2 nm resonance on a 7.5 μm radius disk after the final high-temperature anneal

with power-dependent measurement of the thermo-optic properties of the microdisks, provide evidence supporting the view that optical loss is dominated in these structures by surface ($5 < R < 20$ μm) and bulk free-carrier absorption ($R > 20$ μm), as opposed to surface roughness on the microdisk.

We found that surface treatments and passivations used widely in microelectronics and photovoltaics can form effective encapsulation layers for optical elements operating in the telecommunications wavelengths. The ultra-thin TOX coating (10 nm) is seen to be superior from a loss standpoint, and has admirably stable configuration—persisting for months in ordinary atmospheres.

Chapter 5

Reducing free carrier lifetime

The impacts of free-carrier populations in silicon photonics are manifold. Substantial numbers of free-carriers interacting with the optical fields can lead to reduced efficiency in nonlinear operation, reduced speed of dispersive switching, and the generation of other unwanted effects [20, 39, 99, 100]. Active measures to address this problem have been demonstrated: building a *pn*-junction into the device and reverse biasing it removes free-carriers from the junction region [3, 13], and passive measures based on incorporating lifetime killers into the silicon bulk can reduce free-carrier lifetime [18, 101]. Ideally, free-carrier lifetimes in silicon photonics would be spoiled without inducing undue excess losses in optical devices or components. One path to achieving this is through modification of the surface recombination velocity of the optical devices by introduction of surface states through different passivation schemes. Moreover, these methods can be applied with a minimum of equipment and expense, as the properties of silicon microresonator surfaces are clearly modifiable with wet-chemical treatments, as seen in the previous section.

In this section we present measurements of the impact on free-carrier lifetimes in low-loss silicon-on-insulator (SOI) microdisk resonators under a variety of surface treatments previously applied in silicon photonics. We find that various surface treatments can reduce the free-carrier lifetime to sub-nanosecond levels without preventing the creation of very high quality-Q resonators. Such devices would be ideal for use in utilizing nonlinear optics with extremely low input power requirements, and could be applied to wavelength conversion, coherent light generation, and may be useful in high-speed switching and the amelioration of unwanted effects.

5.1 Modifying free-carrier lifetime through surface chemistry

The SOI microdisks studied here are defined by electron-beam lithography in ZEP501A resist, with transfer of polymer mask achieved by SF_6-C_4F_8 inductively coupled plasma reactive-ion etch. The polymer mask and organic contaminants are removed by a 10 minute soak in acetone and an hour-long Piranha etch, and the microdisk partially undercut in dilute HF. Further fabrication details can be found elsewhere [23, 102] and in previous sections.

In previous work we presented optical loss measurements of different surface treatments of silicon microdisk resonators. The treatments considered were: (i) as-processed resonators; (ii) resonators chemically

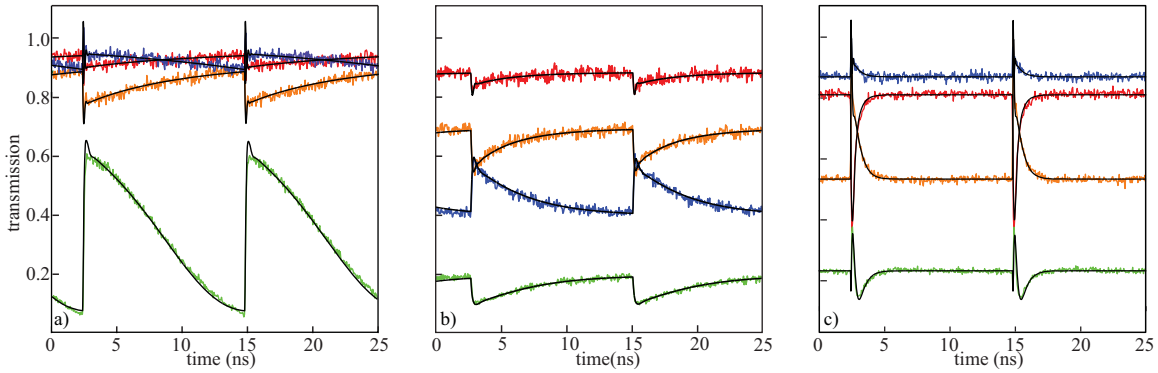

Figure 5.1: Probe transmission versus time for different surface preparations. (a) The time-domain behavior for a microdisk with thermally oxidized surface. The best-fit free-carrier lifetime was 34 ns. (b) The time-domain behavior for a microdisk with surface as-is upon fabrication. The best-fit free-carrier lifetime was 3.6 ns. (c) The time-domain behavior for a microdisk with a surface treated with a mixture of nitric acid and hydrogen peroxide. The best-fit free-carrier lifetime was 0.44 ns.

oxidized with Piranha etch; (iii) H-terminated surfaces via HF dip after Piranha etching resonators [82, 83]; (iv) thermally grown silicon dioxide upon resonators; (v) plasma-enhanced chemical vapor deposition (PECVD) deposited silicon nitride (SiN_x) upon resonators [102]. We have measured the free-carrier lifetimes in silicon microdisk resonators associated with those preparations and present them in Table 5.1 alongside similar measurements of two other simple wet chemical treatments: (vi) growth of chemical oxide on resonators via a solution of concentrated aqueous HNO_3 and H_2O_2; (vii) surface deposition from solution of Au upon resonators.

The conditions of the surface treatments are as follows: (i) upon completion of the microdisk fabrication (dilute HF undercut and DI H2O rinse, then dried with clean, dry, N2), sample is immediately removed to the test enclosure, which is purged with clean, dry N_2; (ii) the

Table 5.1: Summary of treatment, effect on free-carrier lifetime, and observed Q

Preparation	Free-carrier lifetime (ns)	Max observed Q
as processed	3.6	2×10^5
Piranha oxide	1.5	2.5×10^5
H-terminated	11	1.5×10^5
dry thermal oxide	32	3.7×10^5
PECVD SiNx	4.1	2.6×10^5
nitric acid treatment	0.44	1.4×10^5
Au deposition	0.41	4.5×10^4
thinned disk with Piranha	0.23	6×10^5
thinned disk with nitric	0.33	5×10^5

sample is immersed in a solution of 3:1 concentrated aqueous H_2SO_4 (97% by weight):H_2O_2 (30% by weight) heated to 100°C for 10 minutes, rinsed three times for 30 s in deionized (DI) water at 23°C, and dried with clean, dry, N2; (iii) previous chemical oxide (per treatment (ii)) is removed by dip in a 10 : 1 solution of DI H_2O:concentrated aqueous HF (49% by weight) for 1 min and rinsed twice for 15 s in DI H_2O at 23°C, and dried with clean, dry, N2; (iv) sample prepared with H-terminated surface (per treatment (iii)) is oxidized at 1000°C under O_2 for 6.2 min, followed by a 3 hour anneal under N_2 at 1000°C, followed by a 1.5 hour cooldown under N_2 to 400°C before removal; (v) an H-terminated sample (per treatment (iii)) is coated with a near-stoichiometric 30-nm-thick SiN_x layer. The processing conditions were adapted from [60], with gas flows into the deposition chamber of 450 cubic centimeter per minute at STP (SCCM) of 5% SiH_4:N_2 and 50 SCCM of NH_3, chamber pressure held at 200 mTorr, and deposition platen temperature held at

400°C. Only 13.56 MHz radio-frequency (RF) power was applied to the parallel-plate configured chamber at 60 W. By using high-frequency RF only, it is hoped that ion bombardment damage to the silicon can be avoided [97]; (vi) a sample is immersed in a solution of 3 : 1 concentrated aqueous HNO_3 (37% by weight):H_2O_2 (30% by weight), heated to 100°C for 10 minutes, rinsed three times for 30 s in DI H_2O at 23°C, and dried with clean, dry, N2; (vii) a sample is immersed in a solution of 1:30 1μg/ml Au (as $AuCl_3$) in HCl (20% by weight):dilute HF (60:1 DI H_2O:concentrated aqueous HF (49% by weight)) for 5 min, rinsed in DI H_2O, and dried with clean, dry, N2.

A microdisk resonator with thickness 220 nm and radius 6.5μm (on 14–20 ·cm, $\langle 100 \rangle$ p-type silicon) was prepared with the "as-processed" preparations above (no Piranha/HF cycles beyond the initial clean after dry-etch and dilute HF undercut). Via the procedure discussed in section 2.2.3, the free-carrier lifetime was measured and determined to be approximately 3.6 ns. Time-domain transmission (with simultaneous fits) are depicted in Fig. 5.1(b). The same sample was then subjected to a Piranha/HF/Piranha treatment (per above) and the free-carrier lifetime re-measured. The removal of some damaged material and re-growth of chemical oxide resulted in a free carrier lifetime of approximately 1.1 ns. Following this treatment, the same sample was subjected to the dilute-HF dip described above. Upon re-measurement of the free carrier lifetime, the removal of the Piranha oxide and H-termination of many surface states resulted in a free carrier lifetime of

12.8 ns. Additional Piranha treatment resulted in a decrease of the free carrier lifetime to 0.92 ns, which reverted to 14.0 ns after additional H-termination by dilute HF dip, illustrating the approximate reversibility of the chemical oxide/H-termination surface preparation.

This same sample was then subjected to a thermal oxidation as described in recipe (iv) above. When re-measured for free-carrier lifetime, the TOX interface was found to be of excellent quality in terms of preventing surface recombination: the free-carrier lifetime was found to be 34.3 ns. Again, the time-domain transmission and simultaneous fits are depicted in Fig. 5.1(a). Thus, while we have found that the TOX termination produces the highest optical quality factor devices, with outstanding environmental stability, it also creates devices with long free-carrier lifetimes.

The successive treatments on the above sample, corresponding to the surface treatments described in above and in Refs. [96, 102] is graphically depicted in Fig. 5.1.

Devices were fabricated in order to test the effects on free-carrier lifetimes in these devices due to passivation by PECVD growth of SiN_x on the surface (per recipe (v)). Previously found to induce mild excess optical loss in microdisk resonators [102], this type of treatment is used in photovoltaics to passivate surfaces to enhance free-carrier lifetimes and to serve as an element of anti-reflection coating. We prepared a H-terminated surface by following the same initial fabrication process (electron-beam lithography, dry-etch, solvent and Piranha etch clean,

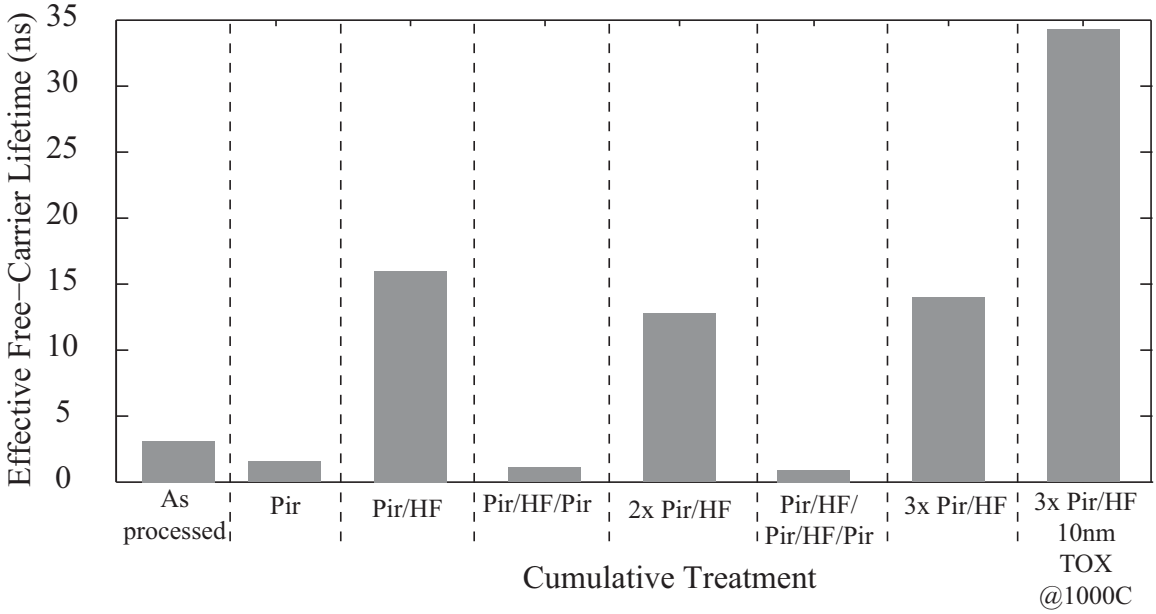

Figure 5.2: Effective free-carrier lifetime vs. treatment for successive treatments. This follows a single resonance of a single device through a series of treatments previously considered in terms of optical loss reduction.

followed by dilute HF undercut) with 3×Piranha/HF cycle. The free-carrier lifetime was measured to be 11.5 ns. Upon deposition of 30 nm of SiN_x, without any annealling (in terms of loss, no anneals were found that improved the loss characteristics of the SiN_x passivation layers), the same devices were re-measured and the effective free-carrier lifetime decreased to 4.1 ns, approximately similar to the "as-processed" effective free-carrier lifetime.

An additional microdisk sample was fabricated with the "as-processed" preparation and then subjected to 3×Piranha/HF cycles. The same method was used to determine the free-carrier lifetime and it was found to be 13.6 ns. The sample was then subjected to treatment by nitric acid, per treatment (vi). After treatment, the device was re-measured

and the free-carrier lifetime was found to be 0.44 ns. Time domain traces (with simultaneous fits) are shown in Fig. 5.1(c).

For similar treatments on ⟨100⟩ and ⟨111⟩ Si, Yamashita et al. found via biased X-ray photoelectron spectroscopy that the chemical oxide-Si interface exhibit states in the silicon bandgap [90]. The energy distribution of gap states is found to be peaked around 0.4 eV and 0.7 eV above the valence band maximum, (Fermi level around 0.41 eV above valence band max) [88, 90]. It is expected that the states induced at the chemical oxide-Si interface facilitate the recombination of excess free carriers, reducing the effective free-carrier lifetime.

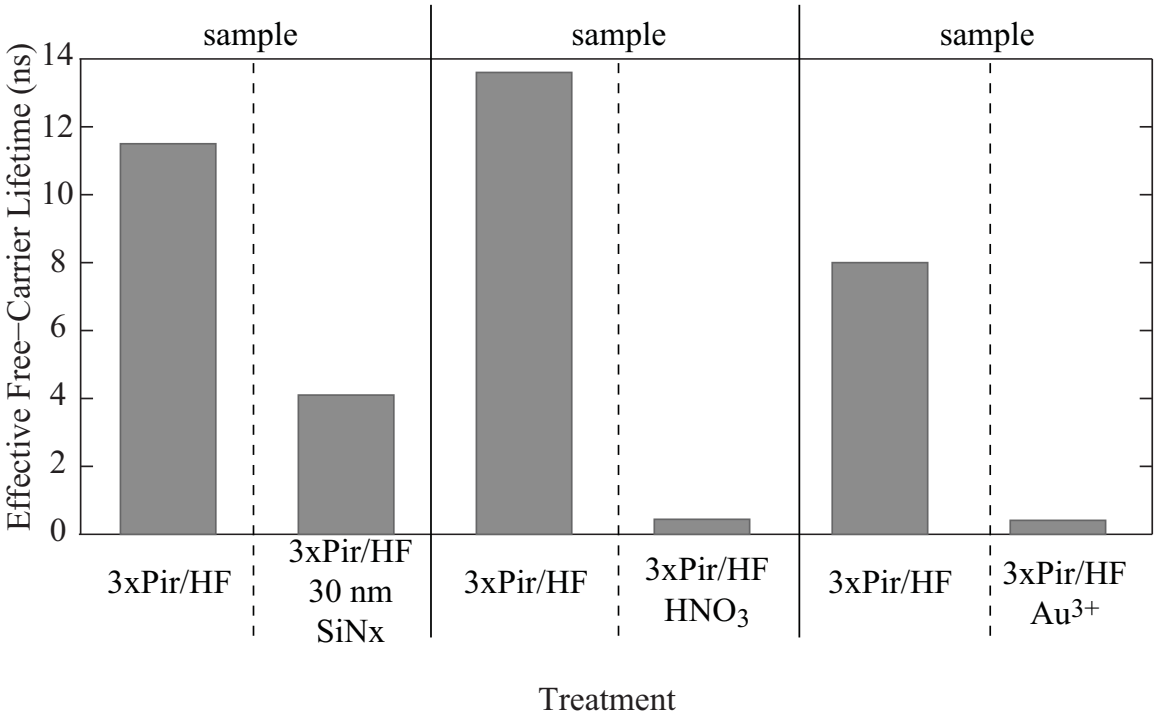

Figure 5.3: Effective free-carrier lifetime versus treatment for successive treatments on several samples

A microdisk resonator was prepared similarly to the above with H-

terminated surfaces and was determined to support resonances of Q-factor at least 2.5×10^5, with free-carrier lifetime approximately 9 ns. Application of the Au treatment and re-test of the same resonance yielded a decrease in Q-factor to 4.5×10^4, and free-carrier lifetime of approximately 0.4 ns. While such a resonator still represents a low-loss device, maintaining a higher-Q is desirable, other things being equal. In this case, the Au from solution is deposited on the surface by metal-ion physisorption, which, for solutions like the one prepared here, proceeds by diffusion-limited, atom-by-atom, nucleation-free deposition [103–105]. The effect of adding each gold ion to the silicon surface is to introduce a surface state (or states) in the forbidden band of silicon that facilitates carrier recombination [51,106] through those sites at the surface.

The PECVD nitride, HNO_3 acid, and Au solution treatments described above are graphically depicted in Fig. 5.1.

5.2 Reduction of free-carrier lifetime through geometry

Additionally, we sought to reduce free-carrier lifetimes while maintaining high-Q resonances by adjusting the geometry of the microdisk resonators. In a slab-like geometry of high-quality silicon, the effective free-carrier lifetime scales like $\tau_{fc} \sim H/S$, where H is the slab thickness and S is the surface recombination velocity. The aspect ratio

of the disks considered here is >15:1, so we can expect the above to be a useful guide to designing our microdisks: reduction in thickness should then yield reduction in free-carrier lifetime for a given surface recombination velocity (i.e., a given surface preparation). To assess the effectiveness, we prepared a series of silicon microdisk resonators of varying thickness, with H of $120, 170, 220$, and 340 nm, and differing as little as possible in other respects either from each other or from the previously discussed samples.

The 340 nm samples were prepared with SOI material with 1–3 Ω·cm p-doped ⟨100⟩ silicon device layer. The 220-nm-thick samples were prepared on SOI material with 10–14 Ω·cm p-doped ⟨100⟩ silicon device layer. The two reduced thickness samples (170 and 120nm thickness) were fabricated from die of the same 220 nm material that was partially oxidized and stripped in dilute HF. Oxidation took place in the same quartz tube furnace used for the other oxidations and anneals discussed in this work.

For the 170-nm-thick samples, die were Piranha cleaned and dipped in dilute HF to begin oxidation with a clean silicon surface. Samples were oxidized at 1100°C for 45 min under 0.3s lm of O_2 and subject to the long 1000°C anneal under 0.3 slm of N_2. The oxide layer grown was removed with a 10 minute dip in 5:1 DI H_2O:HF solution, rinsed in DI H_2O, and blown dry with clean, dry N_2.

120-nm-thick samples were formed from the 220 nm material as well, beginning with Piranha clean and dilute HF dip for cleanliness. Sam-

ples were oxidized at 1100°C for 130 min under 0.3 slm of O_2. Upon completion, the sample was subject to high-T anneal (as with the 170 nm samples) and dilute HF oxide removal.

The microdisks were prepared with H-terminated surfaces and their free-carrier lifetimes measured. The 340-nm-thick device was found to have an effective free-carrier lifetime of 15.1 ns. The 220-nm-thick device had an effective free-carrier lifetime of 9.5 ns. The 170-nm-thick device had effective free-carrier lifetime of 7.2 ns, and the 120-nm-thick device had effective free-carrier lifetime of 6.1 ns. Then a nitric chemical oxide was grown on the microdisks using a recipe as above and the measurement repeated. The 340-nm-thick device with HNO_3 treatment effective free-carrier lifetime was reduced to 2.5 ns, while the treated 220-nm-thick effective lifetime dropped to 1.0 ns. The effective free-carrier lifetime of devices with 170-nm-thickness and nitric acid treatment was found to be 0.6 ns, and the 120-nm-thick treated microdisk had 0.33 ns effective free-carrier lifetime.

Fig. 5.4 illustrates the decrease in free-carrier lifetime with decreasing disk thickness and with surface treatment. We find that the 220-nm-thick microdisk resonator in the geometric variation trial has (upon nitric acid treatment) a free-carrier lifetime of approximately 1.0 ns. In a previous trial a 220-nm-thick microdisk had free-carrier lifetime of approximately 0.44 ns after nitric acid treatment. In both cases, the free-carrier lifetime was reduced by a factor of > 15, and the differences may be due to local temperature or reactant-flow differences during the

nitric treatment (the prior sample was held alone in solution using teflon tweezers, while the geometric variation samples with thickness $\leq$ 220 nm were clamped in a teflon jig and treated simultaneously). The overall trend with geometry is reflected by the nearly parallel lifetime versus thickness curves in Fig. 5.4: with either a well-passivated H-terminated surface or a surface prepared by nitric acid treatment, decreasing the thickness decreases the effective free-carrier lifetime, and the application of nitric treatment reduces the free-carrier lifetimes similarly for different thicknesses.

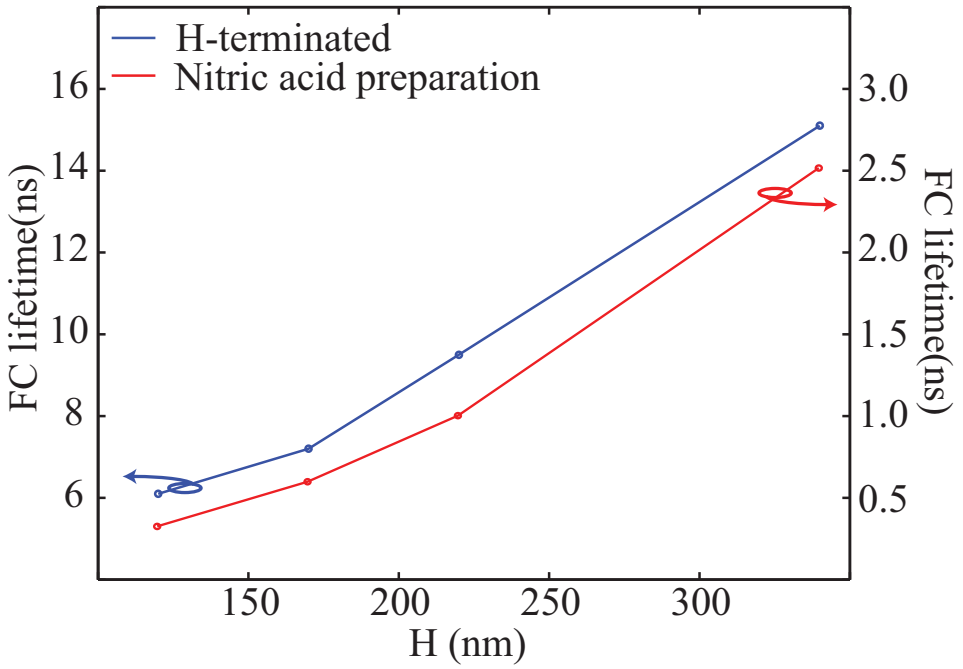

Figure 5.4: Free-carrier lifetime versus disk thickness for H-terminated and nitric-oxide-terminated surfaces

We find that the silicon surfaces produced by dry-etching, stripping resist, and undercutting 220-nm-thick microdisks with HF produced free carrier lifetimes $\sim$ 4 ns. A TOX surface preparation could increase

that lifetime significantly to ~ 30 ns, while a nitric acid treatment of a similar silicon microdisk reduced the lifetime to ~ 0.4 ns. In the series of devices depicted in Figure 5.4, reduction in geometrical scale provided nearly proportionate reduction in free carrier lifetime (see red, blue traces), while the application of nitric acid treatment provided a reduction of free-carrier lifetime by a factor of approximately 6. Comparison between the thickest, untreated, device in that experiment and the thinnest, treated, device in that experiment shows a realizable range of up to a factor of roughly 30 without sacrificing the ability to attain high-Q: the former resonator supported resonances with Q in excess of 2.5×10^5 and the latter in excess of 5×10^5.

Table 5.2: Summary of treatment, effect on free-carrier lifetime, and observed Q in thinned disks

Preparation	Free-carrier lifetime (ns)	Max observed Q
Thinned disk with Piranha	0.23	6×10^5
Thinned disk with nitric	0.33	2.5×10^5

An additional device was prepared on 120-nm-thick device layer silicon (as prepared above via dry-thermal oxidation of 220-nm-thick device layer SOI and removal of grown oxide with dilute HF). The "as-processed" preparation was followed with 2×Piranha/HF cycle plus a third Piranha-oxide layer oxidation. The free-carrier lifetime was measured then using the same technique as described above and the effective free-carrier lifetime of this Piranha oxide treated thinned microdisk was found to be 0.24 ns. This microdisk supported resonances

with Q-factors as high as 6×10^5. Fig. 5.5(a) shows a transmission spectrum of such a resonance, and Fig. 5.5 shows simultaneous fits to the time-domain behavior for a resonance on that microdisk.

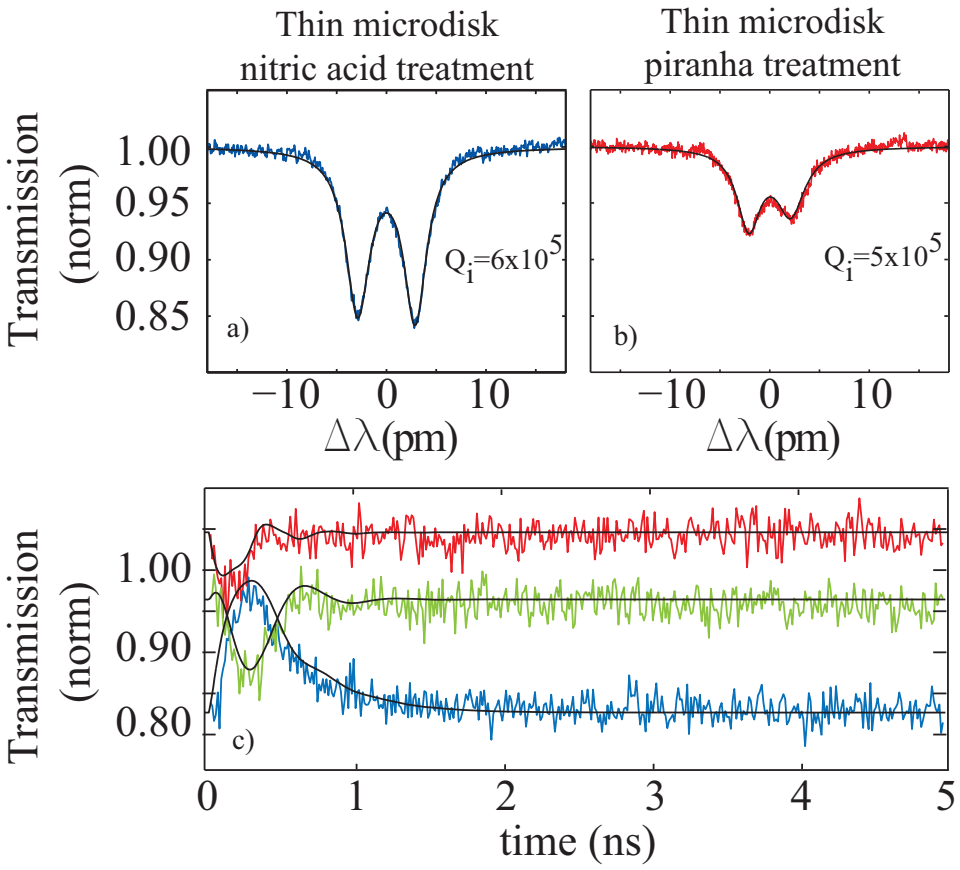

Figure 5.5: a) High-Q mode in 120-nm-thick microdisk with Piranha acid surface treatment. b) High-Q mode in 120-nm-thick microdisk with nitric surface treatment. c) Time-domain behavior of 120-nm-thick microdisk with Piranha surface treatment, with best-fit lifetime of 240 ps

By using the carrier dynamics modeling presented in Section 2.2.3 and comparing it to experimental results, we can infer the surface recombination velocities associated with different surface treatments and use that information to determine the effective carrier lifetime of different structures. Given the effective free-carrier lifetimes from the

standard-thickness devices under different preparations, we find a set of surface recombination velocities we may use to predict the impact of geometric changes in other structures. We find by matching the mode-averaged free-carrier lifetime calculated numerically to the measured effective free-carrier lifetime that the thermally oxidized surface with a mode-averaged free-carrier lifetime of 34.3 ns in a 6.5μm radius disk of height 220 nm (mode wavelength 1.5μm) corresponds to an SRV of 3 m/s. Similarly the hydrogen terminated surfaces in the same structure have SRV of $\sim$ 9 m/s. The nitric-acid-treated surfaces of such a resonator have SRV of approximately $\sim$ 240 m/s.

In a later section we consider the ramifications of using undercut versus planar microdisks and microrings. We will use these inferred parameters to deduce the expected free-carrier lifetimes in those geometries.

5.3 Free-carrier lifetime processing conclusions

Using optically injected free carriers to dynamically modify the transmission properties of silicon microdisk resonators, we inferred the effective free-carrier lifetimes of silicon microdisks under a variety of surface preparations.

We found that surface treatments and passivations used widely in microelectronics and photovoltaics have differing impacts on free-carrier lifetime in these structures. The surface preparations we have examined previously for loss properties and stability modify the free carrier

lifetimes of these devices through changes in surface recombination velocity.

TOX encapsulation, found previously to have highly desirable loss characteristics and stability dramatically enhances effective free-carrier lifetime, while the creation of chemical oxide-Si interfaces very significantly reduces the effective free-carrier lifetimes in microdisk resonators, at the price of increased optical losses.

The use of SiN_x passivation was not found to be a useful treatment: we found previously that the losses are somewhat increased relative to "as-processed" microdisks, and that the effective free-carrier lifetime is hardly affected. Neither high-Q nor short liftime is achieved.

Overall, we find that high-Q silicon microdisk resonators ($Q \sim 6^5$) may be fabricated with surface treatments that result in free carrier lifetimes of $\tau_{fc} \sim 240$ ps.

Chapter 6

Nonlinear Processes

6.1 Overall Framework

In Section 2.1 a framework for incorporating nonlinear and perturbation effects was presented. The pertinent equation is recapitulated below, and extended as needed.

6.1.1 Nonlinear polarization

$$\frac{da_i}{dt} = -\frac{\gamma_i}{2}a_i + i(\omega - \omega_i)a_i + \frac{i\omega}{2\epsilon_0}\frac{\int d\mathbf{r}\tilde{\mathbf{E}}_i^*(\mathbf{r},\omega_i)\cdot\mathbf{P}(\mathbf{r},t)}{\int d\mathbf{r}\epsilon_r(\mathbf{r},\omega_i)\left|\tilde{\mathbf{E}}_i(\mathbf{r},\omega_i)\right|^2}. \tag{6.1}$$

The effects of nonlinear polarization will be important below, as will the impact of photon-generated carrier populations and thermal effects. Nonlinear polarizations which have a broad bandwidth relative to the cavity and input waves may be included in the the time domain equations of motion as though they were instantaneous in effect. We now introduce the nonlinear susceptibility in the form of the tensor quantity $\overleftrightarrow{\chi}^{(3)}_{ijkl}(\mathbf{r},\omega)$, the lowest-order nonlinear response allowed by the

symmetry of the silicon lattice [58]. Typically we will be specializing to the case where the several fields are co-polarized, and so the tensor nature of the response will be unimportant, but shall carry it forward until so noted.

By convention, $\overleftrightarrow{\chi}^{(3)}$ for various nonlinear processes is written in the frequency domain as $\overleftrightarrow{\chi}^{(3)}(-\omega_i;\omega_j,-\omega_k,\omega_l)$, where the waves are at frequency $\omega_\eta(\eta\in\{,j,k\})$ and energy conservation is reflected through $\omega_i=\omega_j-\omega_k+\omega_l$. The convention of writing $\overleftrightarrow{\chi}^{(3)}$ in this form is consistent with Refs. [39, 58]. Third-order susceptibility may generally include bound-electronic effects, as well as inelastic interactions between photons and the crystal lattice (as Raman and Brillouin scattering [107–109]); in what follows, we will consider each where important. The bound-electronic effects result in TPA and Kerr nonlinearity, with the imaginary part of $\overleftrightarrow{\chi}^{(3)}$(due to bound-electronic effects) corresponding to TPA and the real part to Kerr effect [58, 110].

We may now write the nonlinear polarization as a truncated power series in the electric field in the form [58, 111] (again assuming the polarizable units (e.g., crystal unit cells) are much smaller in physical size than the wavelength of light present):

$$\mathbf{P}^{NL}(\mathbf{r},t)=\frac{3}{4}\epsilon_0\sum_{jkl}\overleftrightarrow{\chi}^{(3)}_{ijkl}(\mathbf{r})\tilde{\mathbf{E}}_j(\mathbf{r},\omega_j)\tilde{\mathbf{E}}^*_k(\mathbf{r},\omega_k)\tilde{\mathbf{E}}_l(\mathbf{r},\omega_l)a_j(r)a^*_k(t)a_l(t), \tag{6.2}$$

where the prefactor reflects the process degeneracy [58], and we have al-

ready moved to slowly varying amplitudes. The inclusion of free-carrier-induced polarizability (as noted in Section 2.1), can be accomplished in a similar fashion as Eqn. 2.36. Then we may write the equations of motion for three waves (signal, pump, and idler) participating in FWM as:

$$\frac{da_s}{dt} = \left(i\Delta\omega_s - \frac{\gamma_s}{2}\right) a_s + i\delta\omega_s\left(\overline{N}(t)\right) a_s - \frac{1}{2}\gamma_s\left(\overline{N}(t)\right) a_s \tag{6.3}$$

$$+ i\left(\gamma_s^c U_s + 2\gamma_{sp}^c U_p + 2\gamma_{si}^c U_i\right) a_s + i\gamma_{spip}^c a_p^2 a_i^*, \tag{6.4}$$

$$\frac{da_p}{dt} = \left(i\Delta\omega_p - \frac{\gamma_p}{2}\right) a_p + i\delta\omega_p\left(\overline{N}(t)\right) a_p - \frac{1}{2}\gamma_p\left(\overline{N}(t)\right) a_p \tag{6.5}$$

$$+ i\left(\gamma_p^c U_p + 2\gamma_{ps}^c U_s + 2\gamma_{pi}^c U_i\right) a_p + 2i\gamma_{pspi}^c a_s a_i a_p^* + i\kappa\, S, \tag{6.6}$$

$$\frac{da_i}{dt} = \left(i\Delta\omega_i - \frac{\gamma_i}{2}\right) a_i + i\delta\omega_i\left(\overline{N}(t)\right) a_i - \frac{1}{2}\gamma_i\left(\overline{N}(t)\right) a_i \tag{6.7}$$

$$+ i\left(\gamma_i^c U_i + 2\gamma_{ip}^c U_p + 2\gamma_{is}^c U_s\right) a_i + i\gamma_{ipsp}^c a_p^2 a_s^*, \tag{6.8}$$

where $\Delta\omega_k$ is the detuning between the cavity resonance near ω_{k0} and the wave at ω_k; γ_k is the total loss rate associated with the resonance near ω_k (including output coupling); γ_j^c, γ_{jk}^c, and γ_{jklm}^c are self-phase modulation (SPM), cross-phase modulation (XPM), and FWM parameters (respectively)' and we have assumed co-polarized waves, leading to scalar susceptibility $\chi^{(3)}$. We include the dispersive and loss effects of free-carrier populations in the above as:

$$\delta\omega_j\left(\overline{N}(t)\right) = \frac{\omega_j}{n_{0j}}\left(\sum_k \frac{dn_{Si}}{dN_k}\overline{N}_k\right), \tag{6.9}$$

$$\frac{1}{2}\gamma_j\left(\overline{N}(t)\right) = \frac{c}{2n_{0j}}\left(\sum_k \sigma_k\overline{N}_k\right), \tag{6.10}$$

where $\delta\omega_j(\overline{N}(t))$ is the free-carrier dependent resonance frequency shift of the j-th mode, and $\gamma_j(\overline{N}(t))$ is the free-carrier absorption experienced by the j-th mode. The $\overline{N}(t)$ dependence indicates that we have moved to the mode-averaged equations of motion, and the summations on the RHS of Eqn. 6.10 reflect the fact that electron and hole populations have different crosssections to absorption and influences on refractive index. The RHS of Eqn. 6.10 also reflects the fact that a simple perturbation theory calculation shows the relative change in mode frequency is equal in magnitude to the relative change in refractive index, and that the free-carrier absorption rate is related to the linear absorption constant through a group velocity.

The SPM, XPM, and FWM parameters (as well as Raman parameters, where they apply), γ_j^c, γ_{jk}^c, and γ_{ijkl}^c (respectively), are mode-averaged parameters that reflect the spatially nonuniform nature of the resonant modes. In the process of moving to the mode-averaged equations, treating the modes effectively as lumped elements, it is helpful to introduce a series of overlap factors and mode volumes [19,20,25]. In the present case, we follow the conventions in [25], where the mode-averaged γ_{ijkl}^c is defined as:

$$\gamma^c_{ijkl} = \frac{3\omega_i \eta^c_{ijkl} \chi^{(3)}\left(-\omega_i; \omega_j, -\omega_k, \omega_l\right)}{4\epsilon_0 n_{0i} n_{0j} n_{0k} n_{0l} V_{ijkl}}. \tag{6.11}$$

This definition introduces overlap factors η^c_{ijkl} and mode volumes V_{ijkl} which are defined as:

$$\eta^c_{ijkl} = \frac{\int_{Si} d\mathbf{r}\ \left(\epsilon_{ri}\epsilon_{rj}\epsilon_{rk}\epsilon_{rl}\right)^{1/2} \tilde{E}^*_i \tilde{E}_j \tilde{E}^*_k \tilde{E}_l}{\left\{\Pi_{\nu=i,j,k,l} \int_{Si} d\mathbf{r}\, \epsilon^2_{r\nu} \left|\tilde{\mathbf{E}}_\nu\right|^4\right\}^{1/4}} \tag{6.12}$$

and

$$V_{ijkl} = \left(V_i V_j V_k V_l\right)^{1/4}, \tag{6.13}$$

where V_ν are effective mode volumes for the individual modes at ω_ν as

$$V_\nu = \frac{\left\{\int d\mathbf{r}\, \epsilon_r\left(\mathbf{r}, \omega_\nu\right) \left|\tilde{\mathbf{E}}_\nu\left(\mathbf{r}, \omega_\nu\right)\right|^2\right\}^2}{\int_{Si} d\mathbf{r}\, \epsilon^2_r\left(\mathbf{r}, \omega_\nu\right) \left|\tilde{\mathbf{E}}_\nu\left(\mathbf{r}, \omega_\nu\right)\right|^4}. \tag{6.14}$$

From the EOMs above, we may deduce the time domain behavior of the FWM (or Raman processes (*mutatis mutandis*)). We will return to these EOMs and related analysis in a later section.

An additional source of nonlinear behavior in silicon microresonator systems is the feeding of optical energy into thermal and free-carrier populations and the interactions therewith. The accumulation and dissipation of those additional populations introduces additional dynamical and quasi-static behavior. One interesting effect that is a result of those interactions will be presented and analyzed in a later section.

For organizational purposes, we will present the additional equations of motion here.

6.1.2 Nonlinear behavior due to thermal and free-carrier populations

6.1.2.1 Linear and nonlinear optical losses

In the previous section, loss rates for the standing wave modes were introduced. These loss rates can be separated into terms reflecting the origin and behavior of each loss mechanism:

$$\gamma_{c/s} = \gamma^e_{c/s,0} + \sum_{j>0} \gamma^e_{c/s,j} + \gamma_{c/s,rad} + \gamma_{c/s,lin} + \overline{\gamma}_{c/s,\mathrm{TPA}} + \overline{\gamma}_{c/s,\mathrm{FCA}}. \quad (6.15)$$

The total loss rate for each mode includes loss into the forward and backward fiber-taper fundamental modes ($\gamma^e_{c/s,0}$), parasitic losses into other guided modes of the fiber-taper that are not collected ($\gamma^e_{c/s,j>0}$), radiation and scattering losses ($\gamma_{c/s,rad}$), linear material absorption ($\gamma_{c/s,lin}$), two-photon absorption (TPA) ($\overline{\gamma}_{c/s,\mathrm{TPA}}$), and free-carrier absorption (FCA) ($\overline{\gamma}_{c/s,\mathrm{FCA}}$). Note that the coupling coefficient of optical power into the resonator is related to $\gamma^e_{c/s,0}$ by, $\kappa = \sqrt{\gamma^e_{c/s,0}/2}$.

In WGM resonators the field distribution can be highly localized, and so the calculation of loss rates due to nonlinear processes must take into account the nonuniform field distribution of a given resonance, as well as material properties. We will follow closely the analysis of

Barclay [19], with the modification that our analysis will not assume steady-state conditions.

The wavelength region considered in this work ($\sim 1.5\,\mu$m) is within the bandgap of the silicon material of the microdisk resonator, and so absorption by the silicon material should be small. TPA, however, can be significant in silicon [99]. From [19] we have

$$\overline{\gamma}_{c/s,\mathrm{TPA}}(t) = \Gamma_{\mathrm{TPA}} \frac{\beta_{Si}\, c^2}{V_{\mathrm{TPA}}\, n_g^2} U_{c/s}(t) \tag{6.16}$$

where the n_g is the group index associated with the measurement of the intensity loss per unit length, β_{Si}, and Γ_{TPA} and V_{TPA} are defined as[1]

$$\Gamma_{\mathrm{TPA}} = \frac{\int_{Si} n^4(\mathbf{r}) \left|E_{c/s}(\mathbf{r})\right|^4 d\mathbf{r}}{\int n^4(\mathbf{r}) \left|E_{c/s}(\mathbf{r})\right|^4 d\mathbf{r}}, \tag{6.17}$$

$$V_{\mathrm{TPA}} = \frac{\left(\int n^2(\mathbf{r}) \left|E_{c/s}(\mathbf{r})\right|^2 d\mathbf{r}\right)^2}{\int n^4(\mathbf{r}) \left|E_{c/s}(\mathbf{r})\right|^4 d\mathbf{r}}. \tag{6.18}$$

The total two-photon absorbed power can then be written as,

$$P_{abs,\mathrm{TPA}}(t) = \Gamma_{\mathrm{TPA}} \frac{\beta_{Si}\, c^2}{V_{\mathrm{TPA}}\, n_g^2} \Big(U_c^2(t) + U_s^2(t) \Big). \tag{6.19}$$

It should be noted that the above partitioning of nonlinear TPA absorption into separate terms for each of the standing-wave modes is not exactly correct. There are cross-terms due to the non-orthogonality

[1]Note that the confinement factor and effective mode volume for the two standing-wave modes are identical, hence we drop the c/s subscript.

of the modes for processes such as TPA involving higher-order modal overlaps of the electric field distribution[2]. For the standing-wave modes the correction is small, and we neglect the cross terms in what follows.

The silicon material used in this work has a low doping density ($N_A < 1 \times 10^{16}\,\mathrm{cm}^{-3}$). With this doping level, we expect negligible losses due to ionized dopants ($\alpha_{\mathrm{FCA},0} \sim 10^{-2}\,\mathrm{cm}^{-1} \leftrightarrow Q_{\mathrm{FCA},0} \sim 10^{7}$). As such, we will ignore that initial population in our consideration of free-carrier density below. Free-carrier absorption, however, can be significant due to the presence of TPA-generated free-carriers [19, 99, 112]. Again, following Barclay [19], we model the optical loss rate due to TPA-induced FCA with a simple Drude model:

$$\gamma_{c/s,\mathrm{FCA}}(\mathbf{r},t) = \frac{\sigma_{Si}(\mathbf{r})\,c}{n_g} N(\mathbf{r},t). \tag{6.20}$$

This model has been demonstrated to reproduce the behavior of free-carrier absorption for both electron and hole populations in silicon, though with differing absorption cross-sections σ_{Si} for each carrier population [59]. In this expression (Eqn. 6.20), the distinction between these populations is ignored and a total crosssection $\sigma_{Si} = \sigma_{Si,e} + \sigma_{Si,h}$, and electron-hole pair density are considered. If we perform the required averaging of this loss rate we find

[2]For TPA with the standing wave modes one has an additional term dependent upon the product $U_c U_s$, with cross-confinement factor ($= \Gamma_{c/s,\mathrm{TPA}}$) and cross-mode volume ($= 3V_{c/s,\mathrm{TPA}}$) pre-factors. For FCA, described below, one cannot write the total absorption just in terms of products of powers of the cavity energies, but rather the mode amplitudes themselves must be explicitly used.

$$\overline{\gamma}_{c/s,\mathrm{FCA}}(t) = \frac{\sigma_{Si}\, c}{n_g}\overline{N(t)} \tag{6.21}$$

where again the n_g above is the group-index associated with the measurement of the absorption cross-section, and $\overline{N}$ is defined as

$$\overline{N(t)} = \frac{\int N(\mathbf{r},t) n(\mathbf{r})^2 \left|E(\mathbf{r})\right|^2 d\mathbf{r}}{\int n(\mathbf{r})^2 \left|E(\mathbf{r})\right|^2 d\mathbf{r}}. \tag{6.22}$$

Accumulating all these effects, we arrive at a total absorbed power given by,

$$P_{\mathrm{abs}}(t) = (\gamma_{c,lin} + \overline{\gamma}_{c,\mathrm{TPA}} + \overline{\gamma}_{c,\mathrm{FCA}})U_c(t) + (\gamma_{s,lin} + \overline{\gamma}_{s,\mathrm{TPA}} + \overline{\gamma}_{s,\mathrm{FCA}})U_s(t). \tag{6.23}$$

6.1.2.2 Thermal and free-carrier dispersion

The nonlinear loss mechanisms discussed above, which change the losses of the WGM resonance in a way dependent on the stored energy, also influence the properties of the resonance. Heating of the resonator due to optical absorption changes its temperature, while the generation of excess free carriers via TPA also changes the refractive index through plasma carrier dispersion [59, 113].

From first-order perturbation theory we can estimate the relative change in resonance frequency for a given change in refractive index to be

$$\frac{\Delta\omega_0(t)}{\omega_0} = -\left\langle \frac{\Delta n(\mathbf{r},t)}{n(\mathbf{r})} \right\rangle, \tag{6.24}$$

where the average of the relative local change in refractive index is [114]

$$\overline{\left(\frac{\Delta n(t)}{n}\right)} = \frac{\int \left(\frac{\Delta n(\mathbf{r},t)}{n(\mathbf{r})}\right) n^2(\mathbf{r}) \left|E(\mathbf{r})\right|^2 d\mathbf{r}}{\int n^2(\mathbf{r}) \left|E(\mathbf{r})\right|^2 d\mathbf{r}}. \tag{6.25}$$

Taking into account the effect of heating due to absorption and TPA-induced free-carrier density, and the impact of those effects on the refractive index of the microresonator, we have

$$\frac{\Delta n(\mathbf{r},t)}{n(\mathbf{r})} = \frac{1}{n(\mathbf{r})}\frac{dn(\mathbf{r})}{dT}\Delta T(\mathbf{r},t) + \frac{1}{n(\mathbf{r})}\frac{dn(\mathbf{r})}{dN}N(\mathbf{r},t). \tag{6.26}$$

Substituting Eqn. 6.25 and 6.26 into Eqn. 6.24 we obtain

$$\frac{\Delta\omega_0(t)}{\omega_0} = -\left(\frac{1}{n_{Si}}\frac{dn_{Si}}{dT}\overline{\Delta T(t)} + \frac{1}{n_{Si}}\frac{dn_{Si}}{dN}\overline{N(t)}\right), \tag{6.27}$$

where $\overline{N(t)}$ is defined in Eqn. 6.22 and $\overline{\Delta T(t)}$ is similarly

$$\overline{\Delta T(t)} = \frac{\int \Delta T(\mathbf{r},t) n^2(\mathbf{r}) \left|E(\mathbf{r})\right|^2 d\mathbf{r}}{\int n^2(\mathbf{r}) \left|E(\mathbf{r})\right|^2 d\mathbf{r}}. \tag{6.28}$$

6.1.2.3 Equations of motion incorporating linear and nonlinear loss and dispersion due to thermal and free-carrier effects

We can now write down an equation of motion for the temperature of the microdisk resonator through energy conservation considerations [115]. Power is dissipated by optical absorption in the microdisk, adding

thermal energy to the silicon microdisk. Thermal energy in the silicon microdisk can escape through radiation, convection, and conduction, processes dependent on position within the microdisk. For the geometry and temperatures considered here convection and radiation can be disregarded, and the microdisk temperature can be assumed to be spatially uniform within the Si layer with little error for the timescales under consideration. We then have, integrating over the disk volume and substituting $\Delta T(\mathbf{r},t) = \Delta T(t)$ into Eqn. 6.28,

$$\frac{d\overline{\Delta T(t)}}{dt} = -\gamma_{th}\overline{\Delta T(t)} + \frac{\Gamma_{\text{disk}}}{\rho_{Si}\, c_{p,Si} V_{\text{disk}}} P_{\text{abs}}(t). \tag{6.29}$$

In the above, Γ_{disk} represents the fractional energy overlap of the mode with the differential temperature within the Si microdisk,

$$\Gamma_{\text{disk}} = \frac{\int_{Si} n(\mathbf{r})^2 \left|E(\mathbf{r})\right|^2 d\mathbf{r}}{\int n(\mathbf{r})^2 \left|E(\mathbf{r})\right|^2 d\mathbf{r}}, \tag{6.30}$$

and γ_{th} is the silicon microdisk temperature decay rate given by

$$\gamma_{th} = \frac{k}{\rho_{Si} c_{p,Si} V_{\text{disk}}}, \tag{6.31}$$

where ρ_{Si}, $c_{p,Si}$, V_{disk}, and k are, respectively, the density of silicon, the constant-pressure specific heat capacity of silicon, the volume of the silicon microdisk, and the coefficient of thermal conduction of the SiO_2 pedestal the microdisk rests upon. For this geometry the coefficient of thermal conduction is approximately $k = \kappa_{SiO_2}\pi r_{\text{post}}^2/h$, with κ_{SiO_2} the thermal conductivity, r_{post} an average radius, and h the height of the

SiO_2 pedestal.

We can proceed in a similar fashion to determine the equation of motion for the free-carrier density. A population of free carriers decays through a variety of processes (nonradiative recombination, diffusion out of the region of interest, Auger recombination, etc). In general, the rate of decay will depend on the position in the microcavity (e.g., due to the proximity of surfaces, impurities) and the density of free carriers. We will disregard any density dependence in the free-carrier lifetime. The free-carrier population is generated via TPA, and so

$$\frac{\partial N(\mathbf{r},t)}{\partial t} = -\gamma(\mathbf{r})N(\mathbf{r},t) + \nabla\cdot(D(\mathbf{r})\nabla N(\mathbf{r},t)) + G(\mathbf{r},t). \qquad (6.32)$$

Free-carrier recombination, a process dependent on location (proximity to surfaces, etc.), is represented by the first term on the RHS of Eqn. 6.32, carrier density diffusion is represented by the second, and generation is represented by the third term on the RHS. The local generation rate of free carriers, $G(\mathbf{r},t)$ can be calculated by noting that the local TPA photon-loss generates one electron-hole pair per two photons absorbed.

If we then take the mode-average of Eqn. 6.32 we obtain

$$\frac{d\overline{N(t)}}{dt} = -\overline{\gamma(\mathbf{r})N(t)} + \overline{\nabla\cdot(D(\mathbf{r})\nabla N(\mathbf{r},t))} + \overline{G(t)}. \qquad (6.33)$$

$\overline{G(\mathbf{r},t)}$ is calculated from the mode-averaged local TPA rate, and as discussed in Ref. [19] can be written as,

$$\overline{G(\mathbf{r},t)} = \frac{\Gamma_{\mathrm{FCA}}\beta_{Si}c^2}{2\hbar\omega_p n_g^2 V_{\mathrm{FCA}}^2}(U_c(t)^2 + U_s(t)^2), \tag{6.34}$$

where Γ_{FCA} and V_{FCA} are given by,

$$\Gamma_{\mathrm{FCA}} = \frac{\int_{Si} n^6(\mathbf{r}) \left|E_{c/s}(\mathbf{r})\right|^6 d\mathbf{r}}{\int n^6(\mathbf{r}) \left|E_{c/s}(\mathbf{r})\right|^6 d\mathbf{r}}, \tag{6.35}$$

$$V_{\mathrm{FCA}}^2 = \frac{\left(\int n^2(\mathbf{r}) \left|E_{c/s}(\mathbf{r})\right|^2 d\mathbf{r}\right)^3}{\int n^6(\mathbf{r}) \left|E_{c/s}(\mathbf{r})\right|^6 d\mathbf{r}}. \tag{6.36}$$

As in the case of TPA, we neglect in the FCA higher-order field overlaps between the cosine- and sine-like standing-wave modes, a small approximation in this case.

For free-carrier lifetimes $\gtrsim 1\,\mathrm{ns}$, extensive free-carrier diffusion and the high localization of the field distribution of the resonant mode result in an effectively constant free-carrier density over the regions where there is appreciable optical energy density. We may then approximate the free-carrier density to be constant for purposes of mode-averaging, and the second term in the RHS of Eqn. 6.33 can be neglected. The first term in the RHS of Eqn. 6.33 becomes an effective free-carrier decay rate of the mode-averaged free-carrier density, accounting for both recombination and diffusion, and we finally have

$$\frac{d\overline{N(t)}}{dt} = -\gamma'_{fc}\overline{N(t)} + \frac{\Gamma_{\mathrm{FCA}}\beta_{Si}c^2}{2\hbar\omega_p n_g^2 V_{\mathrm{FCA}}^2}(U_c(t)^2 + U_s(t)^2). \tag{6.37}$$

Eqn. 6.37 is an equation of motion for the mode-averaged free-carrier density, where ω_p is the frequency of the pump photons coupled into the WGM from the fiber-taper.

6.2 Self-induced transmission oscillations due to an interaction between thermo-optical and free-carrier effects

In this section a dynamical effect involving an interactive competition between changing free-carrier populations and temperature is presented and modeled. Despite the current lack of an efficient electrically pumped light emitter in the silicon material system, the infrastructure and knowledge built up by the microelectronics industry has long rendered it attractive to many in the optoelectronics field [56]. Silicon is a high-index-of-refraction material (n = 3.48 at $\lambda = 1.5\,\mu$m), and because SiO_2 and SiN_x have relatively low index (n = 1.4 – 2.0 at $\lambda = 1.5\,\mu$m), high index-contrast optical structures can be fabricated in the silicon material system in a manner compatible with conventional microelectronics processing. This is important both because one of the chief engines of performance improvement in the microelectronics industry has been the scaling and dense integration of devices, and because the

integration of microphotonic devices with microelectronic devices will add functionality to both. In order to achieve scaling with microphotonics, high index-contrast devices will be necessary. The scaling of microphotonic devices can also improve their performance by reducing input powers required for certain functionalities [19, 116–118], or even by making novel functionalities possible [14]. However, as with microelectronics, where scaling devices can lead to unintentional interactions between devices and phenomena, scaling microphotonic devices can also promote unwanted, and in some cases, unanticipated effects.

This section concerns such an unanticipated effect observed in a high-Q silicon-on-insulator (SOI) microdisk optical resonator, first reported in this type of device in Refs. [20, 96]. More recently, other indirect measurements suggestive of this phenomenon have also been presented as well [112]. In this effect, a low-power, continuous-wave laser is evanescently coupled into the whispering-gallery modes (WGMs) of a silicon microdisk optical resonator, and the transmitted optical power monitored. Radio frequency (RF) oscillations in the transmission are observed.

The microdisk optical resonator considered in this work consists of a silicon disk 4.5 μm in radius and 340 nm in thickness resting upon an approximately hourglass-shaped SiO_2 pedestal 1.2 μm high with effective radius 1.6 μm. The silicon is p-doped with resistivity 1–3 Ω·cm (corresponding to $N_A < 1 \times 10^{16}\,\mathrm{cm}^{-3}$). The fabrication details of the silicon microdisk considered here can be found in another work [23].

Images of a Si microdisk with fiber-taper coupling are shown in Fig. 6.1.

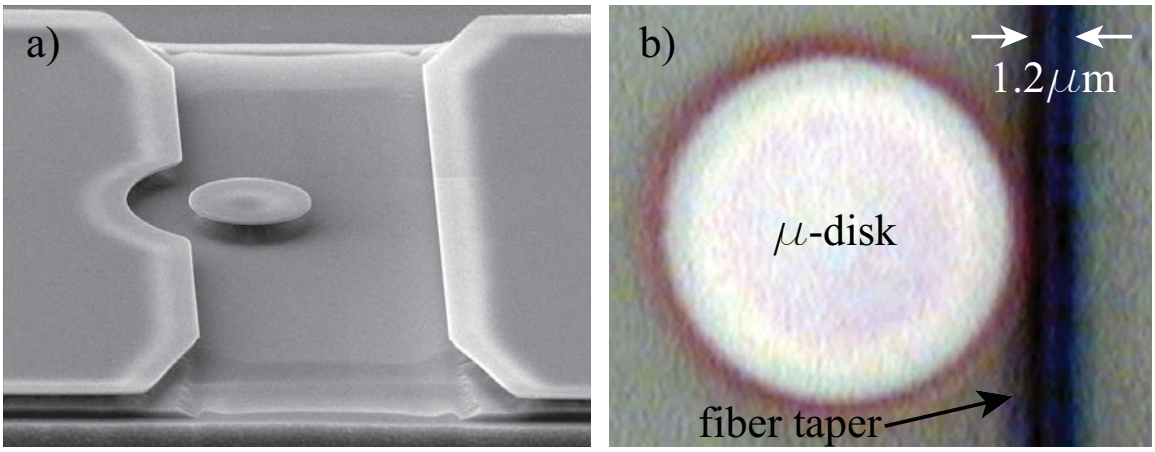

Figure 6.1: (a) Scanning electron microscope image of Si microdisk under study. (b) Optical image (top-view) of microdisk with side-coupled optical fiber taper waveguide

A fiber-taper probe technique is used to excite the WGM resonance [41]. In this technique, a section of a standard single-mode fiber is heated in the flame of a hydrogen torch and drawn down to a diameter of $1.2 \pm 0.2\,\mu$m. At this diameter, the evanescent field of light guided by the fiber-taper extends significantly into the surrounding air. Using mechanical stages with 50 nm step-size, the tapered fiber can be placed in the near field of the microdisk resonator, where the evanescent field of the light carried by the fiber-taper can be coupled into the WGMs of the microdisk (see Fig. 6.1(b)). A swept-wavelength tunable laser source is used to measure the transmission spectra of

the microdisk resonator WGMs and a manual polarization controller is employed to optimize coupling from fiber-taper to WGM. A variable optical attenuator is used to control the amount of power coupled into the fiber-taper. For the high-speed data acquisition measurements of the transmitted optical power described below a New Focus 1554-B 12 GHz photoreceiver was used, either in conjunction with a 22 GHz HP-8563A electronic spectrum analyzer (ESA) for RF power spectrum measurements or an Agilent Infinium 54855A 6 GHz oscilloscope for time-domain measurements.

6.2.0.4 Low-power measurements

At extremely low input powers ($0.5\,\mu$W) we observe (Fig. 6.2(a)) that the transmission through the coupled microdisk-fiber system displays the characteristic "doublet" lineshape seen in high-Q silicon microdisk resonators [22, 23]. The origin of this feature is discussed in Section 3. When the coupling between WGM and fiber-taper is weak, the intrinsic Qs of the doublet modes can be determined to be approximately 3.5×10^5.

At slightly higher input powers ($35\,\mu$W) we observe (Fig. 6.2(a)(ii)) a distorted asymmetric lineshape with sharp recovery, characteristic of thermal bistability [19, 115, 119, 120]. In this effect, power absorbed in the microdisk resonator heats the silicon microdisk, causing a redshift of the resonance wavelength through the thermo-optic effect [113]. If the input laser wavelength is swept from blue to red, the resonance

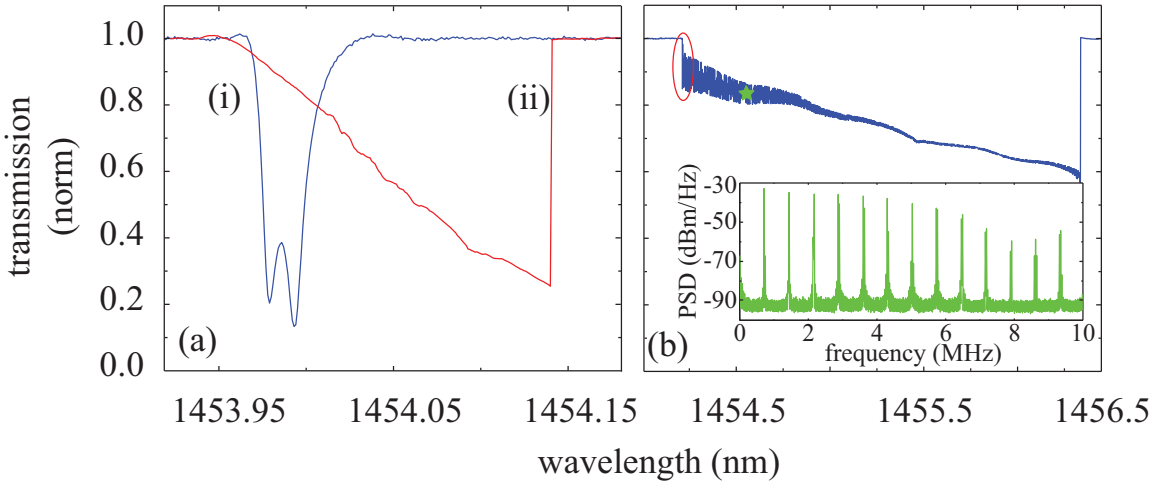

Figure 6.2: Normalized transmission spectrum of a silicon microdisk WGM resonance (a) at 0.5 μW input power (i) and at 35 μW input power (ii). (b) With 480 μW input power. (inset) Power spectrum of transmission at input wavelength 1454.56 nm, indicated by a green star in (b)

wavelength will be "pushed" ahead of the laser wavelength, resulting in the distorted shape observed in Fig. 6.2(a)(ii). The sharp recovery occurs when the dropped optical power and thermally induced redshift reaches its maximum attainable value at resonance. At that point, the input laser cannot further heat the resonator, and the temperature and resonance wavelength quickly return to their initial values, resulting in the sudden increase in transmission. A reversed scan (input laser tuned from red to blue) would result in a qualitatively different transmission spectrum; the system exhibits a hysteresis behavior which, along with the asymmetric transmission spectrum, is characteristic of optical bistability. In the case of a typical resonator, this effect increases with increasing input power. However, in the presence of other phenomena the power-dependent behavior can be significantly altered as described

below.

6.2.1 Higher-power measurements—time domain behavior

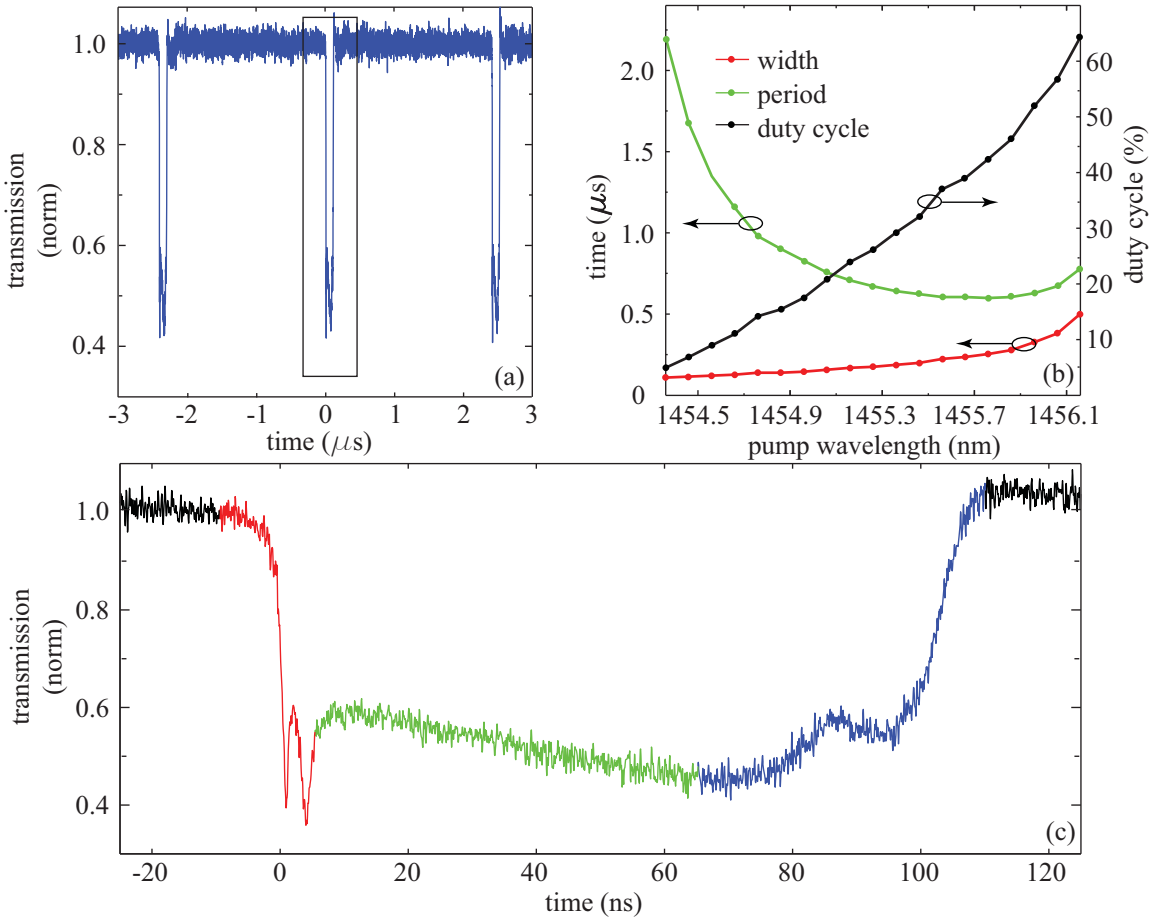

Figure 6.3: (a) Example of time domain behavior. (b) Dependence of time domain behavior upon input laser wavelength. (c) Detail of transmission oscillation depicted in (a)

Fig. 6.2(b) shows the transmission spectrum of the resonance depicted in Fig. 6.2(a) at an input power of 480 μW. Note the qualitative differences between Fig. 6.2(b) and Fig. 6.2(a): the sudden drop in transmission near 1454 nm (red oval), and the fluctuating transmission in the region from 1454.3–1456.2 nm. The irregular transmission in the

region 1454.3–1456.2 nm indicates a rich time-domain behavior, and is present in the transmission spectrum of this resonance for input powers as low as 60 μW. The inset to Fig. 6.2(b) shows the RF power spectrum of the optical transmission intensity at an input wavelength in the fluctuating regime. Note that the initially continuous-wave input has acquired significant nonzero frequency content.

Under high-speed acquisition, the time-domain behavior of the transmitted optical power is revealed to consist of a periodic train of temporally narrow transmission dips. Fig. 6.3(a) shows a characteristic example of the time-domain behavior. The oscillation begins with a pump wavelength corresponding to the sharp drop-off near 1454.3 nm in the wavelength-dependent transmission spectrum (see Fig. 6.2(b)). This behavior persists over the range of wavelengths corresponding to the oscillatory optical transmission as seen in (Fig. 6.2(b), 1454.3–1456.2 nm). Over this laser tuning range, the period of the oscillation initially decreases and then increases near the end of the oscillation range, while the temporal width of the transmission dip increases monotonically with the pump wavelength. Fig. 6.3(b) depicts the tuning behavior of the period, width, and duty cycle of the oscillations in the transmitted optical power.

Closer study of the temporally narrow transmission dip, depicted in more detail in Fig. 6.3(c), reveals that near the beginning of the transmission dip (red curve) a fast ($\sim$ 2 ns) double-dip occurs. This is followed by a slow ($\sim$ 100 ns) increase in the transmission depth (green

curve). Finally, at the end of the transmission dip (blue curve), just before the transmission recovers, there occurs a more elongated double-dip ($\sim$ 20 ns). In the next section a model is developed to explain these observations in terms of oscillations in the resonance frequencies of the standing-wave WGMs of the Si microdisk due to the nonlinear interaction and competition between free-carriers and phonons generated by optical power circulating within the microdisk.

6.2.1.1 Cartoon model

Above, we formulated dynamical equations for the relevant properties of the system, and Figure 6.4 depicts the various physical processes involved in the nonlinear modeling of the Si microdisk.

The high-Q and small volume of the Si microdisks results in large circulating optical intensities for modest input powers. The circulating intensity, I, can be approximated by $I = P\frac{\lambda}{2\pi n}\frac{Q}{V}$, where P is the input power at wavelength λ, n is the group index of the resonant mode and V is the corresponding mode-volume [121]. Assuming a Q-factor of approximately 2.5×10^5, a mode volume of $50\frac{\lambda}{n_{\mathrm{Si}}}^3$, and input power of 0.5 mW, circulating intensities can approach $200\,\frac{\mathrm{MW}}{\mathrm{cm}^2}$ in a high-Q Si microdisk resonator. Such large circulating intensities can result in significant two-photon absorption, producing heat and free-carriers, and other nonlinearities. The generated free carriers produce dispersion, and are themselves optically absorbing, which produces more heat. The refractive index seen by the circulating light within the microdisk

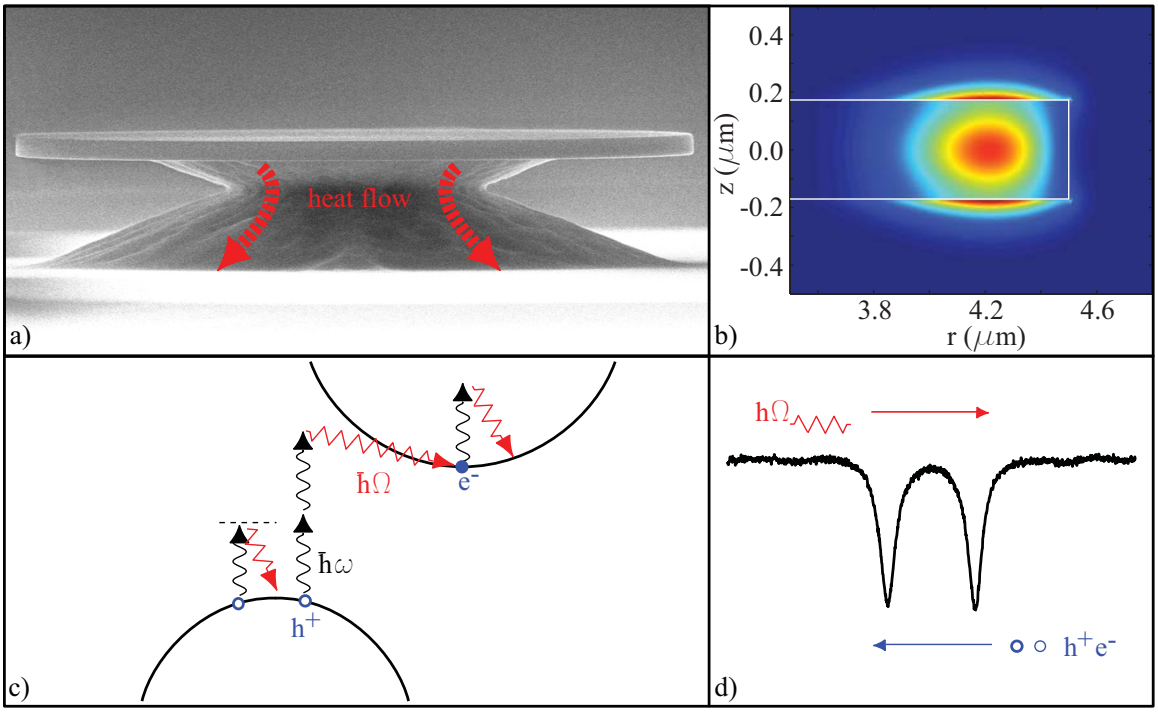

Figure 6.4: A picture of the various physical processes involved in the nonlinear model of the Si microdisk considered here. (a) A scanning electron micrograph of a representative SOI microdisk resonator. As discussed below, heat flows by conduction through the SiO_2 pedestal. (b) Square-magnitude of the electric field for the WGM under consideration as calculated by finite-element method (FEM). High-intensity fields are found in the red regions. High field strengths in the silicon disk (the white box delineates the disk) generate free carriers via TPA. (c) Schematic depiction of dominant processes in the Si microdisk: TPA, TPA-generated free-carrier density (e^-, h^+, denoting electrons and holes, respectively), free-carrier absorption (FCA), and surface-state absorption. (d) Schematic of the dispersive effects of heat and free carriers on the WGM resonance wavelength

is modified both by the stored thermal energy (phonons) within the microdisk through the thermo-optic effect, and by the dispersion due to the excess of free carriers. These two effects produce competing shifts in the resonance wavelength of WGMs of the microdisk, red for the thermo-optic shift and blue for the free-carrier dispersion. The shift in the resonance wavelength and the nonlinear absorption in turn alters the circulating optical intensity, which then feeds back and modifies the generation rate of heat and free carriers.

6.2.1.2 Comparison between experiment and theory

Eqns. 2.12-6.15,6.27,6.29, and 6.37 comprise a model that we can numerically integrate, allowing us to determine the dynamical behavior of the system. The numerical integration is carried out using a variable order, Adams-Bashforth-Moulton predictor-corrector method. In this model, the free-carrier decay rate and the thermal decay rate are taken as free parameters. The fixed parameters of the model are measured values, where possible (input power, resonance Qs and coupling values, geometry of the disk, etc.), values taken from the literature (β_{Si},σ_{Si}, etc.), and values calculated via the finite-element-method for quantities not amenable to measurement (mode-field profiles, overlap factors, mode volumes, etc.). These parameters are presented in Table 6.1.

Fig. 6.5(a) compares the results of simulation and experiment for a pump laser power corresponding to the experimental conditions of Fig. 6.2(b) and a laser wavelength near the onset of oscillation (red

oval) in Fig. 6.2(b)). The data presented in Fig. 6.5(a) corresponds to an input wavelength of 1454.36 nm, as near the beginning of the oscillation as was feasible for data collection. The onset of oscillations in the model occurred at 1454.12 nm, a small discrepancy easily attributable to the high sensitivity of the model results to the parameters. The transmitted optical power of the simulation is shown to accurately estimate both the observed transmission dip, temporal width, and the period of repetition. The salient trends in the period and duty cycle of the transmission oscillations observed experimentally (Fig. 6.3) are also recovered by the model. The inset of Fig. 6.5(a) shows a zoomed-in comparison of the transmission dip. The model is also seen to accurately predict the initial rapid double-dip, slow increase in the transmission depth, and the more elongated double-dip just before transmission recovery. As discussed below, we can now relate these features to the rapid shifting of the two standing-wave WGM resonances back-and-forth through the pump laser.

In Fig. 6.5(b-c) we show the corresponding simulated temporal behavior of the internal optical cavity energy, Si microdisk temperature, free-carrier population, free-carrier dispersion, and thermal dispersion. From these model parameters a clearer picture is revealed of how the oscillations of the transmitted optical power occur, and what the identifiable features of the transmission oscillations correspond to. We have isolated four distinct regions labeled (i)–(iv) in Fig. 6.5: (i) With the microdisk standing-wave WGM resonances initially slightly red detuned

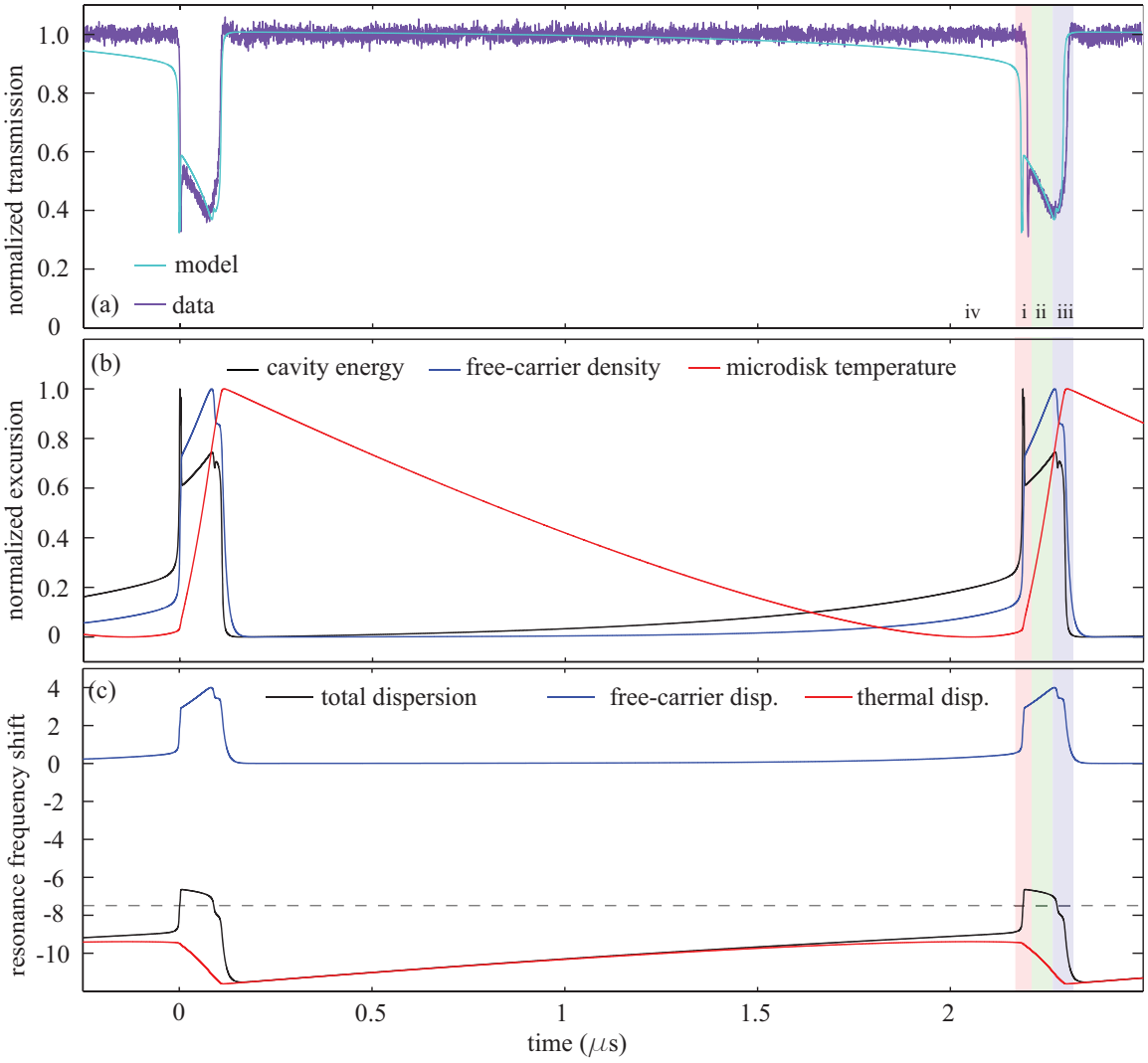

Figure 6.5: Comparison between model and measurement. The shaded regions (i), (ii), (iii), and (iv) correspond to different phases of the dynamics as described in the text. (a) Compares the modeled and measured time-dependent normalized transmission. (b) Depicts the normalized excursion of the cavity energy, free-carrier density, and differential microdisk temperature as modeled. The normalization for a function $f(t)$ is calculated as $\frac{f(t)-\min(f(t))}{\text{range}(f(t))}$. The differential temperature covers the range ΔT =1.9–2.4 K, the free-carrier density covers the range $N = 1\times10^{14}$–$0.9\times10^{17}\text{cm}^{-3}$, and the cavity energy ranges from U = 0.8–29 fJ (c) Resonance frequency shift (in units of γ_β), broken into thermal and free-carrier contributions. The dashed line indicates the pump wavelength.

of the pump laser there occurs a transient rapid generation of free carriers due to TPA which causes the WGMs to rapidly blue shift past the pump laser wavelength; (ii) The heat generation from FCA eventually stops the rapid blue-shift and there begins a slow red-shift of the WGM resonances towards the laser pump and a large build-up of free carriers and thermal energy within the microdisk; (iii) Eventually the WGM resonances red-shift into and through the laser pump, at which time there is a rapid reduction in the internal optical energy and free carrier population (both of which decay much faster than the thermal energy); And this results finally in (iv), a large residual red-shift of the WGM resonances and thermal energy (phonon population) within the microdisk that slowly decays through the SiO_2 pedestal and into the Si substrate. After the microdisk has cooled off and the WGM resonances are only slightly red-detuned from pump laser, the cycle repeats.

A zoomed-in detail of Fig. 6.5 is shown in Fig. 6.6.

From the above description it is apparent that the oscillations are initiated by a transient blue-shift of the microdisk WGM resonances due to free carriers. Eqns. 6.37, 6.29, and 6.27 show that the rapid generation rate of free carriers due to TPA results in a proportional rapid rate of WGM blue-shift, whereas the rate of WGM red-shift due to FCA heating is only proportional to $\overline{N(t)}$ (not $\overline{\dot{N}(t)}$) and is thus delayed relative to the FCD blue-shift. If the mode volume of the microresonator is small enough, the input optical power large enough, and the optical resonance linewidth narrow enough, then the transient

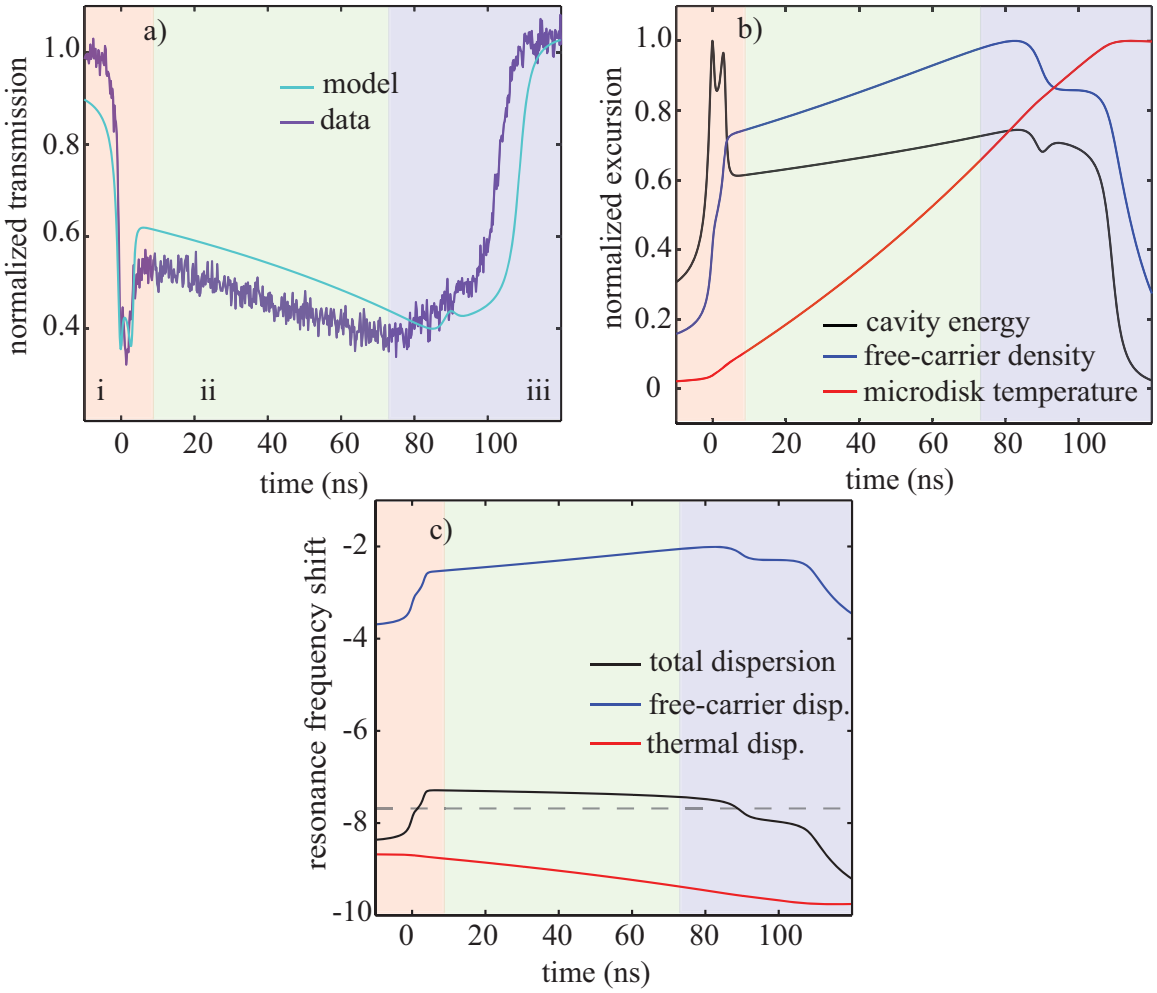

Figure 6.6: Zoomed-in comparison between model and measurement. The shaded regions (i), (ii), and (iii) correspond to different phases of the dynamics as described in the text and shown in Fig. 6.5. (a) Depicts the modeled and measured time-dependent normalized transmission. (b) Depicts the normalized excursion of the cavity energy, free-carrier density, and differential microdisk temperature as modeled. The normalization for a function $f(t)$ is calculated as $\frac{f(t)-\min(f(t))}{\text{range}(f(t))}$. The differential temperature covers the range ΔT =1.9–2.4 K, the free-carrier density covers the range $N = 1\times10^{14}$– 0.9×10^{17} cm^{-3}, and the cavity energy ranges from U =0.8–29 fJ (c) Resonance frequency shift (in units of γ_β), broken into thermal and free-carrier contributions. The dashed line indicates the pump wavelength.

FCD blue-shift can be large enough to sweep the optical resonance through the pump laser wavelength. For geometries and materials in which the thermal resistance of the microresonator is large, then this initial blue-shift will be transient and the thermal red-shift of the optical resonance will eventually dominate, resulting in oscillations of the sort observed in the Si microdisk structures studied here.

Numerical experiments indicate that the system trajectory is a limit-cycle; for a given input wavelength displaying the self-induced oscillations, perturbations of the temperature or free-carrier density from the stable trajectory decay back to the stable trajectory, a characteristic of a limit cycle [122]. Neither the experimental measurements nor the numerical model showed hysteresis in the threshold pump laser wavelength for the onset of oscillations, which is indicative of a super-critical as opposed to sub-critical Hopf-bifurcation [122, 123]. In the language of nonlinear systems theory, as the pump laser wavelength is tuned into resonance from the blue-side of the microdisk WGMs, a super-critical Hopf-bifurcation results and a stable limit cycle ensues, though further examination might be worthwhile.

6.2.1.3 Summary and conclusions

In this work we have presented observations of thermo-optical bistability in a high-Q SOI microdisk resonator with input powers as low as 35 μW. For slightly higher input powers of 60 μW self-induced oscillations in the transnmitted optical power of MHz frequencies and pulse widths

of $\sim$ 100 ns are observed. A time-domain model relating the temperature of the microdisk, the free-carrier density in the microdisk, the optical energy stored in the microdisk, and the WGM resonance wavelength was developed and applied to explain the observations. Good agreement was found between the proposed model and observation. An effective free-carrier lifetime of $\sim$ 10 ns is inferred from the model, a value consistent with those reported in similar SOI microphotonic structures [19, 99].

Significant interest in using Si microresonators for optical modulation [11, 124], all-optical switching [4, 19, 116–118], and optical memory elements [14] suggests that microphotonic resonators will find many applications in future devices. The work presented here, however, illustrates that high-Q microphotonic resonators can be very strongly impacted by optically induced variations in temperature and carrier density. While there may be novel applications for the self-oscillation phenomenon presented here, it is most important as an example of the possible ramifications of using scaled, high-Q devices: decreased optical thresholds for nonlinear processes and the rapid timescales involved may become critically important to device performance. These nonlinearities and their interactions may in some cases necessitate the implementation of dynamic control of the nonlinear system, for example by the active control of carriers in the optical device [3, 7, 118]. Such effects will only become more critical in yet smaller, higher-quality devices, such as the recently demonstrated Si photonic crystal resonators

with $Q \sim 1{\times}10^6$ and $V_{\text{eff}} \sim 1.5\ (\lambda/n)^3$ [125].

Table 6.1: Parameters used in the Si microdisk model

Parameter	Value	Units	Source
n_{Si}	3.485	-	[126]
dn_{Si}/dT	1.86×10^{-4}	K^{-1}	[113, 127]
dn_{Si}/dN	-1.73×10^{-27}	m^3	[59]
β_{Si}	8.4×10^{-12}	$\text{m}{\cdot}\text{W}^{-1}$	[128]
σ_{Si}	9.86×10^{-22}	m^2	[100]
V_{TPA}	46	$(\lambda_0/n_{\text{Si}})^3$	FEM
V_{FCA}	39.9	$(\lambda_0/n_{\text{Si}})^3$	FEM
Γ_{TPA}	0.99	-	FEM
Γ_{FCA}	0.99	-	FEM
ρ_{Si}	2.33	$\text{g}{\cdot}\text{cm}^{-3}$	[49]
$c_{p,Si}$	0.7	$\text{J}{\cdot}\text{g}^{-1}{\cdot}\text{K}^{-1}$	[49]
Γ_{disk}	0.99	-	FEM
$\gamma_{c,o}$	4.1	GHz	low-power meas.
$\gamma_{s,o}$	5.8	GHz	low-power meas.
$\gamma_{\text{c/s,lin}}$	0.86	GHz	low-power meas.
γ_β	14.3	GHz	low-power meas.
κ	1.5	$\text{GHz}^{1/2}$	low-power meas.
λ_o	1453.98	nm	low-power meas.
$\lvert s\rvert^2$	480	μW	measured
λ_p	1454.12	nm	model result
γ'_{fc}	0.98	GHz	fit
γ_{th}	0.15	MHz	fit

6.2.2 A reduced steady-state model of the self-oscillating system

In the previous section, a model of the system, including the dominant physical effects, is developed. We found good agreement between the

model, which consists of a set of coupled nonlinear ODEs for a pair of optical resonances, the free-carrier population of the disk, disk temperature, and experiment. However, the investigation in the previous section is limited to direct numerical integration of the relevant EOM for that particular device geometry and its characteristics. It is of interest to consider similar systems in other geometries, e.g., photonic crystal resonators [19, 125], quasi-planar microring resonators [112], etc. In order to do this (both analytically and numerically), we shall consider a simplified form of the EOM for a range of Q and V_{eff} corresponding to these different device classes, and retain the effective thermal and free-carrier lifetimes as parameters. In the next section, the simplified model will be presented.

6.2.3 Reduced model

Here, we consider only a single mode cavity, to reduce the complexity of the model. We write the complex mode field amplitude, a, as:

$$a = u + iv. \tag{6.38}$$

The detuning between the input light frequency and the bare frequency of the resonant mode is set equal to:

$$\delta\omega_0 = \omega - \omega_0, \tag{6.39}$$

where ω is the input frequency and ω_0 is the bare frequency of the

resonant mode. Initially, we will be interested in the behavior of this system as a function of the frequency of input light, while varying the cavity's quality factor Q and mode volume V_{eff}, to understand the potential benefits (and drawbacks) of exploring nonlinear optics within different geometries (such as microdisks of various sizes, or wavelength-scale photonic crystal cavities). Experimentally realizable values for Q in silicon microdisks have recently reached 5×10^6, while mode volumes of around $(\lambda/n_{\text{Si}})^3$ have been achieved in other geometries, such as planar photonic crystals. The range of Q and V_{eff} to be investigated are thus $[10^3, 10^7]$ and $[1, 1000](\lambda/n_{\text{Si}})^3$, respectively.

To make our intent to investigate system behavior as a function of Q and V_{eff} explicit, we isolate only the parameters we wish to change, setting all others equal to constants that we label A_j, to get:

$$\frac{du}{dt} = -\delta\omega_0 v - A_1\Delta T v - A_2 N v - \gamma_{a,o} u - \frac{A_3(u^2+v^2)u}{V_{\text{eff}}} - A_4 N u \tag{6.40}$$

$$\frac{dv}{dt} = \delta\omega_0 u + A_1\Delta T u + A_2 N u - \gamma_{a,o} v - \frac{A_3(u^2+v^2)v}{V_{\text{eff}}} - A_4 N v - A_5\sqrt{\gamma_{a,0}} \tag{6.41}$$

$$\frac{dN}{dt} = -A_6 N + \frac{A_7(u^2+v^2)^2}{V_{eff}^2} \tag{6.42}$$

$$\frac{d\Delta T}{dt} = -A_8\Delta T + \frac{A_9\gamma_{a,o}(u^2+v^2)}{V_{\text{eff}}} + 2\frac{A_3A_9(u^2+v^2)^2}{V_{\text{eff}}^2} + 2\frac{A_4A_9N(u^2+v^2)}{V_{\text{eff}}^2}. \tag{6.43}$$

The constants A_j are listed in Table 6.2 in terms of the original physical parameters used in the model described in Section 6.2.4 [3]. Note that the important physical parameters $P_{\rm in}$ (the input power), $\gamma'_{\rm fc}$ (the free-carrier decay rate), and $\gamma_{\rm th}$ (the microdisk temperature decay rate) are just given by A_5^2, A_6, and A_8, respectively, so that investigation of system behavior as a function of these important physical parameters can follow in an analogous fashion. For the time being, these parameters have been fixed at the values listed in the table.

Eqns. 6.40-6.43 are a set of four coupled equations in the $\{u, v, N, \Delta T\}$ system. We can make a transformation on our amplitudes u, and v, that should give us physically sensible equations of motion. We have for the energy in the mode, W, the following:

$$W = u^2 + v^2 = |a|^2 = r^2. \tag{6.44}$$

We can write a differential equation for the evolution of the mode amplitude, r:

$$2r\frac{dr}{dt} = u\frac{du}{dt} + v\frac{dv}{dt}, \tag{6.45}$$

which upon substitution becomes

$$\frac{dr}{dt} = -\frac{\gamma_{a,o}}{2}r - \frac{A_3}{2V_{\rm eff}}r^3 - \frac{A_4 N}{2}r - A_5\sqrt{\gamma_{\rm a,o}}\frac{v}{r}. \tag{6.46}$$

[3] Certain relationships between parameters, such as that between $\{V_{\rm TPA}, V_{\rm FCA}, V_{\rm disk}\}$ and $V_{\rm eff}$, are specific to the microdisk geometry we have studied, and may need to be modified for other geometries, such as planar photonic crystals

Table 6.2: Composite coefficients in the reduced model (A_j)

Parameter	Value	Units
A_1	$\omega_0 \frac{1}{n_{\mathrm{Si}}} \frac{dn_{\mathrm{Si}}}{dT}$	$\mathrm{rad{\cdot}K^{-1}}$
A_2	$\omega_0 \frac{1}{n_{\mathrm{Si}}} \frac{dn_{\mathrm{Si}}}{dN}$	$\mathrm{rad{\cdot}m^{-3}}$
A_3	$\frac{\beta_{\mathrm{Si}} c^2}{2n_{\mathrm{Si}}^2}$	$\mathrm{m^3{\cdot}W^{-1}s^{-2}}$
A_4	$\frac{\sigma_{\mathrm{Si}} c}{2n_{\mathrm{Si}}}$	$\mathrm{m^3{\cdot}s^{-1}}$
A_5	$\sqrt{P_{\mathrm{in}}}$	$\mathrm{W^{1/2}}$
A_6	γ'_{FC}	$\mathrm{s^{-1}}$
A_7	$\frac{\beta_{\mathrm{Si}} c^2}{2n_{\mathrm{Si}}^2 \hbar\omega_p}$	$\mathrm{m^3{\cdot}J^{-2}{\cdot}s^{-1}}$
A_8	γ_{Th}	$\mathrm{s^{-1}}$
A_9	$\frac{1}{\rho_{\mathrm{Si}} c_{\mathrm{p,Si}}}$	$\mathrm{m^3{\cdot}K{\cdot}J^{-1}}$
c	3×10^8	$\mathrm{m{\cdot}s^{-1}}$
$\hbar$	1.05×10^{-34}	J·s
n_{Si}	3.485	-
dn_{Si}/dT	1.86×10^{-4}	$\mathrm{K^{-1}}$
dn_{Si}/dN	-1.73×10^{-27}	$\mathrm{m^3}$
β_{Si}	8.4×10^{-12}	$\mathrm{m{\cdot}W^{-1}}$
σ_{Si}	1×10^{-21}	$\mathrm{m^2}$
V_{TPA}	$2 \times V_{\mathrm{eff}}$	$(\lambda_0/n_{\mathrm{Si}})^3$
V_{FCA}	$2 \times V_{\mathrm{eff}}$	$(\lambda_0/n_{\mathrm{Si}})^3$
V_{disk}	$10 \times V_{\mathrm{eff}}$	$\mathrm{m^3}$
Γ_{TPA}	1	-
Γ_{FCA}	1	-
ρ_{Si}	2330	$\mathrm{kg{\cdot}m^{-3}}$
$c_{p,Si}$	700	$\mathrm{J{\cdot}kg^{-1}{\cdot}K^{-1}}$
Γ_{disk}	1	-
λ_o	1.5×10^{-6}	m
P_{in}	1×10^{-3}	W
γ'_{fc}	100	MHz
γ_{th}	0.2	MHz

Consider also the phase between the u and v, given by $\phi = \text{ArcTan}(v/u)$. We can similarly write an ODE for the evolution of the phase:

$$r^2 \frac{d\phi}{dt} = u\frac{dv}{dt} - v\frac{du}{dt}. \tag{6.47}$$

Substituting in the appropriate quantities we then have

$$\frac{d\phi}{dt} = \delta\omega_o + A_1\Delta T + A_2 N - A_5\sqrt{\gamma_{\text{a,o}}}\frac{u}{r^2}. \tag{6.48}$$

If we follow through with the trigonometric substitution, these equations become

$$\frac{dr}{dt} = -\frac{\gamma_{a,o}}{2}r - \frac{A_3}{2V_{\text{eff}}}r^3 - \frac{A_4 N}{2}r - A_5\sqrt{\gamma_{\text{a,o}}}\sin\phi \tag{6.49}$$

$$\frac{d\phi}{dt} = \delta\omega_o + A_1\Delta T + A_2 N - A_5\sqrt{\gamma_{\text{a,o}}}\frac{\cos\phi}{r}. \tag{6.50}$$

Thus we have in the recast form, the following equations of motion:

$$\frac{dr}{dt} = -\frac{\gamma_{a,o}}{2}r - \frac{A_3}{2V_{\text{eff}}}r^3 - \frac{A_4 N}{2}r - A_5\sqrt{\gamma_{\text{a,o}}}\sin\phi \tag{6.51}$$

$$\frac{d\phi}{dt} = \delta\omega_o + A_1\Delta T + A_2 N - A_5\sqrt{\gamma_{\text{a,o}}}\frac{\cos\phi}{r} \tag{6.52}$$

$$\frac{dN}{dt} = -A_6 N + \frac{A_7}{V_{eff}^2}r^4 \tag{6.53}$$

$$\frac{d\Delta T}{dt} = -A_8\Delta T + \frac{A_9\gamma_{a,o}}{V_{\text{eff}}}r^2 + 2\frac{A_3 A_9}{V_{\text{eff}}^2}r^4 + 2\frac{A_4 A_9 N}{V_{\text{eff}}^2}r^2. \tag{6.54}$$

In these equations, we have assumed critical coupling and a single res-

onant optical mode. In addition, for the purposes of calculating A_7, we have assumed that $\lambda_p = \lambda_0$. Eqns.6.51-6.54 above are the starting point for the investigations presented in the rest of this paper. Applying the same numerical integration methods presented in the section above, we find that the reduced model reproduces similar behaviors to the full model. Fig. 6.7(a) depicts transmission oscillations from the reduced model parameters consistent with those deduced above, while (b) shows the period, width, and duty cycle behavior qualitatively similar to that in Fig. 6.3(b).

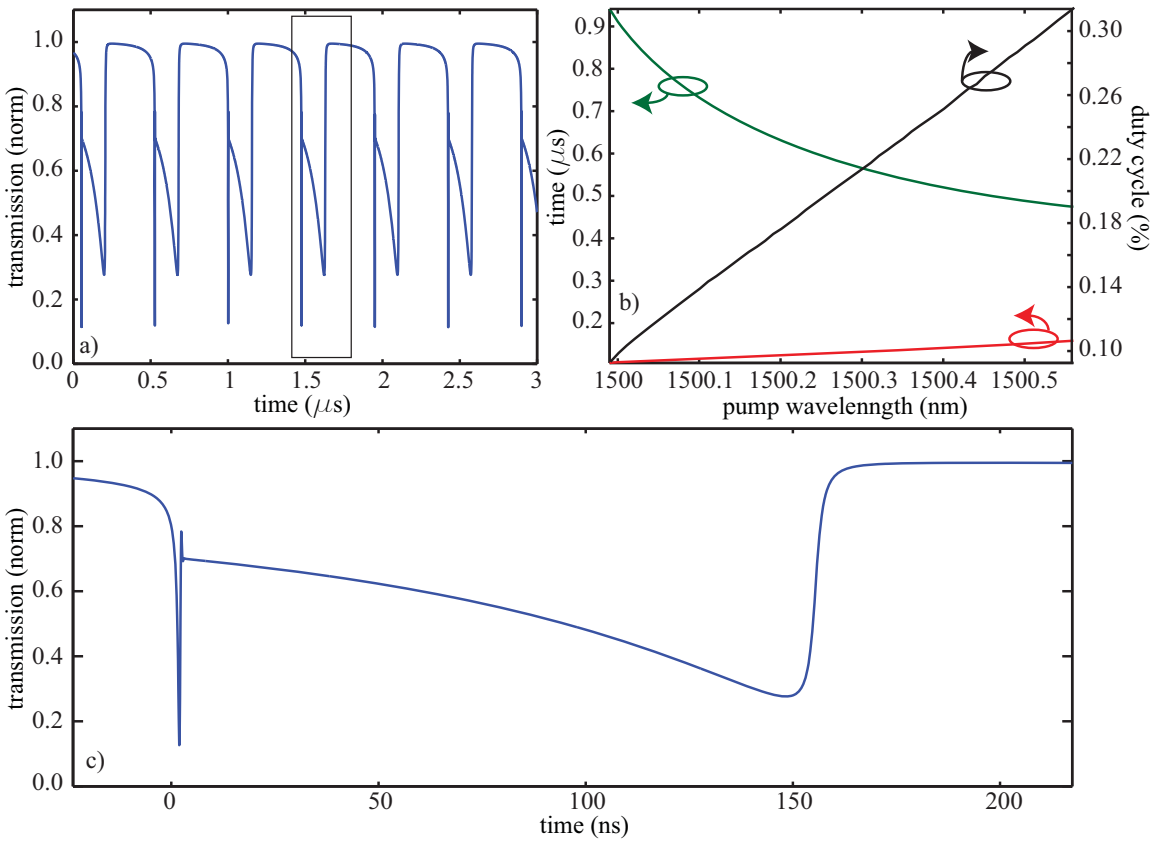

Figure 6.7: Time-domain oscillations from the reduced model. Qualitatively very similar to the behavior in the previous section. (a) Transmission oscillations. (b) Period, width, and duty cycle behavior, again qualitatively similar to the results above. (c) Detail of transmission behavior in (a)

We can also see an interesting picture of the state variables evolving from a variety of initial conditions (different temperatures and carrier densities) to a common trajectory. The shape of the orbit depends on the detuning wavelength.

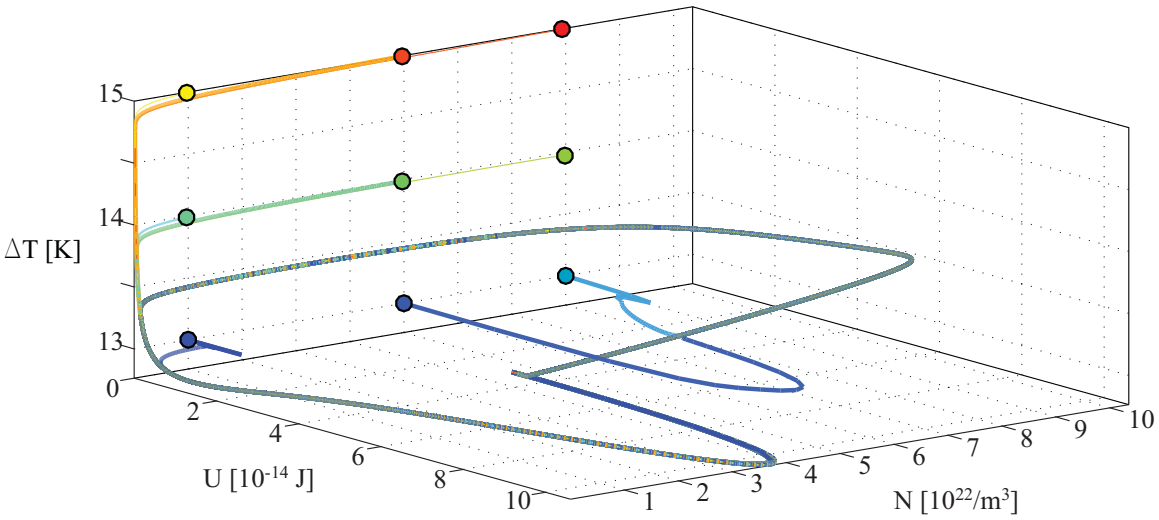

Figure 6.8: Time-domain oscillations from the reduced model, depicted as state variable trajectories. The solid markers edged in black indicate the initial conditions. Note the rapid evolution to a common trajectory. For each detuning, there is some similar trajectory.

6.2.3.1 Model development

The equilibrium points [129] are found by studying the equations of motion in steady-state (all time derivatives are set to zero). Solving first for the steady state carrier density N_{ss} and temperature change ΔT_{ss}, we have:

$$\begin{aligned} N_{ss} &= \frac{A_7}{A_6 V_{eff}^2} r^4 \\ \Delta T_{ss} &= \frac{1}{A_8}\left(\frac{A_9 \gamma_{a,o}}{V_{eff}} r^2 + 2\frac{A_3 A_9}{V_{eff}^2} r^4 + 2\frac{A_4 A_7 A_9}{A_6 V_{eff}^3} r^6\right). \end{aligned} \tag{6.55}$$

These values are then used in the steady-state version of the equations for dr/dt and $d\phi/dt$, to yield:

$$\sin(\phi_{\rm ss}) = \frac{-1}{A_5\sqrt{\gamma_{\rm a,o}}}\left(\gamma_{\rm a,o}r + \frac{A_3}{V_{\rm eff}}r^3 + \frac{A_4A_7}{A_6V_{\rm eff}^2}r^5\right) \tag{6.56}$$

$$\cos(\phi_{\rm ss}) = \frac{r}{A_5\sqrt{\gamma_{\rm a,o}}}\left(\delta\omega_o + \frac{A_1A_9r^2}{A_8V_{\rm eff}}\left(\gamma_{\rm a,o} + \frac{2A_3}{V_{\rm eff}}r^2 + \frac{2A_4A_7}{A_6V_{\rm eff}^2}r^4\right) + \frac{A_2A_7}{A_6V_{\rm eff}^2}r^4\right). \tag{6.57}$$

One method to solve for the equilibrium values of r is to note that $\sin^2(\phi_{\rm ss})+\cos^2(\phi_{\rm ss})=1$, which yields a polynomial equation that is to the $14^{\rm th}$ order in r (all powers are even though, so that it is a $7^{\rm th}$ order equation in r^2). For specific values of Q and $V_{\rm eff}$, this equation is also a function of $\delta\omega_o$, so that $r_{\rm ss}$ as a function of $\delta\omega_o$ is obtained by repeated solution of this polynomial equation for different values of $\delta\omega_o$.

A relatively easy way to compute $r_{\rm ss}$ as a function of $\delta\omega_o$ is to consider $\delta\omega_o$ to be the independent variable, and solve for it in terms of $r_{\rm ss}$. The advantage to this approach is that the equation to be solved is quadratic in $\delta\omega_o$, so that obtaining the solutions in terms of $r_{\rm ss}$ is relatively simple. In particular, the following characteristic equation (determined from $\sin^2(\phi_{\rm ss})+\cos^2(\phi_{\rm ss})=1$) is considered:

$$\delta\omega_o^2 + 2\delta\omega_o B(r_{\rm ss}) + C(r_{\rm ss}) = 0 \tag{6.58}$$

where

$$B(r_{\rm ss}) = 2\left[\frac{A_1 A_9 r_{\rm ss}^2}{A_8 V_{\rm eff}}\left(\gamma_{\rm a,o} + \frac{2A_3 r_{\rm ss}^2}{V_{\rm eff}} + \frac{2A_4 A_7 r_{\rm ss}^4}{A_6 V_{\rm eff}^2}\right) + \frac{A_2 A_7 r_{\rm ss}^4}{A_6 V_{\rm eff}^2}\right]$$
$$C(r_{\rm ss}) = \left[\frac{A_1 A_9 r_{\rm ss}^2}{A_8 V_{\rm eff}}\left(\gamma_{\rm a,o} + \frac{2A_3 r_{\rm ss}^2}{V_{\rm eff}} + \frac{2A_4 A_7 r_{\rm ss}^4}{A_6 V_{\rm eff}^2}\right) + \frac{A_2 A_7 r_{\rm ss}^4}{A_6 V_{\rm eff}^2}\right]^2 \qquad (6.59)$$
$$+ \left(\gamma_{\rm a,o} + \frac{A_3 r_{\rm ss}^2}{V_{\rm eff}} + \frac{A_4 A_7 r_{\rm ss}^4}{A_6 V_{\rm eff}^2}\right)^2 - \frac{A_5^2 \gamma_{\rm a,o}}{r_{\rm ss}^2}.$$

The roots of Eqn. 6.58 are then simply

$$\delta\omega_o^+ = -\frac{1}{2}B(r_{\rm ss}) + \frac{1}{2}\sqrt{B(r_{\rm ss})^2 - 4C(r_{\rm ss})} \qquad (6.60)$$
$$\delta\omega_o^- = -\frac{1}{2}B(r_{\rm ss}) - \frac{1}{2}\sqrt{B(r_{\rm ss})^2 - 4C(r_{\rm ss})}. \qquad (6.61)$$

Of course, $r_{\rm ss}$ is not arbitrary, and must be limited to some range. From its definition in Eqn. 6.44, $r_{\rm ss} \geq 0$ (physically, this makes sense as $r_{\rm ss}$ represents the amplitude of the field, normalized so that $r_{\rm ss}^2$ is the cavity energy). A maximum bound for $r_{\rm ss}$ can be found by examining Eqn. 6.56. The right-hand side of this equation is a monotonically decreasing function, so that $r_{\rm ss}$ is at a maximum when the left-hand side is at a minimum, that is, when $\sin(\phi_{\rm ss}) = -1$. The resulting equation:

$$\frac{A_4 A_7}{A_6 V_{\rm eff}^2} r_{\rm max,ss}^5 + \frac{A_3}{V_{\rm eff}} r_{\rm max,ss}^3 + \gamma_{\rm a,o} r_{\rm max,ss} - A_5\sqrt{\gamma_{\rm a,o}} = 0. \qquad (6.62)$$

This equation has one positive real root (as can be proved by Descartes' rule of signs theorem), which corresponds to the desired value of $r_{\mathrm{max,ss}}$. From this equation, bistability curves such as that shown in Figs. 6.13 and 6.9 can be generated and examined.

6.2.3.2 Numerical results

A plot of r_{ss} as a function of $\delta\omega_o/\gamma_{\mathrm{a,o}}$ is shown in Fig. 6.9(a), where the different colors represent the solutions $\delta\omega_o^+$ (blue) and $\delta\omega_o^-$ (red). Here, we have taken $Q = 3{\times}10^5$ and $V_{\mathrm{eff}} \sim 50(\lambda/n_{\mathrm{Si}})^3$, with the rest of the parameters given in Table 6.2.

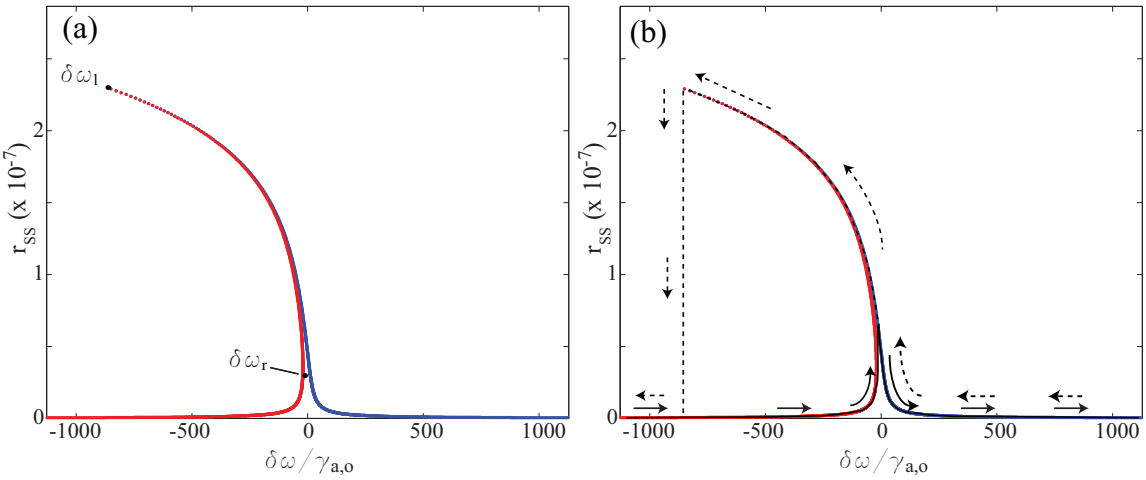

Figure 6.9: (a) Equilibrium cavity field amplitude r_{ss} as a function of the normalized detuning of the input light $\delta\omega_o/\gamma_{\mathrm{a,o}}$. The blue and red parts of the curve correspond to the solutions $\delta\omega_o^+$ and $\delta\omega_o^-$. $\delta\omega_l$ and $\delta\omega_r$ are bifurcation points at which the number of equilibrium points changes. (b) Same as (a), with the hysteresis loop traced out (the lower part follows the solid line, the upper part follows the dashed line). $Q = 3\times10^5$, $V_{\mathrm{eff}} = 50(\lambda/n_{\mathrm{Si}})^3$, and P_{in}=1 mW

From this plot, we clearly see the presence of two bifurcation points. At large negative detuning values, there is only equilibrium solution for r. At some critical detuning value $\delta\omega_l$, this changes and two additional

solutions are picked up, so that there are now three. This persists until a second bifurcation point $\delta\omega_r$, where two of the three equilibrium points disappear, leaving a single solution for all detunings above $\delta\omega_r$.

Physically, this type of behavior is what you would expect for this system, as nonlinear absorption and dispersion cause the cavity's resonance wavelength to shift as power is coupled into it. In an experiment, one would expect to observe hysteresis in the cavity's response as a function of driving frequency, where scanning from low frequency to high frequency causes the system to follow the lower branch shown in Fig. 6.9(b), and scanning in the reverse direction causes the system to follow the upper branch.

The position of the bifurcation points and the width of the hysteresis window are important quantities to characterize the behavior of the system. In particular, in Fig. 6.10, we plot r_{ss} as a function of $\delta\omega_o/\gamma_{\mathrm{a,o}}$ for additional choices of Q and V_{eff}, and we see the significant influence that these parameters have. For more quantitative studies, being able to directly obtain values of $\delta\omega_l$ and $\delta\omega_r$ as a function of Q and V_{eff} would be quite useful (rather than just pulling them off a graph), even if this can only be done numerically.

Let us first consider the point $\delta\omega_l$. This occurs at the point of maximum cavity energy $r_{\mathrm{max,ss}}$, where $\sin(\phi)$=-1. Plugging this into the equation $\cos(\phi) = 0$, we have the following:

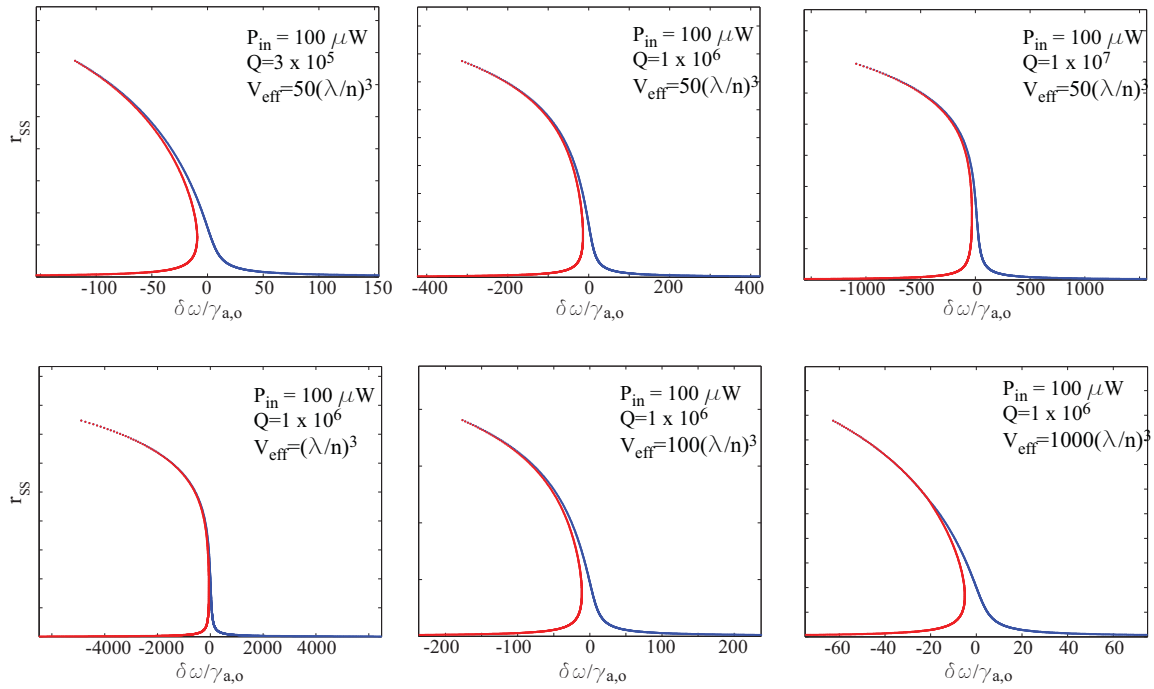

Figure 6.10: Equilibrium cavity field amplitude $r_{\rm ss}$ as a function of the normalized detuning of the input light $\delta\omega_o/\gamma_{\rm a,o}$, for differing values of Q and $V_{\rm eff}$ and with a fixed input power $P_{\rm in} = 100$ μW. In the top row, $V_{\rm eff}$ is held fixed and Q is varied. In the bottom row, Q is held fixed and $V_{\rm eff}$ is varied.

$$\delta\omega_l = -\frac{A_1 A_9}{A_8 V_{\text{eff}}} r_{\text{max,ss}} \left(2A_5 \sqrt{\gamma_{\text{a,o}}} - r_{\text{max,ss}} \gamma_{\text{a,o}} \right) + \frac{A_2 A_7}{A_6 V_{\text{eff}}^2} r_{\text{max,ss}}^4 \quad (6.63)$$

The rightmost critical point $\delta\omega_r$ is found by noting that it is the maximum value of the function $\delta\omega_o^-(r_{\text{ss}})$ (the red branch of the bistability curves in Figs. 6.9 and 6.10). From Eqn. 6.61, we then have:

$$\frac{d\delta\omega^-}{dr} = 0 = \frac{dB(r)}{dr}\sqrt{B(r)^2 - 4C(r)} + \frac{dB(r)}{dr}B(r) - 2\frac{dC(r)}{dr} \quad (6.64)$$

This yields an equation that can be numerically solved to obtain a value of r, from which $\delta\omega_r$ can be calculated through Eqn 6.61.

6.2.3.3 Linear stability analysis

In this section, we linearize the system dynamics about the equilibrium (steady-state) values. That is, we write:

$$\frac{d}{dt}\begin{pmatrix} \delta r \\ \delta\phi \\ \delta N \\ \delta\Delta T \end{pmatrix} = J_{\text{ss}} \begin{pmatrix} \delta r \\ \delta\phi \\ \delta N \\ \delta\Delta T \end{pmatrix} \quad (6.65)$$

.

where J_{ss} is the Jacobian matrix. Writing Eqns. 6.51–6.54 as

$$\begin{aligned}
\frac{dr}{dt} &= f(r,\phi,N,\Delta T) \\
\frac{d\phi}{dt} &= g(r,\phi,N,\Delta T) \\
\frac{dN}{dt} &= h(r,\phi,N,\Delta T) \\
\frac{d\Delta T}{dt} &= k(r,\phi,N,\Delta T),
\end{aligned} \tag{6.66}$$

$J_{\rm ss}$ is given by:

$$J_{\rm ss} = \begin{pmatrix} \frac{df}{dr} & \frac{df}{d\phi} & \frac{df}{dN} & \frac{df}{d\Delta T} \\ \frac{dg}{dr} & \frac{dg}{d\phi} & \frac{dg}{dN} & \frac{dg}{d\Delta T} \\ \frac{dh}{dr} & \frac{dh}{d\phi} & \frac{dh}{dN} & \frac{dh}{d\Delta T} \\ \frac{dk}{dr} & \frac{dk}{d\phi} & \frac{dk}{dN} & \frac{dk}{d\Delta T} \end{pmatrix}_{\rm ss} \tag{6.67}$$

where the subscript 'ss' indicates that the matrix is to be evaluated at the equilibrium points. Calculating the derivatives of the equations of motion, we have:

$$J_{\rm ss} = \begin{pmatrix} -\gamma_{\rm a,o} - \frac{3A_3}{V_{\rm eff}} r_{\rm ss}^2 - A_4 N_{\rm ss} & -A_5\sqrt{\gamma_{\rm a,o}}\cos\phi_{\rm ss} & -A_4 r_{\rm ss} & 0 \\ A_5\sqrt{\gamma_{\rm a,o}}\frac{\cos\phi_{\rm ss}}{r_{\rm ss}^2} & A_5\sqrt{\gamma_{\rm a,o}}\frac{\sin\phi_{\rm ss}}{r_{\rm ss}} & A_2 & A_1 \\ 4\frac{A_7}{V_{\rm eff}^3} r_{\rm ss}^3 & 0 & -A_6 & 0 \\ 2\frac{A_9\gamma_{\rm a,o}}{V_{\rm eff}} r_{\rm ss} + 8\frac{A_3 A_9}{V_{\rm eff}^2} r_{\rm ss}^3 + 4\frac{A_4 A_9}{V_{\rm eff}} N_{\rm ss} r_{\rm ss} & 0 & 2\frac{A_4 A_9}{V_{\rm eff}} r_{\rm ss}^2 & -A_8 \end{pmatrix} \tag{6.68}$$

.

$J_{\rm ss}$ is evaluated at the equilibrium points, as determined numerically using the procedure outlined in the previous section.

Stability is assessed by calculating the eigenvalues (labeled λ_i) of the matrix (four in total), and examining the sign of the real part of these eigenvalues (stability requires all four eigenvalues to have a negative real part). In regions where $r_{\rm ss}$ is multi-valued, eigenvalues for each branch of the $r_{\rm ss}$-$\delta\omega$ are calculated[4]

The results for the example considered in Fig. 6.11 are shown in Fig. 6.11. For large negative detunings ($\delta\omega < \delta\omega_l$), the single branch of the curve is stable. In the region of three equilibrium values ($\delta\omega_l < \delta\omega < \delta\omega_r$), the lowest curve remains stable, while the middle curve is unstable, and the upper curve shows regions of stability and instability. Finally, the system is stable after it returns to a single equilibrium value ($\delta\omega > \delta\omega_r$).

The behavior of the upper branch in the region of three equilibrium points is particularly interesting. In particular, the numerically determined detuning value for which this branch changes between stable and unstable behavior (labeled $\delta\omega_c$) coincides very closely (to better than 0.1% accuracy) with the detuning value at which oscillatory behavior occurs when studying the dynamical properties of the system through direct integration of the time-dependent equations of motion, indicating a prediction of nontrivial system behavior through an analysis that is significantly less computationally intensive than the numerical inte-

[4]In practice, we find that two of the eigenvalues are independent of $r_{\rm ss}$, while the other two are not.

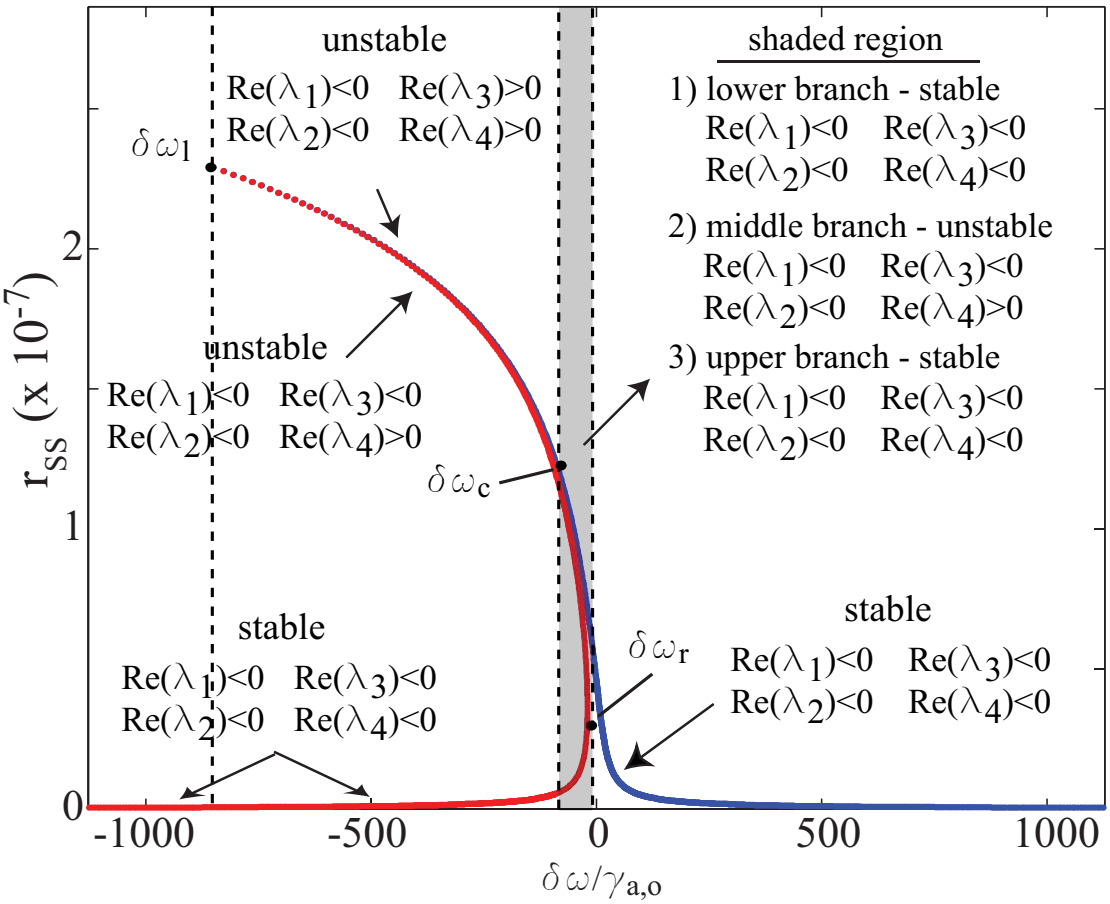

Figure 6.11: Results of the linear stability analysis for the r_{ss}-$\delta\omega$ plot of Fig. 6.9. The stability of each branch of the curve is assessed by examining the eigenvalues of the Jacobian matrix.

gration used elsewhere in this work.

Hysteretic behavior pictured in Fig. 6.9(b) is characteristic of a system response usually classified as a distorted pitchfork bifurcation [130], generally familiar from nonlinear system response (e.g., a softening or stiffening spring). If we simplify the representation of the stability diagrams depicted above, we see that at low powers, the system is consistent with the situation shown in Fig. 6.12. At higher powers, the upper branch becomes unstable for some values of the control parameter (where we understand the control parameter to be the pump wavelength detuning).

The behavior in Fig. 6.12(a) is a supercritical bifurcation of the fixed points, while the behavior in Fig. 6.12(b) has the characteristics of the supercritical fixed-point bifurcation from which a stable-limit cycle is born when the upper branch fixed point loses stability—Hopf bifurcation. Numerical and experimental observations indicate this Hopf bifurcation is supercritical in nature. This change of global characteristics with power regime presents an interesting illustration of the variety of dynamical and steady-state behaviors realizable in the silicon optical microcavity system.

6.2.3.4 Varying input power

From a technological standpoint, examining system behavior as a function of the input power P_{in} is of interest [120]. In particular, for switching applications, studying the change in input power needed to jump

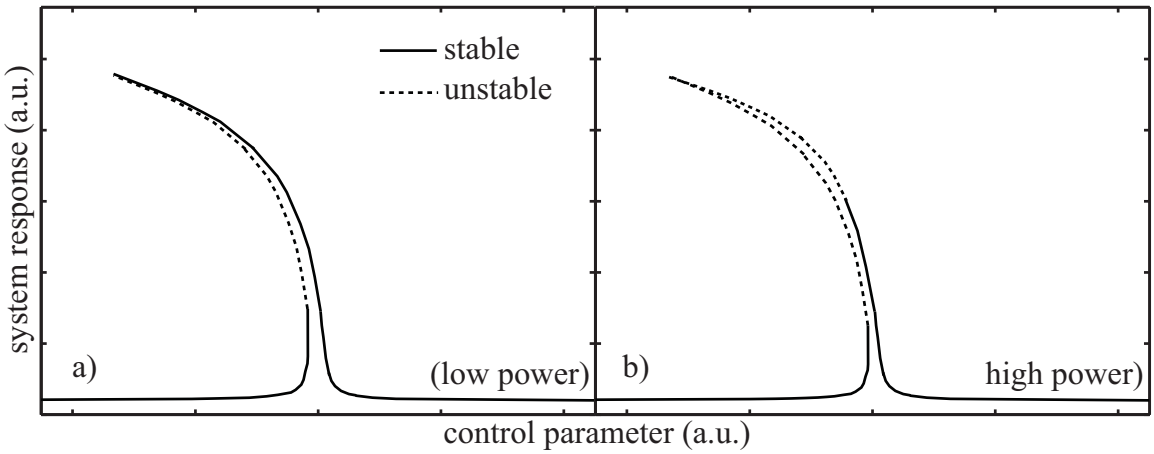

Figure 6.12: Simplified representation of system response versus control parameter (mode-field amplitude versus pump wavelength). (a) System at intermediate powers. (b) System at higher powers

between stable solutions in a bistability curve will be relevant. Similarly, studying the effects of varying parameters such as Q, $V_{\rm eff}$, $\gamma'_{\rm fc}$, and $\gamma_{\rm th}$ on this switching power may give us an indication of what to aim for in future generations of devices.

To do this, we simply re-consider Eqns. 6.58 and 6.59, but now assume that $\delta\omega$ is fixed, and consider $P_{\rm in} = A_5^2$ to be a free variable. We then have the following equation relating $P_{\rm in}$ to $r_{\rm ss}$:

$$P_{\rm in} = \frac{r_{\rm ss}^2}{\gamma_{\rm a,o}}\Bigg\{\delta\omega_o^2 + 2\delta\omega_o\left[\frac{A_1A_9r_{\rm ss}^2}{A_8V_{\rm eff}}\left(\gamma_{\rm a,o} + \frac{2A_3r_{\rm ss}^2}{V_{\rm eff}} + \frac{2A_4A_7r_{\rm ss}^4}{A_6V_{\rm eff}^2}\right) + \frac{A_2A_7r_{\rm ss}^4}{A_6V_{\rm eff}^2}\right] + \left[\frac{A_1A_9r_{\rm ss}^2}{A_8V_{\rm eff}}\left(\gamma_{\rm a,o} + \frac{2A_3r_{\rm ss}^2}{V_{\rm eff}} + \frac{2A_4A_7r_{\rm ss}^4}{A_6V_{\rm eff}^2}\right) + \frac{A_2A_7r_{\rm ss}^4}{A_6V_{\rm eff}^2}\right]^2 + \left(\gamma_{\rm a,o} + \frac{A_3r_{\rm ss}^2}{V_{\rm eff}} + \frac{A_4A_7r_{\rm ss}^4}{A_6V_{\rm eff}^2}\right)^2\Bigg\} \tag{6.69}$$

A plot of $r_{\rm ss}$ versus $P_{\rm in}$ for $Q = 3{\times}10^5$, $V_{\rm eff} = 50(\lambda/n)^3$, and $\delta\omega/\gamma_{\rm a,o} =$

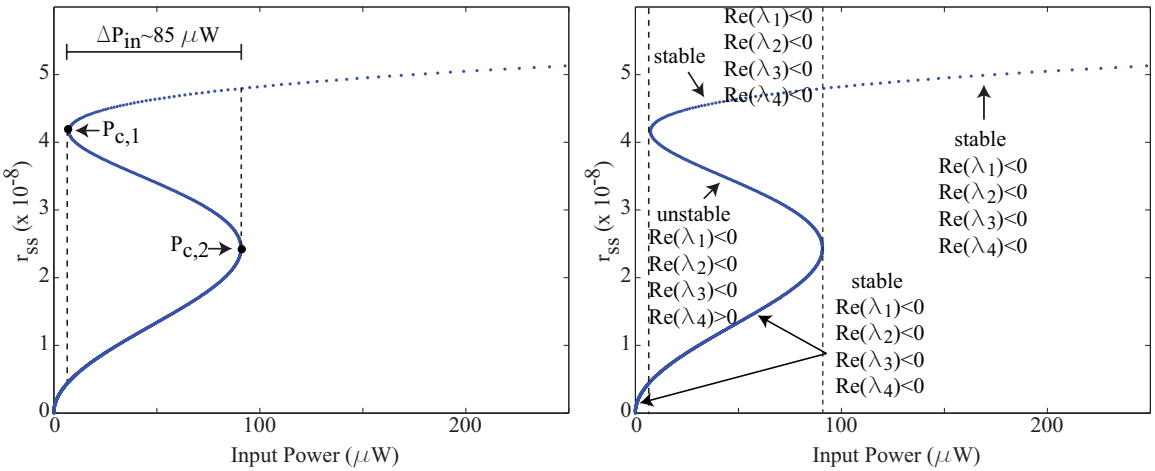

Figure 6.13: (a) Equilibrium cavity field amplitude $r_{\rm ss}$ as a function of the input power $P_{\rm in}$. $P_{\rm c,1}$ and $P_{\rm c,2}$ are bifurcation points at which the number of equilibrium solutions change. (b) Same as (a), with the sign of the eigenvalues of the Jacobian and the corresponding stability assigned. For this simulation, $Q = 3 \times 10^5$, $V_{\rm eff} = 50(\lambda/n_{\rm Si})^3$, and $\delta\omega/\gamma_{\rm a,o}$=-9.

-9 is shown in figure 6.13(a). We see optical bistability as a function of $P_{\rm in}$, with bifurcation points $P_{\rm c,1}$ and $P_{\rm c,2}$ (going from one equilibrium solution to three and back). In Fig. 6.13(b), we note the stability of each of the branches of this bistability curve, as determined through a calculation of the eigenvalues of the Jacobian matrix. We note that switching between the stable lower branch and the stable upper branch can be achieved for changes in input power of around 85 μW for the parameters chosen here.

6.2.4 Future directions

The work presented above can be expanded on in many ways, starting with the equilibrium point analysis. In particular, we can imagine beginning with a systematic investigation of the system's behavior as

a function of Q and V_{eff}, where we consider the internal cavity energy r^2 as a function of both the driving frequency and the input power. Variation of other parameters, such as γ'_{fc} and γ_{th}, may also be considered, particularly if different microcavity geometries (such as planar photonic crystals or non-undercut racetrack resonators) become an object of investigation. A more-thorough understanding of the behavior of the upper branch of the r_{ss}-$\delta\omega$ curve of Fig. 6.11 must also be gained, as it appears to be directly related to the onset of periodic oscillations seen experimentally.

In terms of device design, being able to predict when such behavior will occur, and how to control it, will be very important. One can anticipate that this might be done through design of structures with specific V_{eff} and Q values, which we have reasonably good experimental control of over certain parameter ranges. γ_{th} can also be potentially controlled at some level through design of non-undercut structures, and γ'_{fc} is potentially modifiable as well (in periodic structures, for example), although this requires further investigation. Application of the results of Section 5 offers a strong handle on the free-carrier lifetime as a tuning parameter.

We see in Fig. 6.14 the impact of varying the free carrier lifetime of a resonator similar to those created in Section 5. We find that at both moderate input powers ($P_{in} = 0.5mW$) and higher input powers ($P_{in} = 5mW$), the stability of the shortened lifetime resonator is dramatically improved. In that configuration, steady-state cavity energies

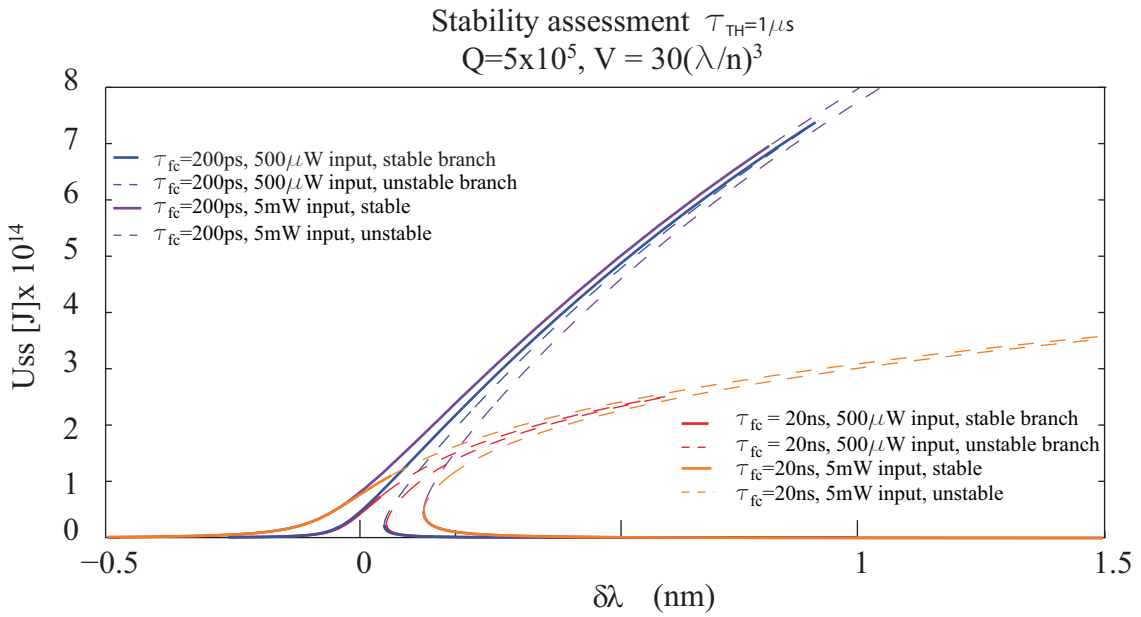

Figure 6.14: Assessment of the stability properties of a representative resonator under free-carrier lifetime modification. We depict the steady-state cavity energy(J [10^{14}]) versus cavity-pump detuning (nm). The blue solid line is the stable branch behavior for τ_{fc} = 200 ps with 500μW input power. The dashed blue is the same for the unstable branch. The red solid line is the stable behavior for τ_{fc} = 20 ns with 500μW input. The purple and orange solid and dashed lines are the corresponding behaviors with 5 mW input power.

can be achieved that are approximately 7 times higher than for the same resonators with longer free-carrier lifetimes.

This dramatic change indicates that the reduction of free-carrier lifetime can also greatly enhance the utility of the silicon microdisk resonator by allowing the system to remain stable even at higher cavity energies—thus accessing CW nonlinear behavior.

6.3 Pulse compression measurement

All of the experiments and measurements considered thus far have focused on configurations where the input pump light, S, was constant in power and wavelength (at least to the extent that changes in the power or wavelength were not crucial to the dynamical or steady state response of the system). However, the nonlinear effects above can still occur in situations where the input light frequency or power is changing. Leaving aside rapid frequency tuning of the pump, perhaps the simplest change that could be made would be to modulate the input power.

In Ref. [25] the dynamics made by this change are investigated. The experimental procedure utilizes conventional optical fiber taper coupling to first characterize silicon microdisk resonators at low, CW, powers. High-resolution transmission scans are taken using piezo-controlled tunable lasers to measure intrinsic and extrinsic losses. Then, the CW output of a tunable diode laser is tuned near to a WGM resonance location and run through a lithium niobate electro-optic modulator (EOM)

and a train of rectangular pulses of 2.5 ns width (10–90% rise/fall-time of $\sim$ 125 ps and 200 ps, respectively) is impressed upon the output. Directed then through an Amonics AEDFA erbium-doped fiber amplifier (EDFA), the pulses are amplified. The amplified pulses are sent through a SANTEK OTF tunable band-pass filter to reject the amplified spontaneous emission from the EDFA, and then launched from the optical fiber into the microdisk resonator. To simply monitor the cavity dynamics, the reflected signal (from standing-wave modes-surface-roughness-induced doublet modes) is collected and detected with an HP83480A DCA with 30 GHz HP83485B Optical plugin, triggered by the AVTEK pulse generator that switches the EOM. The experimental setup is depicted schematically in Fig. 6.15.

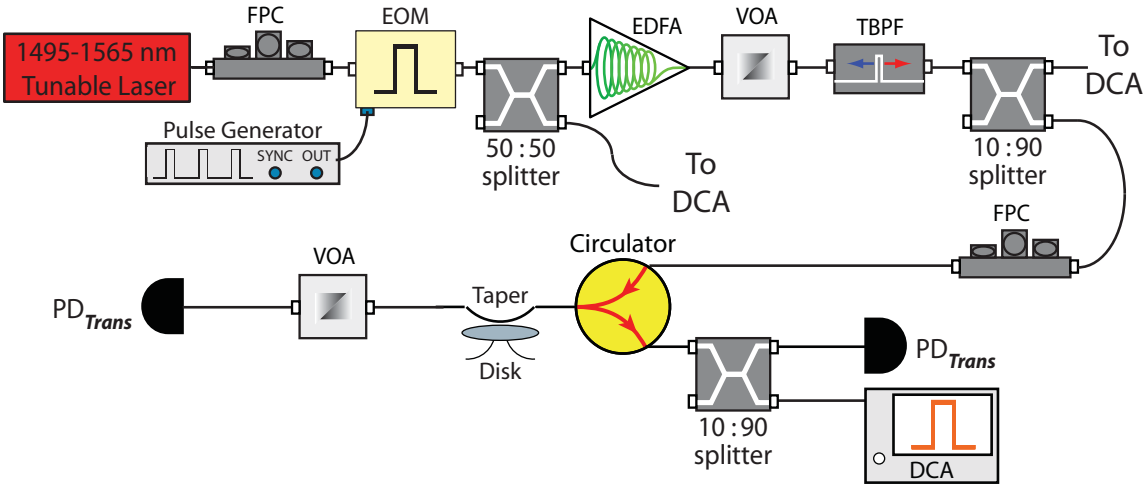

Figure 6.15: Experimental setup for use in the pulse compression measurement

Some time-domain traces of the input pulses at different post-EDFA attenuator settings are shown in Fig. 6.16.

At low input powers, it is expected that the time-domain behavior of a resonator fed with a pulse would just exhibit the classical "charging"

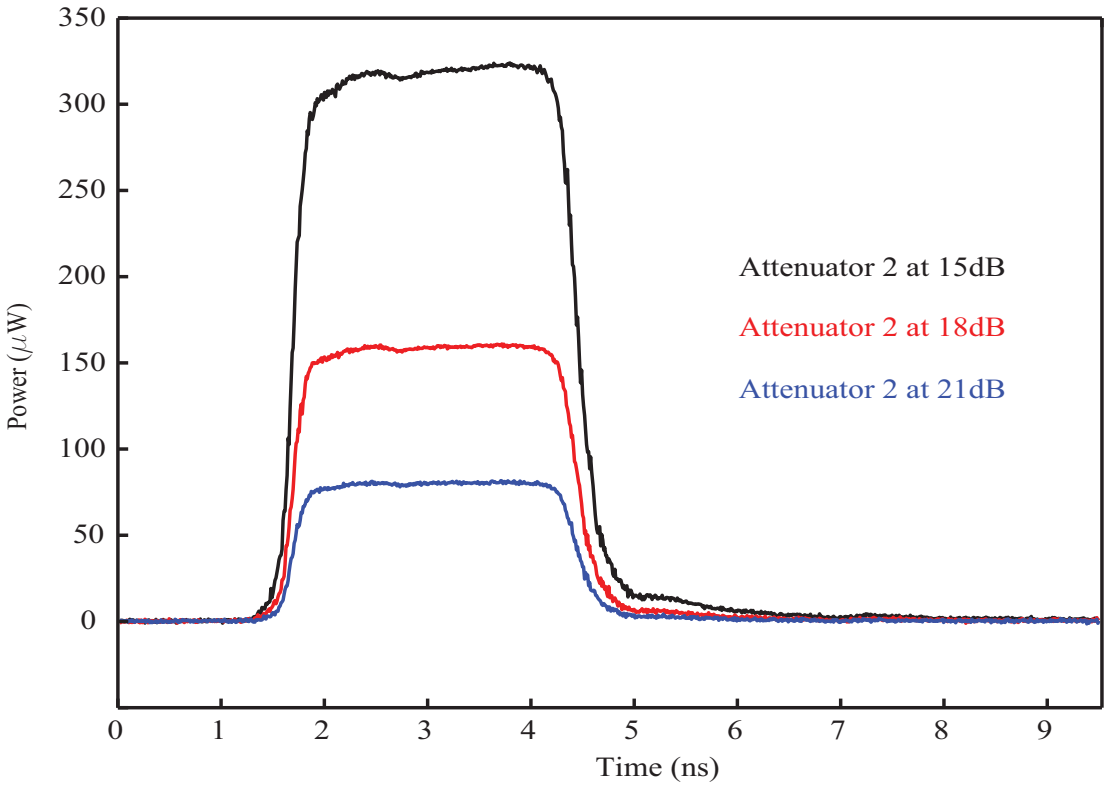

Figure 6.16: Time-domain traces of the input pulses in the PCM experiment. Different attenuator settings correspond to different powers delivered to the microdisk resonator.

behavior during the pulse "on" time, converting to a free decay when the pulse passes [131]. With increasing powers, the build-up of energy in the resonator will begin to result in TPA. The TPA will generate a free carrier population which will tend to dispersively (and absorptively) impact the resonator response. Thus we once again expect a nonlinear dynamical effect to accompany the nonlinear optical effect (TPA). Because the pulses occur on a timescale very short in comparison with thermal relaxation of the bulk system (typically on the microsecond scale, at least, in these undercut microdisks), we expect the thermal effect to be constant in time, and the dynamics to reflect just the interplay of the optical field with TPA-induced free carrier populations. As such, the equations of motion deduced above for the self-induced oscillations can be applied to this system with the changes that the temperature is removed as a variable, and that the input power S must represent the input train of pump pulses. Additionally, the presense of high-radial order modes of the microdisk serves as broad-band reflector (with low reflectivity), an effect that is usually unimportant in our measurements. However, this reflection contributes to the observed reflected power at a level that is detectable here, so it is included in the modeling without comment.

The devices considered in this experiment were silicon microdisks with diameter $\sim 20\mu$m, fabricated from 220-nm-thick device layer SOI (p-doped to 14–22 Ω·cm resistivity, orientation $\langle 100 \rangle$, upon 2-μm-thick SiO_2 buried oxide layer. The devices were patterned via ebeam lithog-

raphy and transferred with an SF_6/C_4F_8 dry etch. One sample was then subjected to 2×Piranha/HF etch and an additional Piranha oxidation, so the Si-chemical oxide interface would control the effective free-carrier lifetime. Another sample was fully processed to H-termination.

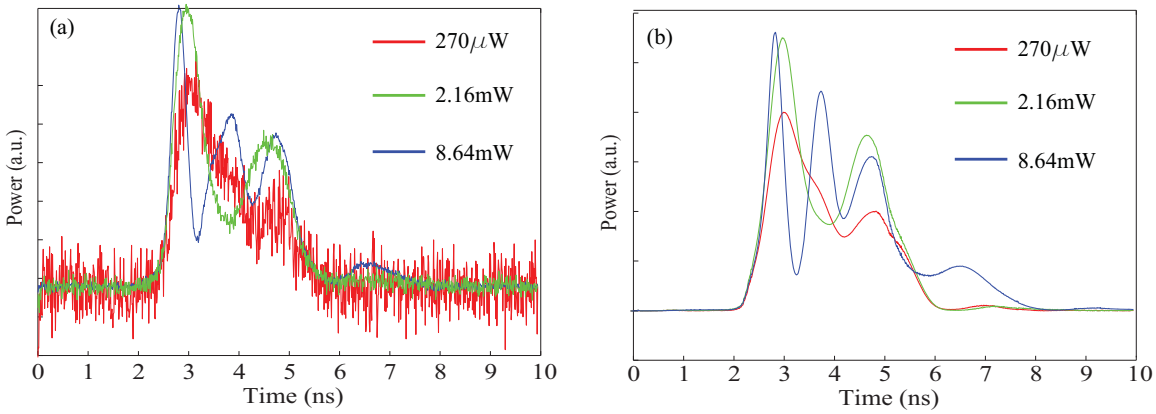

Figure 6.17: Time-domain traces corresponding to different input pump powers. (a) Experimental results. (b) Results of calculation based on measured system parameters and optimization of carrier lifetime as a parameter to the calculation.

For the chemical-oxide treated device, we first took low-power, CW transmission data and fit it to a doublet model, yielding intrinsic and extrinsic decay rates used in the equations of motion. The effective mode volume of this structure is found via FEM to be approximately $16(\lambda/n_{si})^3$. These values, along with knowledge of the input powers (measured by OSA and DCA at low power and scaled appropriately as power is increased (by decreasing optical attenuation), allow us to calculate the dynamical evolution of the system response. By varying the effective free-carrier lifetime assumed, we may "fit" the carrier lifetime, giving an additional approximate measurement, though more complicated than the method used above, of the carrier lifetime.

In Fig. 6.17(a), we see the time domain response of the system at

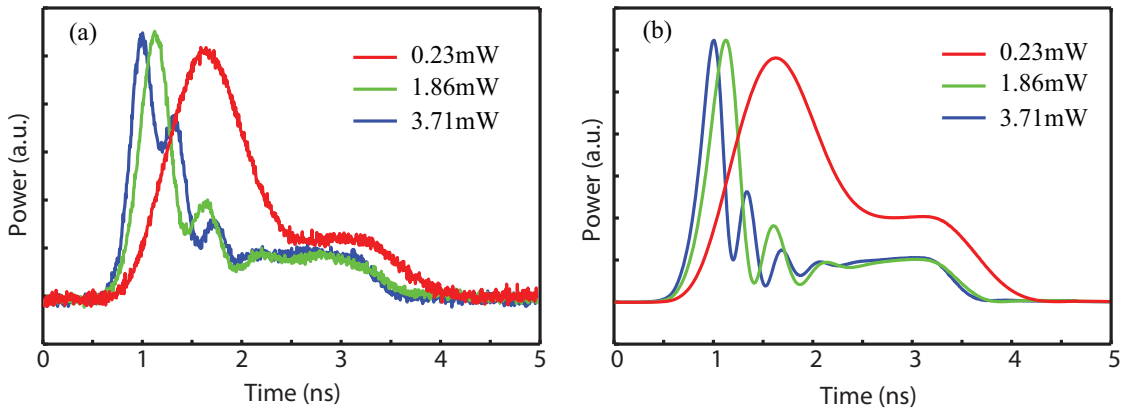

Figure 6.18: Time-domain traces corresponding to different input pump powers for the pulsed pump experiment on H-terminated silicon microdisk. (a) Experimental results. (b) Results of calculation based on measured system parameters and optimization of carrier lifetime as a parameter to the calculation.

several input powers. As the input powers increase, the time-domain response becomes increasingly complicated, developing oscillations as well as a front-peaking trend. The oscillating behavior in this case is due to the interaction between the optical energy in the resonator and carrier populations. Intially the light coupling into the resonator sees no free carrier effects and some becomes trapped in the resonator. As energy builds up quickly in the mode, the free carrier population increases rapidly, frequency-shifting some of the trapped light, and the interference during the rest of the pulse is responsible for the time domain oscillations. Ref. [25] explores this more fully and calculates spectrograms showing the expected frequency conversion.

As is evident from Fig. 6.17(b), the general behavior of the experimental system is quite well reproduced by the dynamical equations. In this case, the best-match of free-carrier lifetime was found to be $\sim$ 140 ps. While very low, this estimate is not inconsistent with our

previous observations of chemical-oxide treated silicon microdisks with effective free-carrier lifetimes in the 240–440 ps range. Similar measurements of the second sample, prepared with H-terminated surfaces were also performed. Under the same assumptions as the previous sample (with regards to effective mode volume, etc), we calculate the system response in Fig. 6.18. Panel (a) again shows the time domain traces of the reflection versus time for several input powers. We note in this case an even more pronounced trend towards a leading peak with increasing power, as well as increasing transmission oscillation. In this instance the best match to the time-domain behavior was found assuming effective free-carrier lifetime of 2.5 ns. This value is significantly less than measured in the external pump measurement but still nanosecond scale, whereas the chemical-oxide surface could achieve deep-subnanosecond lifetimes. More broadly, these effective carrier lifetimes reflect similar relative values to the measurement presented in Section 5.

6.4 Requirements for CW low-power Raman lasing and optical parametric oscillation

As mentioned above, the free-carrier characteristics of silicon photonic resonators are critical when considering nonlinear optical operation. The high intensities required to access the nonlinear regime may also, in the telecommunications wavelength range, generate free-carrier populations by TPA at a significant rate. Consequently, the efficiency

of nonlinear optical operation can be severly impacted [99]. Of course workarounds are available: the inclusion of a reverse-biased *pn*-junction can aid in overcoming the limitations imposed by free-carrier generation, for example. However, simplicity has its rewards, and a fully passive carrier modification strategy, like that pursued in Section 5 may pay dividends if optical losses are not too adversely impacted.

We have found that SOI microdisk resonators can be fabricated with high-Q and ultrashort free-carrier lifetimes with the use of standard fabrication techniques and simple wet-chemical treatments. With their small modal volumes (standing wave resonances at ~ 1.55 μm in 120-nm-thick silicon microdisks with radius ~ 6.5 μm have $V_{\text{eff}} \sim 15(\lambda/n_{si})^3$) and high-$Q$, such microresonators represent a useful building block for realizing nonlinear devices and applications. With the reduction in lifetimes attainable shown here, it may be possible to achieve CW (extended) telecom wavelength OPO, as well as Raman lasing.

We now discuss in a general way the trade-offs between carrier lifetime and optical Q in the context of Raman scattering and optical parametric oscillation (OPO) by four-wave mixing.

Eqns. 6.8 are equations of motion sufficiently general to handle either FWM or Raman scattering, with the only modification being that the appropriate definitions of γ^c_{ijkl} are taken. As noted above, the cavity nonlinear parameters depend on the nonlinear susceptibility of the material. In silicon, the third-order nonlinearity has both bound-electron contributions (Kerr effect and TPA (relevant to OPO, OPO and Ra-

man, respectively)), and photon-lattice contributions (relevant to Raman). By suitably arranging the geometric properties of a resonator to generate the appropriate spectrum of cavity resonance, one may access one effect or the other. Then the theoretical framework is largely similar and all one need do is replace the appropriate $\overleftrightarrow{\chi}^{(3)}$ components [39].

Threshold conditions may be deduced from Eqns. 6.8 in the assumption that phase matching is satisfied and that appropriate higher-order dispersion counteracts the dispersive effects of SPM and XPM, as well as the assumption that the pump energy is not depleted. Then the threshold relation is deduced by diagonalizing the EOMs for the signal and idler mode-field amplitudes, taking the energy stored in the pump mode as an independent variable.

Making the appropriate substitutions for going to the case of Raman gain, we have, modifying the results in Ref. [25] and assuming the pump and signal modes have good overlap, similar modal indicies, a condition between free-carrier lifetime and total loss in the stokes mode for Raman gain:

$$\frac{\tau_{fc}}{Q_{ts}} < \frac{\tau_{th}}{Q_{th,s}} = \left(\frac{\omega_s}{\omega_r}\right)^2 \frac{\hbar\, c}{2n_0\sigma_r} \frac{(g_R^{'} - 2\beta_{TPA}^{'})^2}{\beta_{TPA}^{'}}, \tag{6.70}$$

where τ_0 is the effective free-carrier lifetime, ω_s and Q_s are the frequency and Q of the signal mode, g_R is the effective Raman gain coefficient for the axisymmetric resonator $g_R^{'} = g_R/2$ for TE-TE ($g_R^{'} = g_R$ for TE-TM) configuration and g_R is the material parameter for Raman gain), $\beta_{TPA}^{'} = \beta_{TPA}$ for TE-TE ($\beta_{TPA}^{'} = \beta_{TPA}/3$ for TE-TM) configuration

and β_{TPA} is the material parameter for two-photon absorption (TPA), n_0 is the refractive index of silicon at Stokes mode wavelength, σ_r is the free-carrier absorption cross section at a reference frequency, ω_r. Substituting appropriate parameters, we find numerical relations for the required τ_{fc} and Q_s. We find that for $Q_s \sim 5 \times 10^5$, we must have $\tau_{fc} \sim 0.25$ ns for TE-TE ($\tau_{fc} \sim 10$ ns for TE-TM) configuration. Hence either configuration would be attainable with fully passive components, low power, and ultralow footprint.

The threshold power under those considerations is found in Ref. [39] to be

$$P_{th} = \frac{\omega_p \omega_s n_{gp} n_{gs} V_{eff}}{2c^2 (g_R^{'} - 2\beta_{TPA}^{'})} \frac{Q_{ep}}{Q_{ts} Q_{tp}^2} \left[1 - \left(1 - \frac{\tau_0 Q_{th,s}}{\tau_{th} Q_s} \right)^{1/2} \right]. \qquad (6.71)$$

With appropriate subsititions (assuming that the TPA coefficient is consistent with the values in Refs. [3, 128, 132](0.5 cm/GW), that the coefficient of Raman gain is consistent with an average value (8 cm/GW) between Refs. [6, 133, 134], and that free-carrier absorption cross section is given (at 1.55 μm) as $1.45 \times 10^{-21} m^2$ in Ref. [56]) we find that the threshold input power for TE-TE configuration is $P_{th} = \sim$ 380 μW (TE-TM is $P_{th} = 175$ μW).

Experimentally, we have created silicon microdisk resonators which, under CW pumping in the S-band, display Stokes-shifted light. For WGM resonances spaced in frequency by the zone-center optical phonon frequency in silicon, 15.57 THz, resonant scattering was observed. Fig. 6.19(a)

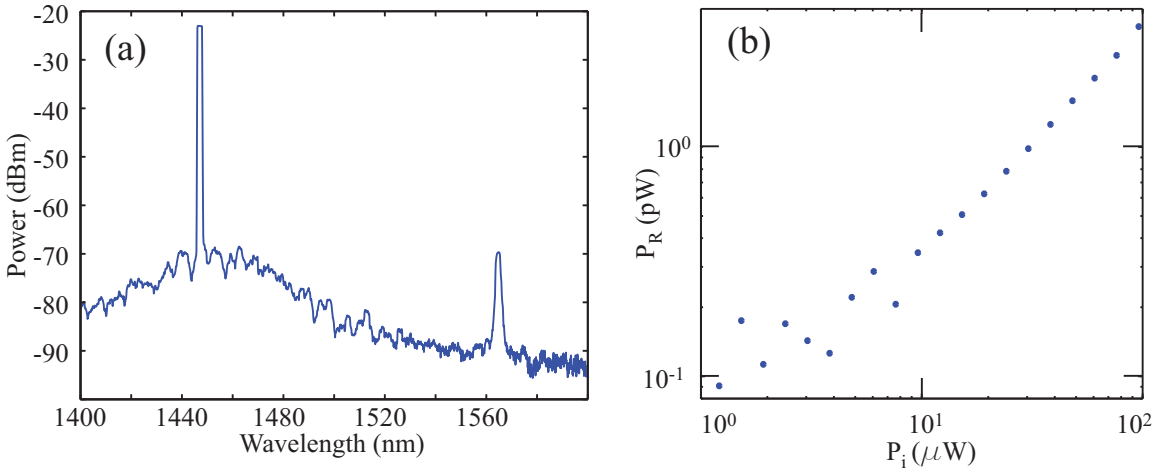

Figure 6.19: Raman scattering in a silicon microdisk. (a) OSA scan showing input pump light centered on a WGM resonance in the S-band and Stokes-shifted light scattered to a WGM resonance near the red end of the C-band. (b) Light-in-light-out relationship of scattering to input pump power.

depicts an OSA scan from 1400–1600 nm, showing the pump light near 1450 nm and the Stokes light near 1565 nm. Resonant Raman scattering was observed even down to the microwatt pump level, as shown in Fig. 6.19(b) for a 5μm radius, 340-nm-thick microdisk resonator fabricated on $\langle 100 \rangle$ silicon, p-doped to 1–3 Ω·cm, and fabricated with the "as-processed" procedure.

Unfortunately, at dropped powers of just ~ 100 μW the time domain oscillations described in the previous sections began to take place, preventing observation of any ultralow CW Raman lasing threshold. Using the steady-state model above with input powers around 500 μW, assuming critical coupling and intrinsic quality factor $\sim 1\times10^6$, $\tau_{th} \sim 5\mu$s, $V_{eff} \sim 50(\lambda/n_{si})^3$, and the fit free carrier lifetime to the self-oscillation behavior above, we find that the threshold for self-oscillations is approximately 80μW. Thus we would indeed expect the self-oscillation

phenomenon to obliterate the CW behavior of the system.

If surface state and geometric modification of the free-carrier lifetime could be made as above, reducing the effective free carrier lifetime to ~ 0.5 ns, the self-oscillation threshold would increase to above 250μW, making observable the cross-polarization Raman operation at ultra-low power. Thus we see that utilization of free carrier lifetime could enable ultralow threshold (as above, thresholds around 175–380 μW) CW Raman lasing in silicon microdisk resonators.

For four-wave mixing (FWM) generated lasing, or optical parametric oscillator (OPO), a similar threshold relationship can be found and is given in Ref. [25] as

$$4\gamma^c_{spip}\gamma^{c*}_{ipsp}U_p^2 = \left(\frac{1}{\tau_{ts}} + \frac{c\alpha_{fs}}{n_{0s}} + 2\beta^c_{Tsp}U_p\right)\left(\frac{1}{\tau_{ti}} + \frac{c\alpha_{fi}}{n_{0i}} + 2\beta^c_{Tip}U_p\right), \tag{6.72}$$

where $\beta^c_{Tuv} = 2Im(\gamma^c_{uv})$. For solutions to the above equation, the input power required to reach threshold is given as:

$$P_{th} = \frac{\tau_{ep}}{4}U_p\left(\frac{1}{\tau_{tp}} + \frac{c\alpha_{fp}}{n_{0p}} + \beta^c_{Tpp}U_p\right)^2. \tag{6.73}$$

In configurations where the pump wave can create free carriers via two-photon absorption (TPA), and under the approximations that the pump is much more intense than the signal or idler, and pump, signal, and idler frequencies and associated quality factors are similar, we may deduce from the requirement that solutions to Eq. 6.72 must be real

and positive, the following approximate relation between the linear and nonlinear parameters:

$$\frac{\tau_{fc}}{Q} < \frac{\tau_{fc,th}}{Q_{th}} = \left(\frac{\omega}{\omega_r}\right)^2 \left(\frac{\hbar}{c\, n_0 \sigma_r}\right) \left(\frac{4\omega^2 n_2^2(\omega) - 3c^2\beta_{TPA}^2(\omega)}{\beta_{TPA}(\omega)}\right), \quad (6.74)$$

a necessary but not sufficient condition, where the parameters are as above. We can further examine the threshold presented in Eqn. 6.72 with an eye to finding the spectral regions with the least stringent requirements on losses and free-carrier lifetimes. Fig. 6.20 depicts graphically the relationship in Eqn. 6.72. We see that the conventional telecom band has relatively much more tight requirements than the more exotic O/E-band and the very long wavelength regions above 2μm.

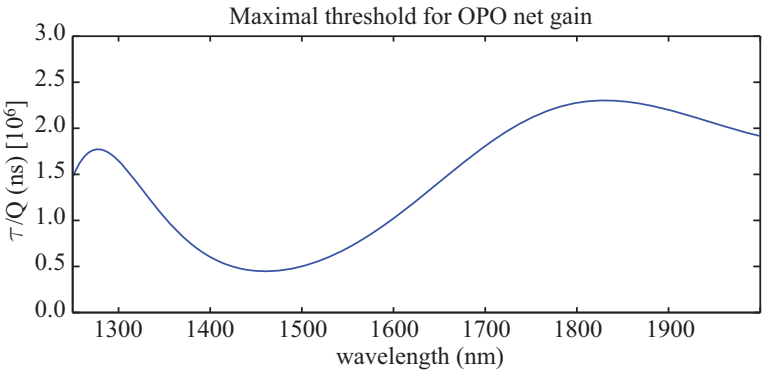

Figure 6.20: A necessary condition for CW OPO operation. This condition reflects Eqn. 6.72. It reflects the nonlinear effects as well as the influence of any free carriers generated by TPA of intense pump waves.

For free-carrier lifetimes achieved here, $\tau_{fc} \sim 300$ ps, $Q \sim 2e6$ is required for lasing under a degenerate pumping scheme with pump located near the center of the telecom C-band, signal/idler located near

the centers of the S-L-bands, with lasing threshold input power less than ~ 400 μW. Lasing operation with the pump located in the O/E-band region can be achieved with parameters consistent with those reported here, at CW pumping at the milliwatt level.

Using the simple chemical treatments discussed above on high-Q resonators, deep subnanosecond free-carrier lifetimes are achievable without undue increases in optical loss. The devices so realized would be useful for application to nonlinear generation of light through either the Raman effect or through the creation of an OPO. Fully passive, CW, low-power, implementation of these devices is thus a possibility. The surface treatments considered here could also be utilized in electrically active devices incorporating a $p-n$ junction operated in accumulation mode: increased lifetime would allow decreased power consumption.

The threshold conditions presented in Eqns. 6.70–6.74 are both quite general to situations where free-carrier generation via TPA is present, and illustrate the importance of the ratio between τ_{fc} and Q, reflect the substantial similarity between the effects (entering in the same order of intensity), and the dependence of threshold values on frequency.

That parameterization reveals a quite general relationship in the case of OPO. Restricting our attention to the case of telecom-band operation, we plot in Fig. 6.21 the dependence of threshold input power (and saturation—where losses due to the generation of free-carriers inhibits lasing action) versus the ratio of free-carrier lifetime to quality factor. We see that the threshold curves for various free-carrier life-

times approach a common maximum in abscissa, indicating that a true threshold exists, as indicated in Eqn. 6.74.

It is clear, then, that the quantity τ_{fc}/Q is a critical parameter for nonlinear processes in silicon photonics–when the operation takes place in spectral regions susceptible to TPA generation of free carrier populations.

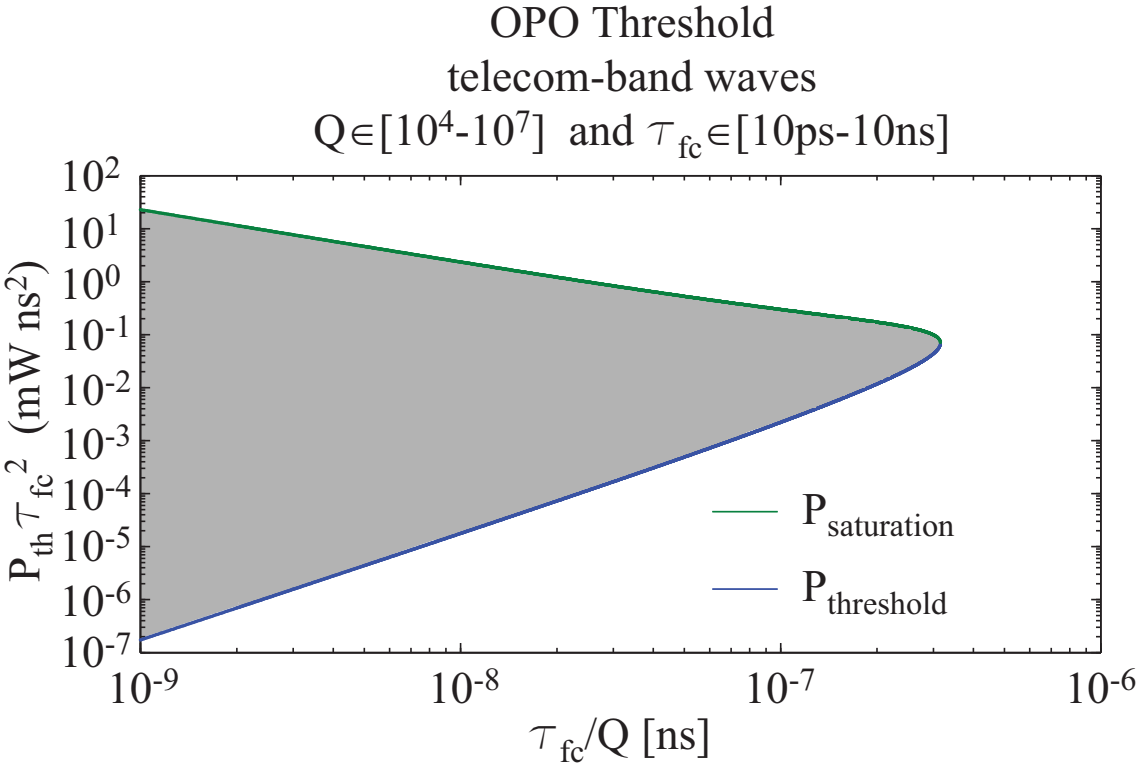

Figure 6.21: OPO universal relationship. This plot depicts the threshold (blue) and saturation (green) for a variety of free-carrier lifetimes and Qs, with operation in the telecom band. Within the shaded grey region OPO operation is possible. The threshold powers are plotted weighted by the square of free-carrier lifetime, and all against the ratio of free-carrier lifetime to quality factor. The combinations of many Qs in the interval [10^4,10^7] and free-carrier lifetimes in the range [10 ps,10 ns].

6.5 Ring resonators

In the above, we have largely ignored the issues surrounding the phase-matching requirements of nonlinear optical processes like FWM. While the ability to achieve GVD control is limited in the TE-modes of a microdisk, it is feasible with the TM-modes of a microdisk. However, the thickness of the epitaxial layer defining the device is perhaps not the ideal parameter to vary in creating devices with the desired dispersive properties.

By incorporating additional geometric restrictions, the waveguide dispersion may be made to play a greater role in the overall modal dispersion (as demonstrated by the purely normal dispersion properties of the TE microdisk modes compared to the regions of anomalous dispersion exhibited by TM microdisk modes). The next geometry that suggests itself is the microring. In Ref. [25] the authors analyze planar microring resonator, finding it is possible to manipulate the ZDWL over a wide range, with geometry varying by lithographic means.

6.5.1 Design

6.5.1.1 Dispersion

As mentioned above, the dispersion properties of the slab-like microdisks mean that for certain applications they are somewhat restricted in utility: the phase matching requirements for FWM operation mean locating the pump wave near the zero-dispersion wavelength (ZDWL)

[25, 110]. Adjustment of the ZDWL in microdisks requires thickness changes—the impact of disk radius is quite weak, while thickness dramatically changes things. Fig. 6.22(a)-(b) show that the group velocity dispersion (GVD) of microdisks is fairly strongly impacted by thickness, with TM-like modes exhibiting a transition from anomalous to normal dispersion near wavelengths of interest, the desired behavior.

However, the thicknesses required for TM-like modes to exhibit ZDWLs are fairly thick, meaning the hoped-for reductions in free-carrier lifetime may be difficult to achieve. By adding the geometrical features of a ring, TE-like modes may be used to greater effect. Achieving the necessary dispersion properties while allowing free-carrier lifetime reduction techniques described above may then be realizable.

In Fig. 6.23 we see that a TM-like mode of a planar ridge waveguide of a given height (in this case, $h = 250$ nm, $d = 220$ nm) has GVD with ZDWL that may be trimmed by width. That is, by varying this property lithographically, we may achieve dispersion characteristics that take on desirable properties. Because the dispersion properties of the ridge waveguide are similar to the case of the ring resonator (for wavelengths not much less than the ridge width), this is a good guide to the behavior of a planar or floating ring. In Fig. 6.23, we see tha by varying the width of the ring, we can move the ZDWL about with ease—and without the need to tune the device performance by height.

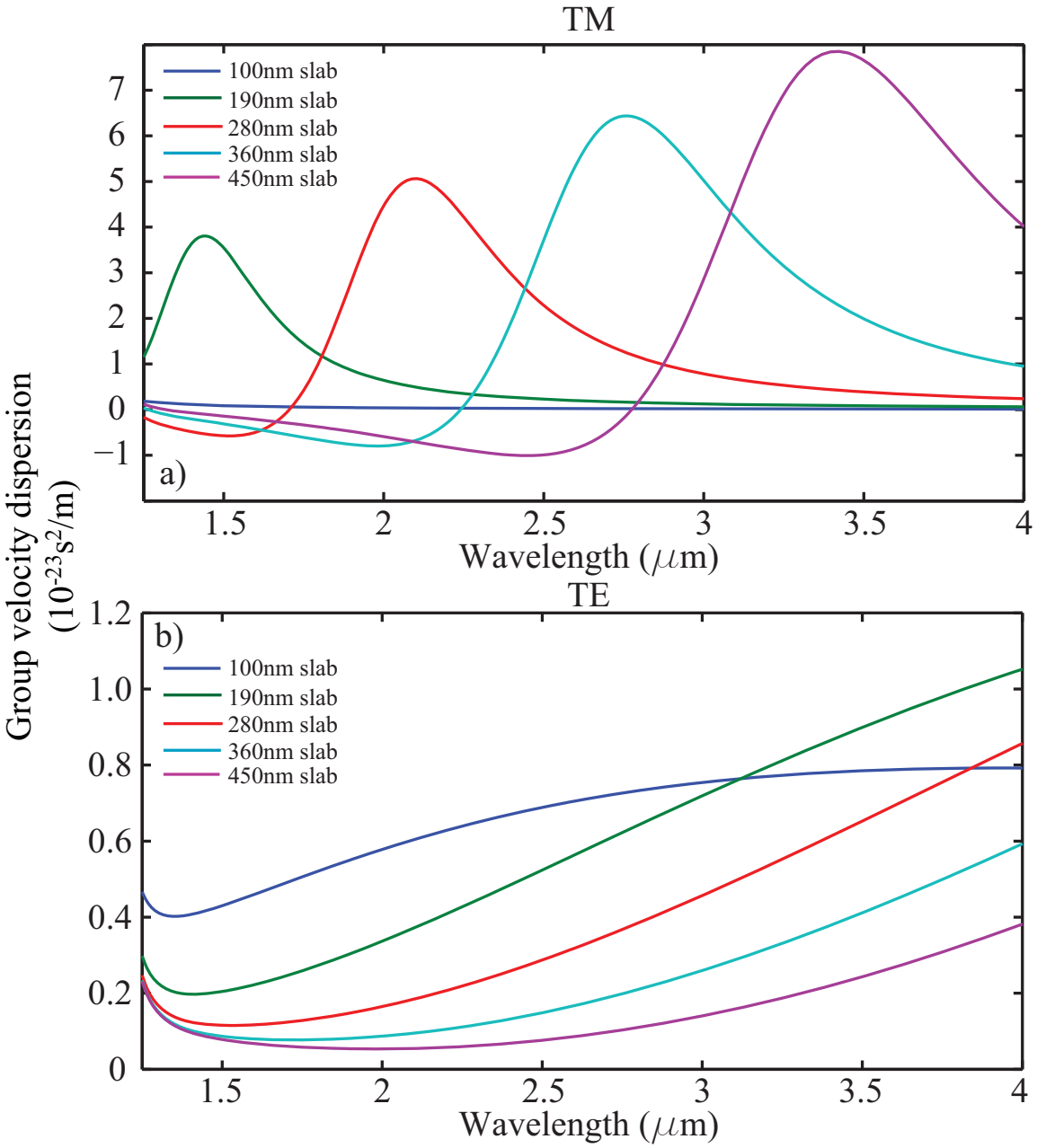

Figure 6.22: Group velocity dispersion for slab-like microdisks. (a) TM-like modes exhibit regions of normal and anomalous dispersion. (b) TE-like modes have only normal dispersion. Note that a wide range of zero dispersion wavelengths may be accessed with thicker slabs.

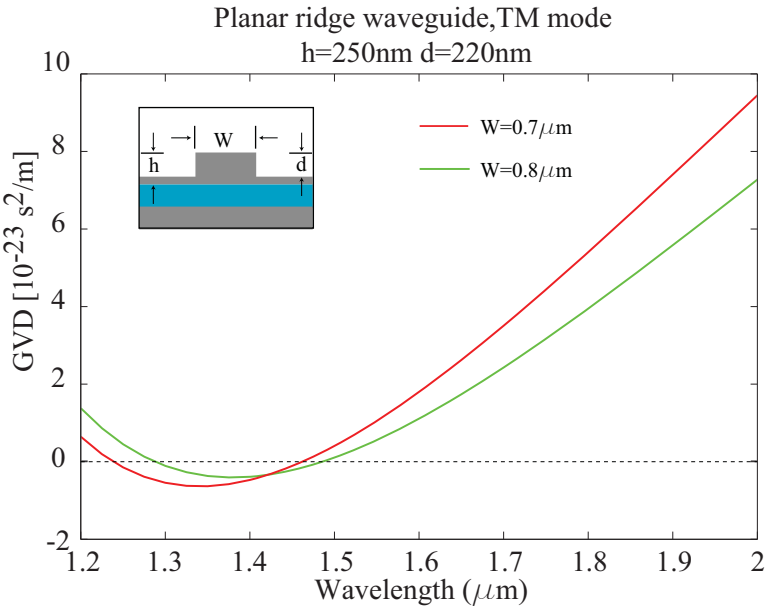

Figure 6.23: Group velocity dispersion for microring-like partially etched waveguides. The height of the device layer is assumed to be 250 nm, and the etch depth 220 nm. A wavelength range of 1.2–4μm is shown, though this geometry is most well suited to OPO operation in the E-O bands, near the ZDWL.

6.5.1.2 Free-carrier lifetime

The free-carrier lifetimes of the resonators used for nonlinear optics are critical, as noted above. But we have also seen that emphasizing the role of surfaces (or at least the manipulation of geometry and surface chemistry) is a workable way to reduce the free-carrier lifetimes in a given structure. Thus the inclusion of additional exposed surfaces in the resonant structure may not only improve our ability to realize the required dispersive properties, but allow us to deploy the techniques developed in Section5.

We find, for example, that a planar microdisk with thickness 220 nm and 6.5μm radius, given surface recombination velocities of 240 m/s (inferred from the mode-averaged lifetimes and simulation to de-

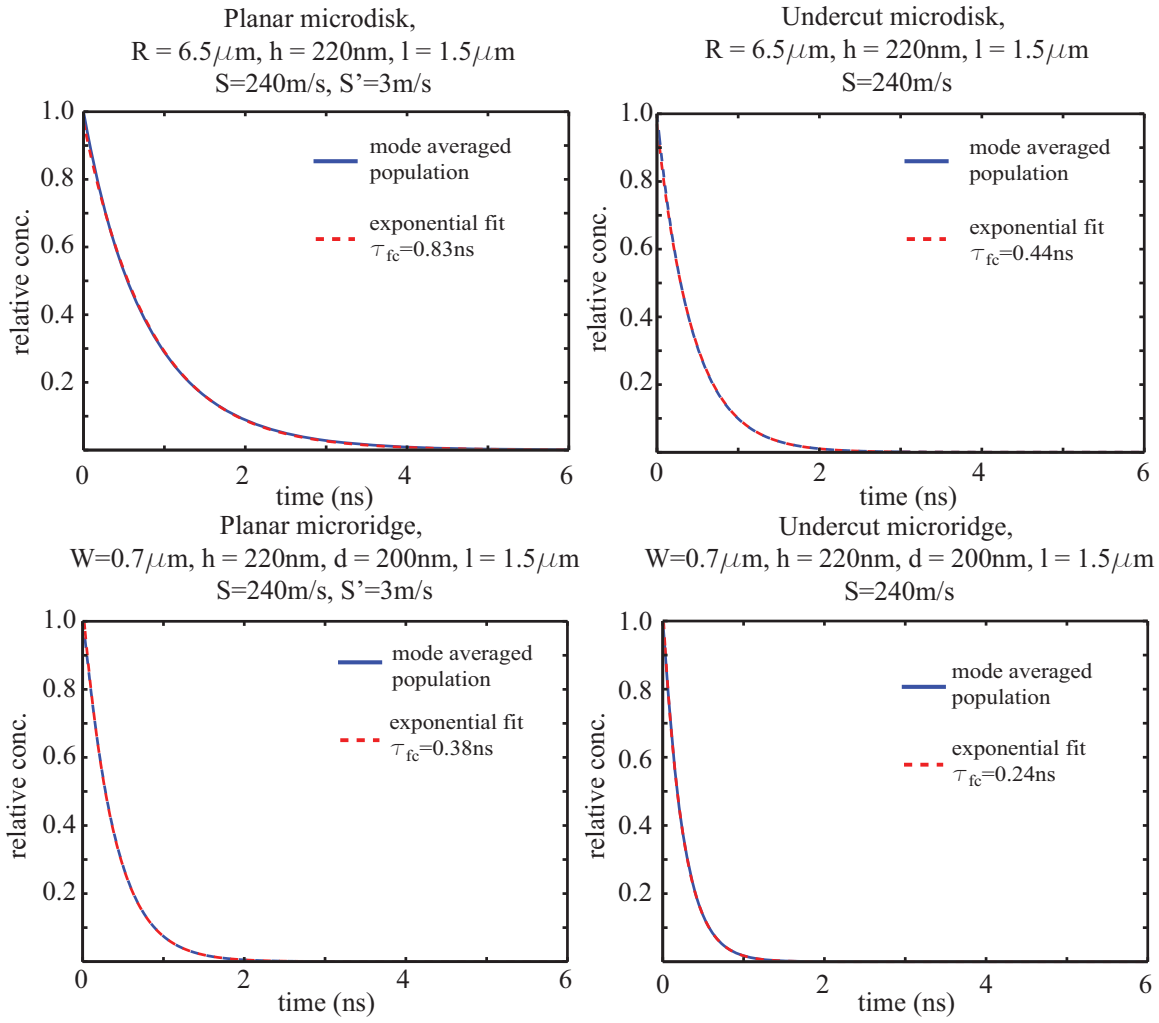

Figure 6.24: Comparison of impact on free-carrier lifetime given different exposed (and treated) surfaces. The surface recombination velocities are inferred from the surface treatments in Section 5 (a) A planar microdisk resonator. Exposed surfaces S = 177 m/s, oxide surface S = 9.8 m/s. Best fit lifetime 1.07 ns. (b) Undercut microdisk resonator, exposed surfaces S = 177 m/s. Best fit lifetime 0.6 ns. (c) Planar microring resonator. properties as in (a). Best fit lifetime 0.43 ns. (d) Floating ring resonator. Properties as (b). Best fit lifetime 0.29 ns

termine the associated SRV) on its exposed surfaces and 3 m/s on the oxide interface (similarly inferred) results in a mode-averaged free carrier lifetime of 0.83 ns. Moving to an undercut structure and applying the same treatments results in a mode-averaged lifetime of 0.44 ns. Utilizing the same height a planar partial ring structure (width = 0.7μm) results in a lifetime of 0.38 ns. Again, by moving to an undercut structure—the floating-ring—we achieve a reduction to mode-averaged free carrier lifetime of 0.24 ns. Thus we see that the lessons learned in microdisks can be applied to excellent effect in the floating-ring geometry, and generically the addition of bounding surfaces in proximity to the optical mode reduces the effective free-carrier lifetime.

6.5.2 Test

The planar and floating-ring structures can be tested with our conventional "dimpled" fiber-taper. One limitation of this technique for use with the planar-ring structure is that the effective index of the planar structure is pinned by $n_{eff} \geq 1.44$. However, this problem is not insurmountable, and the planar ring structure can be probed with the fiber-taper method.

In Fig. 6.25 we see a transmission spectrum of a planar microring resonator coupled with a fiber taper with fit to a doublet model. The resulting quality factors are $Q \sim 4 \times 10^6$, showing that we can, using these conventional fabrication methods, create extremely high Q planar microring resonators.

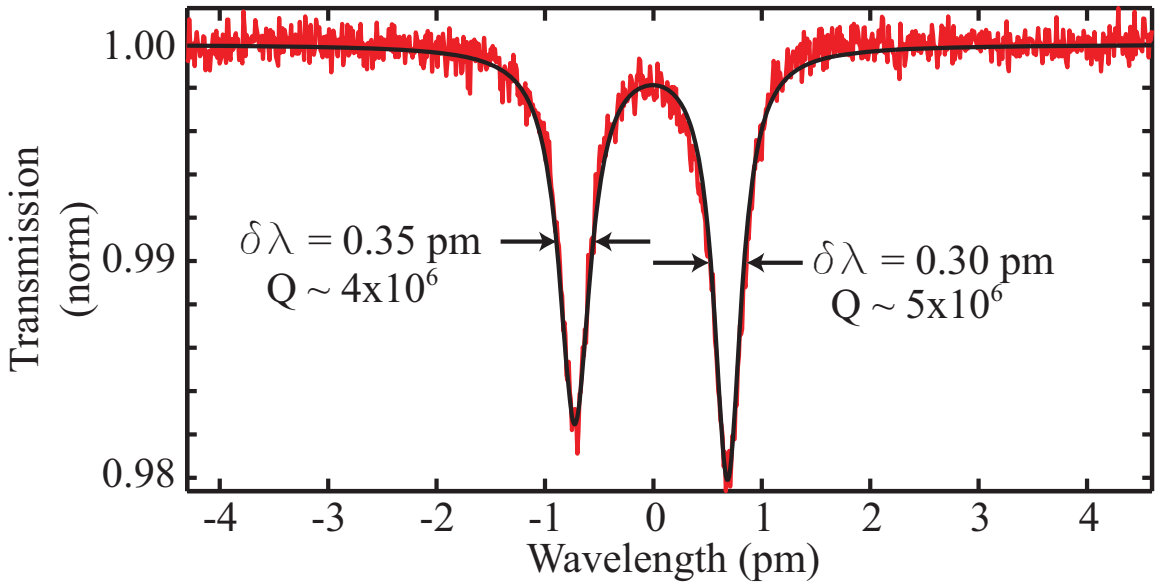

Figure 6.25: Measured transmission for a planar ring resonator with thickness 220 nm, width 2μm, Radius 20μm at $\lambda \sim 1.45\mu$m

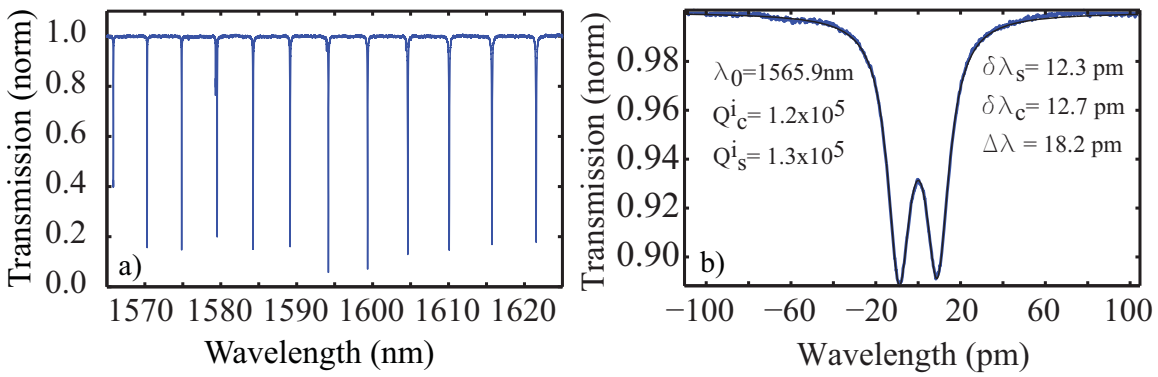

Figure 6.26: Measured transmission for a floating ring resonator with thickness 250 nm, etch depth 220 nm, width = 0.5μm, Radius = 45μm at $\lambda \sim 1.6\mu$m

Fig. 6.26(a)-(b) depict the transmission properties of the TM-like resonances of a floating- ring-type resonator. The first panel is a broad scan of a floating-ring structure with thickness 220 nm, etch depth $\sim$ 190 nm, ring width 0.70 nm, and radius 45μm.

The planar-ring and floating-ring geometries depicted above are shown to have the desired dispersion properties (Fig. 6.23) and the ability to apply the surface engineering methods discussed to reduce free-carrier lifetimes (Fig. 6.24). They are amenable to fabrication (Fig. 3.10) and test (Fig. 6.26) and high-Q operation ($Q > 10^5$) can be achieved.

Taken together, the flexible dispersive, lifetime and test properties of the partially etched, floating-ring geometry are formidable. Using these geometries thus takes advantage of the very easy test methods useful for undercut geometries, including the ability to very efficiently couple light in and out controllably, while availing the excellent capacity for dispersion and device surface modification in the context of high-Q operation. They are thus an ideal structure to pursue nonlinear optical effects.

Bibliography

[1] L. Pavesi and D. J. Lockwood, eds., *Silicon Photonics*, vol. 94 of *Topics in Applied Physics* (Springer-Verlag, Berlin, 2004).

[2] G. T. Reed and A. P. Knights, *Silicon Photonics: An Introduction* (John Wiley & Sons, Ltd., West Sussex, 2004).

[3] A. Liu, R. Jones, L. Liao, D. Samara-Rubio, D. Rubin, O. Cohen, R. Nicolaescu, and M. Paniccia, "A high-speed silicon optical modulator based on a metaloxidesemiconductor capacitor," Nature **427**, 615–618 (2004).

[4] V. R. Almeida, C. A. Barrios, R. R. Panepucci, and M. Lipson, "All-optical control of light on a silicon chip," Nature **431**(7012), 1081–1084 (2004).

[5] O. Boyraz and B. Jalali, "Demonstration of a silicon Raman laser," Opt. Express **12**(21), 5269–5273 (2004).

[6] H. Rong, A. Liu, R. Jones, O. Cohen, D. Hak, R. Nicolaescu, A. Fang, and M. Paniccia, "An all-silicon Raman laser," Nature **433**, 292–294 (2005).

[7] H. Rong, R. Jones, A. Liu, O. Cohen, D. Hak, A. Fang, and M. Paniccia, "A continuous-wave Raman silicon laser," Nature **433**, 725–728 (2005).

[8] K. Okamoto, M. Loncar, T. Yoshie, A. Scherer, Y. M. Qiu, and P.Gogna, "Near-field scanning optical microscopy of photonic crystal nanocavities," Appl. Phys. Lett. **82**(11), 1676–1678 (2003).

[9] B. E. Little and S. T. Chu, "Estimating surface-roughness loss and output coupling in microdisk resonators," Opt. Lett. **21**, 1390–1392 (1996).

[10] D. A. Muller, "A sound barrier for silicon?" Nature Mater. **4**, 645–647 (2005).

[11] Q. Xu, B. Schmidt, J. Shakya, and M. Lipson, "Cascaded silicon micro-ring modulators for WDM optical interconnections," Opt. Express **14**, 9430–9435 (2006).

[12] Q. Xu, B. Schmidt, S. Pradhan, and M. Lipson, "Micrometre-scale silicon electro-optic modulator," Nature **435**(7040), 325–327 (2005).

[13] H. Rong, S. Xu, Y.-H. Kuo, V. Sih, O. Cohen, O. Raday, and M. Paniccia, "Low-threshold continuous-wave Raman silicon laser," Nature Photon. **1**, 232–237 (2007).

[14] T. Tanabe, M. Notomi, S. Mitsugi, A. Shinya, and E. Kuramochi, "All-optical switches on a silicon chip realized using photonic-crystal nanocavities," Appl. Phys. Lett. **87**(15), 151,112–1–151,112–3 (2005).

[15] T. Tanabe, M. Notomi, S. Mitsugi, A. Shinya, and E. Kuramochi, "Fast bistable all-optical switch and memory on a silicon photonic crystal on-chip," Opt. Lett. **30**(19), 2575–2577 (2005).

[16] B. Song, S. Noda, T. Asano, and Y. Akahane, "Ultra-high-Q photonic double-heterostructure nanocavity," Nature Mater. **4**, 207–210 (2005).

[17] D. Dimitropoulos, S. Fathpour, and B. Jalali, "Predicaments in CW Operation of Silicon Raman Lasers and Amplifiers," in *Integrated Photonics Research and Applications/Nanophotonics, Technical Digest (CD)* (OSA, Washington, D.C., 2006).

[18] M. Waldow, T. Plötzing, M. Gottheil, M. Först, J. Bolten, T. Wahlbrink, and H. Kurz, "25 ps all-optical switching in oxygen implanted silicon-on-insulator microring resonator," Opt. Express **16**(11), 7693–7702 (2008).

[19] P. E. Barclay, K. Srinivasan, and O. Painter, "Nonlinear response of silicon photonic crystal microresonators excited via an integrated waveguide and fiber taper," Opt. Express **13**, 801 (2005).

[20] T. J. Johnson, M. G. Borselli, and O. J. Painter, "Self-induced modulation of a high-Q SOI microdisk optical resonator," Opt. Express **14**(2), 817–831 (2006).

[21] Q. Lin, T. J. Johnson, R. Perahia, C. P. Michael, and O. J. Painter, ""A proposal for highly tunable optical parametric oscillation in silicon micro-resonators"," Opt. Express **16**(14), 10,596 (2008).

[22] M. Borselli, K. Srinivasan, P. E. Barclay, and O. Painter, "Rayleigh scattering, mode coupling, and optical loss in silicon microdisks," Appl. Phys. Lett. **85**, 3693 (2004).

[23] M. Borselli, T. J. Johnson, and O. Painter, "Beyond the Rayleigh scattering limit in high-Q silicon microdisks: theory and experiment," Opt. Express **13**, 1515 (2005).

[24] P. E. Barclay, K. Srinivasan, O. Painter, B. Lev, and H. Mabuchi, "Integration of fiber-coupled high-Q SiN_x microdisks with atom chips," Appl. Phys. Lett. **89**, 131,108 (2006).

[25] Q. Lin, T. J. Johnson, C. P. Michael, and O. J. Painter, ""Adiabatic self-tuning in a silicon microdisk optical resonator"," Opt. Express **16**(19), 14,801 (2008).

[26] T. J. Kippenberg, S. M. Spillane, and K. J. Vahala, "Modal coupling in traveling-wave resonators," Opt. Lett. **27**(19), 1669–1671 (2002).

[27] M. L. Gorodetsky and V. S. Ilchenko, "Optical microsphere resonators: optimal coupling to high-Q whispering-gallery modes," J. Opt. Soc. Am. B **16**, 147–154 (1999).

[28] D. S. Weiss, V. Sandoghdar, J. Hare, V. Lefèvre-Seguin, J.-M. Raimond, and S. Haroche, "Splitting of high-Q Mie modes induced by light backscattering in silica microspheres," Opt. Lett. **20**(18), 1835–1837 (1995).

[29] M. Kuznetsov and H. A. Haus, "Radiation Loss in Dielectric Waveguide Structures by the Volume Current Method," IEEE J. Quan. Elec. **19**(10), 1505–1514 (1983).

[30] B. E. Little, S. T. Chu, W. Pan, D. Ripin, T. Kaneko, Y. Kokubun, and E. Ippen, "Vertically Coupled Glass Microring Resonator Channel Dropping Filters," IEEE Photonics Tech. Lett. **11**(2), 215–217 (1999).

[31] M. Oxborrow, "How to simulate the whispering-gallery modes of dielectric microresonators in FEMLAB/COMSOL," vol. 6452, p. 64520J (SPIE, 2007).

[32] J. E. Heebner, T. C. Bond, and J. S. Kallman, "Generalized formulation for performance degradations due to bending and edge scattering loss in microdisk resonators," Opt. Express **15**, 4452–4473 (2007).

[33] M. Heiblum and J. H. Harris, "Analysis of Curved Optical Waveguides by Conformal Transformation," IEEE J. Quan. Elec. **QE-11**(2), 75–83 (1975).

[34] W. Berglund and A. Gopinath, "WKB Analysis of Bend Losses in Optical Waveguides," IEEE J. Lightwave Tech. **18**(8), 1161 (2000).

[35] R. K. Chang and A. J. Campillo, eds., *Optical Processes in Microcavities* (World Scientific, Singapore, 1996).

[36] C. Cohen-Tannoudji, B. Diu, and F. Laloe, *Quantum Mechanics* (John Wiley & Sons, Inc., New York, NY, 1977).

[37] K. Srinivasan, M. Borselli, O. Painter, A. Stintz, and S. Krishna, "Cavity Q, mode volume, and lasing threshold in small diameter AlGaAs microdisks with embedded quantum dots," Opt. Express **14**(3), 1094–1105 (2006).

[38] J. Jin, *The Finite Element Method in Electromagnetics, Second Ed.* (Wiley-IEEE Press, New York, 2002).

[39] Q. Lin, O. J. Painter, and G. P. Agrawal, ""Nonlinear Optical Phenomena in Silicon Waveguides: Modeling and Applications"," Opt. Express **15**(25), 16,604–16,644 (2007).

[40] R. Coccioli, M. Boroditsky, K. W. Kim, Y. Rahmat-Samii, and E. Yablonovitch, "Smallest possible electromagnetic mode volume

in a dielectric cavity," IEE Proc. - Optoelectron. **145**(6), 391–397 (1998).

[41] K. Srinivasan, P. E. Barclay, M. Borselli, and O. Painter, "Optical-fiber-based measurement of an ultrasmall volume, high-Q photonic crystal microcavity," Phys. Rev. B **70**, 081,306R (2004).

[42] P. E. Barclay, K. Srinivasan, M. Borselli, and O. Painter, "Efficient input and output fiber coupling to a photonic crystal waveguide," Opt. Lett. **29**, 697–699 (2004).

[43] S. M. Spillane, T. J. Kippenberg, O. J. Painter, and K. J. Vahala, "Ideality in a fiber-taper-coupled microresonator system for application to cavity quantum electrodynamics," Phys. Rev. Lett. **91**, 043,902 (2003).

[44] J. C. Knight, N. Dubreuil, V. Sandoghdar, J. Hare, V. Lefèvre-Sequin, J. M. Raimond, and S. Haroche, "Characterizing whispering-gallery modes in microspheres by direct observation of the optical standing-wave pattern in the near field," Opt. Lett. **21**(10), 698–700 (1996).

[45] J. C. Knight, G. Cheung, F. Jacques, and T. A. Birks, "Phase-matched excitation of whispering-gallery-mode resonances by a fiber taper," Opt. Lett. **22**, 1129–1131 (1997).

[46] M. Eisenmann and E. Weidel, "Single-mode fused biconical couplers for wavelength division multiplexing with channel spacing between 100 and 300nm," IEEE J. Lightwave Tech. **6**, 113–119 (1988).

[47] T. A. Birks and Y. W. Li, "The shape of fiber tapers," IEEE J. Lightwave Tech. **10**(4), 432–438 (1992).

[48] C. P. Michael, M. Borselli, T. J. Johnson, C. Chrystal, and O. Painter, "An optical fiber-taper probe for wafer-scale microphotonic device characterization," Opt. Express **15**(8), 4745–4752 (2007).

[49] S. Sze, *Physics of Semiconductor Devices*, 2nd ed. (John Wiley and Sons, New York, New York, 1981).

[50] W. Shockley and W. Read, "Statistics of the Recombinations of Holes and Electrons," Phys. Rev. **87**(5), 835–842 (1952).

[51] S. Ghandi, "The Theory and Practice of Microelectronics," (1968).

[52] R. Hall, "Electron-hole recombination in Germanium," Phys. Rev. **87**(2), 387 (1952).

[53] A. Othonos, "Probing ultrafast carrier and phonon dynamics in semiconductors," J. Appl. Phys. **83**(4), 1789–1830 (1998).

[54] A. J. Sabbah and D. M. Riffe, "Femtosecond pump-probe reflectivity study of silicon carrier dynamics," Phys. Rev. B **66**(16), 165,217 (2002).

[55] E. Yablonovitch, D. L. Allara, C. C. Chang, T. Gmitter, and T. B. Bright, "Unusually Low Surface-Recombination Velocity on Silicon and Germanium Surfaces," Phys. Rev. Lett. **57**(2), 249–252 (1986).

[56] R. Soref and J. Larenzo, "All-silicon active and passive guided-wave components for $\lambda = 1.3$ and 1.6 μm," IEEE J. Quan. Elec. **22**(6), 873–879 (1986).

[57] N. W. Ashcroft and N. D. Mermin, *Solid State Physics* (Saunders College Publishing, New York, NY, 1976).

[58] P. Butcher and D. Cotter, *The Elements of Nonlinear Optics*, vol. 9 of *Cambridge Studies in Modern Optics* (Cambridge University Press, New York, 1990).

[59] R. A. Soref and B. R. Bennett, "Electrooptical effects in silicon," IEEE J. Quantum Electron. **23**(1), 123–129 (1987).

[60] J. Schmidt, M. Kerr, and A. Cuevas, "Surface passivation of silicon solar cells using plasma-enhanced chemical-vapour-deposited SiN films and thin thermal SiO_2/plasma SiN stacks," Semicond. Sci. Tech. **16**, 167–170 (2001).

[61] M. Haverlag, D. Vender, and G. S. Oehrlein, "Ellipsometric study of silicon surface damage in electron cyclotron resonance plasma etching using CF_4 and SF_6," Appl. Phys. Lett. **61**(24), 2875–2877 (1992).

[62] D. W. Vernooy, V. S. Ilchenko, H. Mabuchi, E. W. Streed, and H. J. Kimble, "High-Q measurements of fused-silica microspheres in the near infrared," Opt. Lett. **23**(4), 247–249 (1998).

[63] M. Cai, G. Hunziker, and K. Vahala, "Fiber-optic add-drop device based on a silica microsphere-whispering gallery mode system," IEEE Photonics Tech. Lett. **11**(6), 686–687 (1999).

[64] M. Cai, O. Painter, and K. J. Vahala, "Observation of critical coupling in a fiber taper to a silica-microsphere whispering-gallery mode system," Phys. Rev. Lett. **85**, 74–77 (2000).

[65] M. Cai and K. Vahala, "Highly efficient optical power transfer to whispering-gallery modes by use of a symmetrical dual-coupling configuration," Opt. Lett. **25**, 260–262 (2000).

[66] D. K. Armani, T. J. Kippenberg, S. M. Spillane, and K. J. Vahala, "Ultra-high-Q toroid microcavity on a chip," Nature **421**, 925 (2003).

[67] D. S. Weiss, V. Sandoghdar, J. Hare, V. Lefevre-Seguin, J.-M. Raimond, and S. Haroche, "Splitting of high- Q Mie modes in-

duced by light backscattering in silica microspheres," Opt. Lett. **20**(18), 1835–1837 (1995).

[68] M. L. Gorodetsky, A. D. Pryamikov, and V. S. Ilchenko, "Rayleigh scattering in high-Q microspheres," J. Opt. Soc. Am. B **17**, 1051–1057 (2000).

[69] B. E. Little, J.-P. Laine, and S. T. Chu, "Surface-Roughness-Induced Contradirectional Coupling in Ring and Disk Resonators," Opt. Lett. **22**, 4–6 (1997).

[70] A. Yariv, *Optical Electronics*, 4th ed. (Saunder College Publishing, Orlando, 1991).

[71] C. A. Barrios, V. R. Almeida, R. R. Panepucci, B. S. Schmidt, and M. Lipson, "Compact Silicon Tunable Fabry-Pérot Resonator With Low Power Consumption," IEEE Photonics Tech. Lett. **16**, 506–508 (2004).

[72] D. V. Lang, "Fast capacitance tansient appartus: Application to ZnO and O centers in GaP $p-n$ junctions," J. Appl. Phys. **45**, 3014–3022 (1974).

[73] D. V. Lang, "Deep-level transient spectroscopy: A new method to characterize traps i semiconductors," J. Appl. Phys. **45**, 3023–3032 (1974).

[74] J. Linnros, "Carrier lifetime measurements using free carrier absorption transients. II. Lifetime mapping and effects of surface recombination," J. Appl. Phys. **84**(1), 284–291 (1998).

[75] A. Chantre, G. Vincent, and D. Bois, "Deep-level optical spectroscopy in GaAs," Phys. Rev. B **23**(10), 5335–5358 (1981).

[76] I. M. P. Aarts, B. Hoex, A. H. M. Smets, R. Engeln, W. M. M. Kessels, and M. C. M. van de Sanden, "Direct and highly sensitive measurement of defect-related absorption in amorphous silicon thin films by cavity ringdown spectroscopy," Appl. Phys. Lett. **84**(16), 3079–3081 (2004).

[77] W. B. Jackson and N. M. Amer, "Direct measurement of gap-state absorption in hydrogenated amorphous silicon by photothermal deflection spectroscopy," Phys. Rev. B **25**(8), 5559–5562 (1982).

[78] G. Amato and F. Fizzotti, "Gap-states distribution in amorphous-silicon films as obtained by photothermal deflection spectroscopy," Phys. Rev. B **45**(24), 14,108–14,113 (1992).

[79] P. Blood, "On the Dimensionality of Optical Absorption, Gain, and Recombination in Quantum-Confined Structures," IEEE J. Quan. Elec. **36**(3), 354–362 (2000).

[80] F. Li, M. K. Balazs, and S. Anderson, "Effects of Ambient and Dissolved Oxygen Concentration in Ultrapure Water on Initial

Growth of Native Oxide on a Silicon (100) Surface," J. Electrochem. Soc. **152**(8), G669–G673 (2005).

[81] D. Fenner, D. Biegelsen, and R. Bringans, "Silicon surface passivation by hydrogen termination: A comparative study of preparation methods," J. Appl. Phys. **66**(1), 419–424 (1989).

[82] Y. J. Chabal, G. S. Higashi, and K. Raghavachari, "Infrared spectroscopy of Si(111) and Si(100) surfaces after HF treatment: Hydrogen termination and surface morphology," J. Vac. Sci. Tech. A **7**(3), 2104–2109 (1989).

[83] D. K. Sparacin, S. J. Spector, and L. C. Kimerling, "Silicon waveguide sidewall smoothing by wet chemical oxidation," IEEE J. Lightwave Technol. **23**(8), 2455–2461 (2005).

[84] S. Wolf and R. N. Tauber, *Silicon Processing for the VLSI era* (Lattice Press, Sunset Beach, California, 1986).

[85] W. Kern, ed., *Handbook of semiconductor wafer cleaning technology : science, technology, and applications* (Noyes Publications, Park Ridge, NJ, 1993).

[86] W. Kern and D. A. Puotinen, "Cleaning solutions based on hydrogen peroxide for use in silicon semiconductor technology," RCA Rev. **31**, 186 (1970).

[87] S. Petitdidier, V. Bertagna, N. Rochat, D. Rouchon, P. Besson, R. Erre, and M. Chemla, "Growth mechanism and characteri-

zation of chemical oxide films produced in peroxide mixtures on Si(100) surfaces," Thin Solid Films **476**(1), 51 (2005).

[88] H. Kobayashi, Y. Yamashita, Y. Nakato, T. Komeda, and Y. Nishioka, "Interface states at ultrathin oxide/Si(111) interfaces obtained from x-ray photoelectron spectroscopy measurements under biases," Appl. Phys. Lett. **69**(15), 2276–2278 (1996).

[89] M. Borselli, T. J. Johnson, and O. Painter, "Accurate measurement of scattering and absorption loss in microphotonic devices," Opt. Lett. **32**, 2954–2956 (2007).

[90] Y. Yamashita, A. Asano, Y. Nishioka, and H. Kobayashi, "Dependence of interface states in the Si band gap on oxide atomic density and interfacial roughness," Phys. Rev. B **59**(24), 872–881 (1999).

[91] Y. Yamashita, K. Namba, Y. Nakato, , Y. Nishioka, and H. Kobayashi, "Spectroscopic observation of interface states of ultrathin silicon oxide," J. Appl. Phys. **79**(9), 7051–7057 (1996).

[92] Y. Yamashita, K. Namba, Y. Nakato, , Y. Nishioka, and H. Kobayashi, "Spectroscopic observation of interface states of ultrathin silicon oxide," J. Appl. Phys. **79**(9), 7051–7057 (1996).

[93] J. Zhao, A. Wang, P. Altermatt, and M. A. Green, "Twenty-four percent efficient silicon solar cells with double layer antireflection

coatings and reduced resistance loss," Appl. Phys. Lett. **66**, 3636–3638 (1995).

[94] M. McCann, K. Weber, and A. Blakers, "Surface Passivation by Rehydrogenation of Silicon-nitride-coated Silicon Wafers," Progress in Photovoltaics: Research and Applications **13**, 195–200 (2005).

[95] G. Bemski, "Quenched-In Recombination Centers in Silicon," Phys. Rev. **103**(3), 567–569 (1956).

[96] M. Borselli, T. J. Johnson, and O. Painter, "Measuring the role of surface chemistry in silicon microphotonics," Appl. Phys. Lett. **88**, 131,114 (2006).

[97] T. Lauinger, A. G. Aberle, and R. Hezel, "Comparision of direct and remote PECVD silicon nitride films for low-temperature surface passivation of p-type crystalline silicon," in *Proceedings of the 14th European Photovoltaic Solar Energy Conference*, pp. 853–856 (Stephens, Barcelona, 1997).

[98] M. Soltani, S. Yegnanarayanan, and A. Adibi, "Ultra-high Q planar silicon microdisk resonators for chip-scale silicon photonics," Opt. Express **15**, 4694–4704 (2007).

[99] R. Claps, V. Raghunathan, D. Dimitropoulos, and B. Jalali, "Influence of nonlinear absorption on Raman amplification in silicon waveguides," Opt. Express **12**(12), 2774–2780 (2004).

[100] A. Cutolo, M. Iodice, P. Spirito, and L. Zeni, "Silicon Electro-Optic Modulator Based on a Three Terminal Device Integrated in a Low-Loww Single-Mode SOI Waveguide," IEEE J. Lightwave Tech. **15**, 505–518 (1997).

[101] W. D. Walters and A. P. Knights, "Application of defect engineering to silicon Raman lasers and amplifiers," **20**, 48–53 (2007).

[102] M. Borselli, T. J. Johnson, C. P. Michael, M. D. Henry, and O. Painter, "Surface encapsulation for low-loss silicon photonics," Appl. Phys. Lett. **91**, 131,117 (2007).

[103] G. J. Norga, M. Platero, K. A. Black, A. J. Reddy, J. Michel, and L. C. Kimmerling, "Detection of Metallic Contaminants on Silicon by Surface Sensitive Minority Carrier Lifetime Measurements"," J. Electrochem. Soc. **145**(7), 2602–2607 (1998).

[104] J. Chazalviel, M. Stefenel, and T. Truong, "Surface states induced by metal atoms at the Si/electrolyte interface," Surface Science **134**(3), 865 – 885 (1983).

[105] M. Kuisl and E. Sasse, "Gold on silicon surfaces," Surface Science **92**(2-3), 681 – 692 (1980).

[106] W. M. Bullis, "Properties of gold in silicon," Solid-State Electronics **9**(2), 143 – 168 (1966).

[107] P. A. Temple and C. E. Hathaway, "Multiphonon Raman Spectrum of Silicon," Phys. Rev. A **7**, 3685 (1973).

[108] R. A. T.R. Hart and B. Lax, "Temperature dependence of Raman scattering in silicon," Phys. Rev. B **1**, 638–642 (1970).

[109] J. Sandercock, "Brillouin-scattering measurements on silicon and germanium," Phys. Rev. Lett. **28**, 237–240 (1972).

[110] G. P. Agrawal, *Nonlinear Fiber Optics*, 4th ed. (Academic Press, Boston, MA, 2007).

[111] R. W. Boyd, D. J. Gauthier, A. L. Gaeta, and A. E. Willner, "Maximum time delay achievable on propagation through a slow-light medium," Physical Review A (Atomic, Molecular, and Optical Physics) **71**(2), 023801 (pages 4) (2005).

[112] G. Priem, P. Dumon, W. Bogaerts, D. V. Thourhout, G. Morthier, and R. Baets, "Optical bistability and pulsating behaviour in Silicon-On-Insulator ring resonator structures," Opt. Express **13**(23), 9623–9628 (2005).

[113] G. Cocorullo and I. Rendina, "Thermo-optical modulation at 1.5 μm in silicon etalon," IEE Elec. Lett. **28**, 83–85 (1992).

[114] S. G. Johnson, M. Ibanescu, M. A. Skorobogatiy, O. Weisberg, J. D. Joannopoulos, and Y. Fink, "Perturbation theory for Maxwell's equations with shifting material boundaries," Phys. Rev. E **65**, 066,611 (2002).

[115] T. Carmon, L. Yang, and K. J. Vahala, "Dynamical thermal behavior and thermal self-stability of microcavities," Opt. Express **12**, 4742–4750 (2004).

[116] M. Notomi, A. Shinya, K. Yamada, J. Takahashi, C. Takahashi, and I. Yokohama, "Structural tuning of guiding modes of line-defect waveguides of silicon-on-insulator photonic crystal slabs," IEEE J. Quan. Elec. **38**(7), 736–742 (2002).

[117] M. Notomi, A. Shinya, S. Mitsugi, G. Kira, E. Kuramochi, and T. Tanabe, "Optical bistable switching action of Si high-Q photonic-crystal nanocavities," Opt. Express **13**(7), 2678–2687 (2005).

[118] S. F. Preble, Q. Xu, and M. Lipson, "Changing the colour of light in a silicon resonator," Nature Photon. **1**, 293–296 (2007).

[119] V. R. Almeida, R. R. Panepucci, and M. Lipson, "Nanotaper for compact mode conversion," Opt. Lett. **28**, 1302–1304 (2003).

[120] H. M. Gibbs, *Optical Bistability: Controlling Light with Light*, 1st ed. (Academic Press, Orlando, 1985).

[121] K. J. Vahala, "Optical Microcavities," Nature **424**, 839–846 (2003).

[122] S. Wiggins, *Introduction to Applied Nonlinear Dynamical Systems and Chaos*, 2nd ed. (Springer-Verlag, New York, 2003).

[123] K. Aubin, M. Zalalutdinov, T. Alan, R. Reichenbach, R. Rand, A. Zehnder, J. Parpia, and H. Craighead, "Limit Cycle Oscillations in CW Laser Driven NEMS," J. Microelectromech. S. **13**, 1018–1026 (2004).

[124] Luxtera, "Luxtera Inc. Announces Worlds First 10Gbit CMOS Optical Ring Modulator," (2005). URL `http://www.luxtera.com/2005-08-15.html`.

[125] S. Noda, N. Yamamoto, M. Imada, and H. Kobayashi, "Alignment and Stacking of Semiconductor Photonic Bandgaps by Wafer-Fusion," IEEE J. Lightwave Tech. **17**(11), 1948–1955 (1999).

[126] E. Palick, ed., *Handbook of optical constants of solids* (Academic Press, Boston, MA, 1985).

[127] N. A. Nazarova, G. I. Romanova, and A. D. Yaskov, "Refractometric characteristics of silicon," **55**(44) (1988).

[128] M. Dinu, F. Quochi, and H. Garcia, "Third-order nonlinearities in silicon at telecom wavelengths," Appl. Phys. Lett. **82**(18), 2954–2956 (2003).

[129] S. H. Strogatz, *Nonlinear Dynamics and Chaos*, 1st ed. (Westview, Cambridge, MA, 1994).

[130] T. Tel and M. Gruiz, *Chaotic Dynamics:An Introduction Based on Classical Mechanics* (Cambrige University Press, New York, NY, 2006).

[131] P. Horowitz and W. Hill, *The Art of Electronics*, 2nd ed. (Cambridge University Press, New York, NY, 1989).

[132] R. Claps, D. Dimitropoulos, Y. Han, and B. Jalali, "Observation of Raman emission in silicon waveguides at 1.54μm," Opt. Express **11**(15), 1731–1739 (2002).

[133] A. Liu, H. Rong, M. Paniccia, O. Coen, and D.Hak, "Net optical gain in a low loss silicon-on-insulator waveguide by stimulated Raman scattering," Opt. Express **12**, 4261–4268 (2004).

[134] T. Liang and H. Tsang, "Efficient Raman amplification in silicon-on-insulator waveguides," Appl. Phys. Lett. **84**, 3343–3345 (2004).